Quantifying the localization uncertainty of modulation enhanced single-molecule localization microscopy

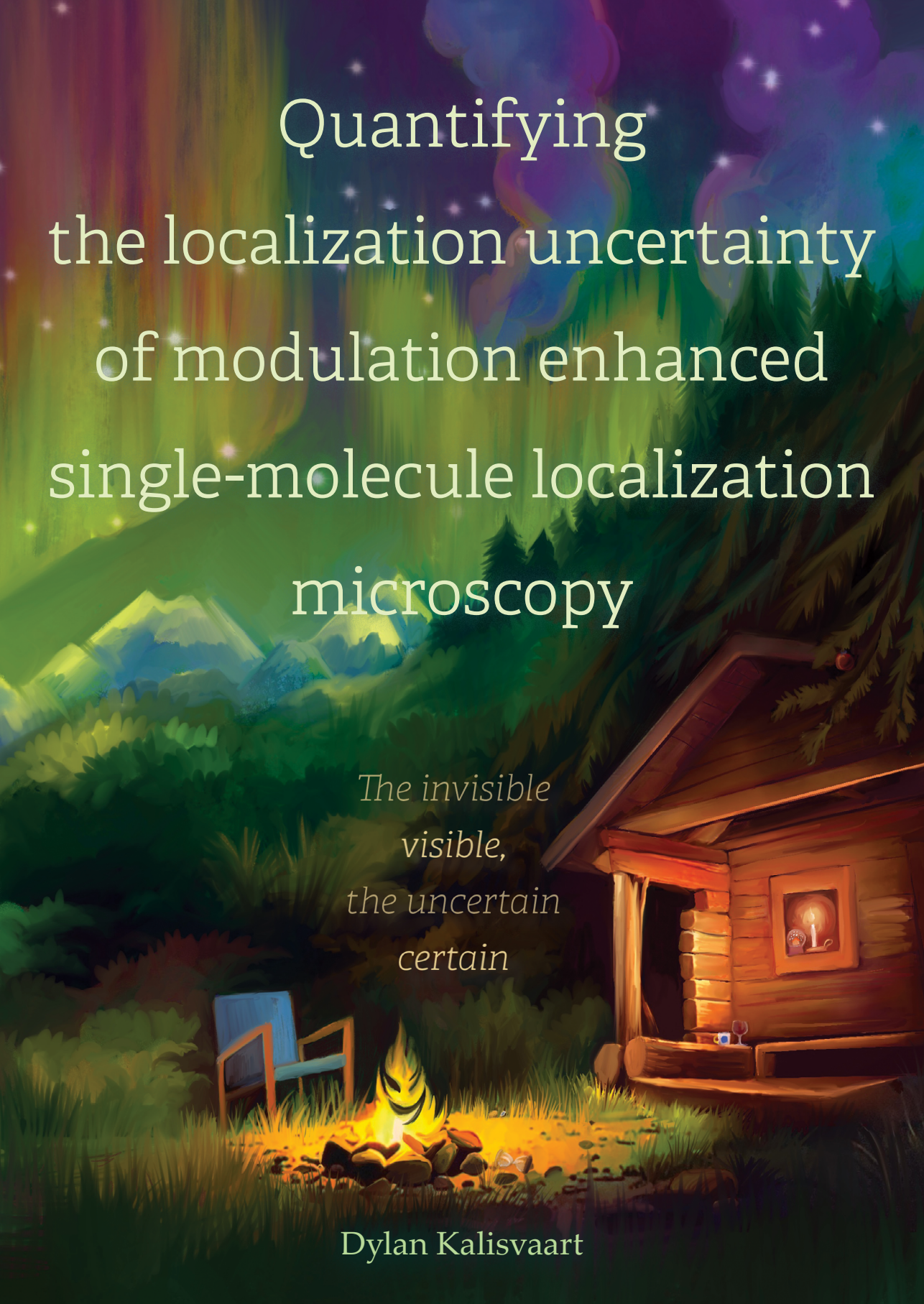

Dylan Kalisvaart

Quantifying the localization uncertainty of modulation enhanced single-molecule localization microscopy

The invisible visible, the uncertain certain

Quantifying the localization uncertainty of modulation enhanced single-molecule localization microscopy

The invisible visible, the uncertain certain

Dissertation

for the purpose of obtaining the degree of doctor
at Delft University of Technology
by the authority of the Rector Magnificus,
prof. dr. ir. H. Bijl,
chair of the Board for Doctorates
to be defended publicly on
Thursday 26 March 2026 at 17:30

by

Dylan Kalisvaart

Master of Science in Systems and Control,
Delft University of Technology, the Netherlands,
born in The Hague, the Netherlands

This dissertation has been approved by the promotors.

Composition of the doctoral committee:

Rector Magnificus	chairperson
Dr. A. Jakobi	Delft University of Technology, *promotor*
Dr. ir. C.S. Smith	Delft University of Technology, *promotor*
Independent members:	
Prof. dr. B. Rieger	Delft University of Technology
Prof. dr. K. A. Lidke	University of New Mexico, United States of America
Prof. dr. J. Ries	University of Vienna, Austria
Dr. F. Balzarotti	Research Institute of Molecular Pathology, Austria
Prof. dr. W. M. J. M. Coene	Delft University of Technology, *reserve member*

This research was funded by the Delft University of Technology through the TU Delft AI Initiative and additionally supported by the Netherlands Organization for Scientific Research (NWO) under NWO START-UP project no. 740.018.015 and NWO Veni project no. 16761.

Keywords: super-resolution microscopy, single-molecule localization microscopy, modulation enhanced single-molecule localization microscopy, MINFLUX, SIMFLUX, image scanning microscopy, spinning disk confocal microscopy, multiple emitter localization, localization uncertainty, localization precision, Cramér-Rao lower bound, reversible jump Markov Chain Monte Carlo, Van Trees inequality

Printed by: Ridderprint, 2952 BD Alblasserdam, The Netherlands

Cover by: Cover art by Anna Sieben in Leeuwarden, 2026

ISBN 978-94-6518-245-2

An electronic version of this dissertation is available at
http://repository.tudelft.nl/.

In the 20^{th} century, it was the lenses which were decisive. And the lens makers were the "kings". One had to go to them and ask them for the best lenses to get the best resolution. But how is it today? No, it is not the lens makers. This resolution game is not about lenses anymore.

Stefan Walter Hell, *Nobel Lecture*

Contents

Summary

To assist in medicine development and microbiological research, microscopy has been an important tool ever since the seventeenth century. Fluorescence microscopy is able to provide the specificity and contrast needed for biological imaging, and the physical resolution limit caused by diffraction can be circumvented through super-resolution microscopy. By combining modulated excitation with sparse activation of fluorescent emitters and subsequent localization of emitter positions, modulation enhanced single-molecule localization microscopy achieves a localization precision in the order of magnitude of nanometres to Ångströms, thereby making the invisible visible.

While these super-resolution methods allow us to access the nanoscale, their findings are accompanied by the statistical uncertainty about whether the molecule positions that we retrieve correspond to the true underlying positions of emitters that are truly present in the sample. A fundamental objective of super-resolution microscopy is thus to give certainty about the localization uncertainty with which the position of a single molecule can be determined.

To make the uncertain certain in single-molecule localization, the Cramér-Rao lower bound is commonly used. The Cramér-Rao lower bound represents the theoretical minimum uncertainty with which unbiased estimators can localize emitters. However, the Cramér-Rao lower bound leads to narrowly applicable, improperly represented or mathematically incorrect characterizations of the localization precision of modulation enhanced single-molecule localization microscopy.

To address this, new and generalizable image formation models are needed. In addition, we need to develop statistical tools that represent the full estimator distribution, as well as the uncertainty of localization methods that use biased estimators.

In this dissertation, we address these issues through three major contributions. As our first contribution, we derive a new and generalizable image formation model that integrates modulation enhanced localization in existing setups that use a spinning disk in the illumination- and emission paths, leading to the theoretical design of a new method called SpinFlux. In the SpinFlux analysis, emitters are localized in the recordings from a sequence of individual pattern acquisitions, taking knowledge about the pattern into account. SpinFlux shows its merit when the excitation intensity is modulated to incorporate the maximum amount of information, reaching a 3.5-fold local precision improvement over single-molecule localization microscopy when using donut-shaped illumination patterns. Combined with the versatility of the image formation model to incorporate arbitrary illumination patterns, this makes SpinFlux the method of choice for local refinements of the localization precision.

Secondly, we analyse the occurrence of multimodality in three-dimensional multiple emitter imaging by reconstructing the full posterior distribution of localization. We develop a Bayesian three-dimensional localization method called three-dimensional reversible jump Markov chain Monte Carlo, which approximates the posterior density of

emitter positions rather than giving point estimates. We show that astigmatic multiple emitter imaging results in a multimodal posterior distribution when two emitters are separated by less than the standard deviation of the in-focus point spread function, which causes ambiguous solutions to the estimation problem. This motivates the importance of including appropriately chosen uncertainty measures in localization algorithms. In particular, estimation of the full posterior distribution makes it possible to detect cases where the localization uncertainty for individual emitters is not accurately represented by Gaussian uncertainty ellipses, which would be misrepresented by the Cramér-Rao lower bound.

Lastly, we quantify and analyse the localization precision of iterative localization microscopy methods, such as MINFLUX. These methods are able to locally improve the localization precision around an emitter position by using prior information derived from measurements in earlier iterations. As the Cramér-Rao lower bound requires estimators to be unbiased, it cannot incorporate prior information, making it inapplicable to iterative localization microscopy. However, the Bayesian Van Trees inequality circumvents this mathematical limitation, and is therefore an appropriate bound to analyse iterative localization microscopy. By taking modulation- and background imperfections into account, we show that the improvement of iterative methods over single-molecule localization is at most fivefold. The Van Trees inequality allows us to nuance existing precision limits for methods resembling MINFLUX when affected by modulation- and background imperfections, by showing that the precision of these methods is not maximized by minimizing the pattern distance, nor exponentially improved by increasing the iteration count.

Based on these findings we argue that, in order to reflect the statistical uncertainty of the localization process, emitter position estimates in single-molecule localization microscopy should be presented in the context of the estimation uncertainty. Image formation models and uncertainty quantification should be tailored to the application, letting the particularities of the application determine the choice of appropriate mathematical tools. As shown in this dissertation, this attitude towards uncertainty leads to new experimental methods to improve the localization precision, and it advances our fundamental understanding of localization uncertainty in super-resolution microscopy.

Samenvatting

Om de ontwikkeling van medicijnen en microbiologisch onderzoek te ondersteunen, is microscopie al sinds de zeventiende eeuw een belangrijk hulpmiddel. Fluorescentiemicroscopie kan de specificiteit en het contrast leveren die nodig zijn voor biologische beeldvorming, en de fysische resolutiegrens die wordt veroorzaakt door diffractie kan worden omzeild door middel van superresolutiemicroscopie. Door gemoduleerde excitatie te combineren met het beperkt activeren van fluorescerende emitters en vervolgens de emitterposities te lokaliseren, bereikt modulatie-versterkte single-molecule lokalisatiemicroscopie een lokalisatieprecisie in de orde van nanometers tot Ångströms, waardoor het onzichtbare zichtbaar wordt.

Hoewel deze superresolutiemethoden ons toegang geven tot de nanoschaal, worden hun bevindingen vergezeld door de statistische onzekerheid over of de gevonden molecuulposities overeenkomen met de werkelijke onderliggende posities van emitters die daadwerkelijk aanwezig zijn in het specimen. Een fundamenteel doel van superresolutiemicroscopie is dan ook om zekerheid te verschaffen over de lokalisatie-onzekerheid waarmee de positie van een enkel molecuul kan worden bepaald.

Om het onzekere zeker te maken in single-molecule lokalisatie wordt vaak de Cramér-Rao ondergrens gebruikt. De Cramér-Rao ondergrens vertegenwoordigt de theoretische minimale onzekerheid waarmee zuivere schatters emitters kunnen lokaliseren. Echter, de Cramér-Rao ondergrens leidt tot beperkt toepasbare, onjuist weergegeven of wiskundig incorrecte karakteriseringen van de lokalisatieprecisie van modulatie versterkte single-molecule lokalisatiemicroscopie.

Om dit aan te pakken, zijn nieuwe en generaliseerbare beeldvormingsmodellen nodig. Daarnaast moeten we statistische hulpmiddelen ontwikkelen die de volledige verdeling van de schatter weergeven, alsmede de onzekerheid van lokalisatiemethoden met onzuivere schatters.

In dit proefschrift verhelpen we deze problemen met drie belangrijke bijdragen. In onze eerste bijdrage leiden we een nieuw en generaliseerbaar beeldvormingsmodel af dat modulatie versterkte lokalisatie integreert in bestaande opstellingen die een draaiende schijf gebruiken in de belichtings- en emissiepaden. Dit leidt tot het theoretisch ontwerp van een nieuwe methode genaamd SpinFlux. In de SpinFlux-analyse worden emitters gelokaliseerd in opnamen uit een reeks individuele patroonregistraties, waarbij rekening wordt gehouden met kennis over het patroon. SpinFlux toont zijn waarde wanneer de excitatie-intensiteit wordt gemoduleerd om de maximale hoeveelheid informatie te incorporeren, wat resulteert in een 3,5-voudige lokale verbetering van de precisie ten opzichte van single-molecule lokalisatiemicroscopie bij gebruik van donutvormige belichtingspatronen. Gecombineerd met de veelzijdigheid van het beeldvormingsmodel om willekeurige belichtingspatronen te incorporeren, maakt dit SpinFlux bij uitstek tot de methode voor lokale verfijningen van de lokalisatieprecisie.

Ten tweede analyseren we het zich voordoen van multimodaliteit in driedimensionale meerdere-emitterbeeldvorming door de volledige a-posteriori kansverdeling van de lokalisatie te reconstrueren. We ontwikkelen een Bayesiaanse driedimensionale lokalisatiemethode, genaamd driedimensionale reversible jump Markov chain Monte Carlo, die de a-posteriori kansdichtheid van emitterposities benadert in plaats van puntschattingen te geven. We tonen aan dat astigmatische meerdere-emitterbeeldvorming resulteert in een multimodale a-posteriori kansverdeling wanneer twee emitters dichter bij elkaar liggen dan de standaardafwijking van de in-focus puntspreidingsfunctie, wat meerduidige oplossingen voor het schattingsprobleem veroorzaakt. Dit onderstreept het belang van het opnemen van passend gekozen onzekerheidsmaten in lokalisatie-algoritmen. In het bijzonder maakt het schatten van de volledige a-posteriori kansverdeling het mogelijk om gevallen te detecteren waarin de lokalisatie-onzekerheid van individuele emitters niet nauwkeurig wordt weergegeven door Gaussische onzekerheidsellipsen, wat verkeerd zou worden weergegeven door de Cramér-Rao ondergrens.

Ten slotte kwantificeren en analyseren we de lokalisatieprecisie van iteratieve lokalisatiemicroscopiemethoden, zoals MINFLUX. Deze methoden kunnen de lokalisatieprecisie lokaal verbeteren rond een emitterpositie door gebruik te maken van a-priori kennis die is afgeleid van metingen in eerdere iteraties. Omdat de Cramér-Rao ondergrens vereist dat schatters zuiver zijn, kan deze geen a-priori kennis verwerken, waardoor deze niet toepasbaar is op iteratieve lokalisatiemicroscopie. Echter, de Bayesiaanse Van Trees ongelijkheid omzeilt deze wiskundige beperking en is daarom een geschikte grens om iteratieve lokalisatiemicroscopie te analyseren. Door modulatie- en achtergrondimperfecties in acht te nemen, tonen we aan dat de verbetering van iteratieve methoden ten opzichte van single-molecule lokalisatie maximaal vijfvoudig is. De Van Trees ongelijkheid stelt ons in staat om bestaande precisiegrenzen te nuanceren voor methodes zoals MINFLUX wanneer ze worden beïnvloed door modulatie- en achtergrondonvolkomenheden, door te laten zien dat de precisie van deze methoden niet wordt gemaximaliseerd door de patroonafstand te minimaliseren, noch exponentieel wordt verbeterd door het aantal iteraties te verhogen.

Op basis van deze bevindingen beargumenteren wij dat, om de statistische onzekerheid van het lokalisatieproces weer te geven, schattingen van emitterposities in single-molecule lokalisatiemicroscopie gepresenteerd moeten worden in de context van de schattingsonzekerheid. Beeldvormingsmodellen en onzekerheidskwantificatie moeten worden afgestemd op de toepassing, waarbij de bijzonderheden van de toepassing de keuze voor de juiste wiskundige hulpmiddelen bepalen. Zoals in dit proefschrift wordt aangetoond, leidt deze houding ten opzichte van onzekerheid tot nieuwe experimentele methoden om de lokalisatieprecisie te verbeteren en draagt zij bij aan ons fundamentele begrip van lokalisatie-onzekerheid in superresolutiemicroscopie.

1

Introduction

Denn die einen sind im Dunkeln
Und die andern sind im Licht.
Und man siehet die im Lichte
Die im Dunkeln sieht man nicht.

Bertolt Brecht, *Die Dreigroschenoper*

1

In October 2020, on the first day of my doctoral studies, the world was in the middle of the coronavirus disease-19 (COVID-19) pandemic. COVID-19 is a respiratory infectious disease, causing symptoms such as fever, coughing, fatigue, breathing difficulties and the loss of smell or taste [1]. This disease, caused by the severe acute respiratory syndrome coronavirus 2 (SARS-CoV-2), broke out in December 2019 in Wuhan. Within a few months COVID-19 spread over the world, reaching the Netherlands in March 2020 [2].

The following years, particularly from 2020 to 2022, were negatively characterized by overcrowded hospitals, social isolation measures and economic malaise. As per July 2025, a cumulative total of 778,407,760 cases of COVID-19 were reported worldwide since January 2020, resulting in 7,098,440 confirmed cases of death [3] with estimates showing that the total amount of casualties is three to five times higher [4]. For survivors, COVID-19 can have long-term effects on the brain, impacting memory, cognitive and executive functions, as well as mental health, causing fatigue, anxiety and mood disorders [5]. Social distancing measures changed the way in which people interacted [6], contributing to an increase in loneliness, depression and anxiety, which has been shown to have disproportionally affected adolescents and young adults [7, 8]. Economically, COVID-19 caused a global recession, with worldwide effects on, for example, gross domestic products, labour markets, productivity and consumption [9].

The COVID-19 pandemic teaches us that medical, societal and economic disasters on a global scale can be caused by a source as tiny as SARS-CoV-2, which is approximately 100 nm in size [10]. To prepare ourselves for a future pandemic, we should thus improve our biological understanding of how cells, bacteria, viruses and proteins function and interact with each other. We can do so by looking at these structures on the micro- to nanoscale. This requires the ability to see them, despite them being invisible to the naked eye (see Fig 1.1*a*). But how can we make the invisible visible?

1.1. A short history of optical microscopy

To the reader of this dissertation who, assuming causality, lives in 2025 or beyond, the answer to this question will likely be unsurprising. We can already image biology at the micro- to nanoscale with optical microscopes. Yet there is a tremendous difference between the microscopes many people use in high schools, and the challenges and designs that led to the state-of-the-art microscopes available now. We will therefore give a concise historical overview of the challenges encountered by researchers on the journey to image the nanoscale, as well as how these challenges were solved (see Fig. 1.1*b*).

1.1.1. Magnification: the first microscopes

As a first step to zoom in to the microscale, we need a way to magnify objects that are too small to be seen by eye. Discussion about the physics of magnification can be traced back to ancient history, where the Greeks and Romans were already aware of this concept. For example around the years 62-64, Seneca the Younger comments in *Natural Questions* that “Letters, although small and dark, appear larger and clearer through a glass ball filled with water” [11]. Throughout the following era, we would see the development of the first lenses, eyeglasses and magnifying glasses.

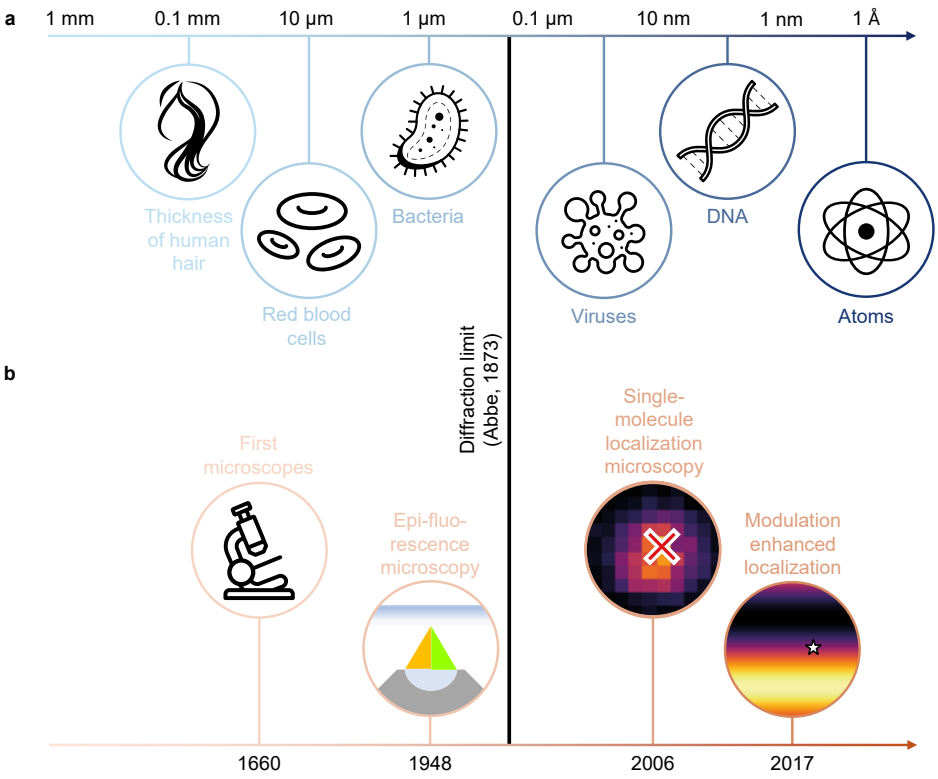

Figure 1.1: Examples of microbiological structures, compared against a timeline of important discoveries in microscopy that made these structures visible. (*a*) Biological and physical structures across eight orders of magnitude, spanning from the millimetre-level to the Ångström-level. (*b*) Timeline of selected breakthrough microscopes, which made it possible to image increasingly small structures.

Around 1600, the first compound microscope was developed, that being an assembly of two lenses which are used together to magnify an object [12]. It is not clear who exactly invented the first compound microscope, but the Dutch spectacle maker Zacharias Janssen is often credited for the invention in 1590. These first compound microscopes were able to magnify objects, limited to about 20 to 30 times its physical size.

Throughout the seventeenth century, microscopes were used to discover various biological microstructures [13, 14]. Around 1660, fellow Delftian Antonie van Leeuwenhoek was able to grind his own lenses, thereby developing a single-lens microscope with which he could achieve magnifications of about 300 times. Using this microscope, Van Leeuwenhoek was able to discover visible life at the microscale, for example by visualizing bacteria. Independently from Van Leeuwenhoek, Jan Swammerdam and Marcello Malpighi respectively observed red blood cells and blood capillaries. In 1665, Robert Hooke popularized microscopy with his book *Micrographia*, in which he collected illustrations of objects he observed with his compound microscope. Together, the discoveries of the seventeenth century provided key evidence to advance the knowledge about

life, thereby firmly connecting microscopy to biological research.

1.1.2. Contrast, specificity and sensitivity: fluorescence microscopy

To enable biological discoveries within complex biological structures, magnification no longer is the sole function a microscope needs to fulfil. Specifically, due to effects as refractive index mismatches and scattering, biological microstructures appear opaque, resulting in images with low contrast [15]. That means that structures of interest are poorly distinguishable from background or adjacent structures.

Fluorescence microscopy is the modality of choice to improve image contrast [16, 17]. By labelling structures of interest in a sample with a fluorescent dye and imaging only the emitted fluorescence signal on a detector, fluorescence microscopy is able to achieve enhanced contrast as background illumination and unlabelled, out-of-interest structures can effectively be removed from the image. Furthermore, it has the ability to image only a single type of fluorescent label, therefore having high specificity. Lastly, fluorescence microscopy is sensitive enough to detect structures as small as single molecules, which would ultimately be demonstrated by William Moerner and Lothar Kador in 1989 [18] as well as by Michel Orrit and Jacky Bernard in 1990 [19].

The scientific origins of fluorescence can be traced back to the nineteenth century [20, 21]. In 1833, David Brewster illuminated chlorophyll and found out that this caused it to emit light, specifically of a different colour than the illumination light. Later, in 1845, Frederik Herschel found a similar result for a quinine solution. These findings were explained in 1852 by George Stokes, who himself repeated the effect while experimenting with a fluoride solution, leading to the name *fluorescence*. In Stokes' namesake, the property that light emitted by a fluorophore is of a longer wavelength than the excitation light is now known as the Stokes shift.

Over the course of the subsequent century, the phenomenon of fluorescence found its way into various microscope designs [16, 20]. Of particular interest for the purpose of this dissertation is the development of the epi-fluorescence microscope, as shown in Fig. 1.2*a*. In this type of microscope, excitation light enters the sample on the same side as emission light is captured by the microscope. Inventions by Evgenii Brumberg in 1948 [22] and Johan Ploem in 1962 [23] resulted in epi-fluorescence microscopes that made use of a dichroic mirror. The defining feature of a dichroic mirror is that depending on the wavelength, incoming light is either reflected or transmitted. Due to this property, excitation and emission light can be separated from each other by choosing the passband of the dichroic mirror. In this way, only emitted light from fluorophores can reach the detector, while excitation light is blocked. This results in the favourable contrast, specificity and sensitivity properties that characterize fluorescence microscopy.

For biological applicability of the fluorescence microscope, it was necessary to find fluorophores that could be integrated in microbiological structures for labelling, while also being bright enough to be clearly visible on a detector. A major breakthrough here came in 1962 by Osamu Shimomura and his collaborators, who discovered and isolated the green fluorescent protein (GFP) as a by-product when attempting to extract the luminescent protein aequorin from *Aequorea victoria* jellyfish [24].

At the time, GFP had no significant application [25]. This changed forty years later, when Douglas Prasher and colleagues were able to clone complementary deoxyribonu-

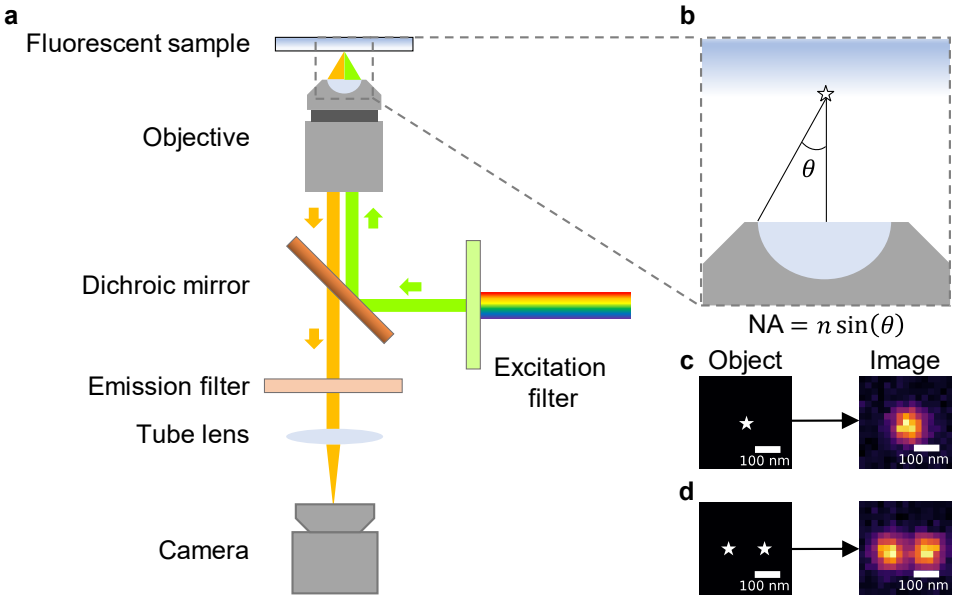

Figure 1.2: Diffraction-limited imaging with an epi-fluorescence microscope. (*a*) Design of an epi-fluorescence microscope. Excitation light consisting of various wavelengths enters the microscope through the excitation filter, which filters out wavelengths outside of the absorption spectrum of the fluorophore. The dichroic mirror reflects the excitation light into the fluorescent sample. Emission light from the sample is captured by the objective and passes through the dichroic mirror and emission filter. Lastly, the tube lens focuses the emission light onto the camera sensor. (*b*) The numerical aperture of the objective is defined by the refractive index of the immersion medium n and the objective half-angle θ. (*c*) When imaging a point source, the resulting image cannot be refocused into an infinitesimally small spot due to diffraction. Instead, the object intensity will be spread out over the image plane, forming an intensity distribution that is determined by the diffraction limit (see Eq. (1.1)). This intensity distribution is called the point spread function. (*d*) Diffraction limits the spatial resolution of an imaging system, as the images of two point sources will start overlapping when they move closer together.

cleic acid (DNA) of GFP [26]. The application of this finding was found in 1994, first by the group of Martin Chalfie and Douglas Prasher [27], and a month later it was also reported by Satoshi Inouye and Frederick Tsuji [28]. Both groups found that expressing the complementary DNA of GFP in *Escherichia coli* (*E. coli*) resulted in the production of a protein of which the excitation and emission bandwidths are effectively equal to that of GFP. Research by the team of Roger Tsien [29] discovered a mutant of GFP, which had increased emission intensity and photostability compared to GFP. Furthermore, the peak excitation frequency of this mutant changed, which made it compatible with commonly available filters. Together, these improvements made GFP useful in practice for fluorescence microscopy. For the discovery, expression and development of GFP, the Nobel Prize in Chemistry of 2008 was awarded to Shimomura, Chalfie and Tsien [30].

1.1.3. Diffraction: super-resolution microscopy

Having addressed the issues of contrast, specificity and sensitivity in biology, we aim to zoom in beyond the microscale. We encounter another roadblock when trying to image the nanoscale: the physics of light itself. Specifically, due to the wave nature of light, diffraction occurs when light propagates through an aperture [31, 32], such as the microscope objective in Fig. 1.2*a*. Therefore when imaging an infinitesimally small object, called a point source, the resulting image cannot be refocused into an infinitesimally small spot. Instead, the object intensity will be spread out over the image plane, forming an intensity distribution that is determined by properties of the optical system. This intensity distribution is called the point spread function (PSF), and it describes the image of a point source when imaged with a particular optical system (see Fig. 1.2*c*). As every optical system is affected by diffraction, a diffraction-limited PSF is the limit of the image intensity distribution. Any optical disturbances, such as phase aberrations due to manufacturing or alignment imperfections of the optical components, can only further distort the PSF.

Diffraction limits the spatial resolution of an optical system. Let us define spatial resolution as the minimum distance two point sources need to be separated from each other, for them to be individually distinguishable in the image plane. Due to the effects of diffraction, the images of two point sources will start overlapping when they move closer together (see Fig. 1.2*d*), thereby limiting the spatial resolution. This resolution limit is called the diffraction limit, as described by Ernst Abbe in 1873 [33]. The Abbe limit represents the maximum spatial frequency, beyond which spatial frequencies can no longer pass through the objective of the microscope due to diffraction. It is given by

$$d = \frac{\lambda_{\text{em}}}{2\text{NA}}, \tag{1.1}$$

where d describes the diffraction-limited spatial resolution, λ_{em} is the wavelength of emission light and $\text{NA} = n\sin(\theta)$ describes the numerical aperture of the objective, given by the refractive index of the immersion medium n and the objective half-angle θ (see Fig. 1.2*b*). If we consider emission wavelengths of visible light, between 380 and 750 nm, and a NA of 1.5, we find that the diffraction limit takes values between 127 and 250 nm. While this is enough to resolve most biological cells (around 1 to 100 μm), it is not enough to resolve viruses (around 100 nm), proteins and small molecules (around 1 to 10 nm) or atoms (around 1 Å).

The Abbe limit in Eq. (1.1) already prescribes a way to improve the resolution, namely by reducing the emission wavelength. This would mean to consider alternative electromagnetic radiation bands, such as in ultraviolet (UV) microscopy, X-ray microscopy or electron microscopy. While these techniques indeed offer improved spatial resolution, they do not offer the contrast and specificity that fluorescence microscopy provides. They are further limited by, for example, the complexity of sample preparation, the likelihood of sample damage and a low throughput, thereby making them unsuitable for live-cell imaging [34].

This shows the need for further improvements to the resolution that fluorescence microscopy can provide, meaning that the physics of diffraction need to be circumvented. The family of methods that pass the diffraction limit are known as super-resolved fluorescence microscopy, or super-resolution microscopy in short. For the development of

super-resolved fluorescence microscopy, the Nobel Prize in Chemistry of 2014 would be awarded to Eric Betzig, Stefan Hell and William Moerner [35]. The routes these Nobel laureates took to circumvent Abbe's limit are fundamentally different though, and we will discuss these alternative approaches in Subsections 1.1.4 and 1.1.5.

1.1.4. Super-resolution through patterned excitation

The route Hell took to circumvent the diffraction limit uses the illumination path of the microscope. We can trace this development back to the first half of the 1990s, when various techniques were developed that use interference to generate illumination intensity patterns in the sample plane. For example, standing-wave intensity patterns were used for microscopy in 1993 [36]. 4Pi microscopy, developed by Hell and colleagues in 1994 [37, 38], and I^5M microscopy, invented by the team of Mats Gustafsson in 1995 [39], both use opposing objectives to generate interference patterns in the illumination and the emission paths. At the time of invention, these methods were mainly aimed at improving the axial resolution of the microscope. Purely by using patterned illumination, none of these techniques were able to circumvent the diffraction limit though.

To beat the Abbe limit, Hell focused on an emitter property called stimulated emission. Initially discovered by Albert Einstein in 1917 [40, 41], stimulated emission is a process in which an emitter can be forced to emit a photon without the need for fluorescence. This is accomplished by illuminating it with light that has a longer wavelength than the fluorescence absorption light. This forced emission has the same wavelength as the incoming illumination, which makes it distinguishable from fluorescent emission light. Additionally, the occurrence of stimulated emission prevents the possibility of fluorescence. As such, emitters that emit light from stimulated emission can be distinguished from those that emit fluorescent light.

By combining patterned illumination and stimulated emission, stimulated emission depletion (STED) microscopy was developed. While a patent for a similar concept already existed in 1986 [42], the development of STED is usually credited to Hell and Jan Wichmann in 1994 [43]. In STED, an illumination beam used for stimulated emission is modulated into an intensity pattern, called the depletion pattern. Typically in STED, the depletion pattern is a diffraction-limited, donut-shaped beam, with an intensity minimum in the centre. The intensity minimum of the depletion pattern is then overlaid with the excitation beam used for fluorescence, thereby limiting the area in which fluorescence can take place to the centre of the depletion beam. By increasing the intensity of the depletion beam, the central region of the donut in which fluorescence can occur is effectively contracted. As the area in which fluorescence can occur is now limited by the centre of the donut-shaped depletion pattern rather than the diffraction limit, the diffraction limit can be circumvented. In the first experimental demonstration by Hell and Thomas Klar in 1999 [44], STED was shown to achieve a lateral resolution of approximately 106 nm, whereas currently the typical spatial resolution of STED is around 50 nm [45, 46].

Various other methodologies were conceived that, similar to STED, use the illumination path of the microscope to circumvent Abbe's limit. In structured illumination microscopy (SIM) [47, 48], invented in 2000, standing-wave intensity patterns are used to illuminate the sample. As the fluorescence intensity is approximately proportional to

the illumination intensity before saturation, brightly illuminated emitters appear bright on the detector, and vice versa. As a result, diffraction-limited high-spatial frequency information in the sample is downshifted to lower spatial frequencies, thereby becoming observable through the objective. By shifting and rotating the standing-wave illumination through the sample and subsequently reconstructing the image from the individual acquisitions, a resolution improvement of at most a factor two can be attained. This resolution improvement can be extended to the axial direction using 3D-SIM [49], which uses illumination patterns with structure in both the lateral and axial directions. Additionally, a higher resolution improvement can be obtained with saturated SIM [50], which increases the illumination intensity to the point where the fluorescence emission starts saturating. While this theoretically allows for unlimited resolution, the increased illumination intensity increases the rate of photobleaching, thereby limiting the resolution to approximately 50 nm in practice.

Effectively the same principles as in SIM are used by image scanning microscopy (ISM) [51–53], experimentally realized in 2010, which scans through the sample with a focused illumination spot. Alternatively, this scanning effect can be achieved in a spinning disk confocal microscope (SDCM) [54, 55], by stroboscopically illuminating the sample while the disk is rotating [56]. As each camera pixel has a different viewing angle of the sample, scan images acquired by different pixels are reassigned either computationally [52, 56] or optically [57–59], ultimately giving a resolution improvement over the diffraction limit of at most a factor $\sqrt{2}$. Using a deconvolution method called Fourier reweighting in post-processing, the resolution improvement of ISM can be increased to a factor 2.

1.1.5. Super-resolution through sparsely activated emission

Concurrently to the development of illumination-based super-resolution microscopy, Moerner and Betzig worked on methods that instead use the emission path to circumvent the diffraction limit. To enable emission-based super-resolution, two separate insights in literature needed to come together. The first insight, as already mentioned before, is the demonstration of the single-molecule specificity of fluorescence microscopes. This happened in 1989 and 1990, when the teams of Moerner [18] and Orrit [19] showed that individual molecules could be detected through fluorescence microscopy. The second insight stems from a research line spanning from 1955 to 1986, which would show that isolated single-molecules can be localized with nanometre precision [60–63]. Betzig brought these findings together in a theoretical study in 1995 [64], in which he proposes to isolate individual molecules based on some, at the time undetermined feature, after which they can be imaged separately and localized with molecule-level precision. The missing puzzle piece was now to find a property that could make individual molecules appear isolated on the detector.

This puzzle piece was found in 1997, when Tsien, Moerner and colleagues discovered photo-activatable GFP [65]. Specifically, they were able to make fluorescent emitters blink, which means the emitters stochastically cycle through fluorescent emissions while being illuminated. Furthermore, they found that fluorescent emitters can be brought into a dark state, from which they can only be reactivated using illumination at a wavelength separate from the fluorescence absorption wavelength. By using either of these

properties, it becomes possible to switch fluorescent emitters on or off.

By switching fluorophores on and off over time as shown in Fig. 1.3*b*, we can observe isolated emitters that are separated in space and time [66]. The separation in space entails that during each image acquisition, all activated emitters should be separated by at minimum the diffraction limit, so that isolated PSFs appear in the image. With separation in time, we mean that emitters within a range defined by the diffraction limit should be switched on sequentially rather than concurrently, until the entire sample has been imaged. Due to the stochastic nature of the switching behaviour, it cannot be guaranteed that neighbouring emitters are never switched on simultaneously. To reduce the probability of overlapping PSFs, the temporal separation requirement enforces that sparse subsets of emitters need to be activated in each acquisition window. Sparsity in the emission signal makes it possible to record isolated PSFs, but this comes at the cost of a reduced labelling density as well as long total acquisition times to image the entire sample.

This combination of sparse activation and sequential acquisition is characteristic of single-molecule localization microscopy (SMLM). The main advantage of SMLM is that it can be used on relatively simple setups. Only minor modifications are needed to an existing epi-fluorescence microscope, mainly in the illumination and sample preparation to achieve stochastic switching. Additionally, the camera used for recording should have single-photon sensitivity, low readout noise and a high quantum efficiency to prevent information loss, as approximately only 1000 to 10,000 signal photons are emitted over the lifetime of one fluorescent emitter. [66, 67].

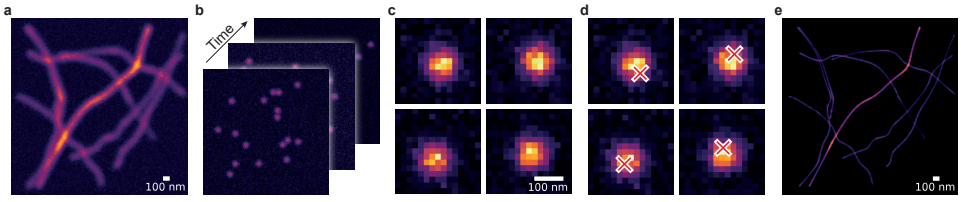

Figure 1.3: SMLM improves the localization precision beyond the diffraction barrier, through sequential, sparse activation of fluorescent emitters, and subsequent detection and localization. Images were simulated using simulated ground truth emitter positions obtained from [67] and enhanced for visualization purposes. (*a*) When using an optical microscope, such as the epi-fluorescence microscope of Fig. 1.2*a*, the resolution is limited by the diffraction limit (see Eq. (1.1)). This limits the resolution to approximately 200 nm. (*b*) In SMLM, rather than imaging the sample all at once, sparse emission signals are sequentially recorded over time. This makes it possible to record isolated emitters, which are separated in space and time. (*c*) In the detection step of the SMLM analysis, regions of interest that contain isolated emitters are cropped out from the acquired frames. (*d*) In the localization step of the SMLM analysis, underlying emitter positions are estimated in each detected region of interest. (*e*) By recombining the estimated emitter positions into one image, a single super-resolution frame with a localization precision of approximately 20 nm can be created.

Yet through acquisition alone, SMLM does not provide an interpretable image with improved precision over the diffraction limit. In fact, a full acquisition typically results in 10,000 to 100,000 camera frames containing isolated, diffraction-limited PSFs belonging to thousands of molecules in the field of view (FOV) [66]. To bring this data to a single image with improved precision, statistical analysis is needed. The two central steps of the analysis are detection and localization, as shown in Fig. 1.3, *c* and *d*.

The detection step (see Fig. 1.3*c*) aims to identify regions of interest (ROIs), that being regions of the data where the emission signal corresponding to a single molecule is located [68]. This is inherently a hypothesis testing problem for classification, where the hypothesis of a region containing a single emitter is compared against, for example, a region containing only noise or a region containing multiple emitters. In cases where the signal-to-background ratio (SBR) is high, ROIs are usually selected by setting a threshold on the recorded intensities. When the SBR is low or when the background is not uniform over the FOV, such a method no longer results in acceptable performance. In this case, statistical tests like the generalized likelihood ratio test (GLRT) can be used to accept or reject regions of interest [69].

Subsequently, the ROIs are processed in the localization step, shown in Fig. 1.3*d*. The goal of localization is to estimate the underlying emitter position, as well as related emitter parameters such as the expected signal intensity or the expected background, from a ROI. A naive approach of simply selecting the brightest pixel or centre pixel within a ROI would be insufficient, as the minimum possible localization error would be limited by the pixel size. To solve the regression problem with subpixel precision, initial approaches used, for example, centre of mass localization [70–72]. However, this method does not consider the camera noise statistics, the PSF model or background fluorescence, and thereby results in biased estimates. As such, maximum likelihood estimation (MLE) instead proved to be more accurate and precise [67, 73], as it is able to take the Poisson statistics of the measurements, the PSF model and background fluorescence into account [74]. Furthermore, MLE is asymptotically efficient if the underlying model is accurate, meaning that it becomes an asymptotically unbiased estimator with a Gaussian distribution which has the theoretically minimum possible variance [75, 76]. In practice for SMLM, this asymptotic limit is approximately attained when 100 or more signal photons are collected [74].

All SMLM methods essentially work the same, by encoding additional position information into sparse data and subsequently decoding said information through detection and localization. The way in which SMLM methods are differentiated usually comes down to the method by which the stochastic switching of fluorescent emitters is achieved. The first SMLM methods came out in 2006, during which three groups concurrently introduced photo-activated localization microscopy (PALM) [77], fluorescence photo-activation localization microscopy (FPALM) [78] and stochastic optical reconstruction microscopy (STORM) [79]. Direct STORM (dSTORM), released in 2008, gained popularity as it could work with conventional fluorescent dyes like Cy5 or Alexa 647 [80, 81]. Points accumulation for imaging in nanoscale topography (PAINT) and DNA-PAINT achieved stochastic switching by binding and unbinding fluorescent probes to the sample [82, 83]. As the binding is reversible, DNA-PAINT does not suffer from photobleaching, as bleached emitters can simply be replenished by new ones. With these methods, localization precisions of approximately 10 to 30 nm can be attained.

Recent developments show that the localization precision, accuracy, labelling density and temporal resolution of SMLM can be improved further. Resolution enhancement by sequential imaging (RESI), published in 2023, sequentially images closely positioned emitters using Exchange-PAINT, a variant of DNA-PAINT which enables multiplexing [84, 85]. RESI shows that it is possible to assign photon measurements to indi-

vidual emitters through sequential imaging, which makes it possible to reach Ångström-level localization precision. The accuracy of the PSF models has been improved through data-driven approaches, such as cubic spline identification and deep learning, reducing the localization error in lateral and axial localization [86, 87]. Imaging at increased labelling densities became possible by trading in traditional analysis methods for deep learning. Methods such as Deep-STORM [88, 89] and deep context dependent (DECODE) [90] are able to localize closely spaced emitters at a localization precision comparable to that of other SMLM methods. Deep learning has also shown promising results to improve the temporal resolution of SMLM. For example, DBlink uses deep learning for spatio-temporal interpolation between super-resolved frames, thereby making SMLM better suited for the imaging of dynamical structures [91].

1.2. Localization uncertainty

In our discussion of the history of microscopy, we have seen that resolution plays a key role throughout its development [92]. In the time of Van Leeuwenhoek, resolution was limited by the degree with which lenses were able to magnify a sample. In the time of Abbe, resolution was limited by diffraction and the size of the PSF. Yet with the invention of super-resolution microscopy, we see that concept of resolution needs to be specified further now that the diffraction barrier can be circumvented. In particular, the spatial resolution of SMLM is determined by a combination of various factors, such as the spatial frequencies present in the sample, the labelling density, the diffraction limit of the system, the measurement noise, the detection precision and recall, the localization error and visual artifacts [93–96].

In the development of SMLM, the localization error has historically played a fundamental role. The localization error consists of two terms: the localization uncertainty, or precision, and the localization bias, or accuracy. The localization accuracy is often omitted in the quantification of the localization error of SMLM, due to the asymptotic unbiasedness of MLE if the underlying model is accurate [75, 76]. This means that the localization performance of SMLM methods is primarily given in terms of the localization precision [97], which describes the estimator variance.

We illustrate the interpretation of the estimator variance using Fig. 1.4, *a-c*. For illustration purposes, Fig. 1.4*c* shows a simplification of the probabilistic image formation model used for MLE, namely as a deterministic model of the expected photon count. The MLE of a parameter is obtained by first determining the likelihood of a parameter subject to the measurements. The intuition behind this is to compare the acquired data with all possible model explanations corresponding to different values of the model parameter. The MLE is then determined by selecting the model parameter that best explains the measurements, which is mathematically equivalent to maximizing the likelihood. Due to the stochastic nature of the data, a resampling of the data would give a different MLE, as a neighbouring model in parameter space now gives a better explanation of this particular resample. This gives rise to a probabilistic estimator distribution, which models the relative frequency of occurrence of all possible estimator outcomes as a result of the inherent randomness of the data. The variance of this distribution is equal to the localization precision.

To determine the localization precision of SMLM methods, the Cramér-Rao lower

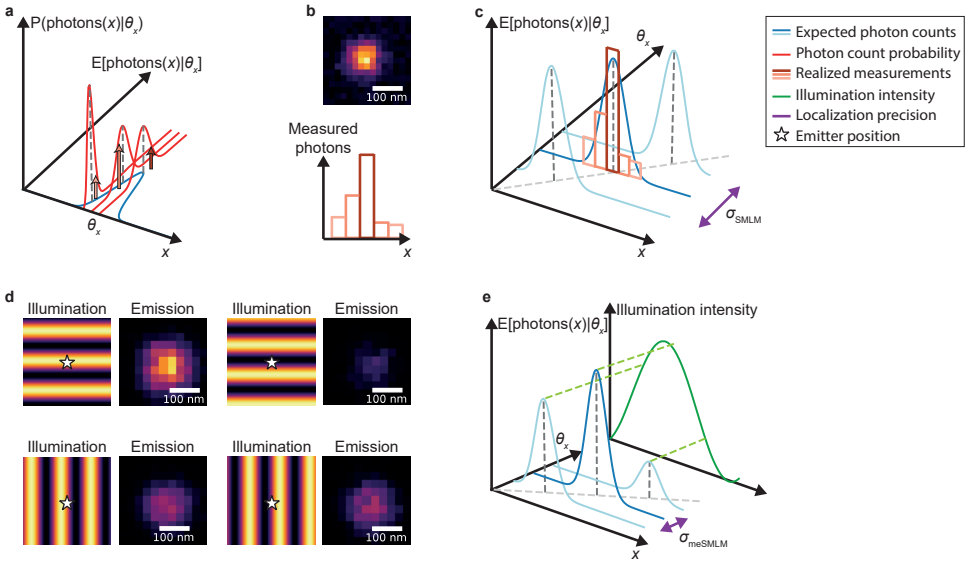

Figure 1.4: Illustration of statistical image formation modelling, MLE and precision in SMLM. (*a*) The image formation model describes the expected amount of photons that would arrive on detector coordinate x, under the condition that the underlying emitter position is θ_x. (*b*) As photon arrivals at the detector follow a Poisson distribution, measurements can be modelled as samples from a Poisson distribution that has the expected photon count as its rate. (*c*) In MLE, the objective is to maximize the probability of realizing the measurements from the image formation model, by choosing the maximizing argument $\hat{\theta}_x$. The intuition behind this, shown here in a simplified manner by means of the expected photon count, is to compare the acquired data with all possible model explanations corresponding to different values of the model parameter and subsequently choosing the best match. Due to the inherent stochasticity of the data, a new measurement will result in a different MLE, as a neighbouring model will give a similar, but better explanation for that particular sample. This estimator variance, which describes the uncertainty about the estimated emitter position due to the inherent stochasticity of the measurements, is the localization precision. (*d*) meSMLM combines patterned illumination with sparse activation and subsequent localization. As the fluorescence intensity is proportional to the illumination intensity, the overall intensity in the ROI now encodes information about where the emitter is located relative to the illumination pattern. (*e*) By combining patterned illumination with sparse activation, neighbouring image formation models in parameter space become more dissimilar as a function of θ_x when compared to SMLM. This increase in information makes it easier to distinguish between models based on the emitter position, which means the localization precision improves.

bound (CRLB) plays a central role. The CRLB, named in honour of Harald Cramér and Calyampudi Rao, provides a lower bound on the covariance of any unbiased estimator $\hat{\boldsymbol{\theta}}$ of the emitter parameter vector $\boldsymbol{\theta}$ [98]. In SMLM, $\boldsymbol{\theta}$ usually contains the emitter position (θ_x, θ_y), the expected signal intensity θ_I and the expected background per pixel θ_b. Under mild assumptions on the likelihood function of the statistical model of the data, it holds for any unbiased estimator $\hat{\boldsymbol{\theta}}$ of the parameter vector $\boldsymbol{\theta}$ that

$$\left(C_{\hat{\boldsymbol{\theta}}} - I^{-1}(\boldsymbol{\theta})\right) \succeq 0, \tag{1.2}$$

which means the left-hand side quantity is positive semi-definite. Here, $C_{\hat{\boldsymbol{\theta}}}$ denotes the estimator covariance, $I(\boldsymbol{\theta})$ is the Fisher information matrix, and $I^{-1}(\boldsymbol{\theta})$ is the CRLB. Each

entry (u, v) of the Fisher information matrix is given by

$$I_{uv}(\boldsymbol{\theta}) = \mathbb{E}\left[\frac{\partial \ell(\boldsymbol{\theta}|\boldsymbol{c})}{\partial \boldsymbol{\theta}_u}\frac{\partial \ell(\boldsymbol{\theta}|\boldsymbol{c})}{\partial \boldsymbol{\theta}_v}\right], \tag{1.3}$$

where $\ell(\boldsymbol{\theta}|\boldsymbol{c})$ describes the log-likelihood of the parameter vector $\boldsymbol{\theta}$ that parametrizes the model describing the data $\boldsymbol{c}$.

A particular result of Eq. (1.2) is that the estimator variance is bounded from below by the diagonal of the CRLB. It is shown in [74] that in SMLM, the variance of MLE converges to the CRLB at approximately 100 signal photons. As MLE attains the CRLB in a finite and experimentally attainable amount of signal photons, the CRLB can be used to quantify the best possible localization precision, or theoretical minimum uncertainty, that can be obtained through SMLM.

To calculate the CRLB for SMLM, we need to formulate a parametrized statistical model of the measurements, as shown in Fig. 1.4, *a* and *b*. The model should describe the amount of photons that are recorded by a camera pixel during a measurement. In the absence of readout noise, such a process can be modelled by the Poisson distribution [74]. The Poisson process is dependent on a single parameter μ_i, which describes the expected amount of photons that fall on camera pixel i during a measurement. Assuming that the measurements on each pixel are mutually independent, equivalent to the absence of crosstalk, each entry (u, v) of the Fisher information matrix for Poisson measurements is given by

$$I_{uv}(\boldsymbol{\theta}) = \sum_{i=1}^{N_{\text{pixels}}} \frac{1}{\mu_i}\frac{\partial \mu_i}{\partial \boldsymbol{\theta}_u}\frac{\partial \mu_i}{\partial \boldsymbol{\theta}_v}. \tag{1.4}$$

Here, N_{pixels} describes the total amount of pixels on the camera. The model for the Poisson mean μ_i is given by

$$\mu_i(x_i, y_i, \boldsymbol{\theta}) = \theta_I \int_{x_i-\frac{\Delta x}{2}}^{x_i+\frac{\Delta x}{2}} \int_{y_i-\frac{\Delta y}{2}}^{y_i+\frac{\Delta y}{2}} h(x-\theta_x, y-\theta_y)\mathrm{d}x\mathrm{d}y + \theta_b, \tag{1.5}$$

where (x_i, y_i) describe the centre coordinates of pixel i, $(\Delta x, \Delta y)$ describe the pixel size and $h(x, y)$ is the PSF model.

As a model for the PSF $h(x, y)$, a Gaussian is commonly used. It is given by

$$h(x, y) = \frac{1}{2\pi\sigma_{\text{PSF}}^2} e^{\frac{-x^2-y^2}{2\sigma_{\text{PSF}}^2}}, \tag{1.6}$$

where σ_{PSF} denotes the standard deviation of the PSF. The standard deviation of the Gaussian PSF is often treated as a known constant [74, 97], and least-squares approximations for σ_{PSF} have been derived in literature [99]. Alternatively, the PSF standard deviation can also be included as an estimation parameter [100]. However, the Gaussian PSF model is no longer accurate in the presence of, for example, aberrations [101]. In these cases, other PSF models should be considered, such as the vectorial model [102] or data-driven models such as cubic splines [86, 103].

Under the Gaussian PSF model, the Poisson mean of Eq. (1.5) reduces to

$$\mu_i(x_i, y_i, \boldsymbol{\theta}) = \theta_I E(x_i - \theta_x, \Delta x, \sigma_{\text{PSF}}^2) E(y_i - \theta_y, \Delta y, \sigma_{\text{PSF}}^2) + \theta_b, \tag{1.7}$$

where the function $E(x, \Delta x, \sigma^2)$ is given by

$$E(x, \Delta x, \sigma^2) = \frac{1}{2}\text{erf}\left(\frac{x + \frac{\Delta x}{2}}{\sqrt{2}\sigma}\right) - \frac{1}{2}\text{erf}\left(\frac{x - \frac{\Delta x}{2}}{\sqrt{2}\sigma}\right). \tag{1.8}$$

Using Eqs. (1.4)-(1.8), the CRLB can be computed numerically. Closed-form analytical approximations of the CRLB of SMLM are also available [104–107]. From [106, 107], we find that the theoretical minimum localization uncertainty σ_x of SMLM can be approximated as

$$\sigma^2_{x,\text{SMLM}} = \frac{\sigma^2_{\text{PSF}} + \Delta x^2/12}{\theta_I}\left(1 + 4\tau + \sqrt{\frac{2\tau}{1+4\tau}}\right). \tag{1.9}$$

Here, τ is a normalized dimensionless background parameter, given by

$$\tau = \frac{2\pi\theta_b(\sigma^2_{\text{PSF}} + \Delta x^2/12)}{\theta_I \Delta x^2}. \tag{1.10}$$

As an example to illustrate Eq. (1.9), for $\sigma_{\text{PSF}} = 100$ nm, $\Delta x = 65$ nm, $\theta_I = 2000$ photons and $\theta_b = 8$ photons per pixel, we find $\sigma_{x,\text{SMLM}} = 2.8$ nm.

Furthermore, Eq. (1.9) shows that the theoretical minimum uncertainty of SMLM is inversely proportional to the square root of the signal photon count, that is

$$\sigma_{x,\text{SMLM}} \propto \frac{1}{\sqrt{\theta_I}}. \tag{1.11}$$

In principle, the uncertainty of SMLM can thus be arbitrarily reduced given enough signal photons. In practice however, the signal photon budget per emitter is limited due to the effect of, for example, photobleaching. Furthermore, acquiring an increasing amount of signal photons per emitter also increases the imaging time, thereby reducing the acquisition speed and temporal resolution of SMLM [108].

To improve the localization precision beyond that of SMLM, it is therefore important to increase the amount of information each signal photon contains about the model parameters, such as the emitter position. In light of the interpretation of the localization precision established in Fig. 1.4, *a-c*, this equivalently means that we need to increase the dissimilarity between neighbouring models in parameter space. This makes it easier to distinguish between possible estimates under the inherent stochasticity of the measurements and thus reduces the localization uncertainty.

1.3. Modulation enhanced single-molecule localization microscopy

To find a method that increases the amount of information each signal photon carries about the emitter position, we take a second look at the invention of super-resolution methods. As seen in Subsections 1.1.4 and 1.1.5, historically super-resolution methods either used the illumination path of the microscope or the emission path of the microscope to circumvent the diffraction barrier, but not both. Therefore to increase the information content per signal photon, we can look at synergistically combining insights

from both fields. The resulting type of microscopy that combines patterned illumination with sparse activation and subsequent localization is called modulation enhanced SMLM (meSMLM) [109].

To explain the information increase gained through meSMLM, we look at Fig. 1.4*d*. As the fluorescence intensity is proportional to the illumination intensity, the overall intensity in the ROI now encodes information about where an emitter is located relative to the illumination pattern. That is, if the intensity in the ROI is bright, then the emitter must have been located in a bright spot of the illumination pattern, and vice versa. The shape of the PSF does not change as a result of patterned illumination, which means the emission information used by SMLM remains unchanged. By combining these information sources, the total amount of information encoded in the measurements has thus increased. As shown in Fig. 1.4*e*, the differences between models in parameter space increase, which means the theoretically minimum localization uncertainty is reduced. Yet in contrast to widefield SMLM, the localization precision improvements of meSMLM are local to the neighbourhood of a targeted emitter, as they are tied to the relative distance between emitters and illumination patterns.

meSMLM has been demonstrated in both scanning and widefield configurations. The most well-known example of a scanning meSMLM methodology is minimal photon fluxes (MINFLUX), which was first published in 2017 [110–112]. In MINFLUX, the donut-shape intensity pattern known from STED is used, but for fluorescence excitation rather than for stimulated emission. After acquiring an initial estimate of an emitter position through a first scan, MINFLUX is used to refine the emitter position through a procedure resembling triangulation. By probing around the emitter position with the intensity minima of four donut-patterns in a ring with diameter L, we obtain information about where the emitter is located with respect to each of the patterns. MINFLUX claims that this leads to the following scaling law for the theoretical minimum uncertainty:

$$\sigma_{x,\mathrm{MINFLUX}} \propto \frac{L}{\sqrt{\theta_I}}. \tag{1.12}$$

Eq. (1.12) indicates that MINFLUX allows for two ways to improve the precision. Either the signal photon count can be increased, as is the case for SMLM, or the diameter L of the triangulation region can be reduced.

This finding led to iterative MINFLUX, published in 2020 [112]. At the start of iterative MINFLUX, the position of an emitter is estimated through triangulation with donut-shaped illumination patterns, in a triangulation region with size L. This estimate and its localization uncertainty are used as prior information for a new iteration. The emitter estimate determines the centre of the triangulation region in the next iteration. Similarly, the size L of the triangulation region shrinks proportionally to the localization precision achieved during the previous iteration. After reconfiguring the triangulation region, a new MINFLUX acquisition is started and new estimates of the emitter position and localization uncertainty are made, which will again be used as prior information during the subsequent iteration. This iterative process repeats until K iterations are completed.

From Eq. (1.12), we can infer that due to the decrease of L, photons acquired in each additional iteration are more informative. It is claimed that this leads to the following

precision improvement:

$$\sigma_{x,\text{iterative MINFLUX}} \propto \frac{L}{\left(\sqrt{\theta_I}\right)^K}. \tag{1.13}$$

Based on this scaling law, distributing the finite signal photon budget over as many iterations as possible is preferred over increasing the amount of signal photons per iteration, as the information content of signal photons increases exponentially over the course of iterations. Using MINFLUX and its variants, nanometre-level localization precision can be achieved in three dimensions [112–114] and the localization uncertainty can even be reduced to the Ångström-level [115, 116].

While the resolution improvement of MINFLUX made it a well-known technique, its original implementation was technologically complicated. This was addressed through raster scanning a minimum of light (RASTMIN) [117–120]. By raster scanning a sample with a donut-shaped beam, rather than the MINFLUX triangulation, RASTMIN shows that similar precision improvements to those of MINFLUX can be obtained.

A drawback of scanning meSMLM modalities is that scanning reduces the throughput. While parallelization of scanning is possible to mitigate the throughput limitation [110], widefield meSMLM entirely does not suffer from it [109]. Rather than the donut-shaped intensity pattern from STED, these methods use the standing-wave intensity pattern from SIM. SIMFLUX [121], SIMPLE [122] and repetitive optical selective exposure (ROSE) [123] all use sinusoidally shaped intensity patterns to improve the lateral resolution. By using structured illumination with structure in both the lateral and axial directions, patterned illumination can also be used to improve axial resolution, as done in ZIMFLUX [124], modulated localization (ModLoc) [125–127] and axial localization with repetitive optical selective exposure (ROSE-Z) [128].

Specifically for SIMFLUX [121], the localization precision is improved by at most a factor 2.4 over SMLM. Furthermore, SIMFLUX uses six patterns in total, rather than nine patterns as done in SIM. Therefore, the combination of structured illumination with sparse activation and subsequent localization in meSMLM can result in a better resolution over existing reconstruction approaches, while using less illumination patterns in the process.

1.4. Thesis motivation

At the start of this chapter, we reasoned that understanding the biology of cells, bacteria, viruses and proteins requires visualizing them on the micro- to nanoscale. We asked ourselves the question: how can we make the invisible visible?

History provided us with answers to this question. The microscopes of the 1600s magnified the microworld, the epi-fluorescence microscope of the 20$^{\text{th}}$ century tailored the microscope to biology, and the limits of diffraction were circumvented through the various super-resolution methods of the recent years. By sparsely activating emitters and sequentially localizing their positions through statistical methods, SMLM reaches a localization precision of approximately 20 nm [77–79]. Through modern methods such as RESI [84, 85] or meSMLM [110, 112, 116], a localization precision in the order of magnitude of nanometres to Ångströms can now be attained. Viewed through the lens of these developments, we are succeeding in making the invisible visible.

Yet these successes in microscopy have given rise to new questions. Before the invention of super-resolution microscopy, images were directly observed through a microscope, which in principle gives the certainty that what we observe is present in reality. When circumventing the diffraction limit through, for example, SMLM, RESI or meSMLM, we forfeit the directly observed image in favour of computational image analysis. The end product of super-resolution microscopy is no longer a directly measured image, but rather a list of estimated emitter positions that can be recombined into an image in postprocessing.

While these super-resolution methods allow us to access the nanoscale, their findings are accompanied by the statistical uncertainty about whether the molecule positions that we retrieve correspond to the true underlying positions of emitters that are truly present in the sample. A fundamental objective of super-resolution microscopy is thus to give certainty about the localization uncertainty with which the position of a single molecule can be determined. But how can we make the uncertain certain?

To bound the uncertainty of SMLM, statistical lower bounds on the estimation uncertainty are commonly used, such as the CRLB [97]. The CRLB represents the theoretical minimum uncertainty with which unbiased estimators can localize emitters [98]. As the variance of MLE converges asymptotically to the CRLB if the underlying model is accurate, and even reaches it within finite and experimentally realizable signal photon counts, the CRLB is a reliable predictor for the best possible localization precision [74]. Furthermore, as the CRLB relies only on a model and not on experimental data, it can be used in silico to design and optimize the experimental design [129, 130].

This suggests that the CRLB successfully brings certainty to the localization uncertainty of state-of-the-art meSMLM. If this were to be the reality, designing meSMLM through the CRLB would allow for the optimization of the localization precision. In addition, it would enable fundamentally reliable and trustworthy discoveries in our understanding of cells, bacteria, viruses and proteins, which would make it an invaluable contribution to biological research and medicine development.

However, the mathematical limitations of the CRLB prevent this reality from occurring. Specifically, the CRLB leads to narrowly applicable, improperly represented or mathematically incorrect characterizations of the localization uncertainty of meSMLM.

Firstly, the improvements obtained through methods such as MINFLUX [110, 112] and SIMFLUX [121] motivate the incorporation of meSMLM in existing systems, in which image reconstruction instead of localization is the current state-of-the-art. Yet a standardized structure for meSMLM image formation models with general applicability is still lacking, which staggers the application of the CRLB to meSMLM and complicates the comparison of meSMLM modalities. Additionally, the lack of method-appropriate image formation models hinders the design and optimization of new meSMLM systems, as well as the optimization of the localization precision of existing methods.

Furthermore, the CRLB only bounds the variance of the emitter position estimator, but it does not reveal the complete distribution of the estimator. This would not be problematic in cases where the underlying image formation model used for MLE is accurate, as the MLE has an asymptotic Gaussian distribution [75, 76]. Yet when the underlying image formation model is not accurate or when it does not uniquely explain the measurements, the Gaussian limit of the estimator distribution might no longer hold [131].

Trusting the CRLB would then give a false sense of confidence in the obtained localizations, whereas only a quantification of the full estimator distribution would appropriately represent the localization error.

Lastly, the CRLB only bounds the variance of unbiased estimators from below. However, an increasing amount of estimation methods in SMLM are biased, as they use prior information to improve the localization precision. While Bayesian methods have been used for localization for over a decade [132], recent methods in deep learning and iterative localization microscopy have put the use prior information back into the limelight. For example, deep learning methods such as Deep-STORM [88, 89] and deep context dependent (DECODE) [90] use prior information, obtained from seeing examples during training, to obtain their resolution improvement at high labelling densities. Iterative meSMLM methods, such as iterative MINFLUX [112], use prior information obtained from previous iterations to improve the localization precision in subsequent iterations. In these cases, the CRLB is no longer applicable and its usage will give mathematically unfounded limits on the localization precision.

These three issues highlight the necessity of new statistical models and methods to quantify the localization uncertainty of meSMLM. Specifically, a standardized general structure is needed for image formation models in meSMLM, to be used in conjunction with the CRLB and MLE. This standardized structure can then be specified for individual applications, leading to a tailor-made models for new and existing applications. In addition, we need to develop statistical tools that represent the full estimator distribution, as well as methods that quantify the uncertainty of localization methods that use prior information. Together, these are necessary steps to future-proof our understanding of localization uncertainty in super-resolution microscopy, thereby improving its trustworthiness for biological research and medicine development.

1.5. Outline

This dissertation aims to solve these three issues, making it possible to quantify the localization uncertainty of existing and future meSMLM methods with awareness of the full estimator distribution. We develop image formation models for meSMLM and show how they can be used to design new meSMLM methods. Subsequently, we leverage reversible jump Markov chain Monte Carlo (RJMCMC) to approximate the full posterior estimator distribution and use it to show how estimation degeneracy can occur in three-dimensional multiple emitter localization. Lastly, we introduce the Van Trees inequality (VTI) as a replacement for the CRLB in case prior information is available. We apply the VTI to iterative meSMLM to show where it obtains its precision improvement from.

In Chapter 2, we develop a new image formation model which enables modulation enhanced localization in spinning disk-based ISM setups [133]. Our method, called SpinFlux, uses a spinning disk with pinholes in its illumination and emission paths, to sequentially illuminate regions in the sample during each measurement. The resulting intensity-modulated emission signal is analysed for each individual pattern to localize emitters with improved precision. Using our image formation model, we quantify the best possible localization uncertainty of SpinFlux using the CRLB. Furthermore, we compare SpinFlux to an alternative localization approach which has since been realized experimentally [134], where emitters are instead localized in Fourier reweighted ISM re-

constructions. As SpinFlux retrieves its precision improvement from an alternative analysis compared to ISM, only minor modifications to setups are needed. In addition, the SpinFlux image formation model generalizes to arbitrary spinning disk setups and therefore enables the optimization of the design of spinning disks.

In Chapter 3, we develop a three-dimensional Bayesian multiple emitter fitting algorithm using RJMCMC [135]. Multiple emitter fitting becomes important when increasing the labelling density of the sample, as the probability of overlapping emitter signals increases. Unfortunately due to the shape of the PSF, the overlap of emitters can cause cases where multiple localization pairs explain the measurements with equal statistical likelihood. As now no model uniquely explains the measurements, the estimator distribution becomes multimodal, which is not captured by the CRLB. RJMCMC [136] reconstructs the posterior density of both the model and the estimation parameters [131, 137]. This makes it able to better estimate the model, parameters and their uncertainties. We apply RJMCMC to an astigmatic point spread function, to research the occurrence of degeneracy in the position estimation.

In Chapter 4, we introduce the VTI and apply it to iterative meSMLM [138–140]. The VTI bounds the mean squared error of arbitrary estimators from below in case prior information is available [75, 141]. For biased estimators, the VTI is therefore suited to replace the CRLB, which only applies to unbiased estimators. This makes the VTI a suitable mathematical framework to analyse iterative meSMLM, as it uses prior information obtained in previous iterations to improve the precision in the current iteration [112]. We consider an iterative meSMLM method, which uses standing-wave illumination patterns over the course of multiple iterations. We formulate an image formation model for this method, which includes the effects of imperfect pattern modulation and background fluorescence. Subsequently we use the VTI to analytically and, through Monte Carlo simulations [142], numerically approximate lower bounds on the maximum localization precision. We compare these results against those reported in MINFLUX, as shown in Eqs. (1.12) and (1.13), to investigate these scaling laws in the context of imperfect modulation and non-zero background.

Lastly in Chapter 5, we conclude this dissertation by reflecting on our findings. In addition, we provide recommendations for future research related to this thesis, as well as an outlook on expected future developments in the field of quantitative nanoscopy.

References

[1] D. Yesudhas, A. Srivastava, and M. M. Gromiha. “COVID-19 outbreak: history, mechanism, transmission, structural studies and therapeutics”. In: *Infection* 49.2 (2020), pp. 199–213.

[2] National Institute for Public Health and the Environment. *Behavioural research on COVID-19*. 2025. (Visited on 07/24/2025).

[3] World Health Organization. *WHO Coronavirus (COVID-19) dashboard*. 2025. (Visited on 07/24/2025).

[4] E. Mathieu, H. Ritchie, L. Rodés-Guirao, C. Appel, D. Gavrilov, C. Giattino, J. Hasell, B. Macdonald, S. Dattani, D. Beltekian, E. Ortiz-Ospina, and M. Roser. “Excess mortality during the Coronavirus pandemic (COVID-19)”. In: *Our World in Data* (2024).

[5] J. D. Bremner, S. J. Russo, R. Gallagher, and N. M. Simon. “Acute and long-term effects of COVID-19 on brain and mental health: A narrative review”. In: *Brain, Behavior, and Immunity* 123 (2025), pp. 928–945.

[6] C. Courtemanche, J. Garuccio, A. Le, J. Pinkston, and A. Yelowitz. “Strong Social Distancing Measures In The United States Reduced The COVID-19 Growth Rate”. In: *Health Affairs* 39.7 (2020), pp. 1237–1246.

[7] L. Magis-Weinberg, M. Arreola Vargas, A. Carrizales, C. T. Trinh, D. E. Muñoz Lopez, A. M. Hussong, and J. E. Lansford. “The impact of COVID-19 on the peer relationships of adolescents around the world: A rapid systematic review”. In: *Journal of Research on Adolescence* 35.1 (2024).

[8] C. Hong and B. Skiba. “Mental health outcomes, associated factors, and coping strategies among LGBTQ adolescent and young adults during the COVID-19 pandemic: A systematic review”. In: *Journal of Psychiatric Research* 182 (2025), pp. 132–141.

[9] W. McKibbin and R. Fernando. “The global economic impacts of the COVID-19 pandemic”. In: *Economic Modelling* 129 (2023), p. 106551.

[10] Y. M. Bar-On, A. Flamholz, R. Phillips, and R. Milo. “SARS-CoV-2 (COVID-19) by the numbers”. In: *eLife* 9 (2020).

[11] Seneca the Younger. *Natural Questions*. Ed. by T. H. Corcoran. 1971.

[12] D. Bardell. “The Biologists’ Forum: The invention of the microscope”. In: *BIOS* 75.2 (2004), pp. 78–84.

[13] B. R. Masters. “History of the Optical Microscope in Cell Biology and Medicine”. In: *Encyclopedia of Life Sciences*. John Wiley & Sons, Ltd, 2008.

[14] J. van Zuylen. “The microscopes of Antoni van Leeuwenhoek”. In: *Journal of Microscopy* 121.3 (1981), pp. 309–328.

[15] Z. Ou, Y. Duh, N. J. Rommelfanger, C. H. C. Keck, S. Jiang, K. Brinson, S. Zhao, E. L. Schmidt, X. Wu, F. Yang, B. Cai, H. Cui, W. Qi, S. Wu, A. Tantry, R. Roth, J. Ding, X. Chen, J. A. Kaltschmidt, M. L. Brongersma, and G. Hong. “Achieving optical transparency in live animals with absorbing molecules”. In: *Science* 385.6713 (2024).

[16] F. H. Kasten. “The Origins of Modern Fluorescence Microscopy and Fluorescent Probes”. In: *Cell Structure and Function by Microspectrofluorometry*. Elsevier, 1989, pp. 3–50.

[17] J. Ploem and H. Tanke. *Introduction to Fluorescence Microscopy*. Microscopy handbooks. New York, NY: Oxford University Press, 1987.

[18] W. E. Moerner and L. Kador. “Optical detection and spectroscopy of single molecules in a solid”. In: *Physical Review Letters* 62.21 (1989), pp. 2535–2538.

[19] M. Orrit and J. Bernard. “Single pentacene molecules detected by fluorescence excitation in ap-terphenyl crystal”. In: *Physical Review Letters* 65.21 (1990), pp. 2716–2719.

[20] B. R. Masters. “The Development of Fluorescence Microscopy”. In: *Encyclopedia of Life Sciences*. John Wiley & Sons, Ltd, 2010.

[21] M. Renz. “Fluorescence microscopy—A historical and technical perspective”. In: *Cytometry Part A* 83.9 (2013), pp. 767–779.

[22] E. M. Brumberg. “Fluorescence microscopy of biological objects using light from above”. In: *Biophysics* 4 (1959), pp. 97–104.

[23] J. S. Ploem. “The use of a vertical illuminator with interchangeable dichroic mirrors for fluorescence microscopy with incidental light”. In: *Zeitschrift für Wissenschaftliche Mikroskopie und Mikroskopische Technik* 68 (1967), pp. 129–142.

[24] O. Shimomura, F. H. Johnson, and Y. Saiga. “Extraction, Purification and Properties of Aequorin, a Bioluminescent Protein from the Luminous Hydromedusan, Aequorea”. In: *Journal of Cellular and Comparative Physiology* 59.3 (1962), pp. 223–239.

[25] O. Shimomura. “The discovery of aequorin and green fluorescent protein”. In: *Journal of Microscopy* 217.1 (2005), pp. 3–15.

[26] D. C. Prasher, V. K. Eckenrode, W. W. Ward, F. G. Prendergast, and M. J. Cormier. “Primary structure of the Aequorea victoria green-fluorescent protein”. In: *Gene* 111.2 (1992), pp. 229–233.

[27] M. Chalfie, Y. Tu, G. Euskirchen, W. W. Ward, and D. C. Prasher. “Green Fluorescent Protein as a Marker for Gene Expression”. In: *Science* 263.5148 (1994), pp. 802–805.

[28] S. Inouye and F. I. Tsuji. “Aequorea green fluorescent protein: Expression of the gene and fluorescence characteristics of the recombinant protein”. In: *FEBS Letters* 341.2–3 (1994), pp. 277–280.

[29] R. Heim, A. B. Cubitt, and R. Y. Tsien. “Improved green fluorescence”. In: *Nature* 373.6516 (1995), pp. 663–664.

[30] Nobel Foundation. *The Nobel Prize in Chemistry 2008*. 2008.

[31] M. Born and E. Wolf. *Principles of Optics*. 7th ed. Cambridge, England: Cambridge University Press, 1999.

[32] J. W. Goodman. *Introduction to Fourier Optics*. Physical & Quantum Electronics S. New York, NY: McGraw-Hill, 1968.

[33] E. Abbe. “Beiträge zur Theorie des Mikroskops und der mikroskopischen Wahrnehmung”. In: *Archiv für Mikroskopische Anatomie* 9.1 (1873), pp. 413–468.

[34] K. Prakash, B. Diederich, R. Heintzmann, and L. Schermelleh. “Super-resolution microscopy: a brief history and new avenues”. In: *Philosophical Transactions of the Royal Society A: Mathematical, Physical and Engineering Sciences* 380.2220 (2022).

[35] Nobel Foundation. *The Nobel Prize in Chemistry 2014*. 2014.

[36] B. Bailey, D. L. Farkas, D. L. Taylor, and F. Lanni. “Enhancement of axial resolution in fluorescence microscopy by standing-wave excitation”. In: *Nature* 366.6450 (1993), pp. 44–48.

[37] S. Hell and E. H. K. Stelzer. “Properties of a 4Pi confocal fluorescence microscope”. In: *Journal of the Optical Society of America A* 9.12 (1992), p. 2159.

[38] S. W. Hell, S. Lindek, C. Cremer, and E. H. K. Stelzer. “Measurement of the 4Pi-confocal point spread function proves 75 nm axial resolution”. In: *Applied Physics Letters* 64.11 (1994), pp. 1335–1337.

[39] M. G. L. Gustafsson, D. A. Agard, and J. W. Sedat. “Evenfold improvement of axial resolution in 3D wide-field microscopy using two objective lenses”. In: *Three-Dimensional Microscopy: Image Acquisition and Processing II*. Ed. by T. Wilson and C. J. Cogswell. Vol. 2412. SPIE, 1995, pp. 147–156.

[40] A. Einstein. “Strahlungs-Emission und Absorption nach der Quantentheorie”. In: *Deutsche Physikalische Gesellschaft* 18 (1916), pp. 318–323.

[41] A. Einstein. “Zur Quantentheorie der Strahlung”. In: *Physikalische Zeitschrift* 18 (1917), pp. 121–128.

[42] V. Okhonin. “Method of investigating specimen microstructure”. SU 1374922 A1. 1986.

[43] S. W. Hell and J. Wichmann. “Breaking the diffraction resolution limit by stimulated emission: stimulated-emission-depletion fluorescence microscopy”. In: *Optics Letters* 19.11 (1994), p. 780.

[44] T. A. Klar and S. W. Hell. “Subdiffraction resolution in far-field fluorescence microscopy”. In: *Optics Letters* 24.14 (1999), p. 954.

[45] G. Vicidomini, P. Bianchini, and A. Diaspro. “STED super-resolved microscopy”. In: *Nature Methods* 15.3 (2018), pp. 173–182.

[46] K. Prakash, D. Baddeley, C. Eggeling, R. Fiolka, R. Heintzmann, S. Manley, A. Radenovic, H. Shroff, C. Smith, and L. Schermelleh. “Resolution in super-resolution microscopy – facts, artifacts, technological advancements and biological applications”. In: *Journal of Cell Science* 138.10 (2025).

[47] R. Heintzmann and C. G. Cremer. “Laterally modulated excitation microscopy: improvement of resolution by using a diffraction grating”. In: *Optical Biopsies and Microscopic Techniques III*. Ed. by I. J. Bigio, H. Schneckenburger, J. Slavik, K. Svanberg, and P. M. Viallet. SPIE, 1999.

[48] M. G. L. Gustafsson. “Surpassing the lateral resolution limit by a factor of two using structured illumination microscopy”. In: *Journal of Microscopy* 198.2 (2000), pp. 82–87.

[49] M. G. Gustafsson, L. Shao, P. M. Carlton, C. J. R. Wang, I. N. Golubovskaya, W. Z. Cande, D. A. Agard, and J. W. Sedat. “Three-Dimensional Resolution Doubling in Wide-Field Fluorescence Microscopy by Structured Illumination”. In: *Biophysical Journal* 94.12 (2008), pp. 4957–4970.

[50] M. G. L. Gustafsson. “Nonlinear structured-illumination microscopy: Wide-field fluorescence imaging with theoretically unlimited resolution”. In: *Proceedings of the National Academy of Sciences* 102.37 (2005), pp. 13081–13086.

[51] C. Sheppard. “Super-resolution in confocal imaging”. In: *Optik (Jena)* 80.2 (1988), pp. 53–54.

[52] C. B. Müller and J. Enderlein. “Image Scanning Microscopy”. In: *Physical Review Letters* 104.19 (2010).

[53] I. Gregor and J. Enderlein. “Image scanning microscopy”. In: *Current Opinion in Chemical Biology* 51 (2019), pp. 74–83.

[54] G. Sirinakis, E. S. Allgeyer, J. Cheng, and D. St Johnston. “Quantitative comparison of spinning disk geometries for PAINT based super-resolution microscopy”. In: *Biomedical Optics Express* 13.7 (2022), p. 3773.

[55] A. R. Halpern, M. Y. Lee, M. D. Howard, M. A. Woodworth, P. R. Nicovich, and J. C. Vaughan. “Versatile, do-it-yourself, low-cost spinning disk confocal microscope”. In: *Biomedical Optics Express* 13.2 (2022), p. 1102.

[56] O. Schulz, C. Pieper, M. Clever, J. Pfaff, A. Ruhlandt, R. H. Kehlenbach, F. S. Wouters, J. Großhans, G. Bunt, and J. Enderlein. “Resolution doubling in fluorescence microscopy with confocal spinning-disk image scanning microscopy”. In: *Proceedings of the National Academy of Sciences* 110.52 (2013), pp. 21000–21005.

[57] A. G. York, P. Chandris, D. D. Nogare, J. Head, P. Wawrzusin, R. S. Fischer, A. Chitnis, and H. Shroff. “Instant super-resolution imaging in live cells and embryos via analog image processing”. In: *Nature Methods* 10.11 (2013), pp. 1122–1126.

[58] S. Roth, C. J. Sheppard, K. Wicker, and R. Heintzmann. “Optical photon reassignment microscopy (OPRA)”. In: *Optical Nanoscopy* 2.1 (2013).

[59] G. M. De Luca, R. M. Breedijk, R. A. Brandt, C. H. Zeelenberg, B. E. de Jong, W. Timmermans, L. N. Azar, R. A. Hoebe, S. Stallinga, and E. M. Manders. “Re-scan confocal microscopy: scanning twice for better resolution”. In: *Biomedical Optics Express* 4.11 (2013), p. 2644.

[60] G. Toraldo di Francia. “Resolving Power and Information”. In: *Journal of the Optical Society of America* 45.7 (1955), p. 497.

[61] J. L. Harris. “Diffraction and Resolving Power”. In: *Journal of the Optical Society of America* 54.7 (1964), p. 931.

[62] C. W. McCutchen. “Superresolution in Microscopy and the Abbe Resolution Limit”. In: *Journal of the Optical Society of America* 57.10 (1967), p. 1190.

[63] N. Bobroff. “Position measurement with a resolution and noise-limited instrument”. In: *Review of Scientific Instruments* 57.6 (1986), pp. 1152–1157.

[64] E. Betzig. “Proposed method for molecular optical imaging”. In: *Optics Letters* 20.3 (1995), p. 237.

[65] R. M. Dickson, A. B. Cubitt, R. Y. Tsien, and W. E. Moerner. “On/off blinking and switching behaviour of single molecules of green fluorescent protein”. In: *Nature* 388.6640 (1997), pp. 355–358.

[66] M. Lelek, M. T. Gyparaki, G. Beliu, F. Schueder, J. Griffié, S. Manley, R. Jungmann, M. Sauer, M. Lakadamyali, and C. Zimmer. “Single-molecule localization microscopy”. In: *Nature Reviews Methods Primers* 1.1 (2021).

[67] D. Sage, H. Kirshner, T. Pengo, N. Stuurman, J. Min, S. Manley, and M. Unser. “Quantitative evaluation of software packages for single-molecule localization microscopy”. In: *Nature Methods* 12.8 (2015), pp. 717–724.

[68] J.-C. Olivo-Marin. “Extraction of spots in biological images using multiscale products”. In: *Pattern Recognition* 35.9 (2002), pp. 1989–1996.

[69] C. S. Smith, S. Stallinga, K. A. Lidke, B. Rieger, and D. Grunwald. “Probability-based particle detection that enables threshold-free and robust in vivo single-molecule tracking”. In: *Molecular Biology of the Cell* 26.22 (2015). Ed. by J. Lippincott-Schwartz, pp. 4057–4062.

[70] A. J. Berglund, M. D. McMahon, J. J. McClelland, and J. A. Liddle. “Fast, bias-free algorithm for tracking single particles with variable size and shape”. In: *Optics Express* 16.18 (2008), p. 14064.

[71] A. J. Berglund. “Statistics of camera-based single-particle tracking”. In: *Physical Review E* 82.1 (2010).

[72] R. Henriques, M. Lelek, E. F. Fornasiero, F. Valtorta, C. Zimmer, and M. M. Mhlanga. “QuickPALM: 3D real-time photoactivation nanoscopy image processing in ImageJ”. In: *Nature Methods* 7.5 (2010), pp. 339–340.

[73] D. Sage, T. Pham, H. Babcock, T. Lukes, T. Pengo, J. Chao, R. Velmurugan, A. Herbert, A. Agrawal, S. Colabrese, A. Wheeler, A. Archetti, B. Rieger, R. Ober, G. M. Hagen, J.-B. Sibarita, J. Ries, R. Henriques, M. Unser, and S. Holden. "Super-resolution fight club: assessment of 2D and 3D single-molecule localization microscopy software". In: *Nature Methods* 16.5 (2019), pp. 387–395.

[74] C. S. Smith, N. Joseph, B. Rieger, and K. A. Lidke. "Fast, single-molecule localization that achieves theoretically minimum uncertainty". In: *Nature Methods* 7.5 (2010), pp. 373–375.

[75] H. L. Van Trees. *Detection, Estimation and Modulation Theory: Part 1*. Detection, Estimation, and Modulation Theory. Set (Volumes: I,II, III,IV). Nashville, TN: John Wiley & Sons, 2001.

[76] C. S. Smith, K. Jouravleva, M. Huisman, S. M. Jolly, P. D. Zamore, and D. Grunwald. "An automated Bayesian pipeline for rapid analysis of single-molecule binding data". In: *Nature Communications* 10.1 (2019).

[77] E. Betzig, G. H. Patterson, R. Sougrat, O. W. Lindwasser, S. Olenych, J. S. Bonifacino, M. W. Davidson, J. Lippincott-Schwartz, and H. F. Hess. "Imaging Intracellular Fluorescent Proteins at Nanometer Resolution". In: *Science* 313.5793 (2006), pp. 1642–1645.

[78] S. T. Hess, T. P. Girirajan, and M. D. Mason. "Ultra-High Resolution Imaging by Fluorescence Photoactivation Localization Microscopy". In: *Biophysical Journal* 91.11 (2006), pp. 4258–4272.

[79] M. J. Rust, M. Bates, and X. Zhuang. "Sub-diffraction-limit imaging by stochastic optical reconstruction microscopy (STORM)". In: *Nature Methods* 3.10 (2006), pp. 793–796.

[80] P. Lemmer, M. Gunkel, D. Baddeley, R. Kaufmann, A. Urich, Y. Weiland, J. Reymann, P. Müller, M. Hausmann, and C. Cremer. "SPDM: light microscopy with single-molecule resolution at the nanoscale". In: *Applied Physics B* 93.1 (2008), pp. 1–12.

[81] M. Heilemann, S. van de Linde, M. Schüttpelz, R. Kasper, B. Seefeldt, A. Mukherjee, P. Tinnefeld, and M. Sauer. "Subdiffraction-Resolution Fluorescence Imaging with Conventional Fluorescent Probes". In: *Angewandte Chemie International Edition* 47.33 (2008), pp. 6172–6176.

[82] A. Sharonov and R. M. Hochstrasser. "Wide-field subdiffraction imaging by accumulated binding of diffusing probes". In: *Proceedings of the National Academy of Sciences* 103.50 (2006), pp. 18911–18916.

[83] R. Jungmann, C. Steinhauer, M. Scheible, A. Kuzyk, P. Tinnefeld, and F. C. Simmel. "Single-Molecule Kinetics and Super-Resolution Microscopy by Fluorescence Imaging of Transient Binding on DNA Origami". In: *Nano Letters* 10.11 (2010), pp. 4756–4761.

[84] R. Jungmann, M. S. Avendaño, J. B. Woehrstein, M. Dai, W. M. Shih, and P. Yin. "Multiplexed 3D cellular super-resolution imaging with DNA-PAINT and Exchange-PAINT". In: *Nature Methods* 11.3 (2014), pp. 313–318.

[85] S. C. M. Reinhardt, L. A. Masullo, I. Baudrexel, P. R. Steen, R. Kowalewski, A. S. Eklund, S. Strauss, E. M. Unterauer, T. Schlichthaerle, M. T. Strauss, C. Klein, and R. Jungmann. "Ångström-resolution fluorescence microscopy". In: *Nature* 617.7962 (2023), pp. 711–716.

[86] Y. Li, W. Shi, S. Liu, I. Cavka, Y. Wu, U. Matti, D. Wu, S. Koehler, and J. Ries. "Global fitting for high-accuracy multi-channel single-molecule localization". In: *Nature Communications* 13.1 (2022).

[87] S. Fu, W. Shi, T. Luo, Y. He, L. Zhou, J. Yang, Z. Yang, J. Liu, X. Liu, Z. Guo, C. Yang, C. Liu, Z. Huang, J. Ries, M. Zhang, P. Xi, D. Jin, and Y. Li. "Field-dependent deep learning enables high-throughput

whole-cell 3D super-resolution imaging". In: *Nature Methods* 20.3 (2023), pp. 459–468.

[88] E. Nehme, L. E. Weiss, T. Michaeli, and Y. Shechtman. "Deep-STORM: super-resolution single-molecule microscopy by deep learning". In: *Optica* 5.4 (2018), p. 458.

[89] E. Nehme, D. Freedman, R. Gordon, B. Ferdman, L. E. Weiss, O. Alalouf, T. Naor, R. Orange, T. Michaeli, and Y. Shechtman. "DeepSTORM3D: dense 3D localization microscopy and PSF design by deep learning". In: *Nature Methods* 17.7 (2020), pp. 734–740.

[90] A. Speiser, L.-R. Müller, P. Hoess, U. Matti, C. J. Obara, W. R. Legant, A. Kreshuk, J. H. Macke, J. Ries, and S. C. Turaga. "Deep learning enables fast and dense single-molecule localization with high accuracy". In: *Nature Methods* 18.9 (2021), pp. 1082–1090.

[91] A. Saguy, O. Alalouf, N. Opatovski, S. Jang, M. Heilemann, and Y. Shechtman. "DBlink: dynamic localization microscopy in super spatiotemporal resolution via deep learning". In: *Nature Methods* 20.12 (2023), pp. 1939–1948.

[92] A. J. den Dekker and A. van den Bos. "Resolution: a survey". In: *Journal of the Optical Society of America A* 14.3 (1997), p. 547.

[93] R. P. J. Nieuwenhuizen, K. A. Lidke, M. Bates, D. L. Puig, D. Grünwald, S. Stallinga, and B. Rieger. "Measuring image resolution in optical nanoscopy". In: *Nature Methods* 10.6 (2013), pp. 557–562.

[94] B. Rieger, I. Droste, F. Gerritsma, T. ten Brink, and S. Stallinga. "Single image Fourier ring correlation". In: *Optics Express* 32.12 (2024), p. 21767.

[95] J. Demmerle, E. Wegel, L. Schermelleh, and I. M. Dobbie. "Assessing resolution in super-resolution imaging". In: *Methods* 88 (2015), pp. 3–10.

[96] Y. Li and F. Huang. "A statistical resolution measure of fluorescence microscopy with finite photons". In: *Nature Communications* 15.1 (2024).

[97] R. J. Ober, S. Ram, and E. S. Ward. "Localization Accuracy in Single-Molecule Microscopy". In: *Biophysical Journal* 86.2 (2004), pp. 1185–1200.

[98] S. M. Kay. *Fundamentals of Statistical Signal Processing: Estimation Theory*. Prentice Hall international editions. London, England: Prentice Hall, 1993.

[99] B. Zhang, J. Zerubia, and J.-C. Olivo-Marin. "Gaussian approximations of fluorescence microscope point-spread function models". In: *Applied Optics* 46.10 (2007), p. 1819.

[100] R. Starr, S. Stahlheber, and A. Small. "Fast maximum likelihood algorithm for localization of fluorescent molecules". In: *Optics Letters* 37.3 (2012), p. 413.

[101] S. Stallinga and B. Rieger. "Accuracy of the Gaussian Point Spread Function model in 2D localization microscopy". In: *Optics Express* 18.24 (2010), p. 24461.

[102] M. Siemons, C. N. Hulleman, R. Ø. Thorsen, C. S. Smith, and S. Stallinga. "High precision wavefront control in point spread function engineering for single emitter localization". In: *Optics Express* 26.7 (2018), p. 8397.

[103] Y. Li, M. Mund, P. Hoess, J. Deschamps, U. Matti, B. Nijmeijer, V. J. Sabinina, J. Ellenberg, I. Schoen, and J. Ries. "Real-time 3D single-molecule localization using experimental point spread functions". In: *Nature Methods* 15.5 (2018), pp. 367–369.

[104] R. E. Thompson, D. R. Larson, and W. W. Webb. "Precise Nanometer Localization Analysis for Individual Fluorescent Probes". In: *Biophysical Journal* 82.5 (2002), pp. 2775–2783.

[105] K. I. Mortensen, L. S. Churchman, J. A. Spudich, and H. Flyvbjerg. “Optimized localization analysis for single-molecule tracking and super-resolution microscopy”. In: *Nature Methods* 7.5 (2010), pp. 377–381.

[106] S. Stallinga and B. Rieger. “The effect of background on localization uncertainty in single emitter imaging”. In: *2012 9th IEEE International Symposium on Biomedical Imaging (ISBI)*. IEEE, 2012, pp. 988–991.

[107] B. Rieger and S. Stallinga. “The Lateral and Axial Localization Uncertainty in Super-Resolution Light Microscopy”. In: *ChemPhysChem* 15.4 (2013), pp. 664–670.

[108] N. Radmacher, A. I. Chizhik, O. Nevskyi, J. I. Gallea, I. Gregor, and J. Enderlein. “Molecular Level Super-Resolution Fluorescence Imaging”. In: *Annual Review of Biophysics* 54.1 (2025), pp. 163–184.

[109] L. Reymond, T. Huser, V. Ruprecht, and S. Wieser. “Modulation-enhanced localization microscopy”. In: *Journal of Physics: Photonics* 2.4 (2020), p. 041001.

[110] F. Balzarotti, Y. Eilers, K. C. Gwosch, A. H. Gynnå, V. Westphal, F. D. Stefani, J. Elf, and S. W. Hell. “Nanometer resolution imaging and tracking of fluorescent molecules with minimal photon fluxes”. In: *Science* 355.6325 (2017), pp. 606–612.

[111] J. K. Pape, T. Stephan, F. Balzarotti, R. Büchner, F. Lange, D. Riedel, S. Jakobs, and S. W. Hell. “Multicolor 3D MINFLUX nanoscopy of mitochondrial MICOS proteins”. In: *Proceedings of the National Academy of Sciences* 117.34 (2020), pp. 20607–20614.

[112] K. C. Gwosch, J. K. Pape, F. Balzarotti, P. Hoess, J. Ellenberg, J. Ries, and S. W. Hell. “MINFLUX nanoscopy delivers 3D multicolor nanometer resolution in cells”. In: *Nature Methods* 17.2 (2020), pp. 217–224.

[113] T. Deguchi and J. Ries. “Simple and robust 3D MINFLUX excitation with a variable phase plate”. In: *Light: Science & Applications* 13.1 (2024).

[114] L. Scheiderer, Z. Marin, and J. Ries. “MINFLUX achieves molecular resolution with minimal photons”. In: *Nature Photonics* 19.3 (2025), pp. 238–247.

[115] M. Weber, M. Leutenegger, S. Stoldt, S. Jakobs, T. S. Mihaila, A. N. Butkevich, and S. W. Hell. “MINSTED fluorescence localization and nanoscopy”. In: *Nature Photonics* 15.5 (2021), pp. 361–366.

[116] M. Weber, H. von der Emde, M. Leutenegger, P. Gunkel, S. Sambandan, T. A. Khan, J. Keller-Findeisen, V. C. Cordes, and S. W. Hell. “MINSTED nanoscopy enters the Ångström localization range”. In: *Nature Biotechnology* 41.4 (2022), pp. 569–576.

[117] L. A. Masullo, F. Steiner, J. Zähringer, L. F. Lopez, J. Bohlen, L. Richter, F. Cole, P. Tinnefeld, and F. D. Stefani. “Pulsed Interleaved MINFLUX”. In: *Nano Letters* 21.1 (2020), pp. 840–846.

[118] L. A. Masullo, L. F. Lopez, and F. D. Stefani. “A common framework for single-molecule localization using sequential structured illumination”. In: *Biophysical Reports* 2.1 (2022), p. 100036.

[119] L. A. Masullo, A. M. Szalai, L. F. Lopez, M. Pilo-Pais, G. P. Acuna, and F. D. Stefani. “An alternative to MINFLUX that enables nanometer resolution in a confocal microscope”. In: *Light: Science & Applications* 11.1 (2022).

[120] P. Zdańkowski, L. F. Lopez, G. P. Acuna, and F. D. Stefani. “Nanometer Resolution Imaging and Tracking of Single Fluorophores by Sequential Structured Illumination”. In: *ACS Photonics* 9.12 (2022), pp. 3777–3785.

[121] J. Cnossen, T. Hinsdale, R. Ø. Thorsen, M. Siemons, F. Schueder, R. Jungmann, C. S. Smith, B. Rieger, and S. Stallinga. “Localization microscopy at doubled precision with patterned illumination”.

In: *Nature Methods* 17.1 (2019), pp. 59–63.

[122] L. Reymond, J. Ziegler, C. Knapp, F.-C. Wang, T. Huser, V. Ruprecht, and S. Wieser. “SIMPLE: Structured illumination based point localization estimator with enhanced precision”. In: *Optics Express* 27.17 (2019), p. 24578.

[123] L. Gu, Y. Li, S. Zhang, Y. Xue, W. Li, D. Li, T. Xu, and W. Ji. “Molecular resolution imaging by repetitive optical selective exposure”. In: *Nature Methods* 16.11 (2019), pp. 1114–1118.

[124] P. van Velde, B. Rieger, T. Hindsdale, J. Cnossen, D. Fan, S. Hung, D. Grunwald, and C. Smith. “ZIMFLUX: Single molecule localization microscopy with patterned illumination in 3D”. In: *Optics Express* 31.25 (2023), p. 42701.

[125] P. Jouchet, C. Cabriel, N. Bourg, M. Bardou, C. Poüs, E. Fort, and S. Lévêque-Fort. “In Depth 3D Single Molecule Localization Microscopy with Time Modulated Excitation”. In: *Biophysical Journal* 118.3 (2020), 149a.

[126] P. Jouchet, C. Cabriel, N. Bourg, M. Bardou, C. Poüs, E. Fort, and S. Lévêque-Fort. “Nanometric axial localization of single fluorescent molecules with modulated excitation”. In: *Nature Photonics* 15.4 (2021), pp. 297–304.

[127] P. Jouchet, C. Poüs, E. Fort, and S. Lévêque-Fort. “Time-modulated excitation for enhanced single-molecule localization microscopy”. In: *Philosophical Transactions of the Royal Society A: Mathematical, Physical and Engineering Sciences* 380.2220 (2022).

[128] L. Gu, Y. Li, S. Zhang, M. Zhou, Y. Xue, W. Li, T. Xu, and W. Ji. “Molecular-scale axial localization by repetitive optical selective exposure”. In: *Nature Methods* 18.4 (2021), pp. 369–373.

[129] Y. Shechtman, S. J. Sahl, A. S. Backer, and W. E. Moerner. “Optimal Point Spread Function Design for 3D Imaging”. In: *Physical Review Letters* 113.13 (2014).

[130] Y. Shechtman, L. E. Weiss, A. S. Backer, S. J. Sahl, and W. E. Moerner. “Precise Three-Dimensional Scan-Free Multiple-Particle Tracking over Large Axial Ranges with Tetrapod Point Spread Functions”. In: *Nano Letters* 15.6 (2015), pp. 4194–4199.

[131] M. Fazel, M. J. Wester, H. Mazloom-Farsibaf, M. B. M. Meddens, A. S. Eklund, T. Schlichthaerle, F. Schueder, R. Jungmann, and K. A. Lidke. “Bayesian Multiple Emitter Fitting using Reversible Jump Markov Chain Monte Carlo”. In: *Scientific Reports* 9.1 (2019).

[132] S. Cox, E. Rosten, J. Monypenny, T. Jovanovic-Talisman, D. T. Burnette, J. Lippincott-Schwartz, G. E. Jones, and R. Heintzmann. “Bayesian localization microscopy reveals nanoscale podosome dynamics”. In: *Nature Methods* 9.2 (2011), pp. 195–200.

[133] D. Kalisvaart, S. Hung, and C. S. Smith. “Quantifying the minimum localization uncertainty of image scanning localization microscopy”. In: *Biophysical Reports* 4.1 (2024), p. 100143.

[134] N. Radmacher, O. Nevskyi, J. I. Gallea, J. C. Thiele, I. Gregor, S. O. Rizzoli, and J. Enderlein. “Doubling the resolution of fluorescence-lifetime single-molecule localization microscopy with image scanning microscopy”. In: *Nature Photonics* 18.10 (2024), pp. 1059–1066.

[135] R. van Dijk, D. Kalisvaart, J. Cnossen, and C. S. Smith. “Bayesian posterior density estimation reveals degeneracy in three-dimensional multiple emitter localization”. In: *Scientific Reports* 13.1 (2023).

[136] P. J. Green. “Reversible Jump Markov Chain Monte Carlo Computation and Bayesian Model Determination”. In: *Biometrika* 82.4 (1995), pp. 711–732.

[137] J. Min, C. Vonesch, H. Kirshner, L. Carlini, N. Olivier, S. Holden, S. Manley, J. C. Ye, and M. Unser. “FALCON: fast and unbiased reconstruction of high-density super-resolution microscopy data”. In: *Scientific Reports* 4.1 (2014).

[138] D. Kalisvaart, J. Cnossen, S. Hung, S. Stallinga, M. Verhaegen, and C. S. Smith. “Precision in iterative modulation enhanced single-molecule localization microscopy”. In: *Biophysical Journal* 121.12 (2022), pp. 2279–2289.

[139] A. R. Small. “Prior information improves resolution”. In: *Biophysical Journal* 121.12 (2022), pp. 2221–2222.

[140] C. Smith, D. Kalisvaart, and K. Prakash. “Unveiling the limits of precision in iterative MINFLUX”. In: *Journal of Microscopy* 296.2 (2024), pp. 129–132.

[141] R. D. Gill and B. Y. Levit. “Applications of the van Trees Inequality: A Bayesian Cramér-Rao Bound”. In: *Bernoulli* 1.1/2 (1995), p. 59.

[142] J. M. Hammersley and D. C. Handscomb. *Monte Carlo Methods*. Monographs on Statistics & Applied Probability. London, England: Chapman and Hall, 1964.

2

Quantifying the Minimum Localization Uncertainty of Image Scanning Localization Microscopy

You are like a lantern swathed and covered, hidden away in a dark place. Yet the light shines; they could not put out the light. They could not hide you. As I know the light, as I know you, I know your name, Tenar. That is my gift, my power.

Ursula Kroeber Le Guin, *The Tombs of Atuan*

Dylan Kalisvaart
Shih-Te Hung
Carlas S. Smith

Biophysical Journal, vol. 4, no. 1, (2024), p. 100143

2

Abstract

Modulation enhanced single-molecule localization microscopy (meSMLM), where emitters are sparsely activated with sequentially applied patterned illumination, increases the localization precision over single-molecule localization microscopy (SMLM). The precision improvement of modulation enhanced SMLM is derived from retrieving the position of an emitter relative to individual illumination patterns, which adds to existing point spread function information from SMLM. Here, we introduce SpinFlux: modulation enhanced localization for spinning disk confocal microscopy. SpinFlux uses a spinning disk with pinholes in its illumination and emission paths, to sequentially illuminate regions in the sample during each measurement. The resulting intensity-modulated emission signal is analysed for each individual pattern to localize emitters with improved precision. We derive a statistical image formation model for SpinFlux and we quantify the theoretical minimum localization uncertainty in terms of the Cramér-Rao lower bound. Using the theoretical minimum uncertainty, we compare SpinFlux to localization on Fourier reweighted image scanning microscopy reconstructions. We find that localization on image scanning microscopy reconstructions with Fourier reweighting ideally results in a global precision improvement of 2.1 over SMLM. When SpinFlux is used for sequential illumination with three patterns around the emitter position, the localization precision improvement over SMLM is twofold when patterns are focused around the emitter position. If four donut-shaped illumination patterns are used for SpinFlux, the maximum local precision improvement over SMLM is increased to 3.5. Localization of image scanning microscopy reconstructions thus has the largest potential for global improvements of the localization precision, where SpinFlux is the method of choice for local refinements.

Significance

One of the main objectives of SMLM is to improve the precision with which single molecules can be localized. This has been successfully achieved through modulation enhanced SMLM, which uses patterned illumination to increase the information content of signal photons. However, this technique relies on setups with increased technical complexity over SMLM. With SpinFlux, we enable a 2- to 3.5-fold maximum precision improvement over SMLM when the emitter is in the pattern focus. These improvements can be achieved with only minor modifications to existing spinning disk confocal microscopy setups (e.g., a phase mask in the illumination and emission paths). In addition, our modelling framework enables evaluation of a wide variety of spinning disk setups and therefore paves the way for optimal spinning disk design.

2.1. Introduction

Single-molecule localization microscopy (SMLM) increases the precision with which single molecules can be localized beyond the diffraction limit [1–3]. Methods in SMLM require sparse activation of single emitters, after which emitters can be localized sequentially with reduced uncertainty.

In recent years, various modulation enhanced SMLM (meSMLM) methods were introduced that increase the localization precision over SMLM by sparsely activating emitters with intensity-modulated illumination patterns [4]. As a result, information is added to the data about the relative position of the emitter with respect to the illumination patterns. meSMLM methods include SIMFLUX [5], SIMPLE [6] and repetitive optical selective exposure (ROSE) [7], which use sinusoidally shaped intensity patterns, and MINFLUX [8] and RASTMIN [9, 10], which use a donut-shaped illumination pattern. Patterned illumination can also be used to improve axial resolution, for example, with modulated localization (ModLoc) [11, 12] and ROSE-Z [13], which use illumination with both axial and lateral structure. Additional improvements to the localization precision can be attained through iterative meSMLM [14, 15], where patterns are iteratively moved through the sample using prior information from earlier measurements, to improve the localization precision locally around single emitters.

Specifically for SIMFLUX [5], it has been shown that meSMLM with sinusoidal patterns improves the resolution over both SMLM and structured illumination microscopy (SIM) [16]. SIM uses nine sinusoidal patterns in total aligned on three lateral axes, and subsequent reconstruction results in at most a 2-fold resolution improvement over the diffraction limit. SIMFLUX on the other hand only uses six patterns in total aligned on two lateral axes, and subsequent localization results in a 2.4-fold maximum improvement of the localization precision over SMLM. Therefore, the combination of structured illumination with sparse localization in meSMLM can result in a better resolution over existing reconstruction approaches, while using less illumination patterns in the process. These factors motivate the incorporation of meSMLM in existing systems, in which image reconstruction instead of localization is the current state-of-the-art.

A promising candidate system is spinning disk confocal microscopy (SDCM) [17–21] (see Fig. 2.1*a*). SDCM introduces a spinning disk with pinholes in the illumination and emission paths. Rapidly pulsing the excitation laser causes stroboscopic illumination of the sample with moving illumination foci. If used for image scanning microscopy (ISM) [22], the fluorescent emission signal is recorded on an image detector. Subsequent reconstruction of the recorded images results in an expected resolution improvement of a factor 2 over diffraction limited imaging [18, 19].

Recently, SDCM was used for PAINT- and STORM-based localization microscopy, where SMLM localization algorithms were used to localize emitters in raw camera data [20, 21]. It is shown that this improves the detection rate and signal-to-background ratio compared with widefield SMLM at the cost of a reduced signal photon count, resulting in a localization precision that is at best comparable with that of SMLM [20].

However, these methods do not take the information contained in the illumination pattern into account, as one would do in meSMLM. In this chapter, we therefore develop a statistical image formation model, suited for modulation enhanced localization in SDCM (see Fig. 2.1*b*). Our method, called SpinFlux, sequentially applies patterned

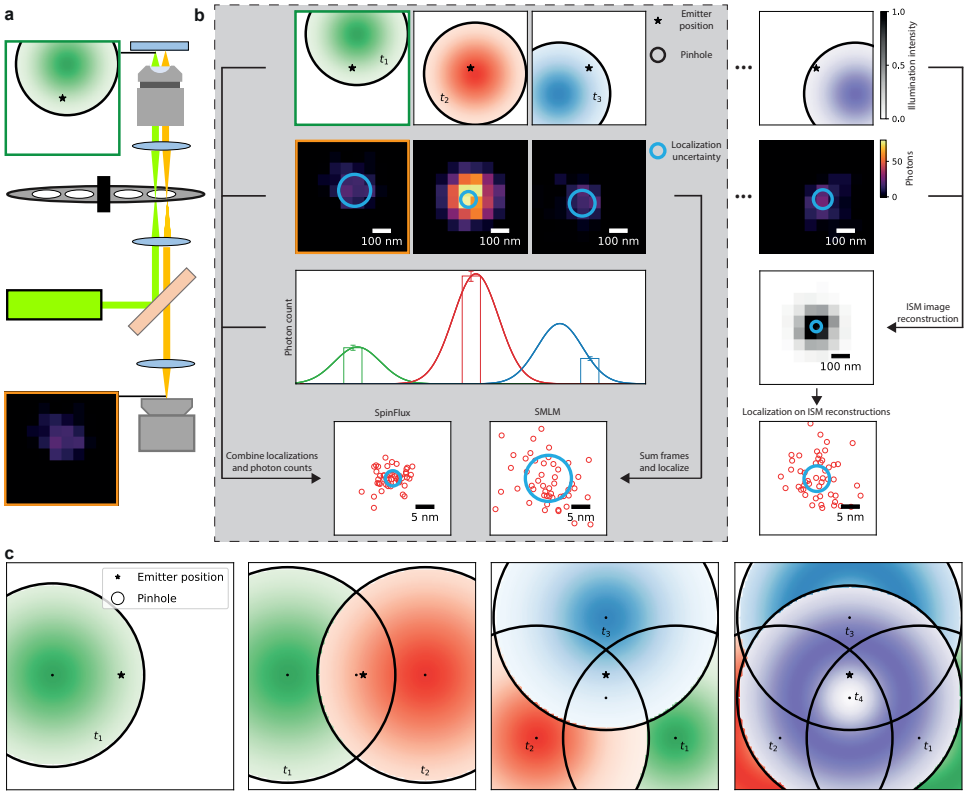

Figure 2.1: Schematic overview of SpinFlux image formation and analysis. (*a*) In SpinFlux, a rotating disk containing pinholes is placed in the illumination- and emission paths. This causes patterned illumination (*green cadre*) in the sample, modulating the emission intensity of emitters in the sample based on their relative distance to the pattern. Subsequently, the emission signal (*orange cadre*) is windowed by the pinhole. Rapidly switching the laser on and off causes stroboscopic illumination of emitters in the sample with stationary illumination patterns. (*b*) SpinFlux obtains its localization precision improvement by merging localized emitter data with information about the relative distance between an illumination pattern and the emitter, derived from photon counts. In this way, it improves the localization precision over SMLM, which only uses localized emitter data and ignores pattern information. We compare SpinFlux with an idealized approach, in which first an ISM acquisition and reconstruction are performed. Afterward, isolated emitters are localized in the ISM reconstruction. (*c*) Schematic overview of SpinFlux localization variants. In this chapter, we consider SpinFlux with one, two, three, and four sequentially applied illumination patterns. The configurations with one, two, and three patterns use Gaussian beams, the configuration with four patterns uses donut beams. Additional configurations are explored in the supporting information.

illumination generated by a spinning disk to excite the sample. Subsequently, emitters are localized in the recordings from a sequence of individual pattern acquisitions, taking knowledge about the pattern into account. The resulting intensity-modulated emission signal is then described by our image formation model.

To evaluate the potential localization precision improvements of SpinFlux, we need to study the information contained in a single-pattern exposure, the localization precision obtained by sequential illumination with multiple patterns and the optimal pattern

configuration to maximally improve the precision. To accomplish this, we calculate the theoretical minimum uncertainty of SpinFlux in terms of the Cramér-Rao lower bound (CRLB) [23, 24]. The CRLB is often used in (me)SMLM to quantify the theoretical minimum uncertainty of localizations. Using the SpinFlux image formation model, we calculate the CRLB for various illumination pattern configurations. Based on the CRLB, we compare SpinFlux with SMLM.

Secondly, we consider a localization approach that is comparable with SpinFlux. Here, isolated emitters are localized directly in ISM reconstructions [25], rather than in individual pattern acquisitions as done in SpinFlux. Specifically, we consider localization in ISM reconstructions with a factor $\sqrt{2}$-reduction in the point spread function (PSF) width. We also consider ISM reconstructions that are Fourier reweighted (see Fig. 2.1*b*), resulting in a factor 2 reduction in the PSF width. We approximate the maximum localization precision of these approaches and compare it with SpinFlux.

2.2. Methods

In SpinFlux (see Fig. 2.1*a*), a spinning disk containing pinholes is placed in the illumination and emission paths. The spinning disk is rotated, thereby sequentially moving illumination patterns over the sample. As in SDCM [19], the excitation laser is rapidly switched on and off. Within the time frame where the laser is on, the spinning disk can be considered stationary. This causes stroboscopic illumination of emitters in the sample. Furthermore, the illumination has a nonuniform intensity profile over the field of view due to the spinning disk architecture. This causes patterned illumination of emitters in the sample, which in turn results in intensity modulation of the emission signal. The rotation angle of the spinning disk determines the position of each illumination pattern with respect to the emitter position. Subsequently, the intensity-modulated emission signal is windowed by the same pinhole, after which the signal is imaged on a camera.

The image analysis (see Fig. 2.1*b*) consists of extracting localized emitters from the recordings, as well as retrieving the relative distance between the illumination pattern and emitter from the photon count. To evaluate the total amount of information that can be extracted from the measurements with this approach, we first develop an image formation model for SpinFlux. We subsequently use this model to calculate the theoretical minimum uncertainty of SpinFlux in terms of the CRLB. The CRLB will allow us to quantify the maximum amount of information contained in each exposure with a single pattern. In turn, we use this to derive the localization precision that can be attained through sequential exposures with multiple patterns. In addition, we can explore how the pattern configuration, the pinhole radius, and the mutual spacing between patterns affect the maximum localization precision.

2.2.1. Model for SpinFlux image formation

To calculate the theoretical minimum uncertainty that can be attained with SpinFlux localization, we need a model to describe the amount of photons collected by a camera pixel. Existing models for (me)SMLM [5, 8, 14, 26, 27] do not suffice for this, as they do not include a pinhole in the illumination and emission paths. In this subsection, we therefore develop a statistical image formation model for SpinFlux. A detailed derivation

of this model can be found in Section 2.S2.

For the image formation, we assume that pinholes are separated far enough on the spinning disk, such that only one pinhole can appear in a region of interest during each camera frame. This assumption is valid for the magnifications, pinhole sizes, and pinhole separations in existing SDCM setups [19–21]. In line with this, we can assume that there is no crosstalk of emission signals between different pinholes. This allows us to describe the regions of interest on the camera frames as separate regions of interest from individual patterns.

We model the pinhole in the emission path as a circular window. In the absence of readout noise, the measurements on each camera pixel can be described as independent realizations of a Poisson process [26]. For each pixel i with centre coordinates (x_i, y_i) and for the measurement corresponding to illumination pattern k, the expected photon count $\mu_{i,k}$ after illumination through the pinhole with position $(x_{\mathrm{p},k}, y_{\mathrm{p},k})$ is described by (see Section 2.S2):

$$\mu_{i,k}(x_i, x_{\mathrm{p},k}, y_i, y_{\mathrm{p},k}) = A\theta_I P(\theta_x - x_{\mathrm{p},k}, \theta_y - y_{\mathrm{p},k}) H(\theta_x, \theta_y, x_i, y_i) + A\theta_b B_{i,k}. \tag{2.1}$$

Here, (θ_x, θ_y) is the emitter position, θ_I is the expected signal photon count under maximum illumination, and θ_b is the expected background photon count.

Each illumination pattern $P(\theta_x - x_{\mathrm{p},k}, \theta_y - y_{\mathrm{p},k})$ is assumed to be a known function with a known pinhole position $(x_{\mathrm{p},k}, y_{\mathrm{p},k})$ in our image formation model. We model each illumination pattern as a Gaussian PSF in the centre of the pinhole, with standard deviation σ_{illum}. Alternate illumination patterns can be generated by placing a phase mask in the illumination path. We therefore also include a model of the donut-shaped pattern from, e.g., MINFLUX [8], with a zero-intensity minimum at the centre of the pinhole and standard deviation σ_{illum}.

Note that the signal photon budget of a single emitter stays constant when going from one pattern location to multiple pattern locations. In particular, this means that one pattern exhausts the full signal photon budget, whereas multiple patterns need to share the same signal photon budget. Each pattern in a multiple-pattern illumination sequence gets a share of the signal photon budget proportional to their illumination intensity on the emitter position.

We model the emission PSF as a Gaussian, with standard deviation σ_{PSF}. The term $H(\theta_x, \theta_y, x_i, y_i)$ describes the discretized emission PSF after windowing by the pinhole (see Subsection 2.S2.2).

In existing work on meSMLM, such as in MINFLUX [8], it is assumed that meSMLM is able to record the same amount of signal photons as SMLM. This assumption allows benchmarking between methods on the same signal photon count. However, the assumption is not trivial, as additional illumination power or time is needed to exhaust the signal photon budget with nonmaximum illumination intensity. Properly adjusting the illumination power to compensate for the reduced photon flux requires accurate prior knowledge about the emitter position, which is generally unavailable. Increasing the illumination time increases the probability of sample degradation. As such, we should include the possibility that meSMLM will not exhaust the signal photon budget in the image formation model.

The normalizing constant A describes how the signal photon budget is affected by nonmaximum illumination intensity. This constant plays a vital role in benchmarking meSMLM (when the summed intensity over all patterns does not result in a uniform profile), as it gives a physical explanation of the fair signal photon count against which meSMLM should be compared [14]. Specifically when comparing meSMLM to SMLM, the normalization constant models whether meSMLM would have had recorded the same amount of signal photons as SMLM, despite the additional illumination power or time needed to do so. Results on the improvement of meSMLM compared with SMLM should thus only be given in the context of the normalizing constant A.

We choose A to model two scenarios (see Subsection 2.S2.4). In the first scenario, which we explore in this chapter, we assume that the entire signal photon budget is exhausted after illumination with all patterns, independent of the total brightness on the emitter position. We thus assume the illumination power and time is sufficient to exhaust the signal photon budget of the emitter. Here, A is inversely proportional to the summed illumination patterns. The only signal photon loss in this scenario comes from the windowing effect of the emission pinhole. This scenario is consistent with the assumption used in, e.g., MINFLUX [8], stating that meSMLM will record the same amount of photons as SMLM. In the second scenario, the illumination power and time are constant for each pattern such that the total illumination power and time equal that of SMLM, even though this does not exhaust the signal photon budget for nonmaximum illumination. Instead, the maximum possible signal photon count occurs when the emitter is placed at the brightest position of the total illumination pattern. Here, A is inversely proportional to the amount of illumination patterns K.

The constant $B_{i,k}$ describes how the background is affected by illumination pattern k. As such, the term $A\theta_b B_{i,k}$ represents the effective background under patterned illumination. It depends on the camera pixel area, the pinhole area, the PSF, and the illumination pattern, but not on the emitter position (see Subsection 2.S2.3). In the analysis of, e.g., MINFLUX [8], the pattern dependency of the background is neglected. We can incorporate this in our image formation model for SpinFlux by modelling $B_{i,k}$ as the overlapping area between the camera pixel i and the approximation of pinhole k (see Subsection 2.S2.5).

2.2.2. Cramér-Rao lower bound

To quantify the theoretical minimum uncertainty of localizations, the CRLB is often used [23, 24]. Under regularity conditions on the likelihood of the data [23], the CRLB states that the estimator covariance $C_{\hat{\boldsymbol{\theta}}}$ of any unbiased estimator $\hat{\boldsymbol{\theta}}$ of the parameters $\boldsymbol{\theta}$ satisfies the property that $\left(C_{\hat{\boldsymbol{\theta}}} - I^{-1}(\boldsymbol{\theta})\right)$ is positive semidefinite. Here, $I(\boldsymbol{\theta})$ is the Fisher information, of which entry (u, v) is described by:

$$I_{uv}(\boldsymbol{\theta}) = \mathbb{E}\left[\frac{\partial \ell(\boldsymbol{\theta}|\boldsymbol{c})}{\partial \boldsymbol{\theta}_u}\frac{\partial \ell(\boldsymbol{\theta}|\boldsymbol{c})}{\partial \boldsymbol{\theta}_v}\right], \tag{2.2}$$

where $\ell(\boldsymbol{\theta}|\boldsymbol{c})$ is the log-likelihood function given the recorded photon counts $\boldsymbol{c}$ on the camera pixels. The matrix $I^{-1}(\boldsymbol{\theta})$ is the CRLB. Consequently, the diagonal of the CRLB bounds the estimator variance from below.

Specifically for SMLM, the CRLB is attained by the covariance of the maximum like-

lihood estimator (MLE) for 100 or more signal photons [26]. As the localization uncertainty of the MLE converges asymptotically to the CRLB [28, 29], we can also use the CRLB to investigate the theoretical minimum uncertainty of SpinFlux.

Using the image formation model from Eq. (2.1), we can derive the CRLB for SpinFlux. When using K pinholes and a camera consisting of an array with N_{pixels} pixels, any entry (u, v) of the Fisher information is given by (see Section 2.S3):

$$I_{uv}(\boldsymbol{\theta}) = \sum_{i=1}^{N_{\text{pixels}}} \sum_{k=1}^{K} \frac{1}{\mu_{i,k}} \frac{\partial \mu_{i,k}}{\partial \boldsymbol{\theta}_u} \frac{\partial \mu_{i,k}}{\partial \boldsymbol{\theta}_v}. \tag{2.3}$$

To evaluate Eq. (2.3), the partial derivatives of the image formation model of Eq. (2.1) with respect to the unknown parameters θ_x, θ_y, θ_I and θ_b need to be computed. Expressions for these partial derivatives are found in Section 2.S4.

2.2.3. Simulations and parameter values

We sampled measurements from the image formation model and evaluated the CRLB using representative in silico experiments. The model parameters (see Table 2.S1) are considered to be representative of an SDCM experiment [20].

To maximize the information contained in the Gaussian illumination and emission PSFs, we choose their standard deviations to be diffraction limited [30]. Specifically, we approximate the standard deviation of the illumination $\sigma_{\text{illum}} = 0.21\frac{\lambda_{\text{ex}}}{\text{NA}}$ and the standard deviation of the PSF $\sigma_{\text{PSF}} = 0.21\frac{\lambda_{\text{em}}}{\text{NA}}$. Here, λ_{ex} and λ_{em}, respectively, describe the excitation and emission wavelengths and NA is the numerical aperture.

Emitters are located in the centre of the region of interest, consisting of 10×10 pixels. The pinhole was discretized on a mesh with $N_{\text{M},x}$, $N_{\text{M},y} = 100$ pixels in each direction. For $N_{\text{M},x}$, $N_{\text{M},y} = 100$ mesh pixels, the relative error in the CRLB caused by the discretized pinhole approximation is at most 0.02% (see Fig. 2.S2).

2.3. Results

A spinning disk can be designed with various pinhole sizes, spacing, and arrangements [20]. In addition, the rotation of the spinning disk gives additional freedom, as patterns and pinholes can appear arbitrarily close to each other via sequential illumination with a rotating spinning disk. For SpinFlux, this means that a wide variety of illumination pattern configurations can be created via the appropriate spinning disk and rotation angle. Furthermore, donut-shaped illumination patterns can be used by adding a phase mask in the illumination path (see Fig. 2.S3). In this section, we explore how the theoretical minimum localization uncertainty of SpinFlux depends on pattern configurations and positions.

In Figs. 2.2-2.5 and 2.S4-2.S17, we calculate the theoretical minimum uncertainty for the scenario where the entire signal photon budget is exhausted after illumination with all patterns. We compute the theoretical minimum localization uncertainty for three standard configurations. These pattern configurations can be created via sequential illumination with a rotating spinning disk, where the rotation angle of the spinning disk determines the position of an illumination pattern. In Subsection 2.3.1, we establish localization on ISM reconstruction data as a benchmark for SpinFlux. In Subsection 2.3.2, we

simulate the theoretical minimum uncertainty using a single pattern and pinhole, akin to confocal microscopy. In Subsection 2.3.3, we compute the CRLB for a two-pattern configuration where pinholes are separated by a distance s along the x-axis, resembling raster-like configurations of earlier work on meSMLM [9, 10, 14]. In Subsection 2.3.4, patterns and pinholes are arranged in an equilateral triangle configuration, similar to the configuration found in MINFLUX [8, 15]. Subsection 2.3.5 shows the effect of donut-shaped illumination patterns. A summary of the most important simulation results is found in Table 2.1.

To rigorously quantify the improvement of SpinFlux, we also evaluate the localization precision in the two other scenarios described in Subsection 2.2.1. Figs. 2.S18-2.S31 show the theoretical minimum uncertainty in the case in which the illumination power and time are constant for each pattern. There, the maximum possible signal photon count occurs when the emitter is placed at the brightest position of the total illumination pattern. Figs. 2.S32-2.S45 show the CRLB where the pattern dependency of the background is neglected and where the entire signal photon budget is exhausted after illumination with all patterns.

2.3.1. Localization on image scanning microscopy reconstruction data

As a straightforward implementation of localization, we consider localizing isolated emitters in ISM reconstruction data. In this approach, an ISM image is first acquired and reconstructed, resulting in a reduction of the PSF width by at most a factor $\sqrt{2}$ [18, 19]. If the ISM image is subsequently Fourier reweighted [18], the PSF width is reduced further by a total factor 2. Subsequently, individual emitters are localized in the ISM reconstruction data.

We approximate the CRLB for this localization approach (see Section 2.S1). For a signal photon count of 2000 photons per emitter and a background photon count of 8 photons per pixel, the best-case localization precision of localization on the ISM reconstructions is 1.77 nm, or 1.25 nm with Fourier reweighting, whereas SMLM would achieve a localization precision of at most 2.62 nm. The improvement of localization on the ISM reconstructions over SMLM is thus 1.48, or 2.10 with Fourier reweighting. These results agree with the improvements that were recently found experimentally [25].

Fig. 2.2 shows the localization precision of localization of individual emitters in the ISM data over a range of signal and background photon counts, PSF standard deviations, and camera pixel sizes. From Fig. 2.2*b*, we see that the improvement of localization on the ISM data over SMLM for a PSF standard deviation of 93.3 nm and a camera pixel size of 65 nm is at most 1.8, or 3.0 with Fourier reweighting. This is achieved at a signal photon count of 200 photons and a background photon count of 16 photons per pixel. Furthermore, the improvement decreases to 1.4, or 1.9 with Fourier reweighting, as the background goes to zero. For zero background, the improvement over SMLM is constant as a function of the signal photon count. In our approximation, the localization precision of localization on ISM reconstructions is proportional to $\frac{1}{\sqrt{\theta_I}}$ if the background is zero, and therefore the improvement over widefield SMLM is constant.

Fig. 2.S1 shows the localization precision of localization of individual emitters in the ISM data over a range of PSF standard deviations and camera pixel sizes. From Fig. 2.S1*b*, we see that the improvement of localization on the ISM data over SMLM for a

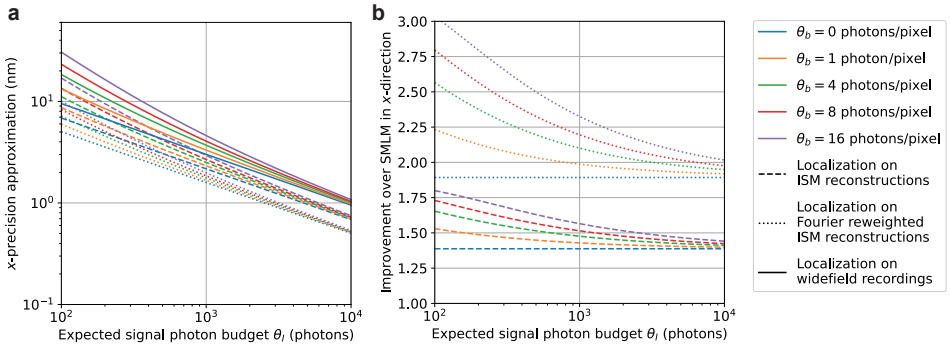

Figure 2.2: Approximation of the theoretical minimum localization uncertainty of SMLM on reconstructions acquired from (Fourier reweighted) ISM. For this simulation, a PSF standard deviation of 93.3 nm and a camera pixel size of 65 nm were used. (*a*) Approximate CRLB in the x-direction as a function of the expected signal photon budget for varying values of the expected background photon count. (*b*) Improvement of the approximate CRLB over SMLM as a function of the expected signal photon budget for varying values of the expected background photon count.

signal photon count of 2000 photons and a background photon count of 8 photons per pixel is at most 1.7, or 2.8 with Fourier reweighting, achieved at a PSF standard deviation of 250 nm and a camera pixel size of 50 nm. Furthermore, the improvement decreases to 1.3, or 1.5 with Fourier reweighting, for an increasing camera pixel size and a decreasing PSF size.

2.3.2. Single pattern configuration

In Fig. 2.3, we evaluate the theoretical minimum uncertainty in the case in which a single pinhole is used for illumination and emission, as illustrated in Fig. 2.3*a*. Results are shown for the scenario where the entire signal photon budget is exhausted after illumination with all patterns.

From Fig. 2.3, *d* and *e*, we see that the localization precision is optimal when the pinhole and pattern are centred directly on the emitter position. Without a pinhole, this results in an improvement of at most 1.17 over SMLM. For a pinhole with radius $r_\mathrm{p} = 4\sigma_\mathrm{PSF}$, the difference with SMLM is negligible, indicating that the confocal effect of the pinhole has been lost. The improvement can thus be attributed to the effect of pattern-dependent background, as the background is reduced on camera pixels that are not located on the maximum of the Gaussian illumination pattern. This background reduction is visualized in Fig. 2.S4*g*, showing a 10.2-fold reduction in the average background count per pixel compared with SMLM for $r_\mathrm{p} = 4\sigma_\mathrm{PSF}$ and $x_\mathrm{p} = \theta_x$.

For pinholes of radius $r_\mathrm{p} = 3\sigma_\mathrm{PSF}$ and below, the localization precision deteriorates with respect to the no-pinhole case. Already for $r_\mathrm{p} = 2\sigma_\mathrm{PSF}$, no position of the pinhole results in an improvement over SMLM. In these cases, the pinhole not only blocks background photons, but also signal photons carrying information about the emitter position. Fig. 2.S4, *f* and *g* show that, in the best case (for $x_\mathrm{p} = \theta_x$) 248 signal photons are lost when going from $r_\mathrm{p} = 3\sigma_\mathrm{PSF}$ to $r_\mathrm{p} = 2\sigma_\mathrm{PSF}$, whereas the average background is reduced with only 0.21 photons per pixel. As such, more information about the emitter position is

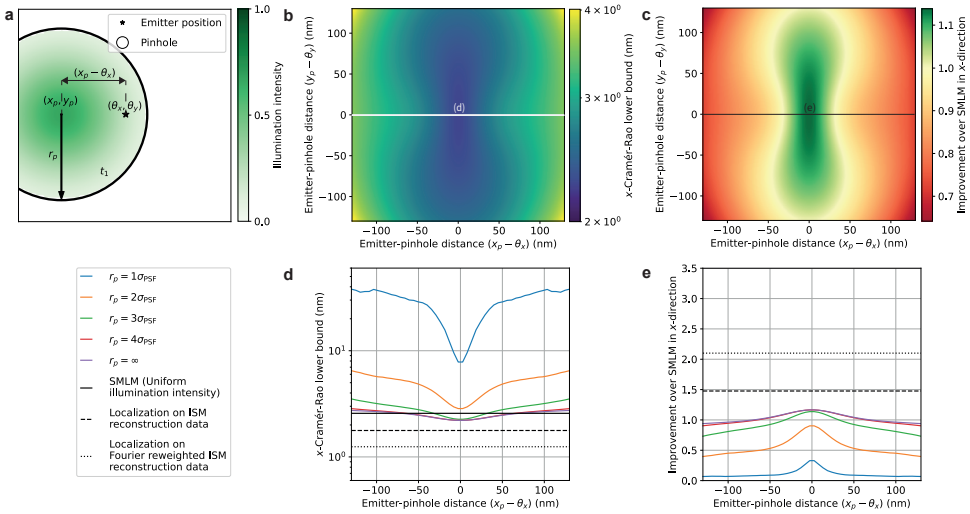

Figure 2.3: Theoretical minimum localization uncertainty of SpinFlux localization with one x-offset pinhole and pattern. For this simulation, 2000 expected signal photons and 8 expected background photons per pixel were used. Results are evaluated for the scenario where the entire signal photon budget is exhausted after illumination with the pattern (disregarding signal photons blocked by the spinning disk). (*a*) Schematic overview of SpinFlux localization with one pinhole with radius r_p, centred at coordinates $(x_\mathrm{p}, y_\mathrm{p})$. In (*d*) and (*e*), the x-distance $(x_\mathrm{p} - \theta_x)$ between the pinhole and the emitter is varied, where $y_\mathrm{p} = \theta_y$. (*b*) SpinFlux CRLB in the x-direction as a function of the emitter-pinhole x- and y-distances for pinhole radius $r_\mathrm{p} = 3\sigma_\mathrm{PSF}$. (*c*) Improvement of the SpinFlux CRLB over SMLM as a function of the emitter-pinhole x- and y-distances, for pinhole radius $r_\mathrm{p} = 3\sigma_\mathrm{PSF}$. (*d*) CRLB in the x-direction as a function of the emitter-pinhole x-distance. Simulations show SpinFlux with varying pinhole sizes, widefield SMLM, and localization on ISM reconstructions. (*e*) Improvement of the SpinFlux CRLB over SMLM as a function of the emitter-pinhole x-distance for varying pinhole sizes.

lost due to the loss of signal photons than that we gain by blocking background, resulting in a reduction of the improvement factor from 1.14 to 0.90. Similarly, moving the pinhole away from the emitter position blocks signal photons, thereby reducing the localization precision. For $r_\mathrm{p} = 3\sigma_\mathrm{PSF}$, the improvement over SMLM goes from 1.14 at $x_\mathrm{p} = \theta_x$ to 0.73 at a 130 nm distance between x_p and θ_x. From this, we can conclude that larger pinholes are in principle better for SpinFlux, as more information about the underlying signal is revealed through the larger pinhole.

2.3.3. Two-pattern configuration

In Figs. 2.4 and 2.S6, we evaluate the theoretical minimum uncertainty in the case in which multiple patterns are used sequentially for illumination and emission. We first consider the scenario of pinholes that are separated in the x-direction around focus coordinates $(x_\mathrm{f}, y_\mathrm{f})$ as illustrated in Fig. 2.4, *a-e*. Results are shown for the scenario where the entire signal photon budget is exhausted after illumination with all patterns. For these simulations, the pinhole radius was set to $r_\mathrm{p} = 3\sigma_\mathrm{PSF}$ for both pinholes.

From Fig. 2.4, *d* and *e*, we see that using multiple patterns is beneficial for SpinFlux, maximally resulting in a 2.62-fold precision improvement over SMLM in the x-direction

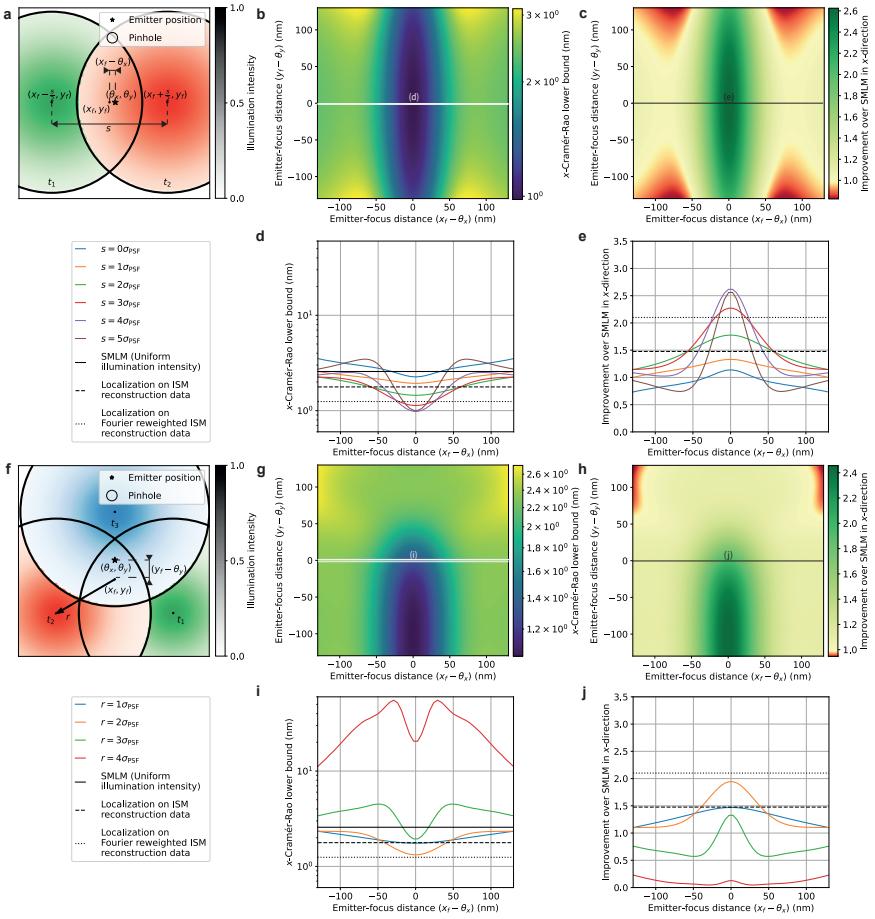

Figure 2.4: Theoretical minimum localization uncertainty of SpinFlux localization with multiple pinholes and patterns. For this simulation, 2000 expected signal photons and 8 expected background photons per pixel were used, with pinhole radius $r_p = 3\sigma_{PSF}$. Results are evaluated for the scenario where the entire signal photon budget is exhausted after illumination with all patterns (disregarding signal photons blocked by the spinning disk). (*a*) Schematic overview of SpinFlux localization with two pinholes, separated in x by distance s and centred around the focus coordinates (x_f, y_f). In (*d*) and (*e*), the x-distance $(x_f - \theta_x)$ between the pattern focus and the emitter is varied, where $y_f = \theta_y$. (*b*) SpinFlux CRLB in the x-direction as a function of the emitter-pinhole x- and y-distances for pinhole separation $r_p = 4\sigma_{PSF}$. (*c*) Improvement of the SpinFlux CRLB over SMLM as a function of the emitter-pinhole x- and y-distances for pinhole separation $r_p = 4\sigma_{PSF}$. (*d*) CRLB in the x-direction as a function of the emitter-focus x-distance. Simulations show SpinFlux with varying pinhole separations, widefield SMLM, and localization on ISM reconstructions. (*e*) Improvement of the SpinFlux CRLB over SMLM as a function of the emitter-focus x-distance for varying pinhole separations. (*f*) Schematic overview of SpinFlux localization with a triangle of three pinholes, centred at focus coordinates (x_f, y_f) at a radius r. In (*i*) and (*j*), the x-distance $(x_f - \theta_x)$ between the pattern focus and the emitter is varied, where $y_f = \theta_y$. (*g*) SpinFlux CRLB in the x-direction as a function of the emitter-pinhole x- and y-distances for pinhole spacing $r = 2\sigma_{PSF}$. (*h*) Improvement of the SpinFlux CRLB over SMLM as a function of the emitter-pinhole x- and y-distances for pinhole spacing $r = 2\sigma_{PSF}$. (*i*) CRLB in the x-direction as a function of the emitter-focus x-distance. Simulations show SpinFlux with varying pinhole spacing, widefield SMLM, and localization on ISM reconstructions. (*j*) Improvement of the SpinFlux CRLB over SMLM as a function of the emitter-focus x-distance for varying pinhole spacing.

when using a pinhole separation $s = 4\sigma_{\mathrm{PSF}}$. This improvement decreases only moderately to 2.17 when the pattern y-coordinate is moved 130 nm out of focus (see Fig. 2.S7). When the illumination time and power are adjusted to exhaust the entire signal photon budget, the low-intensity tails of the Gaussian intensity profile increase the information content of signal photons, as these contain increased information about the relative position of the emitter with respect to the illumination pattern. As discussed in Section 2.2.1, the multiple-pattern configuration has the same signal photon budget as the single-pattern configuration. These results therefore show that the same signal photon budget is utilized more efficiently by using multiple pattern locations.

However, increasing the pinhole separation also reduces the region where SpinFlux improves over SMLM. For a pinhole separation $s = 3\sigma_{\mathrm{PSF}}$, the domain where SpinFlux improves over SMLM by at least a factor 1.2 spans 175 nm, whereas this domain spans 111 nm for $s = 4\sigma_{\mathrm{PSF}}$. In the case where the pinholes are not centred around the emitter position, one of the patterns takes more of the signal photon budget than the other. As such, highly informative signal photons carrying information from the tails of the Gaussian illumination pattern are traded in for lowly informative photons coming from the centre of the pattern. This is shown in Fig. 2.S6*f*: for a pinhole separation $s = 4\sigma_{\mathrm{PSF}}$, 1573 signal photons are collected in total when the $x_{\mathrm{f}} = \theta_x$, with the remaining 427 photons being blocked by the spinning disk. When considering a 130 nm distance between x_{f} and θ_x, 1956 signal photons are being collected in total as one pinhole has moved close to the emitter position. Yet these photons are lowly informative, resulting in a precision improvement of 1.09 over SMLM. For increasing separations, the relative difference in illumination intensity between noncentred patterns increases, thereby reducing the domain of improvement.

Furthermore, Fig. 2.4, *d* and *e* show that there is an optimal pinhole separation of $s = 4\sigma_{\mathrm{PSF}}$ for SpinFlux. When increasing the pinhole separation beyond this, the localization precision decreases again. This is caused by a combination of two factors. First of all, as shown in Fig. 2.S6*f*, the spinning disk blocks an increasing amount of signal photons for increasing pinhole separations, as the overlap between the pinhole and emission PSF is reduced. Between $s = 4\sigma_{\mathrm{PSF}}$ and $s = 5\sigma_{\mathrm{PSF}}$, the amount of signal photons is reduced by 324 when $x_{\mathrm{f}} = \theta_x$. This effect is eliminated when the pinhole is removed, as shown in Fig. 2.S8.

Secondly, increasing the pinhole separation results in illumination with the low-intensity tails of the Gaussian illumination patterns. As we exhaust the signal photon budget in this scenario and as the background is pattern dependent, this results in an amplification of the background. Fig. 2.S6*g* shows that the average background count increases from 7.75 photons per pixel at $s = 4\sigma_{\mathrm{PSF}}$ to 26.7 photons per pixel at $s = 5\sigma_{\mathrm{PSF}}$.

Up until now, we have only considered the localization precision in the x-direction. Because the pattern has a different structure in the x- and y-directions, the modulated emission intensity will carry different information about the emitter x- and y-positions. Specifically in this configuration, both patterns lie on the x-axis. Therefore, the intensity difference in the modulated emission signal is strongly affected by the emitter x-position. However, as both patterns have the same y-coordinate, there is no difference in the effect of the emitter y-coordinate on the modulated emission intensity between the patterns. Therefore minimal information is carried about the emitter y-position.

To investigate how the two-pattern configuration of Fig. 2.4*a* affects the y-precision, we equivalently consider the x-precision that can be obtained with the rotated pattern (see Fig. 2.S9). From Fig. 2.S9, we see that the x-precision for the rotated pattern results in negligible improvements or even reductions over SMLM if the entire signal photon budget is exhausted. Specifically for $s = 4\sigma_{\mathrm{PSF}}$, the improvement factor over SMLM is 0.83 when the patterns are perfectly centred around the emitter position, whereas the improvement increases to 1.12 when the distance between y_{f} and θ_y is 130 nm. From the equivalence, we can thus conclude that the two-pattern configuration of Fig. 2.4*a* results in optimal x-precision, but the associated y-precision is diminished.

2.3.4. Triangular pattern configuration

In Figs. 2.4, *f*-*j* and 2.S10, we evaluate the theoretical minimum uncertainty in the case in which multiple pinholes are used for illumination and emission in an equilateral triangle configuration, centred around focus coordinates $(x_{\mathrm{f}}, y_{\mathrm{f}})$. Results are shown for the scenario where the entire signal photon budget is exhausted after illumination with all patterns. For these simulations, the pinhole radius was set to $r_{\mathrm{p}} = 3\sigma_{\mathrm{PSF}}$ for all pinholes.

From Fig. 2.4, *i* and *j*, we see that the triangle configuration from Fig. 2.4*f* results in a precision improvement in the x-direction of at most 1.94 compared with SMLM, when the distance between the pinholes and the centre of the triangle is $r = 2\sigma_{\mathrm{PSF}}$. As seen for the two-pattern case, this optimum is a result of two contrasting factors. On one hand, increasing the pattern distance illuminates the emitter with the tail of the Gaussian intensity profile, thereby increasing the information that signal photons carry about the relative distance between the illumination pattern and the emitter. On the other hand, increasing the distance between the emitter and the pinholes also increases the amount of signal photons that are blocked by the spinning disk, while the pattern-dependent background increases due to the low illumination intensity.

Note that the x-localization precision of the triangle configuration is worse than that of the two-pattern configuration described in Subsection 2.3.3. The reason for this is that the triangle configuration contains one pinhole, of which the x-coordinate is located close to the true emitter x-coordinate (i.e., the blue pattern in Fig. 2.4*f*). As such, signal photons that are collected after illumination with this pattern contain little information about the emitter x-position. The two-pattern configuration of Subsection 2.3.3 is thus able to distribute signal photons more efficiently to maximize the information about the emitter x-position.

On the other hand, as discussed earlier for Fig. 2.S9, the two-pattern configuration contains little information about the emitter y-position. To investigate this for the triangle configuration, Fig. 2.S11 shows the x-localization precision that can be achieved when the triangle pattern is rotated clockwise by 90° for all three scenarios under consideration. Equivalently, these results also hold for the y-precision that can be attained with the nonrotated pattern. It can be seen that the optimal spacing r and the localization precision are comparable with those for the nonrotated triangle configuration. We find a precision improvement in y-direction of 2.05 over SMLM. As the rotated pattern is asymmetric along the x-axis, the precision also scales asymmetrically around the optimum. In addition, the asymmetry causes a shift to the optimal x-coordinate of the pattern focus. For example, the optimal focus position is $x_{\mathrm{f}} = \theta_x - 0.13$ nm when considering

the scenario where the entire signal photon budget is exhausted. From the equivalence, we find that the triangle configuration balances the localization precision in the x- and y-directions at approximately a twofold improvement in either direction at the cost of suboptimal precision in each individual direction.

In MINFLUX [8, 15], a triangle configuration was also used for illumination, where an additional fourth pattern was added in the centre of the configuration. As such, we also consider the scenario where an additional pinhole and pattern are added in the centre of the triangle for both rotations of the configuration (see Figs. 2.S12 and 2.S13).

From Figs. 2.S12 and 2.S13, we find that adding a centre pinhole causes a deterioration of the localization precision compared with the triangle configuration without a centre pinhole. The precision improvement over SMLM is at most 1.44 for the nonrotated pattern, and at most 1.78 for the rotated pattern. On the other hand, the domain where SpinFlux attains an improvement over SMLM has increased due to the addition of the centre pinhole. For the nonrotated pattern with spacing $r = 2\sigma_{\mathrm{PSF}}$, the improvement over SMLM varies between 1.39 and 1.44 as long as the pattern focus and the emitter remain in a 130 nm distance from each other.

The explanation for both these effects is that the centre pinhole blocks the least amount of signal photons, and also claims the majority of the signal photon budget due to illumination with near-maximum intensity. As such, as shown in Figs. 2.S12, f and g and 2.S13, f and g, the effect of the pinhole spacing r on the usage of the signal photon budget and background count is strongly reduced. For pattern spacings between $r = 0.5\sigma_{\mathrm{PSF}}$ and $r = 2\sigma_{\mathrm{PSF}}$, pattern focus positions within a 130 nm range of the emitter position and either rotation, signal photon counts vary between 1753 and 1968 photons, and average backgrounds vary between 0.88 and 4.30 photons per pixel. When the centre of the triangle is displaced from the emitter position, another pinhole is able to cover the emitter position, thereby enlarging the range of similar photon counts and increasing the domain of precision improvement.

2.3.5. Donut-shaped intensity patterns

Note that MINFLUX uses a donut-shaped intensity pattern for illumination, which contains an intensity minimum in the centre. As described until now, SpinFlux uses a Gaussian intensity profile, with an intensity maximum in the centre. By incorporating two phase masks in the system (see Fig. 2.S3), SpinFlux can be adapted to utilize donut-shaped illumination. As the donut-shaped pattern increases the information content of signal photons in its centre rather than at its boundary [8], it will mitigate the situation where highly informative signal photons are blocked by the pinhole, which in turn improves the theoretically minimum localization uncertainty. We explore this effect in Figs. 2.5 and 2.S14-2.S17.

Figs. 2.S14 and 2.S15 show the SpinFlux localization precision of the triangular configuration without a centre pinhole, in the scenario where the entire signal photon budget is exhausted. Here, the improvement of SpinFlux with donut-shaped illumination over SMLM is approximately 1.64 in the x-direction and 1.74 in the y-direction at a pinhole spacing $r = 3\sigma_{\mathrm{PSF}}$. This improvement is comparable with that of SpinFlux with Gaussian illumination, as the intensity minimum of the illumination donut is placed $3\sigma_{\mathrm{PSF}}$ away from the emitter. The Gaussian pattern at $r = 2\sigma_{\mathrm{PSF}}$ and the donut-shaped

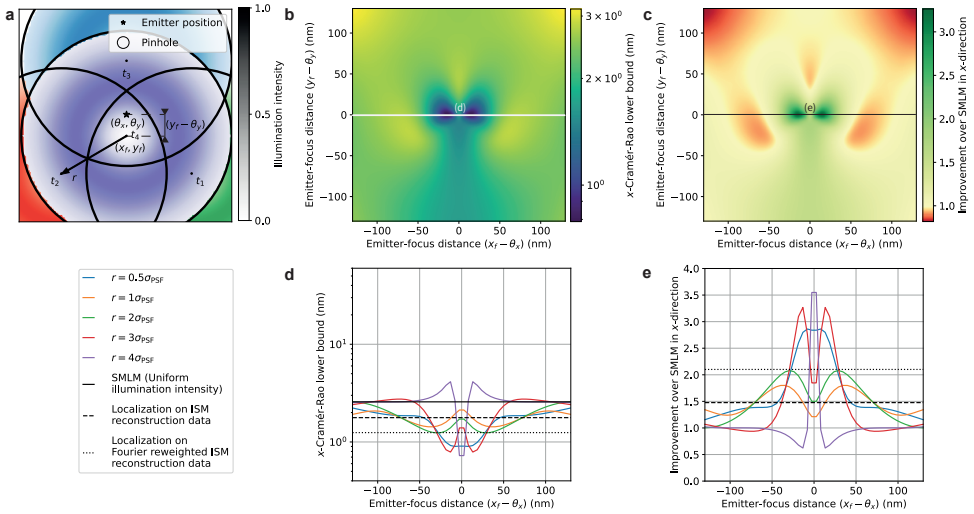

Figure 2.5: Theoretical minimum localization uncertainty of SpinFlux localization with four pinholes and donut-shaped patterns in an equilateral triangle configuration with a centre pinhole. For this simulation, 2000 expected signal photons and 8 expected background photons per pixel were used, with pinhole radius $r_p = 3\sigma_{PSF}$. Results are evaluated for the scenario where the entire signal photon budget is exhausted after illumination with all patterns (disregarding signal photons blocked by the spinning disk). (*a*) Schematic overview of SpinFlux localization with a triangle of three pinholes with an additional centre pinhole centred at focus coordinates (x_f, y_f). In (*d*) and (*e*), the x-distance $(x_f - \theta_x)$ between the pattern focus and the emitter is varied, where $y_f = \theta_y$. (*b*) SpinFlux CRLB in the x-direction as a function of the emitter-pinhole x- and y-distances for pinhole spacing $r = 3\sigma_{PSF}$. (*c*) Improvement of the SpinFlux CRLB over SMLM as a function of the emitter-pinhole x- and y-distances for pinhole spacing $r = 3\sigma_{PSF}$. (*d*) CRLB in the x-direction as a function of the emitter-focus x-distance. Simulations show SpinFlux with varying pinhole spacing, widefield SMLM, and localization on ISM reconstructions. (*e*) Improvement of the SpinFlux CRLB over SMLM as a function of the emitter-focus x-distance for varying pinhole spacing.

pattern at $r = 3\sigma_{PSF}$ are comparable on the emitter coordinates, thereby negating the advantages of the donut-shaped pattern.

This changes when including a centre pinhole in the triangular configuration, as shown in Figs. 2.5, 2.S16 and 2.S17. Here, the maximum improvement over SMLM is 3.5 in the x- and y-directions at a pinhole spacing of $r = 4\sigma_{PSF}$. When increasing the spacing r between the pinholes (beyond the width of the donut-shaped beam), a larger share of the signal photon budget will be claimed by the centre pinhole. The intensity minimum of the centre pinhole increases the information content of signal photons, thereby improving the resolution over SpinFlux with Gaussian illumination. However, this improvement decays sharply when the pattern focus is not centred on the emitter position. Specifically for $r = 4\sigma_{PSF}$, the improvement exceeds 1.5 in either direction only when the emitter-focus distance is smaller than 5 nm. Therefore, it is more practical to choose a smaller spacing between the pinholes. For $r = 3\sigma_{PSF}$, the maximum improvement over SMLM is 3.3 in the x- and y-directions, and the improvement is larger than 1.5 in either direction when the emitter-focus distance is at most 37 nm.

Table 2.1: Summary of simulation results for localization on ISM reconstructions and SpinFlux variants considered in this chapter.

Variant	Amount of patterns	Illumination type	Maximum x-improvement
ISM reconstructions	$\gg 4$	Gaussian	1.48
Fourier reweighted ISM reconstructions	$\gg 4$	Gaussian	2.10
SpinFlux	1	Gaussian	1.17
	2	Gaussian	2.62
	3	Gaussian	1.94
	4	Donut	3.50

2.4. Discussion

In meSMLM, sparse activation of single emitters with patterned illumination results in improved localization precision over SMLM. The precision improvement of meSMLM is derived from retrieving the position of an emitter relative to individual illumination patterns, which adds to existing PSF information from SMLM. In addition, meSMLM improves the resolution over image reconstruction in SIM while reducing the required amount of illumination patterns. This suggests that meSMLM can improve the localization precision in existing setups, which are limited by image reconstruction in processing.

We developed SpinFlux, which incorporates meSMLM into SDCM setups. In SpinFlux, patterned illumination is generated using a spinning disk with pinholes to sequentially illuminate the sample. Subsequently, the emission signal is windowed by the same pinhole before being imaged on the camera. During the analysis, emitters are localized in the recordings from a sequence of individual pattern acquisitions, taking knowledge about the pattern into account.

We have derived a statistical image formation model for SpinFlux, which includes the effects of patterned illumination, windowing of the emission signal by the pinhole and pattern-dependent background. For our analysis, we considered Gaussian illumination patterns and a Gaussian emission PSF. We also consider donut-shaped illumination patterns, which can be generated by incorporating a phase mask in the illumination path. In addition, we have derived and evaluated the CRLB for this model. We applied the CRLB to various illumination pattern configurations to quantify the theoretical minimum uncertainty that can be gained with SpinFlux. We compared SpinFlux with SMLM and with localization on ISM reconstruction data, which results in an average global improvement of 1.48 over SMLM, or 2.10 with Fourier reweighting.

When using one pattern only, pattern-dependency of the background causes an improvement of at most 1.17 over SMLM, whereas no improvement is found when neglecting this effect. In the single-pattern case, the pinhole blocks signal photons that carry information about the emitter position. As such, it is beneficial for SpinFlux to use pinholes that are as large as possible to reduce the amount of signal photons blocked by the pinhole. In other words, we find that a spinning disk with pinholes is convenient to generate patterned illumination, although the pinhole itself has an adverse effect on the localization precision due to the blockage of signal photons.

However, we have not considered neighbouring emitters in our analysis, nor have we modelled out-of-focus background. In ISM, optical sectioning is achieved with the

spinning disk by reducing the effects of neighbouring or out-of-focus fluorescent signals, thereby improving the resolution. We expect that the pinhole has a similar effect on the localization precision that can be attained with SpinFlux, thereby resulting in an optimal pinhole radius. Future research should focus on incorporating these effects into the image formation model.

Based on the single-pattern results, we conclude that SpinFlux requires multiple patterns to generate a significant precision improvement over SMLM. We explored various multiple-pattern configurations, which can be obtained via sequential illumination. We found that a configuration of two pinholes with radius $3\sigma_{\mathrm{PSF}}$, separated in the x-direction around the emitter position by a distance of $4\sigma_{\mathrm{PSF}}$, results in a precision improvement of 2.62 in the x-direction compared with SMLM, while the y-improvement is at most 1.12. For larger separations, the information content of signal photons increases due to illumination with the low-intensity tails of the Gaussian illumination pattern. However, when the separation increases above $4\sigma_{\mathrm{PSF}}$, the loss of signal photons due to the windowing effect of the pinhole causes deterioration of the localization precision.

We also evaluated the theoretical minimum uncertainty of a triangular pattern configuration, where pinholes are sequentially placed at the corners of an equilateral triangle around the emitter position. This results in approximately a twofold x-precision improvement over SMLM, which is a reduction compared with the two-pattern configuration. However, the triangle configuration also attains approximately a twofold precision improvement in the y-direction. As such, the triangle configuration balances the localization precision in the x- and y-directions at the cost of suboptimal precision in each individual direction. Including a centre pinhole in the triangle does not improve the maximum localization improvement, but it extends the domain on which any improvement can be attained.

By including a phase mask in the illumination and emission paths, illumination patterns with arbitrary diffraction-limited intensity profiles can be created. We evaluated the localization precision of SpinFlux with donut-shaped illumination. As the donut-shaped pattern increases the information content of signal photons in its centre rather than at its boundary, it will mitigate the situation where highly informative signal photons are blocked by the pinhole. We find that, in the triangular configuration with a centre pinhole, the maximum improvement over SMLM is increased to 3.5 in the x- and y-directions at a pinhole spacing $r = 4\sigma_{\mathrm{PSF}}$.

We conclude that localization on ISM reconstruction data results is the most straightforward implementation and results in the largest global average improvement of the localization precision. On the other hand, SpinFlux is the method of choice for local refinements of the localization precision. In addition, the versatility of the image formation model makes SpinFlux analysis on non-Gaussian illumination patterns straightforward.

Data and Code Availability

The data that support the findings of this study are openly available in 4TU.ResearchData [31]. The code that supports the findings of this study is openly available on GitHub [32].

Supporting Citations

The following references appear in the supporting information: [33–38].

References

[1] E. Betzig, G. H. Patterson, R. Sougrat, O. W. Lindwasser, S. Olenych, J. S. Bonifacino, M. W. Davidson, J. Lippincott-Schwartz, and H. F. Hess. “Imaging Intracellular Fluorescent Proteins at Nanometer Resolution”. In: *Science* 313.5793 (2006), pp. 1642–1645.

[2] M. J. Rust, M. Bates, and X. Zhuang. “Sub-diffraction-limit imaging by stochastic optical reconstruction microscopy (STORM)”. In: *Nature Methods* 3.10 (2006), pp. 793–796.

[3] B. Huang, M. Bates, and X. Zhuang. “Super-Resolution Fluorescence Microscopy”. In: *Annual Review of Biochemistry* 78.1 (2009), pp. 993–1016.

[4] L. Reymond, T. Huser, V. Ruprecht, and S. Wieser. “Modulation-enhanced localization microscopy”. In: *Journal of Physics: Photonics* 2.4 (2020), p. 041001.

[5] J. Cnossen, T. Hinsdale, R. Ø. Thorsen, M. Siemons, F. Schueder, R. Jungmann, C. S. Smith, B. Rieger, and S. Stallinga. “Localization microscopy at doubled precision with patterned illumination”. In: *Nature Methods* 17.1 (2019), pp. 59–63.

[6] L. Reymond, J. Ziegler, C. Knapp, F.-C. Wang, T. Huser, V. Ruprecht, and S. Wieser. “SIMPLE: Structured illumination based point localization estimator with enhanced precision”. In: *Optics Express* 27.17 (2019), p. 24578.

[7] L. Gu, Y. Li, S. Zhang, Y. Xue, W. Li, D. Li, T. Xu, and W. Ji. “Molecular resolution imaging by repetitive optical selective exposure”. In: *Nature Methods* 16.11 (2019), pp. 1114–1118.

[8] F. Balzarotti, Y. Eilers, K. C. Gwosch, A. H. Gynnå, V. Westphal, F. D. Stefani, J. Elf, and S. W. Hell. “Nanometer resolution imaging and tracking of fluorescent molecules with minimal photon fluxes”. In: *Science* 355.6325 (2017), pp. 606–612.

[9] L. A. Masullo, L. F. Lopez, and F. D. Stefani. “A common framework for single-molecule localization using sequential structured illumination”. In: *Biophysical Reports* 2.1 (2022), p. 100036.

[10] L. A. Masullo, A. M. Szalai, L. F. Lopez, M. Pilo-Pais, G. P. Acuna, and F. D. Stefani. “An alternative to MINFLUX that enables nanometer resolution in a confocal microscope”. In: *Light: Science & Applications* 11.1 (2022).

[11] P. Jouchet, C. Cabriel, N. Bourg, M. Bardou, C. Poüs, E. Fort, and S. Lévêque-Fort. “In Depth 3D Single Molecule Localization Microscopy with Time Modulated Excitation”. In: *Biophysical Journal* 118.3 (2020), 149a.

[12] P. Jouchet, C. Cabriel, N. Bourg, M. Bardou, C. Poüs, E. Fort, and S. Lévêque-Fort. “Nanometric axial localization of single fluorescent molecules with modulated excitation”. In: *Nature Photonics* 15.4 (2021), pp. 297–304.

[13] L. Gu, Y. Li, S. Zhang, M. Zhou, Y. Xue, W. Li, T. Xu, and W. Ji. “Molecular-scale axial localization by repetitive optical selective exposure”. In: *Nature Methods* 18.4 (2021), pp. 369–373.

[14] D. Kalisvaart, J. Cnossen, S. Hung, S. Stallinga, M. Verhaegen, and C. S. Smith. “Precision in iterative modulation enhanced single-molecule localization microscopy”. In: *Biophysical Journal* 121.12 (2022), pp. 2279–2289.

[15] K. C. Gwosch, J. K. Pape, F. Balzarotti, P. Hoess, J. Ellenberg, J. Ries, and S. W. Hell. “MINFLUX nanoscopy delivers 3D multicolor nanometer resolution in cells”. In: *Nature Methods* 17.2 (2020), pp. 217–224.

[16] M. G. L. Gustafsson. “Surpassing the lateral resolution limit by a factor of two using structured illumination microscopy”. In: *Journal of Microscopy* 198.2 (2000), pp. 82–87.

[17] F. Schueder, J. Lara-Gutiérrez, B. J. Beliveau, S. K. Saka, H. M. Sasaki, J. B. Woehrstein, M. T. Strauss, H. Grabmayr, P. Yin, and R. Jungmann. "Multiplexed 3D super-resolution imaging of whole cells using spinning disk confocal microscopy and DNA-PAINT". In: *Nature Communications* 8.1 (2017).

[18] O. Schulz, C. Pieper, M. Clever, J. Pfaff, A. Ruhlandt, R. H. Kehlenbach, F. S. Wouters, J. Großhans, G. Bunt, and J. Enderlein. "Resolution doubling in fluorescence microscopy with confocal spinning-disk image scanning microscopy". In: *Proceedings of the National Academy of Sciences* 110.52 (2013), pp. 21000–21005.

[19] S. Qin, S. Isbaner, I. Gregor, and J. Enderlein. "Doubling the resolution of a confocal spinning-disk microscope using image scanning microscopy". In: *Nature Protocols* 16.1 (2020), pp. 164–181.

[20] G. Sirinakis, E. S. Allgeyer, J. Cheng, and D. St Johnston. "Quantitative comparison of spinning disk geometries for PAINT based super-resolution microscopy". In: *Biomedical Optics Express* 13.7 (2022), p. 3773.

[21] A. R. Halpern, M. Y. Lee, M. D. Howard, M. A. Woodworth, P. R. Nicovich, and J. C. Vaughan. "Versatile, do-it-yourself, low-cost spinning disk confocal microscope". In: *Biomedical Optics Express* 13.2 (2022), p. 1102.

[22] C. B. Müller and J. Enderlein. "Image Scanning Microscopy". In: *Physical Review Letters* 104.19 (2010).

[23] S. M. Kay. *Fundamentals of Statistical Signal Processing: Estimation Theory*. Prentice Hall international editions. London, England: Prentice Hall, 1993.

[24] R. J. Ober, S. Ram, and E. S. Ward. "Localization Accuracy in Single-Molecule Microscopy". In: *Biophysical Journal* 86.2 (2004), pp. 1185–1200.

[25] N. Radmacher, O. Nevskyi, J. I. Gallea, J. C. Thiele, I. Gregor, S. O. Rizzoli, and J. Enderlein. "Doubling the resolution of fluorescence-lifetime single-molecule localization microscopy with image scanning microscopy". In: *Nature Photonics* 18.10 (2024), pp. 1059–1066.

[26] C. S. Smith, N. Joseph, B. Rieger, and K. A. Lidke. "Fast, single-molecule localization that achieves theoretically minimum uncertainty". In: *Nature Methods* 7.5 (2010), pp. 373–375.

[27] Q. Houwink, D. Kalisvaart, S. Hung, J. Cnossen, D. Fan, P. Mos, A. Can Ülkü, C. Bruschini, E. Charbon, and C. S. Smith. "Theoretical minimum uncertainty of single-molecule localizations using a single-photon avalanche diode array". In: *Optics Express* 29.24 (2021), p. 39920.

[28] H. L. Van Trees. *Detection, Estimation and Modulation Theory: Part 1*. Detection, Estimation, and Modulation Theory. Set (Volumes: I,II, III,IV). Nashville, TN: John Wiley & Sons, 2001.

[29] C. S. Smith, K. Jouravleva, M. Huisman, S. M. Jolly, P. D. Zamore, and D. Grunwald. "An automated Bayesian pipeline for rapid analysis of single-molecule binding data". In: *Nature Communications* 10.1 (2019).

[30] B. Zhang, J. Zerubia, and J.-C. Olivo-Marin. "Gaussian approximations of fluorescence microscope point-spread function models". In: *Applied Optics* 46.10 (2007), p. 1819.

[31] D. Kalisvaart, S. Hung, and C. S. Smith. *Data underlying the publication: Quantifying the minimum localization uncertainty of image scanning localization microscopy*. 2023.

[32] D. Kalisvaart, S. Hung, and C. S. Smith. *Software underlying the publication: Quantifying the minimum localization uncertainty of image scanning localization microscopy*. 2023.

[33] S. Stallinga and B. Rieger. “The effect of background on localization uncertainty in single emitter imaging”. In: *2012 9th IEEE International Symposium on Biomedical Imaging (ISBI)*. IEEE, 2012, pp. 988–991.

[34] B. Rieger and S. Stallinga. “The Lateral and Axial Localization Uncertainty in Super-Resolution Light Microscopy”. In: *ChemPhysChem* 15.4 (2013), pp. 664–670.

[35] G. M. De Luca, R. M. Breedijk, R. A. Brandt, C. H. Zeelenberg, B. E. de Jong, W. Timmermans, L. N. Azar, R. A. Hoebe, S. Stallinga, and E. M. Manders. “Re-scan confocal microscopy: scanning twice for better resolution”. In: *Biomedical Optics Express* 4.11 (2013), p. 2644.

[36] J. Mertz. *Introduction to Optical Microscopy*. 2nd ed. Cambridge, England: Cambridge University Press, 2019.

[37] J. Pawley, ed. *Handbook of Biological Confocal Microscopy*. 3rd ed. New York, NY: Springer, 2006.

[38] E. Slenders and G. Vicidomini. “ISM-FLUX: MINFLUX with an array detector”. In: *Physical Review Research* 5.2 (2023).

Supporting Information for: Quantifying the Minimum Localization Uncertainty of Image Scanning Localization Microscopy

2.S1. Theoretical approximation of the best-case localization precision of localization on image scanning microscopy data

In this section, we derive a theoretical approximation of the best-case localization precision that can be achieved by localizing emitters on ISM reconstructions. Concretely, we assume that enough illumination patterns are used to uniformly illuminate the sample. For ideal ISM reconstructions [1, 2], the effective PSF standard deviation after reconstruction is reduced by a factor $\sqrt{2}$. If the ISM reconstructions are subsequently Fourier reweighted, the effective PSF standard deviation is reduced further, up to a total factor 2.

From [3, 4], we find that the theoretical minimum localization uncertainty σ_x of SMLM can be approximated as:

$$\sigma_x^2 = \frac{\sigma_{\mathrm{PSF}}^2 + \Delta x^2/12}{\theta_I}\left(1 + 4\tau + \sqrt{\frac{2\tau}{1+4\tau}}\right). \tag{2.S1}$$

Here, σ_{PSF} denotes the standard deviation of the Gaussian PSF, Δx is the pixel size and θ_I is the expected signal photon budget. In addition, τ is a normalized dimensionless background parameter

$$\tau = \frac{2\pi\theta_b(\sigma_{\mathrm{PSF}}^2 + \Delta x^2/12)}{\theta_I \Delta x^2}, \tag{2.S2}$$

where θ_b denotes the expected amount of background photons per pixel.

If individual emitters are localized in ISM data, the standard deviation of the best-case ISM PSF is given by

$$\sigma_{\mathrm{PSF,\,ISM}} = \frac{\sigma_{\mathrm{PSF}}}{\sqrt{2}}. \tag{2.S3}$$

The approximation of the theoretically minimum localization precision is then given by:

$$\sigma^2_{x,\,\mathrm{ISM}} = \frac{\sigma^2_{\mathrm{PSF}}/2 + \Delta x^2/12}{\theta_I}\left(1 + 4\tau_{\mathrm{ISM}} + \sqrt{\frac{2\tau_{\mathrm{ISM}}}{1+4\tau_{\mathrm{ISM}}}}\right), \tag{2.S4}$$

$$\tau_{\mathrm{ISM}} = \frac{2\pi\theta_b(\sigma^2_{\mathrm{PSF}}/2 + \Delta x^2/12)}{\theta_I \Delta x^2}. \tag{2.S5}$$

For ISM reconstructions with Fourier reweighting, the analysis is identical with a reduction of σ_{PSF} by a factor two.

As described in Eqs. (2.S4) and (2.S5), the localization precision depends on a combination of the PSF size and the pixel size. If the PSF size is small compared to the pixel size, the localization precision becomes proportional to the pixel size. On the other hand, if the PSF size is large compared to the pixel size, the localization precision becomes a (non-proportional) function of the PSF size. In that case, the ratio between the PSF size and the pixel size influences the weighting of the signal-to-background ratio in determining the localization precision, through the parameter τ_{ISM} in Eq. (2.S5). This dependency is shown in Fig. 2.S1.

2.S2. Image formation model for SpinFlux localization

In this section, we derive a statistical image formation model for SpinFlux meSMLM. We start by formulating a model for one pinhole and one illumination pattern, then we extend the model for arbitrary amounts of pinholes and patterns.

In Section 2.S3, we will model the amount of photons that are acquired by a camera pixel through the Poisson distribution. As such, we aim to find a model for the Poisson mean μ_i here, to describe the expected amount of photons recorded on each camera pixel i. We follow a similar modelling procedure as [5–8] to derive a model for the Poisson mean μ_i.

An image $\tilde{g}(x,y)$ of an object $f(x,y)$ is formed through an optical system with PSF $h(x,y)$ through a convolution, as shown in Eq. (2.S6).

$$\tilde{g}(x,y) = h(x,y) \otimes f(x,y). \tag{2.S6}$$

In Eq. (2.S6), $\otimes$ denotes the two-dimensional convolution operator. In this equation, we need to ensure that the total area under the PSF equals 1, to avoid that the optical system adds energy to the image formation process. This results in the normalization condition of Eq. (2.S7).

$$\iint_{\mathbb{R}^2} h(x,y)\mathrm{d}x\mathrm{d}y = 1. \tag{2.S7}$$

We will now propose a model for the object function $f(x)$ when a single pinhole and illumination pattern are used. Consider a point emitter, located at a position (θ_x, θ_y). Such an emitter can be modelled as $\delta(x-\theta_x, y-\theta_y)$, where δ denotes the two-dimensional delta function. Under non-uniform illumination with a pattern $P(x-x_{\mathrm{p}}, y-y_{\mathrm{p}})$ centred at pinhole centre coordinates $(x_{\mathrm{p}}, y_{\mathrm{p}})$, the expected amount of signal photons emitted by this emitter is $P(x-x_{\mathrm{p}}, y-y_{\mathrm{p}})\theta_I$ and the expected pattern-dependent background count is $P(x-x_{\mathrm{p}}, y-y_{\mathrm{p}})\theta_b$. Here, the (dimensionless) illumination intensity needs to satisfy

$0 \leq P(x-x_\mathrm{p}, y-y_\mathrm{p}) \leq 1$ for all $(x,y) \in \mathbb{R}^2$, and $P(x-x_\mathrm{p}, y-y_\mathrm{p}) = 1$ for some $(x,y) \in \mathbb{R}^2$ to ensure there exists a coordinate which receives maximum illumination. The resulting object function $f(x, x_\mathrm{p}, y, y_\mathrm{p})$ is shown in Eq. (2.S8).

$$f(x, x_\mathrm{p}, y, y_\mathrm{p}) = P(x-x_\mathrm{p}, y-y_\mathrm{p})(\theta_I \delta(x-\theta_x, y-\theta_y) + \theta_b). \tag{2.S8}$$

To obtain an expression for the image function $\tilde{g}(x,y)$, we evaluate the convolution in Eq. (2.S6). This ultimately results in the expression for $\tilde{g}(x,y)$ as shown in Eq. (2.S9).

$$\begin{aligned}\tilde{g}(x, x_\mathrm{p}, y, y_\mathrm{p}) = \theta_I P(\theta_x - x_\mathrm{p}, \theta_y - y_\mathrm{p}) h(x-\theta_x, y-\theta_y) \\ + \theta_b \iint_{\mathbb{R}^2} h(\tau,\gamma) P(x-x_\mathrm{p}-\tau, y-y_\mathrm{p}-\gamma) \mathrm{d}\tau \mathrm{d}\gamma.\end{aligned} \tag{2.S9}$$

For SpinFlux, the image $\tilde{g}(x,y)$ is not imaged on the camera directly. Instead, $\tilde{g}(x, x_\mathrm{p}, y, y_\mathrm{p})$ passes through a circular pinhole, resulting in the circularly windowed image $g(x,y)$. Let r_p describe the radius of the pinhole. For notation convenience, we define the pinhole area $S_\mathrm{p} = \left\{(x,y) | (x-x_\mathrm{p})^2 + (y-y_\mathrm{p})^2 \leq r_\mathrm{p}^2\right\}$. We describe the pinhole with centre coordinates $(x_\mathrm{p}, y_\mathrm{p})$ by the pinhole mask $\Pi(x, x_\mathrm{p}, y, y_\mathrm{p})$.

$$\Pi(x, x_\mathrm{p}, y, y_\mathrm{p}) = \begin{cases} 1, & \text{if } (x,y) \in S_\mathrm{p}, \\ 0, & \text{otherwise.} \end{cases} \tag{2.S10}$$

We identified two different ways of modelling a confocal pinhole in literature. In the first type of models [1, 9, 10], the pinhole is included as a product with emission point-spread function. A second class of models exists, where the confocal aperture is modelled as a convolution with the emission point-spread function [11, 12].

From [9], we infer that that the product model is valid in case the pupil stop of the objective lens is much smaller than the pupil stop of the pinhole. We therefore choose this model and limit ourselves to simulation conditions where this is the case. This means our image formation model is not suited for the case where the pinhole stop is more limiting than the objective lens.

The image $g(x,y)$ on the camera after windowing by the pinhole is now given by:

$$g(x,y) = \Pi(x, x_\mathrm{p}, y, y_\mathrm{p}) \tilde{g}(x,y). \tag{2.S11}$$

As a next step, we need to discretize the image function $g(x,y)$ on the camera pixel array. Let $S_{\mathrm{c},i}$ denote the area belonging to the camera pixel with index i. To discretize the image function on camera pixel i, we integrate it over all $(x,y) \in S_{\mathrm{c},i}$ to obtain the expected amount of photons on the i'th pixel, μ_i. Let (x_i, y_i) denote the centre coordinates of the i'th pixel. We then find:

$$\begin{aligned}\mu_i(x_i, x_\mathrm{p}, y_i, y_\mathrm{p}) = \theta_I P(\theta_x - x_\mathrm{p}, \theta_y - y_\mathrm{p}) \iint_{(x,y)\in S_{\mathrm{c},i}} \Pi(x, x_\mathrm{p}, y, y_\mathrm{p}) h(x-\theta_x, y-\theta_y) \mathrm{d}x\mathrm{d}y \\ + \theta_b \iint_{(x,y)\in S_{\mathrm{c},i}} \Pi(x, x_\mathrm{p}, y, y_\mathrm{p}) \left(\iint_{\mathbb{R}^2} h(\tau,\gamma) P(x-x_\mathrm{p}-\tau, y-y_\mathrm{p}-\gamma) \mathrm{d}\tau\mathrm{d}\gamma \right) \mathrm{d}x\mathrm{d}y.\end{aligned} \tag{2.S12}$$

The aperture mask $\Pi(x, x_\mathrm{p}, y, y_\mathrm{p})$ from Eq. (2.S10) acts as a window on the integrands, thereby constraining the relevant domain of integration to the overlapping area between the camera pixel area $S_{\mathrm{c},i}$ and the pinhole area S_p. We denote this overlapping area as $\left(S_{\mathrm{c},i} \cap S_\mathrm{p}\right)$. Eq. (2.S12) then becomes Eq. (2.S13).

$$\begin{aligned}\mu_i(x_i, x_\mathrm{p}, y_i, y_\mathrm{p}) = \theta_I P(\theta_x - x_\mathrm{p}, \theta_y - y_\mathrm{p}) \iint_{(x,y)\in(S_{\mathrm{c},i}\cap S_\mathrm{p})} h(x-\theta_x, y-\theta_y)\mathrm{d}x\mathrm{d}y \\ + \theta_b \underbrace{\iint_{(x,y)\in(S_{\mathrm{c},i}\cap S_\mathrm{p})} \left(\iint_{\mathbb{R}^2} h(\tau,\gamma) P(x - x_\mathrm{p} - \tau, y - y_\mathrm{p} - \gamma)\mathrm{d}\tau\mathrm{d}\gamma \right) \mathrm{d}x\mathrm{d}y}_{B_i}.\end{aligned} \tag{2.S13}$$

Note that the effective background B_i is a constant, which does not depend on the emitter position, but only on the camera pixel area, the pinhole area, the PSF and the illumination pattern. We can thus give a compact expression for the Poisson mean μ_i, as shown in Eq. (2.S14).

$$\mu_i(x_i, x_\mathrm{p}, y_i, y_\mathrm{p}) = \theta_I P(\theta_x - x_\mathrm{p}, \theta_y - y_\mathrm{p}) \iint_{(x,y)\in(S_{\mathrm{c},i}\cap S_\mathrm{p})} h(x-\theta_x, y-\theta_y)\mathrm{d}x\mathrm{d}y + \theta_b B_i. \tag{2.S14}$$

2.S2.1. Approximation of domain of integration

To evaluate the integrations in Eq. (2.S14), we need to describe the domain of integration $\left(S_{\mathrm{c},i} \cap S_\mathrm{p}\right)$. That is, we have to find the overlapping area of the camera pixel with centre coordinates (x_i, y_i) and the pinhole with centre coordinates $(x_\mathrm{p}, y_\mathrm{p})$. To this extent, let us assume a camera for which all pixels have the same shape and size. Let all pixels be rectangular, with length Δx in the x-direction and length Δy in the y-direction. Furthermore, let N_x, N_y be the amount of camera pixels in each direction (with the total amount of pixels being $N_\mathrm{pixels} = N_x N_y$).

To simplify our analysis, we resort to a numerical approximation of the intersection, where we approximate the pinhole S_p and the overlapping area $\left(S_{\mathrm{c},i} \cap S_\mathrm{p}\right)$ on a square mesh. Let $(x_{\mathrm{M},j}, y_{\mathrm{M},j})$ describe the centre coordinates of mesh pixel j, defined in the same coordinate system as the pixel coordinates (x_i, y_i). We define the mesh to have $N_{\mathrm{M},x}, N_{\mathrm{M},y}$ pixels in each direction (with the total amount of mesh pixels being $N_\mathrm{M} = N_{\mathrm{M},x} N_{\mathrm{M},y}$). We parametrize the mesh width as $\Delta x_\mathrm{M} = \frac{N_x}{N_{\mathrm{M},x}} \cdot \Delta x$ in the x-direction and as $\Delta y_\mathrm{M} = \frac{N_y}{N_{\mathrm{M},y}} \cdot \Delta y$ in the y-direction. To avoid cases where mesh pixels partially overlap with camera pixels, we restrict choices of $N_{\mathrm{M},x}$ and $N_{\mathrm{M},y}$ to integer multiples of N_x and N_y. Note that increasing the amount of mesh pixels $N_{\mathrm{M},x}$ and $N_{\mathrm{M},y}$ decreases the mesh widths Δx_M and Δy_M and thus improves the accuracy of the numerical approximation.

On the mesh, we approximate the pinhole area S_p as $\tilde{S}_\mathrm{p}$. We propose the following midpoint approximation, which assigns the area of mesh pixel j to the approximated

pinhole area $\tilde{S}_\mathrm{p}$ if its centre coordinate $(x_{\mathrm{M},j}, y_{\mathrm{M},j})$ falls within S_p:

$$\left[x_{\mathrm{M},j} - \frac{\Delta x_\mathrm{M}}{2}, x_{\mathrm{M},j} + \frac{\Delta x_\mathrm{M}}{2}\right] \times \left[y_{\mathrm{M},j} - \frac{\Delta y_\mathrm{M}}{2}, y_{\mathrm{M},j} + \frac{\Delta y_\mathrm{M}}{2}\right] \subseteq \tilde{S}_\mathrm{p} \text{ if } \left(x_{\mathrm{M},j}, y_{\mathrm{M},j}\right) \in S_\mathrm{p}. \tag{2.S15}$$

As $\tilde{S}_\mathrm{p}$ is a square mesh in the same coordinate system as the camera pixel area $S_{\mathrm{c},i}$, the intersection $\left(S_{\mathrm{c},i} \cap \tilde{S}_\mathrm{p}\right)$ is straightforward to evaluate. Namely, this intersection consists of those mesh pixels in $\tilde{S}_\mathrm{p}$ that are also contained in $S_{\mathrm{c},i}$. Formally, this is the set of all mesh pixels j for which the centre coordinates satisfy $(x_{\mathrm{M},j}, y_{\mathrm{M},j}) \in \left(S_{\mathrm{c},i} \cap \tilde{S}_\mathrm{p}\right)$. This is illustrated in Fig. 2.1*c*.

Using this numerical approximation, Eq. (2.S14) can be rewritten as follows:

$$\mu_i(x_i, x_\mathrm{p}, y_i, y_\mathrm{p}) = \theta_I P(\theta_x - x_\mathrm{p}, \theta_y - y_\mathrm{p}) \cdot \sum_{(x_{\mathrm{M},j}, y_{\mathrm{M},j}) \in \left(S_{\mathrm{c},i} \cap \tilde{S}_\mathrm{p}\right)} \int_{x_{\mathrm{M},j} - \frac{\Delta x_\mathrm{M}}{2}}^{x_{\mathrm{M},j} + \frac{\Delta x_\mathrm{M}}{2}} \int_{y_{\mathrm{M},j} - \frac{\Delta y_\mathrm{M}}{2}}^{y_{\mathrm{M},j} + \frac{\Delta y_\mathrm{M}}{2}} h(x - \theta_x, y - \theta_y) \mathrm{d}x \mathrm{d}y + \theta_b B_i. \tag{2.S16}$$

2.S2.2. Illumination and emission point spread functions

As a model for the illumination PSF $P(x - x_\mathrm{p}, y - y_\mathrm{p})$ and the emission PSF $h(x, y)$, we choose to use Gaussians. The illumination PSF is given by Eq. (2.S17), where σ_illum denotes the standard deviation of the illumination PSF.

$$P_\mathrm{Gaussian}(x - x_\mathrm{p}, y - y_\mathrm{p}) = e^{\frac{-(x-x_\mathrm{p})^2 - (y-y_\mathrm{p})^2}{2\sigma_\mathrm{illum}^2}}. \tag{2.S17}$$

Alternate illumination patterns can be generated by placing a phase mask in the illumination path. We therefore also include a model of the donut-shaped pattern from e.g. MINFLUX [13], with a zero-intensity minimum at the centre of the pinhole and standard deviation σ_illum:

$$P_\mathrm{donut}(x - x_\mathrm{p}, y - y_\mathrm{p}) = e \cdot \left(\frac{(x - x_\mathrm{p})^2 + (y - y_\mathrm{p})^2}{2\sigma_\mathrm{illum}^2}\right) e^{\frac{-(x-x_\mathrm{p})^2 - (y-y_\mathrm{p})^2}{2\sigma_\mathrm{illum}^2}}. \tag{2.S18}$$

Note that for the Gaussian and donut illumination models, the condition $0 \leq P(x - x_\mathrm{p}, y - y_\mathrm{p}) \leq 1$ is satisfied, with $P_\mathrm{Gaussian}(x - x_\mathrm{p}, y - y_\mathrm{p}) = 1$ for $x = x_\mathrm{p}$, $y = y_\mathrm{p}$ and with $P_\mathrm{donut}(x - x_\mathrm{p}, y - y_\mathrm{p}) = 1$ for $(x - x_\mathrm{p})^2 + (y - y_\mathrm{p})^2 = 2\sigma_\mathrm{illum}^2$.

The emission PSF is given by Eq. (2.S19), where σ_PSF denotes the standard deviation of the emission PSF.

$$h(x, y) = \frac{1}{2\pi\sigma_\mathrm{PSF}^2} e^{\frac{-x^2 - y^2}{2\sigma_\mathrm{PSF}^2}}. \tag{2.S19}$$

Note that for the Gaussian emission PSF model, the condition of Eq. (2.S7) is satisfied. Furthermore, note that the exponential term in Eq. (2.S19) can be split up as a product of two exponentials, of which one is dependent on x and of which the other is dependent

on y. Using this property, we can further simplify the expression for the Poisson mean μ_i:

$$\mu_i(x_i, x_\mathrm{p}, y_i, y_\mathrm{p}) = \theta_I P(\theta_x - x_\mathrm{p}, \theta_y - y_\mathrm{p}) \cdot \sum_{(x_{\mathrm{M},j}, y_{\mathrm{M},j}) \in (S_{\mathrm{c},i} \cap \tilde{S}_\mathrm{p})} \underbrace{\left(\int_{x_{\mathrm{M},j} - \frac{\Delta x_\mathrm{M}}{2}}^{x_{\mathrm{M},j} + \frac{\Delta x_\mathrm{M}}{2}} \frac{1}{\sigma_\mathrm{PSF}\sqrt{2\pi}} e^{-\frac{(x-\theta_x)^2}{2\sigma_\mathrm{PSF}^2}} \mathrm{d}x \right)}_{E(x_{\mathrm{M},j} - \theta_x, \Delta x_\mathrm{M}, \sigma_\mathrm{PSF}^2)} \underbrace{\left(\int_{y_{\mathrm{M},j} - \frac{\Delta y_\mathrm{M}}{2}}^{y_{\mathrm{M},j} + \frac{\Delta y_\mathrm{M}}{2}} \frac{1}{\sigma_\mathrm{PSF}\sqrt{2\pi}} e^{-\frac{(y-\theta_y)^2}{2\sigma_\mathrm{PSF}^2}} \mathrm{d}y \right)}_{E(y_{\mathrm{M},j} - \theta_y, \Delta y_\mathrm{M}, \sigma_\mathrm{PSF}^2)} + \theta_b B_i. \tag{2.S20}$$

We will use the error function to evaluate the integrations from Eq. (2.S20). To this extent, we introduce the function $E(x, \Delta x, \sigma^2)$:

$$E(x, \Delta x, \sigma^2) = \frac{1}{2}\mathrm{erf}\left(\frac{x + \frac{\Delta x}{2}}{\sqrt{2}\sigma} \right) - \frac{1}{2}\mathrm{erf}\left(\frac{x - \frac{\Delta x}{2}}{\sqrt{2}\sigma} \right). \tag{2.S21}$$

The integrations then evaluate to:

$$E(x_{\mathrm{M},j} - \theta_x, \Delta x_\mathrm{M}, \sigma_\mathrm{PSF}^2) = \frac{1}{2}\mathrm{erf}\left(\frac{x_{\mathrm{M},j} - \theta_x + \frac{\Delta x_\mathrm{M}}{2}}{\sqrt{2}\sigma_\mathrm{PSF}} \right) - \frac{1}{2}\mathrm{erf}\left(\frac{x_{\mathrm{M},j} - \theta_x - \frac{\Delta x_\mathrm{M}}{2}}{\sqrt{2}\sigma_\mathrm{PSF}} \right), \tag{2.S22}$$

$$E(y_{\mathrm{M},j} - \theta_y, \Delta y_\mathrm{M}, \sigma_\mathrm{PSF}^2) = \frac{1}{2}\mathrm{erf}\left(\frac{y_{\mathrm{M},j} - \theta_y + \frac{\Delta y_\mathrm{M}}{2}}{\sqrt{2}\sigma_\mathrm{PSF}} \right) - \frac{1}{2}\mathrm{erf}\left(\frac{y_{\mathrm{M},j} - \theta_y - \frac{\Delta y_\mathrm{M}}{2}}{\sqrt{2}\sigma_\mathrm{PSF}} \right). \tag{2.S23}$$

In final, we obtain the Poisson mean μ_i as shown in Eq. (2.S24).

$$\mu_i(x_i, x_\mathrm{p}, y_i, y_\mathrm{p}) = \theta_I P(\theta_x - x_\mathrm{p}, \theta_y - y_\mathrm{p}) \cdot \sum_{(x_{\mathrm{M},j}, y_{\mathrm{M},j}) \in (S_{\mathrm{c},i} \cap \tilde{S}_\mathrm{p})} E(x_{\mathrm{M},j} - \theta_x, \Delta x_\mathrm{M}, \sigma_\mathrm{PSF}^2) E(y_{\mathrm{M},j} - \theta_y, \Delta y_\mathrm{M}, \sigma_\mathrm{PSF}^2) + \theta_b B_i. \tag{2.S24}$$

For convenience, we collect the terms

$$\sum_{(x_{\mathrm{M},j}, y_{\mathrm{M},j}) \in (S_{\mathrm{c},i} \cap \tilde{S}_\mathrm{p})} E(x_{\mathrm{M},j} - \theta_x, \Delta x_\mathrm{M}, \sigma_\mathrm{PSF}^2) E(y_{\mathrm{M},j} - \theta_y, \Delta y_\mathrm{M}, \sigma_\mathrm{PSF}^2)$$

in the discretized emission PSF term $H(\theta_x, \theta_y, x_i, y_i)$. By doing so, we retrieve the image formation model as in Chapter 2:

$$\mu_i(x_i, x_\mathrm{p}, y_i, y_\mathrm{p}) = \theta_I P(\theta_x - x_\mathrm{p}, \theta_y - y_\mathrm{p}) H(\theta_x, \theta_y, x_i, y_i) + \theta_b B_i. \tag{2.S25}$$

2.S2.3. Effective background B_i

In Eq. (2.S13), a constant term B_i was identified which describes the effective background, given the camera pixel area, the pinhole area, the PSF and the illumination

pattern. Using the discretized approximation of the pinhole area, $B_{i,\text{Gaussian}}$ can be expressed as follows:

$$B_i = \sum_{(x_{\text{M},j},y_{\text{M},j})\in(S_{\text{c},i}\cap\tilde{S}_\text{p})} \int_{x_{\text{M},j}-\frac{\Delta x_\text{M}}{2}}^{x_{\text{M},j}+\frac{\Delta x_\text{M}}{2}} \int_{y_{\text{M},j}-\frac{\Delta y_\text{M}}{2}}^{y_{\text{M},j}+\frac{\Delta y_\text{M}}{2}} \left(\iint_{\mathbb{R}^2} h(\tau,\gamma) P(x-x_\text{p}-\tau, y-y_\text{p}-\gamma)\mathrm{d}\tau\mathrm{d}\gamma \right) \mathrm{d}x\mathrm{d}y. \tag{2.S26}$$

Under the Gaussian model of the illumination and emission PSFs, we can explicitly evaluate the integrals contained in the effective background B_i. For the convolution, we find:

$$\iint_{\mathbb{R}^2} h(\tau,\gamma) P_\text{Gaussian}(x-x_\text{p}-\tau, y-y_\text{p}-\gamma)\mathrm{d}\tau\mathrm{d}\gamma =$$

$$\iint_{\mathbb{R}^2} \frac{1}{2\pi\sigma_\text{PSF}^2} e^{\frac{-\tau^2-\gamma^2}{2\sigma_\text{PSF}^2}} e^{\frac{-(x-x_\text{p}-\tau)^2-(y-y_\text{p}-\gamma)^2}{2\sigma_\text{illum}^2}} \mathrm{d}\tau\mathrm{d}\gamma \tag{2.S27}$$

$$= \left(\int_\mathbb{R} \frac{1}{\sqrt{2\pi}\sigma_\text{PSF}} e^{\frac{-\tau^2}{2\sigma_\text{PSF}^2}+\frac{-(x-x_\text{p}-\tau)^2}{2\sigma_\text{illum}^2}} \mathrm{d}\tau \right) \cdot \left(\int_\mathbb{R} \frac{1}{\sqrt{2\pi}\sigma_\text{PSF}} e^{\frac{-\gamma^2}{2\sigma_\text{PSF}^2}+\frac{-(y-y_\text{p}-\gamma)^2}{2\sigma_\text{illum}^2}} \mathrm{d}\gamma \right) \tag{2.S28}$$

$$= \left(\frac{\sigma_\text{illum}}{\sqrt{\sigma_\text{PSF}^2+\sigma_\text{illum}^2}} e^{\frac{-(x-x_\text{p})^2}{2\left(\sigma_\text{PSF}^2+\sigma_\text{illum}^2\right)}} \right) \cdot \left(\frac{\sigma_\text{illum}}{\sqrt{\sigma_\text{PSF}^2+\sigma_\text{illum}^2}} e^{\frac{-(y-y_\text{p})^2}{2\left(\sigma_\text{PSF}^2+\sigma_\text{illum}^2\right)}} \right) \tag{2.S29}$$

$$= \frac{\sigma_\text{illum}^2}{\sigma_\text{PSF}^2+\sigma_\text{illum}^2} e^{\frac{-(x-x_\text{p})^2-(y-y_\text{p})^2}{2\left(\sigma_\text{PSF}^2+\sigma_\text{illum}^2\right)}} \tag{2.S30}$$

$$= 2\pi\sigma_\text{illum}^2 \left(\frac{1}{2\pi(\sigma_\text{PSF}^2+\sigma_\text{illum}^2)} e^{\frac{-(x-x_\text{p})^2-(y-y_\text{p})^2}{2\left(\sigma_\text{PSF}^2+\sigma_\text{illum}^2\right)}} \right). \tag{2.S31}$$

For the effective background $B_{i,\text{Gaussian}}$, we now have:

$$B_{i,\text{Gaussian}} = 2\pi\sigma_\text{illum}^2$$

$$\cdot \sum_{(x_{\text{M},j},y_{\text{M},j})\in(S_{\text{c},i}\cap\tilde{S}_\text{p})} \int_{x_{\text{M},j}-\frac{\Delta x_\text{M}}{2}}^{x_{\text{M},j}+\frac{\Delta x_\text{M}}{2}} \int_{y_{\text{M},j}-\frac{\Delta y_\text{M}}{2}}^{y_{\text{M},j}+\frac{\Delta y_\text{M}}{2}} \frac{1}{2\pi\left(\sigma_\text{PSF}^2+\sigma_\text{illum}^2\right)} e^{\frac{-(x-x_\text{p})^2-(y-y_\text{p})^2}{2\left(\sigma_\text{PSF}^2+\sigma_\text{illum}^2\right)}} \mathrm{d}x\mathrm{d}y \tag{2.S32}$$

$$= 2\pi\sigma_\text{illum}^2 \sum_{(x_{\text{M},j},y_{\text{M},j})\in(S_{\text{c},i}\cap\tilde{S}_\text{p})} \underbrace{\left(\int_{x_{\text{M},j}-\frac{\Delta x_\text{M}}{2}}^{x_{\text{M},j}+\frac{\Delta x_\text{M}}{2}} \frac{1}{\sqrt{2\pi}\sqrt{\sigma_\text{PSF}^2+\sigma_\text{illum}^2}} e^{\frac{-(x-x_\text{p})^2}{2\left(\sigma_\text{PSF}^2+\sigma_\text{illum}^2\right)}} \mathrm{d}x \right)}_{E\left(x_{\text{M},j}-x_\text{p},\Delta x_\text{M},\sigma_\text{PSF}^2+\sigma_\text{illum}^2\right)}$$

$$\cdot \underbrace{\left(\int_{y_{\text{M},j}-\frac{\Delta y_\text{M}}{2}}^{y_{\text{M},j}+\frac{\Delta y_\text{M}}{2}} \frac{1}{\sqrt{2\pi}\sqrt{\sigma_\text{PSF}^2+\sigma_\text{illum}^2}} e^{\frac{-(y-y_\text{p})^2}{2\left(\sigma_\text{PSF}^2+\sigma_\text{illum}^2\right)}} \mathrm{d}y \right)}_{E\left(y_{\text{M},j}-y_\text{p},\Delta y_\text{M},\sigma_\text{PSF}^2+\sigma_\text{illum}^2\right)}. \tag{2.S33}$$

Note that Eq. (2.S33) requires us to compute definite integrals over Gaussian functions, as was also necessary in Eq. (2.S20). As such, we can again use error functions to simplify the expression. Using the definition of $E(x, \Delta x, \sigma^2)$ from Eq. (2.S21), we find:

$$E\left(x_{\mathrm{M},j} - x_\mathrm{p}, \Delta x_\mathrm{M}, \sigma^2_\mathrm{PSF} + \sigma^2_\mathrm{illum}\right) = \frac{1}{2}\mathrm{erf}\left(\frac{x_{\mathrm{M},j} - x_\mathrm{p} + \frac{\Delta x_\mathrm{M}}{2}}{\sqrt{2\sigma^2_\mathrm{PSF} + 2\sigma^2_\mathrm{illum}}}\right) - \frac{1}{2}\mathrm{erf}\left(\frac{x_{\mathrm{M},j} - x_\mathrm{p} - \frac{\Delta x_\mathrm{M}}{2}}{\sqrt{2\sigma^2_\mathrm{PSF} + 2\sigma^2_\mathrm{illum}}}\right), \tag{2.S34}$$

$$E\left(y_{\mathrm{M},j} - y_\mathrm{p}, \Delta y_\mathrm{M}, \sigma^2_\mathrm{PSF} + \sigma^2_\mathrm{illum}\right) = \frac{1}{2}\mathrm{erf}\left(\frac{y_{\mathrm{M},j} - y_\mathrm{p} + \frac{\Delta y_\mathrm{M}}{2}}{\sqrt{2\sigma^2_\mathrm{PSF} + 2\sigma^2_\mathrm{illum}}}\right) - \frac{1}{2}\mathrm{erf}\left(\frac{y_{\mathrm{M},j} - y_\mathrm{p} - \frac{\Delta y_\mathrm{M}}{2}}{\sqrt{2\sigma^2_\mathrm{PSF} + 2\sigma^2_\mathrm{illum}}}\right). \tag{2.S35}$$

In the end, we find the following expression for the effective background under Gaussian illumination:

$$B_{i,\mathrm{Gaussian}} = 2\pi\sigma^2_\mathrm{illum} \cdot \sum_{(x_{\mathrm{M},j}, y_{\mathrm{M},j}) \in (S_{\mathrm{c},i} \cap \tilde{S}_\mathrm{p})} E\left(x_{\mathrm{M},j} - x_\mathrm{p}, \Delta x_\mathrm{M}, \sigma^2_\mathrm{PSF} + \sigma^2_\mathrm{illum}\right) E\left(y_{\mathrm{M},j} - y_\mathrm{p}, \Delta y_\mathrm{M}, \sigma^2_\mathrm{PSF} + \sigma^2_\mathrm{illum}\right). \tag{2.S36}$$

The donut-shaped illumination pattern is not separable in x and y, which means we cannot separate the convolutions as was done in Eq. (2.S28). For the convolution between the donut-shaped illumination pattern and the PSF, we find:

$$\iint_{\mathbb{R}^2} h(\tau,\gamma) P_\mathrm{donut}(x - x_\mathrm{p} - \tau, y - y_\mathrm{p} - \gamma)\mathrm{d}\tau\mathrm{d}\gamma \tag{2.S37}$$

$$= \iint_{\mathbb{R}^2} \frac{1}{2\pi\sigma^2_\mathrm{PSF}} e^{\frac{-\tau^2-\gamma^2}{2\sigma^2_\mathrm{PSF}}} \cdot e \cdot \left(\frac{(x - x_\mathrm{p} - \tau)^2 + (y - y_\mathrm{p} - \gamma)^2}{2\sigma^2_\mathrm{illum}}\right) e^{\frac{-(x-x_\mathrm{p}-\tau)^2-(y-y_\mathrm{p}-\gamma)^2}{2\sigma^2_\mathrm{illum}}} \mathrm{d}\tau\mathrm{d}\gamma \tag{2.S38}$$

$$= e \cdot \frac{\sigma^2_\mathrm{illum}\left(\sigma^2_\mathrm{illum}\left((x - x_\mathrm{p})^2 + (y - y_\mathrm{p})^2 + 2\sigma^2_\mathrm{PSF}\right) + 2\sigma^4_\mathrm{PSF}\right)}{2\left(\sigma^2_\mathrm{PSF} + \sigma^2_\mathrm{illum}\right)^3} e^{\frac{-(x-x_\mathrm{p})^2-(y-y_\mathrm{p})^2}{2\left(\sigma^2_\mathrm{PSF}+\sigma^2_\mathrm{illum}\right)}}. \tag{2.S39}$$

For the effective background $B_{i,\mathrm{donut}}$, we now have:

$$B_{i,\mathrm{donut}} = \sum_{(x_{\mathrm{M},j}, y_{\mathrm{M},j}) \in (S_{\mathrm{c},i} \cap \tilde{S}_\mathrm{p})} F\left(x_{\mathrm{M},j} + \frac{\Delta x_\mathrm{M}}{2}, y_{\mathrm{M},j} + \frac{\Delta y_\mathrm{M}}{2}\right) - F\left(x_{\mathrm{M},j} + \frac{\Delta x_\mathrm{M}}{2}, y_{\mathrm{M},j} - \frac{\Delta y_\mathrm{M}}{2}\right) - F\left(x_{\mathrm{M},j} - \frac{\Delta x_\mathrm{M}}{2}, y_{\mathrm{M},j} + \frac{\Delta y_\mathrm{M}}{2}\right) + F\left(x_{\mathrm{M},j} - \frac{\Delta x_\mathrm{M}}{2}, y_{\mathrm{M},j} - \frac{\Delta y_\mathrm{M}}{2}\right). \tag{2.S40}$$

where $F(x,y)$ is the function:

$$F(x,y) = \frac{e\pi}{2}\sigma^2_{\text{illum}}\text{erf}\left(\frac{x-x_\text{p}}{\sqrt{2\sigma^2_{\text{PSF}}+2\sigma^2_{\text{illum}}}}\right)\text{erf}\left(\frac{y-y_\text{p}}{\sqrt{2\sigma^2_{\text{PSF}}+2\sigma^2_{\text{illum}}}}\right) - \frac{e\sqrt{\pi}\sigma^4_{\text{illum}}}{\sqrt{\left(2\sigma^2_{\text{PSF}}+2\sigma^2_{\text{illum}}\right)^3}}\left(\left(x-x_\text{p}\right)e^{\frac{-\left(x-x_\text{p}\right)^2}{2\sigma^2_{\text{PSF}}+2\sigma^2_{\text{illum}}}}\text{erf}\left(\frac{y-y_\text{p}}{\sqrt{2\sigma^2_{\text{PSF}}+2\sigma^2_{\text{illum}}}}\right)\right. \\ \left. + \left(y-y_\text{p}\right)e^{\frac{-\left(y-y_\text{p}\right)^2}{2\sigma^2_{\text{PSF}}+2\sigma^2_{\text{illum}}}}\text{erf}\left(\frac{x-x_\text{p}}{\sqrt{2\sigma^2_{\text{PSF}}+2\sigma^2_{\text{illum}}}}\right)\right). \tag{2.S41}$$

2.S2.4. Multiple illumination patterns

In Eq. (2.S8), we assumed that only one illumination pattern is used for illumination. In SpinFlux, we have the opportunity to use multiple pinholes and patterns for illumination. In this subsection, we extend our image formation model to this situation.

For the image formation, we assume that pinholes are separated far enough on the spinning disk, such that only one pinhole can appear in a region of interest during each camera frame. This assumption is valid for the magnifications, pinhole sizes and pinhole separations in existing SDCM setups [2, 14, 15]. Accordingly, we assume there is no crosstalk between emission signal coming from different pinholes. This allows us to describe the regions of interest on the camera frames as separate regions of interest from individual patterns.

In the K-pattern case, the object on each camera frame is the result of single-pattern illumination, where the illumination patterns are centred at pinhole positions $\boldsymbol{x}_\text{p} = [x_{\text{p},1},\ldots,x_{\text{p},K}]$, $\boldsymbol{y}_\text{p} = [y_{\text{p},1},\ldots,y_{\text{p},K}]$, each corresponding to the pinhole with area $S_{\text{p},k} = \left\{(x,y)|(x-x_{\text{p},k})^2+(y-y_{\text{p},k})^2 \leq r^2_{\text{p},k}\right\}$. This gives rise to the following object function $f_k(x,x_{\text{p},k},y,y_{\text{p},k})$ for the object corresponding to pattern k:

$$f_k(x,x_{\text{p},k},y,y_{\text{p},k}) = A_k P(x-x_{\text{p},k},y-y_{\text{p},k})(\theta_I\delta(x-\theta_x,y-\theta_y)+\theta_b). \tag{2.S42}$$

In existing work on meSMLM, such as in MINFLUX [13], it is assumed that meSMLM is able to record the same amount of signal photons as SMLM. This assumption allows benchmarking between methods on the same signal photon count. However, the assumption is not trivial, as additional illumination power or time is needed to exhaust the signal photon budget with non-maximum illumination intensity. Properly adjusting the illumination power to compensate for the reduced photon flux requires accurate prior knowledge about the emitter position, which is generally unavailable, and is limited by saturation of the illumination intensity profile. Increasing the illumination time increases the probability of sample degradation. As such, it is reasonable to assume that meSMLM will not exhaust the signal photon budget completely.

The normalizing constant A_k describes how the signal photon budget is affected by non-maximum illumination. This constant plays a vital role in benchmarking meSMLM (when the summed intensity over all patterns does not result in a uniform profile), as

it gives a physical explanation of the fair signal photon count against which meSMLM should be compared [8]. Specifically when comparing meSMLM to SMLM, the normalization constant models whether meSMLM would have had recorded the same amount of signal photons as SMLM, despite the additional illumination power or time needed to do so. Results on the improvement of meSMLM compared to SMLM should thus only be given in the context of the normalizing constant A_k.

We choose A_k to model two different scenarios in this work, to explore how SpinFlux is affected by these conditions. In the first scenario, the entire signal photon budget is exhausted after illumination with all patterns (aside from signal photons that are blocked by the spinning disk), disregarding the illumination power and time needed to accomplish this for each pattern. This scenario is consistent with the assumption used in e.g. MINFLUX [13], stating that meSMLM will record the same amount of photons as SMLM. For this scenario, the sum of the illumination patterns should satisfy the conditions $\sum_{k=1}^{K} P(x - x_{\mathrm{p},k}, y - y_{\mathrm{p},k}) \geq 0$ for all $(x, y) \in \mathbb{R}^2$ and $\sum_{k=1}^{K} P(\theta_x - x_{\mathrm{p},k}, \theta_y - y_{\mathrm{p},k}) = 1$ to exhaust the expected signal photon budget on the emitter position. Under these conditions, $A_k = A$ is a constant applied equally to all patterns. If the individual patterns satisfy $P(x - x_{\mathrm{p},k}, y - y_{\mathrm{p},k}) \geq 0$ for all $(x, y) \in \mathbb{R}^2$, A must be given by Eq. (2.S43) to satisfy the constraints on $\sum_{k=1}^{K} P(\theta_x - x_{\mathrm{p},k}, \theta_y - y_{\mathrm{p},k})$:

$$A_k = A = \frac{1}{\sum_{k=1}^{K} P(\theta_x - x_{\mathrm{p},k}, \theta_y - y_{\mathrm{p},k})}. \tag{2.S43}$$

In the second scenario, the illumination power and time are constant for each pattern such that the total illumination power and time equal that of SMLM, even though this does not exhaust the signal photon budget for non-maximum illumination. For this scenario, the sum of the illumination patterns should satisfy the conditions $0 \leq \sum_{k=1}^{K} P(x - x_{\mathrm{p},k}, y - y_{\mathrm{p},k}) \leq 1$ for all $(x, y) \in \mathbb{R}^2$. If the individual patterns satisfy $0 \leq P(x - x_{\mathrm{p},k}, y - y_{\mathrm{p},k}) \leq 1$ for all $(x, y) \in \mathbb{R}^2$ and $P(x - x_{\mathrm{p},k}, y - y_{\mathrm{p},k}) = 1$ for some $(x, y) \in \mathbb{R}^2$, A must be given by Eq. (2.S44) to satisfy the constraint on $\sum_{k=1}^{K} P(x - x_{\mathrm{p},k}, y - y_{\mathrm{p},k})$ for arbitrary x and y:

$$A_k = A = \frac{1}{K}. \tag{2.S44}$$

We now continue the derivation of the image formation model. We approximate every pinhole area $S_{\mathrm{p},k}$ by the discretized pinhole $\tilde{S}_{\mathrm{p},k}$ following the discretization procedure described before. This gives the following model for the Poisson mean $\mu_{i,k}(x_i, x_{\mathrm{p}}, y_i, y_{\mathrm{p}})$ on pixel i with pinhole and pattern k:

$$\begin{aligned}\mu_{i,k}(x_i, x_{\mathrm{p},k}, y_i, y_{\mathrm{p},k}) = {} & A\theta_I P(\theta_x - x_{\mathrm{p},k}, \theta_y - y_{\mathrm{p},k}) \\ & \cdot \sum_{(x_{\mathrm{M},j}, y_{\mathrm{M},j}) \in (S_{\mathrm{c},i} \cap \tilde{S}_{\mathrm{p},k})} E(x_{\mathrm{M},j} - \theta_x, \Delta x_{\mathrm{M}}, \sigma^2_{\mathrm{PSF}}) E(y_{\mathrm{M},j} - \theta_y, \Delta y_{\mathrm{M}}, \sigma^2_{\mathrm{PSF}}) \\ & + A\theta_b B_{i,k},\end{aligned} \tag{2.S45}$$

$$\begin{aligned}B_{i,k} = {} & 2\pi\sigma^2_{\mathrm{illum}} \\ & \cdot \sum_{(x_{\mathrm{M},j}, y_{\mathrm{M},j}) \in (S_{\mathrm{c},i} \cap \tilde{S}_{\mathrm{p},k})} E\left(x_{\mathrm{M},j} - x_{\mathrm{p},k}, \Delta x_{\mathrm{M}}, \sigma^2_{\mathrm{PSF}} + \sigma^2_{\mathrm{illum}}\right) E\left(y_{\mathrm{M},j} - y_{\mathrm{p},k}, \Delta y_{\mathrm{M}}, \sigma^2_{\mathrm{PSF}} + \sigma^2_{\mathrm{illum}}\right).\end{aligned} \tag{2.S46}$$

2.S2.5. Pattern-independent background

In Eq. (2.S8), we assumed that the illumination pattern modulates both the signal coming from the emitter PSF, as well as the background. In existing meSMLM work, such as in the analysis of e.g. MINFLUX [13], the pattern-dependency of the background is neglected. To allow for a fair comparison between these methods and SpinFlux, we derive and adapted image formation model, where the background is assumed to be pattern-independent. In this scenario, the object $f(x, x_\mathrm{p}, y, y_\mathrm{p})$ for a single pinhole and illumination pattern is modelled as follows:

$$f_{\text{patt.-indep. b.g.}}(x, x_\mathrm{p}, y, y_\mathrm{p}) = P(x - x_\mathrm{p}, y - y_\mathrm{p})(\theta_I \delta(x - \theta_x, y - \theta_y)) + \theta_b. \tag{2.S47}$$

Following the same derivation as for the pattern-dependent background, we find the following expression for the Poisson mean μ:

$$\begin{aligned}\mu_{i,\text{patt.-indep. b.g.}}(x_i, x_\mathrm{p}, y_i, y_\mathrm{p}) = \theta_I P(\theta_x - x_\mathrm{p}, \theta_y - y_\mathrm{p}) \\ \cdot \sum_{(x_{\mathrm{M},j}, y_{\mathrm{M},j}) \in (S_{\mathrm{c},i} \cap \tilde{S}_\mathrm{p})} E(x_{\mathrm{M},j} - \theta_x, \Delta x_\mathrm{M}, \sigma^2_\mathrm{PSF}) E(y_{\mathrm{M},j} - \theta_y, \Delta y_\mathrm{M}, \sigma^2_\mathrm{PSF}) \\ + \theta_b B_{i,\text{patt.-indep. b.g.}},\end{aligned} \tag{2.S48}$$

$$B_{i,\text{patt.-indep. b.g.}} = \sum_{(x_{\mathrm{M},j}, y_{\mathrm{M},j}) \in (S_{\mathrm{c},i} \cap \tilde{S}_{\mathrm{p},k})} \Delta x_\mathrm{M} \cdot \Delta y_\mathrm{M}. \tag{2.S49}$$

Note that for this case, the constant $B_{i,\text{patt.-indep. b.g.}}$ only depends on the intersection area $(S_{\mathrm{c},i} \cap \tilde{S}_\mathrm{p})$ between the camera pixel i and the approximation of pinhole k.

To extend the model with pattern-independent background to multiple illumination patterns, we formulate the following object function:

$$f_{k,\text{patt.-indep. b.g.}}(x, x_{\mathrm{p},k}, y, y_{\mathrm{p},k}) = A_k P(x - x_{\mathrm{p},k}, y - y_{\mathrm{p},k})(\theta_I \delta(x - \theta_x, y - \theta_y)) + \theta_b. \tag{2.S50}$$

For the Poisson mean $\mu_{i,k,\text{patt.-indep. b.g.}}(x_i, x_\mathrm{p}, y_i, y_\mathrm{p})$ on pixel i for the camera frame with pattern k, this gives the following model:

$$\begin{aligned}\mu_{i,k,\text{patt.-indep. b.g.}}(x_i, x_{\mathrm{p},k}, y_i, y_{\mathrm{p},k}) = A\theta_I P(\theta_x - x_{\mathrm{p},k}, \theta_y - y_{\mathrm{p},k}) \\ \sum_{(x_{\mathrm{M},j}, y_{\mathrm{M},j}) \in (S_{\mathrm{c},i} \cap \tilde{S}_{\mathrm{p},k})} E(x_{\mathrm{M},j} - \theta_x, \Delta x_\mathrm{M}, \sigma^2_\mathrm{PSF}) E(y_{\mathrm{M},j} - \theta_y, \Delta y_\mathrm{M}, \sigma^2_\mathrm{PSF}) \\ + \theta_b B_{i,\text{patt.-indep. b.g.}},\end{aligned} \tag{2.S51}$$

$$B_{i,\text{patt.-indep. b.g.}} = \sum_{(x_{\mathrm{M},j}, y_{\mathrm{M},j}) \in (S_{\mathrm{c},i} \cap \tilde{S}_{\mathrm{p},k})} \Delta x_\mathrm{M} \cdot \Delta y_\mathrm{M}. \tag{2.S52}$$

Here, A is as in Eq. (2.S43) for the scenario where the entire signal photon budget is exhausted after illumination with all patterns.

2.S3. Cramér-Rao lower bound for SpinFlux localization

In this section, we derive the CRLB for SpinFlux meSMLM.

2.S3.1. Log-likelihood function for SpinFlux localization

In this subsection, we describe a statistical model for photon collection. The model should describe the amount of photons that are recorded by a camera pixel during a measurement, in the absence of readout noise. From [5], we infer that such a process can be modelled by the Poisson distribution. The Poisson distribution describes the amount of event occurrences within a certain time interval and it is therefore a proper probabilistic model for photon collection.

The Poisson process is dependent on a single parameter μ, which in our case describes the expected amount of photons that fall on a camera pixel during a measurement (see Section 2.S2). The probability mass function $p(c)$ of the Poisson distribution is given by Eq. (2.S53).

$$p(c) = \mathbb{P}(C = c) = \frac{\mu^c e^{-\mu}}{c!}. \tag{2.S53}$$

We start by considering single-pinhole and single-pattern SpinFlux. Let the random variables $\{C_i\}_{i=1}^{N_{\text{pixels}}}$ describe the amount of photons acquired by camera pixels $i \in \{1,2,\ldots,N_{\text{pixels}}\}$ during a measurement with a pattern $P(x-x_{\text{p}}, y-y_{\text{p}})$. Therefore, $\{C_i\}_{i=1}^{N_{\text{pixels}}}$ can be considered mutually independent [5] and they all have a Poisson distribution with Poisson parameter $\mu_i(x_i, x_{\text{p}}, y_i, y_{\text{p}})$. Furthermore, let $\boldsymbol{c} = \{c_i\}_{i=1}^{N_{\text{pixels}}}$ denote the acquired measurements, which can be seen as realizations of $\{C_i\}_{i=1}^{N_{\text{pixels}}}$. We then find the Poisson likelihood $L(\boldsymbol{\theta}|\boldsymbol{c})$ and log-likelihood $\ell(\boldsymbol{\theta}|\boldsymbol{c})$ of Eqs. (2.S54) and (2.S55), respectively.

$$L(\boldsymbol{\theta}|\boldsymbol{c}) = \prod_{i=1}^{N_{\text{pixels}}} \frac{\mu_i^{c_i}(x_i, x_{\text{p}}, y_i, y_{\text{p}}) e^{-\mu_i(x_i, x_{\text{p}}, y_i, y_{\text{p}})}}{c_i!}, \tag{2.S54}$$

$$\ell(\boldsymbol{\theta}|\boldsymbol{c}) = \sum_{i=1}^{N_{\text{pixels}}} \left(c_i \log(\mu_i(x_i, x_{\text{p}}, y_i, y_{\text{p}})) - \log(c_i!) - \mu_i(x_i, x_{\text{p}}, y_i, y_{\text{p}}) \right). \tag{2.S55}$$

2.S3.2. Cramér-Rao lower bound for SpinFlux localization

In this subsection, we compute the CRLB for single-pinhole and single-pattern SpinFlux, using the log-likelihood function of Eq. (2.S55). For notation convenience, we leave out the arguments $(x_i, x_{\text{p}}, y_i, y_{\text{p}})$ of μ_i. We compute the partial derivative of $\ell(\boldsymbol{\theta}|\boldsymbol{c})$ with respect to the u'th element of $\boldsymbol{\theta}$, $\boldsymbol{\theta}_u$:

$$\frac{\partial \ell(\boldsymbol{\theta}|\boldsymbol{c})}{\partial \boldsymbol{\theta}_u} = \sum_{i=1}^{N_{\text{pixels}}} \left(c_i \frac{1}{\mu_i} \frac{\partial \mu_i}{\partial \boldsymbol{\theta}_u} - \frac{\partial \mu_i}{\partial \boldsymbol{\theta}_u} \right) \tag{2.S56}$$

$$= \sum_{k=1}^{N_{\text{pixels}}} \left((c_i - \mu_i) \frac{1}{\mu_i} \frac{\partial \mu_i}{\partial \boldsymbol{\theta}_u} \right). \tag{2.S57}$$

We can compute entry (u, v) of the Fisher information matrix as shown in Eq. (2.S58) [16, 17].

$$I_{uv}(\boldsymbol{\theta}) = \mathbb{E}\left[\frac{\partial \ell(\boldsymbol{\theta}|\boldsymbol{c})}{\partial \boldsymbol{\theta}_u} \frac{\partial \ell(\boldsymbol{\theta}|\boldsymbol{c})}{\partial \boldsymbol{\theta}_v} \right]. \tag{2.S58}$$

The Fisher information for single-pinhole and single-pattern SpinFlux is then given by:

$$I_{uv}(\boldsymbol{\theta}) = \mathbb{E}\left[\left(\sum_{i=1}^{N_{\text{pixels}}}(c_i-\mu_i)\frac{1}{\mu_i}\frac{\partial\mu_i}{\partial\boldsymbol{\theta}_u}\right)\left(\sum_{j=1}^{N_{\text{pixels}}}(c_j-\mu_j)\frac{1}{\mu_j}\frac{\partial\mu_j}{\partial\boldsymbol{\theta}_v}\right)\right] \tag{2.S59}$$

$$= \sum_{i=1}^{N_{\text{pixels}}}\sum_{j=1}^{N_{\text{pixels}}}\mathbb{E}\left[(c_i-\mu_i)(c_j-\mu_j)\frac{1}{\mu_i\mu_j}\frac{\partial\mu_i}{\partial\boldsymbol{\theta}_u}\frac{\partial\mu_j}{\partial\boldsymbol{\theta}_v}\right] \tag{2.S60}$$

$$= \sum_{i=1}^{N_{\text{pixels}}}\sum_{j=1}^{N_{\text{pixels}}}\frac{1}{\mu_i\mu_j}\frac{\partial\mu_i}{\partial\boldsymbol{\theta}_u}\frac{\partial\mu_j}{\partial\boldsymbol{\theta}_v}\mathbb{E}\left[(c_i-\mu_i)(c_j-\mu_j)\right]. \tag{2.S61}$$

Note that $\mathbb{E}\left[(c_i-\mu_i)(c_j-\mu_j)\right]$ denotes the covariance of C_i and C_j. As $\{C_i\}_{i=1}^{N_{\text{pixels}}}$ were assumed to be mutually independent, the covariance is 0 if $i \neq j$ and it is equal to the variance if $i = j$. Furthermore, recall that the variance of a Poisson distribution is equal to its mean. We can hence express the Fisher information as shown in Eq. (2.S62).

$$I_{uv}(\boldsymbol{\theta}) = \sum_{i=1}^{N_{\text{pixels}}}\frac{1}{\mu_i}\frac{\partial\mu_i}{\partial\boldsymbol{\theta}_u}\frac{\partial\mu_i}{\partial\boldsymbol{\theta}_v}. \tag{2.S62}$$

The CRLB states that for any unbiased estimator $\hat{\boldsymbol{\theta}}$ of the parameter vector $\boldsymbol{\theta}$, $\left(\Sigma_{\hat{\boldsymbol{\theta}}} - I^{-1}(\boldsymbol{\theta})\right)$ is positive semi-definite [16]. Here, $\Sigma_{\hat{\boldsymbol{\theta}}}$ denotes the estimator covariance, $I(\boldsymbol{\theta})$ is the Fisher information and $I^{-1}(\boldsymbol{\theta})$ is the CRLB. In particular, the diagonal of $I^{-1}(\boldsymbol{\theta})$ thus bounds the estimator variance from below.

2.S3.3. Log-likelihood function and Cramér-Rao lower bound for multiple-pattern SpinFlux

In the multiple-pattern case, the use of multiple single-pattern camera frames leads to an additional product term in the likelihood function of Eq. (2.S54). This leads to the following log-likelihood function:

$$\ell(\boldsymbol{\theta}|\boldsymbol{c}) = \sum_{i=1}^{N_{\text{pixels}}}\sum_{k=1}^{K}\left(c_{i,k}\log(\mu_{i,k}(x_i,x_{\text{p},k},y_i,y_{\text{p},k})) - \log(c_{i,k}!) - \mu_{i,k}(x_i,x_{\text{p},k},y_i,y_{\text{p},k})\right). \tag{2.S63}$$

Analogous to the derivation of the single-pattern Fisher information, we find the following expression for the multiple-pattern case:

$$I_{uv}(\boldsymbol{\theta}) = \sum_{i=1}^{N_{\text{pixels}}}\sum_{k=1}^{K}\frac{1}{\mu_{i,k}}\frac{\partial\mu_{i,k}}{\partial\boldsymbol{\theta}_u}\frac{\partial\mu_{i,k}}{\partial\boldsymbol{\theta}_v}. \tag{2.S64}$$

2.S4. Derivatives of the SpinFlux image formation model, needed to compute the Cramér-Rao lower bound

In this section, we derive expressions for $\frac{\partial\mu_i}{\partial\theta_x}$, $\frac{\partial\mu_i}{\partial\theta_y}$, $\frac{\partial\mu_i}{\partial\theta_I}$, and $\frac{\partial\mu_i}{\partial\theta_b}$, which allow us to compute the Fisher information from Eq. (2.S62).

Derivative with respect to x-position (single pattern)

$$\frac{\partial \mu_i}{\partial \theta_x} = \theta_I \frac{\partial P(\theta_x - x_\mathrm{p}, \theta_y - y_\mathrm{p})}{\partial \theta_x} \sum_{(x_{\mathrm{M},j}, y_{\mathrm{M},j}) \in (S_{\mathrm{c},i} \cap \tilde{S}_\mathrm{p})} E(x_{\mathrm{M},j} - \theta_x, \Delta x_\mathrm{M}, \sigma^2_\mathrm{PSF}) E(y_{\mathrm{M},j} - \theta_y, \Delta y_\mathrm{M}, \sigma^2_\mathrm{PSF}) + \theta_I P(\theta_x - x_\mathrm{p}, \theta_y - y_\mathrm{p}) \sum_{(x_{\mathrm{M},j}, y_{\mathrm{M},j}) \in (S_{\mathrm{c},i} \cap \tilde{S}_\mathrm{p})} \frac{\partial E(x_{\mathrm{M},j} - \theta_x, \Delta x_\mathrm{M}, \sigma^2_\mathrm{PSF})}{\partial \theta_x} E(y_{\mathrm{M},j} - \theta_y, \Delta y_\mathrm{M}, \sigma^2_\mathrm{PSF}) \tag{2.S65}$$

Here, $\frac{\partial P(\theta_x - x_\mathrm{p}, \theta_y - y_\mathrm{p})}{\partial \theta_x}$ and $\frac{\partial E(x_{\mathrm{M},j} - \theta_x, \Delta x_\mathrm{M}, \sigma^2_\mathrm{PSF})}{\partial \theta_x}$ are as follows:

$$\frac{\partial P_\mathrm{Gaussian}(\theta_x - x_\mathrm{p}, \theta_y - y_\mathrm{p})}{\partial \theta_x} = \left(\frac{x_\mathrm{p} - \theta_x}{\sigma^2_\mathrm{illum}} \right) e^{\frac{-(\theta_x - x_\mathrm{p})^2 - (\theta_y - y_\mathrm{p})^2}{2\sigma^2_\mathrm{illum}}} \tag{2.S66}$$

$$\frac{\partial P_\mathrm{donut}(\theta_x - x_\mathrm{p}, \theta_y - y_\mathrm{p})}{\partial \theta_x} = e \left(\frac{\theta_x - x_\mathrm{p}}{\sigma^2_\mathrm{illum}} \right) e^{\frac{-(\theta_x - x_\mathrm{p})^2 - (\theta_y - y_\mathrm{p})^2}{2\sigma^2_\mathrm{illum}}} + e \left(\frac{(\theta_x - x_\mathrm{p})^2 + (\theta_y - y_\mathrm{p})^2}{2\sigma^2_\mathrm{illum}} \right) \left(\frac{x_\mathrm{p} - \theta_x}{\sigma^2_\mathrm{illum}} \right) e^{\frac{-(\theta_x - x_\mathrm{p})^2 - (\theta_y - y_\mathrm{p})^2}{2\sigma^2_\mathrm{illum}}} \tag{2.S67}$$

$$\frac{\partial E(x_{\mathrm{M},j} - \theta_x, \Delta x_\mathrm{M}, \sigma^2_\mathrm{PSF})}{\partial \theta_x} = \frac{1}{\sqrt{2\pi}\sigma_\mathrm{PSF}} \left(e^{\frac{-\left(x_{\mathrm{M},j} - \theta_x - \frac{\Delta x_\mathrm{M}}{2}\right)^2}{2\sigma^2_\mathrm{PSF}}} - e^{\frac{-\left(x_{\mathrm{M},j} - \theta_x + \frac{\Delta x_\mathrm{M}}{2}\right)^2}{2\sigma^2_\mathrm{PSF}}} \right) \tag{2.S68}$$

Derivative with respect to y-position (single pattern)

$$\frac{\partial \mu_i}{\partial \theta_y} = \theta_I \frac{\partial P(\theta_x - x_\mathrm{p}, \theta_y - y_\mathrm{p})}{\partial \theta_y} \sum_{(x_{\mathrm{M},j}, y_{\mathrm{M},j}) \in (S_{\mathrm{c},i} \cap \tilde{S}_\mathrm{p})} E(x_{\mathrm{M},j} - \theta_x, \Delta x_\mathrm{M}, \sigma^2_\mathrm{PSF}) E(y_{\mathrm{M},j} - \theta_y, \Delta y_\mathrm{M}, \sigma^2_\mathrm{PSF}) + \theta_I P(\theta_x - x_\mathrm{p}, \theta_y - y_\mathrm{p}) \sum_{(x_{\mathrm{M},j}, y_{\mathrm{M},j}) \in (S_{\mathrm{c},i} \cap \tilde{S}_\mathrm{p})} E(x_{\mathrm{M},j} - \theta_x, \Delta x_\mathrm{M}, \sigma^2_\mathrm{PSF}) \frac{\partial E(y_{\mathrm{M},j} - \theta_y, \Delta y_\mathrm{M}, \sigma^2_\mathrm{PSF})}{\partial \theta_y} \tag{2.S69}$$

Here, $\frac{\partial P(\theta_x - x_\mathrm{p}, \theta_y - y_\mathrm{p})}{\partial \theta_y}$ and $\frac{\partial E(y_{\mathrm{M},j} - \theta_y, \Delta y_\mathrm{M}, \sigma^2_\mathrm{PSF})}{\partial \theta_y}$ are as follows:

$$\frac{\partial P_\mathrm{Gaussian}(\theta_x - x_\mathrm{p}, \theta_y - y_\mathrm{p})}{\partial \theta_y} = \left(\frac{y_\mathrm{p} - \theta_y}{\sigma^2_\mathrm{illum}} \right) e^{\frac{-(\theta_x - x_\mathrm{p})^2 - (\theta_y - y_\mathrm{p})^2}{2\sigma^2_\mathrm{illum}}} \tag{2.S70}$$

$$\begin{aligned} \frac{\partial P_\mathrm{donut}(\theta_x - x_\mathrm{p}, \theta_y - y_\mathrm{p})}{\partial \theta_y} &= e \left(\frac{\theta_y - y_\mathrm{p}}{\sigma^2_\mathrm{illum}} \right) e^{\frac{-(\theta_x - x_\mathrm{p})^2 - (\theta_y - y_\mathrm{p})^2}{2\sigma^2_\mathrm{illum}}} \\ &+ e \left(\frac{(\theta_x - x_\mathrm{p})^2 + (\theta_y - y_\mathrm{p})^2}{2\sigma^2_\mathrm{illum}} \right) \left(\frac{y_\mathrm{p} - \theta_y}{\sigma^2_\mathrm{illum}} \right) e^{\frac{-(\theta_x - x_\mathrm{p})^2 - (\theta_y - y_\mathrm{p})^2}{2\sigma^2_\mathrm{illum}}} \end{aligned} \tag{2.S71}$$

$$\frac{\partial E(y_{\mathrm{M},j} - \theta_y, \Delta y_\mathrm{M}, \sigma^2_\mathrm{PSF})}{\partial \theta_y} = \frac{1}{\sqrt{2\pi}\sigma_\mathrm{PSF}} \left(e^{\frac{-\left(y_{\mathrm{M},j} - \theta_y - \frac{\Delta y_\mathrm{M}}{2}\right)^2}{2\sigma^2_\mathrm{PSF}}} - e^{\frac{-\left(y_{\mathrm{M},j} - \theta_y + \frac{\Delta y_\mathrm{M}}{2}\right)^2}{2\sigma^2_\mathrm{PSF}}} \right) \tag{2.S72}$$

Derivative with respect to expected signal photon count (single pattern)

$$\frac{\partial \mu_i}{\partial \theta_I} = P(\theta_x - x_\mathrm{p}, \theta_y - y_\mathrm{p}) \sum_{(x_{\mathrm{M},j}, y_{\mathrm{M},j}) \in (S_{\mathrm{c},i} \cap \tilde{S}_\mathrm{p})} E(x_{\mathrm{M},j} - \theta_x, \Delta x_\mathrm{M}, \sigma^2_\mathrm{PSF}) E(y_{\mathrm{M},j} - \theta_y, \Delta y_\mathrm{M}, \sigma^2_\mathrm{PSF}) \tag{2.S73}$$

Derivative with respect to expected background count (single pattern)

$$\frac{\partial \mu_i}{\partial \theta_b} = B_i \tag{2.S74}$$

$$= 2\pi\sigma^2_\mathrm{illum} \cdot \sum_{(x_{\mathrm{M},j}, y_{\mathrm{M},j}) \in (S_{\mathrm{c},i} \cap \tilde{S}_\mathrm{p})} E\left(x_{\mathrm{M},j} - x_\mathrm{p}, \Delta x_\mathrm{M}, \sigma^2_\mathrm{PSF} + \sigma^2_\mathrm{illum}\right) E\left(y_{\mathrm{M},j} - y_\mathrm{p}, \Delta y_\mathrm{M}, \sigma^2_\mathrm{PSF} + \sigma^2_\mathrm{illum}\right) \tag{2.S75}$$

Derivative with respect to x-position (multiple pattern)

$$\begin{aligned} \frac{\partial \mu_{i,k}}{\partial \theta_x} &= A\theta_I \frac{\partial P(\theta_x - x_{\mathrm{p},k}, \theta_y - y_{\mathrm{p},k})}{\partial \theta_x} \\ &\cdot \sum_{(x_{\mathrm{M},j}, y_{\mathrm{M},j}) \in (S_{\mathrm{c},i} \cap \tilde{S}_{\mathrm{p},k})} E(x_{\mathrm{M},j} - \theta_x, \Delta x_\mathrm{M}, \sigma^2_\mathrm{PSF}) E(y_{\mathrm{M},j} - \theta_y, \Delta y_\mathrm{M}, \sigma^2_\mathrm{PSF}) \\ &+ A\theta_I P(\theta_x - x_{\mathrm{p},k}, \theta_y - y_{\mathrm{p},k}) \\ &\cdot \sum_{(x_{\mathrm{M},j}, y_{\mathrm{M},j}) \in (S_{\mathrm{c},i} \cap \tilde{S}_{\mathrm{p},k})} \frac{\partial E(x_{\mathrm{M},j} - \theta_x, \Delta x_\mathrm{M}, \sigma^2_\mathrm{PSF})}{\partial \theta_x} E(y_{\mathrm{M},j} - \theta_y, \Delta y_\mathrm{M}, \sigma^2_\mathrm{PSF}) \end{aligned} \tag{2.S76}$$

Here, $\frac{\partial P(\theta_x - x_{\mathrm{p},k}, \theta_y - y_{\mathrm{p},k})}{\partial \theta_x}$ is as follows:

$$\frac{\partial P_{\mathrm{Gaussian}}(\theta_x - x_{\mathrm{p},k}, \theta_y - y_{\mathrm{p},k})}{\partial \theta_x} = \left(\frac{x_{\mathrm{p},k} - \theta_x}{\sigma^2_{\mathrm{illum}}} \right) e^{\frac{-(\theta_x - x_{\mathrm{p},k})^2 - (\theta_y - y_{\mathrm{p},k})^2}{2\sigma^2_{\mathrm{illum}}}} \tag{2.S77}$$

$$\begin{aligned} \frac{\partial P_{\mathrm{donut}}(\theta_x - x_{\mathrm{p},k}, \theta_y - y_{\mathrm{p},k})}{\partial \theta_x} &= e \left(\frac{\theta_x - x_{\mathrm{p},k}}{\sigma^2_{\mathrm{illum}}} \right) e^{\frac{-(\theta_x - x_{\mathrm{p},k})^2 - (\theta_y - y_{\mathrm{p},k})^2}{2\sigma^2_{\mathrm{illum}}}} + e \left(\frac{x_{\mathrm{p},k} - \theta_x}{\sigma^2_{\mathrm{illum}}} \right) \\ &\cdot \left(\frac{(\theta_x - x_{\mathrm{p},k})^2 + (\theta_y - y_{\mathrm{p},k})^2}{2\sigma^2_{\mathrm{illum}}} \right) e^{\frac{-(\theta_x - x_{\mathrm{p},k})^2 - (\theta_y - y_{\mathrm{p},k})^2}{2\sigma^2_{\mathrm{illum}}}} \end{aligned} \tag{2.S78}$$

$\frac{\partial E(x_{\mathrm{M},j} - \theta_x, \Delta x_{\mathrm{M}}, \sigma^2_{\mathrm{PSF}})}{\partial \theta_x}$ remains unchanged from Eq. (2.S68).

Derivative with respect to y-position (multiple pattern)

$$\begin{aligned} \frac{\partial \mu_{i,k}}{\partial \theta_y} &= A\theta_I \frac{\partial P(\theta_x - x_{\mathrm{p},k}, \theta_y - y_{\mathrm{p},k})}{\partial \theta_y} \\ &\cdot \sum_{(x_{\mathrm{M},j}, y_{\mathrm{M},j}) \in (S_{\mathrm{c},i} \cap \tilde{S}_{\mathrm{p},k})} E(x_{\mathrm{M},j} - \theta_x, \Delta x_{\mathrm{M}}, \sigma^2_{\mathrm{PSF}}) E(y_{\mathrm{M},j} - \theta_y, \Delta y_{\mathrm{M}}, \sigma^2_{\mathrm{PSF}}) \\ &+ A\theta_I P(\theta_x - x_{\mathrm{p},k}, \theta_y - y_{\mathrm{p},k}) \\ &\cdot \sum_{(x_{\mathrm{M},j}, y_{\mathrm{M},j}) \in (S_{\mathrm{c},i} \cap \tilde{S}_{\mathrm{p},k})} E(x_{\mathrm{M},j} - \theta_x, \Delta x_{\mathrm{M}}, \sigma^2_{\mathrm{PSF}}) \frac{\partial E(y_{\mathrm{M},j} - \theta_y, \Delta y_{\mathrm{M}}, \sigma^2_{\mathrm{PSF}})}{\partial \theta_y} \end{aligned} \tag{2.S79}$$

Here, $\frac{\partial P(\theta_x - x_{\mathrm{p},k}, \theta_y - y_{\mathrm{p},k})}{\partial \theta_y}$ is as follows:

$$\frac{\partial P_{\mathrm{Gaussian}}(\theta_x - x_{\mathrm{p},k}, \theta_y - y_{\mathrm{p},k})}{\partial \theta_y} = \left(\frac{y_{\mathrm{p},k} - \theta_y}{\sigma^2_{\mathrm{illum}}} \right) e^{\frac{-(\theta_x - x_{\mathrm{p},k})^2 - (\theta_y - y_{\mathrm{p},k})^2}{2\sigma^2_{\mathrm{illum}}}} \tag{2.S80}$$

$$\begin{aligned} \frac{\partial P_{\mathrm{donut}}(\theta_x - x_{\mathrm{p},k}, \theta_y - y_{\mathrm{p},k})}{\partial \theta_y} &= e \left(\frac{\theta_y - y_{\mathrm{p},k}}{\sigma^2_{\mathrm{illum}}} \right) e^{\frac{-(\theta_x - x_{\mathrm{p},k})^2 - (\theta_y - y_{\mathrm{p},k})^2}{2\sigma^2_{\mathrm{illum}}}} + e \left(\frac{y_{\mathrm{p},k} - \theta_y}{\sigma^2_{\mathrm{illum}}} \right) \\ &\cdot \left(\frac{(\theta_x - x_{\mathrm{p},k})^2 + (\theta_y - y_{\mathrm{p},k})^2}{2\sigma^2_{\mathrm{illum}}} \right) e^{\frac{-(\theta_x - x_{\mathrm{p},k})^2 - (\theta_y - y_{\mathrm{p},k})^2}{2\sigma^2_{\mathrm{illum}}}} \end{aligned} \tag{2.S81}$$

$\frac{\partial E(y_{\mathrm{M},j} - \theta_y, \Delta y_{\mathrm{M}}, \sigma^2_{\mathrm{PSF}})}{\partial \theta_y}$ remains unchanged from Eq. (2.S72).

Derivative with respect to expected signal photon count (multiple pattern)

$$\begin{aligned} \frac{\partial \mu_{i,k}}{\partial \theta_I} &= AP(\theta_x - x_{\mathrm{p},k}, \theta_y - y_{\mathrm{p},k}) \\ &\cdot \sum_{(x_{\mathrm{M},j}, y_{\mathrm{M},j}) \in (S_{\mathrm{c},i} \cap \tilde{S}_{\mathrm{p},k})} E(x_{\mathrm{M},j} - \theta_x, \Delta x_{\mathrm{M}}, \sigma^2_{\mathrm{PSF}}) E(y_{\mathrm{M},j} - \theta_y, \Delta y_{\mathrm{M}}, \sigma^2_{\mathrm{PSF}}) \end{aligned} \tag{2.S82}$$

Derivative with respect to expected background count (multiple pattern)

$$\frac{\partial \mu_{i,k}}{\partial \theta_b} = AB_{i,k} \tag{2.S83}$$

$$= 2\pi\sigma^2_{\text{illum}} A \cdot \sum_{(x_{\text{M},j}, y_{\text{M},j}) \in \left(S_{\text{c},i} \cap \tilde{S}_{\text{p},k}\right)} E\left(x_{\text{M},j} - x_{\text{p},k}, \Delta x_{\text{M}}, \sigma^2_{\text{PSF}} + \sigma^2_{\text{illum}}\right) E\left(y_{\text{M},j} - y_{\text{p},k}, \Delta y_{\text{M}}, \sigma^2_{\text{PSF}} + \sigma^2_{\text{illum}}\right) \tag{2.S84}$$

2.S5. Supporting figures and tables

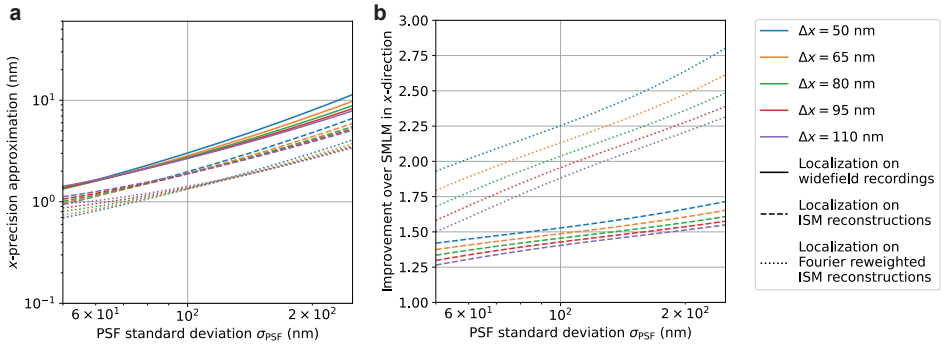

Figure 2.S1: Approximation of the theoretical minimum localization uncertainty of SMLM reconstructions acquired from (Fourier reweighted) ISM. For this simulation, 2000 expected signal photons and 8 expected background photons per pixel were used. (*a*) Approximate CRLB in the x-direction as a function of the PSF standard deviation for varying camera pixel sizes. (*b*) Improvement of the approximate CRLB over SMLM as a function of the PSF standard deviation for varying camera pixel sizes.

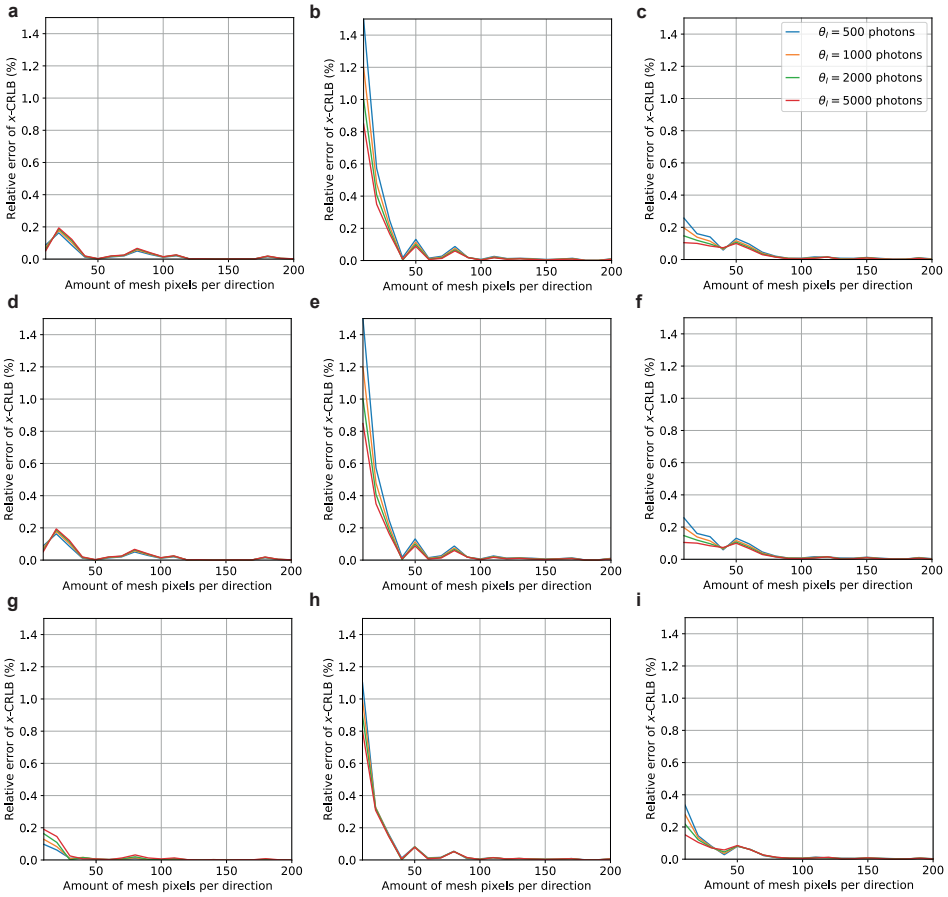

Figure 2.S2: Relative error in the x-CRLB resulting from the discretized pinhole approximation as a function of the amount of mesh pixels $N_{\mathrm{M},x}, N_{\mathrm{M},y}$ in each direction. To determine the error, the CRLB approximation for a fine-mesh pinhole approximation with $N_{\mathrm{M},x}, N_{\mathrm{M},y} = 1000$ mesh pixels was assumed as the ground truth. $\theta_b = 8$ expected background photons per pixel were used and the expected signal photon count θ_I is varied. (*a*)-(*c*) Relative errors for the scenario where the entire signal photon budget is exhausted after illumination with all patterns (disregarding signal photons blocked by the spinning disk). (*d*)-(*f*) Relative errors for the scenario where the illumination power and time are constant during illumination with all patterns. (*g*)-(*i*) Relative errors for the scenario where the entire signal photon budget is exhausted after illumination with all patterns (disregarding signal photons blocked by the spinning disk), neglecting the effects of pattern-dependent background. (*a*), (*d*), (*g*) Relative errors for the one-pattern configuration, with pinhole radius $r_{\mathrm{p}} = 3\sigma_{\mathrm{PSF}}$ and pinhole position $(x_{\mathrm{p}}, y_{\mathrm{p}}) = (\theta_x, \theta_y)$. (*b*), (*e*), (*h*) Relative errors for the two-pattern configuration, separated in x, with pinhole radius $r_{\mathrm{p}} = 3\sigma_{\mathrm{PSF}}$, pinhole separation $s = 4\sigma_{\mathrm{PSF}}$ and focus position $(x_{\mathrm{f}}, y_{\mathrm{f}}) = (\theta_x, \theta_y)$. (*c*), (*f*), (*g*) Relative errors for the non-rotated equilateral triangle pattern configuration, with pinhole radius $r_{\mathrm{p}} = 3\sigma_{\mathrm{PSF}}$, pinhole spacing $r = 2\sigma_{\mathrm{PSF}}$ and focus position $(x_{\mathrm{f}}, y_{\mathrm{f}}) = (\theta_x, \theta_y)$.

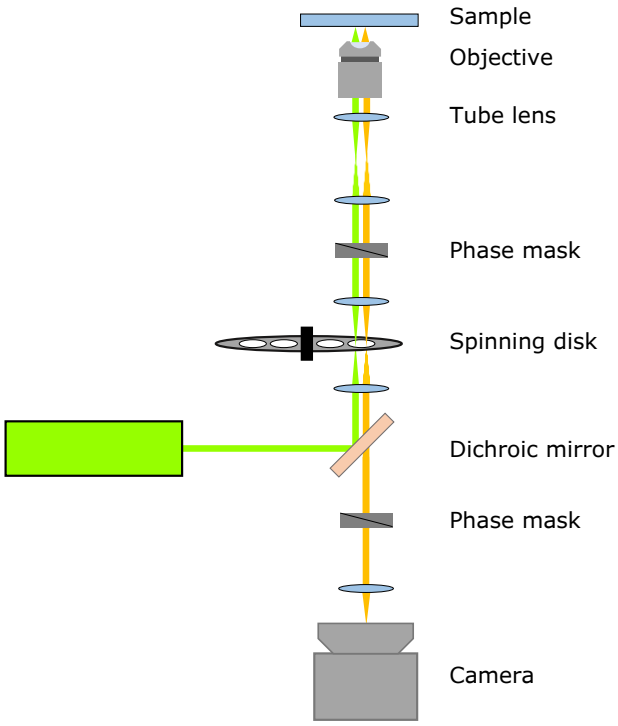

Figure 2.S3: Schematic overview of SpinFlux image formation with donut-shaped illumination patterns. A spinning disk is placed in the illumination- and emission paths. This causes patterned illumination of emitters in the sample and subsequent windowing of the emission signal. Rapidly switching the laser on and off causes stroboscopic illumination of emitters in the sample with stationary illumination patterns. A phase mask in the illumination path modulates the illumination pattern into a donut-shaped beam. As the emission path also passes through the phase mask, the emission signal is demodulated using an additional phase mask in the emission path.

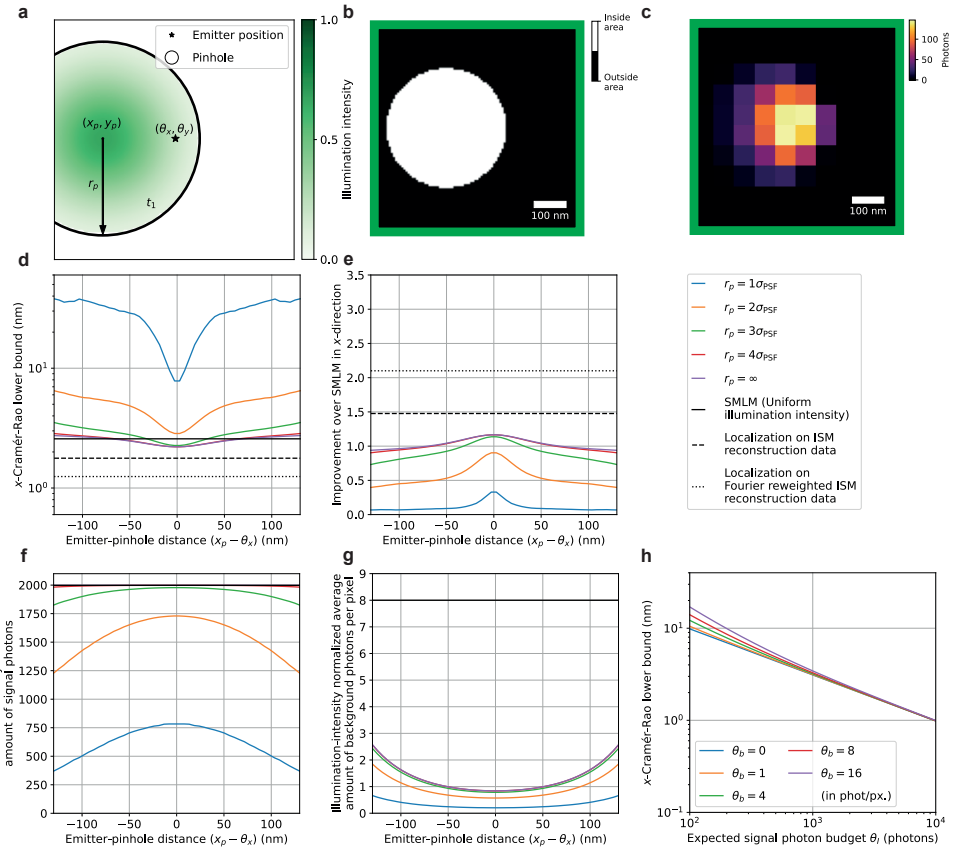

Figure 2.S4: Theoretical minimum localization uncertainty of SpinFlux localization with one x-offset pinhole and pattern. In (*c*)-(*g*), 2000 expected signal photons and 8 expected background photons per pixel were used. Results are evaluated for the scenario where the entire signal photon budget is exhausted after illumination with the pattern (disregarding signal photons blocked by the spinning disk). (*a*) Schematic overview of SpinFlux localization with one pinhole with radius r_p, centred at coordinates $(x_\mathrm{p}, y_\mathrm{p})$. In (*d*)-(*g*), the x-distance $(x_\mathrm{p} - \theta_x)$ between the pinhole and the emitter is varied, where $y_\mathrm{p} = \theta_y$. (*b*) Example of pinhole in the region of interest (650 × 650 nm). The pinhole radius $r_\mathrm{p} = 2\sigma_\mathrm{PSF}$ was used. The pinhole mask was discretized with $N_{\mathrm{M},x}$, $N_{\mathrm{M},y} = 100$ mesh pixels in each direction. (*c*) Example of fluorescent response in the region of interest, resulting from illumination and emission through the pinhole in (*b*). (*d*) CRLB in the x-direction as a function of the emitter-pinhole x-distance. Simulations show SpinFlux with varying pinhole sizes and widefield SMLM. (*e*) Improvement of the SpinFlux CRLB over SMLM as a function of the emitter-pinhole x-distance for varying pinhole sizes. (*f*) Average amount of signal photons after compensation for non-maximum illumination intensity as a function of the emitter-pinhole x-distance, for SpinFlux with varying pinhole sizes and widefield SMLM. (*g*) Average amount of background photons per pixel after compensation for non-maximum illumination intensity as a function of the emitter-pinhole x-distance, for SpinFlux with varying pinhole sizes and widefield SMLM. (*h*) CRLB in the x-direction as a function of the expected signal photon count for varying values of the expected background photon count. The pinhole radius $r_\mathrm{p} = 3\sigma_\mathrm{PSF}$ was used and $(x_\mathrm{p}, y_\mathrm{p}) = (\theta_x, \theta_y)$.

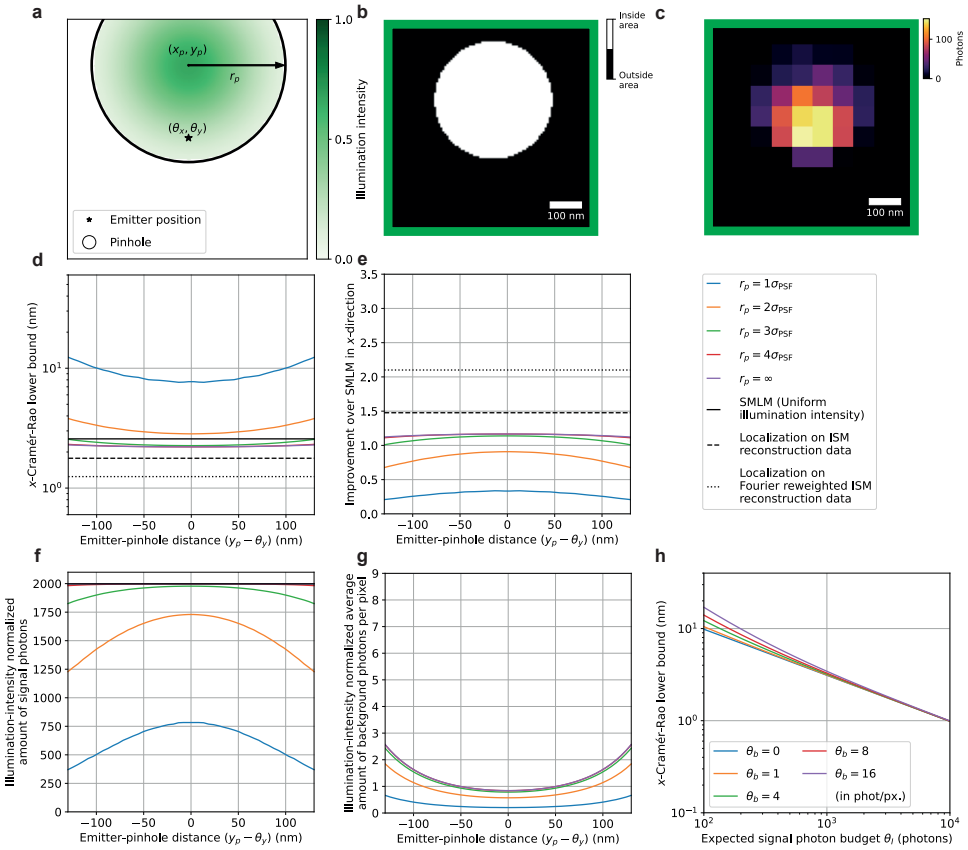

Figure 2.S5: Theoretical minimum localization uncertainty of SpinFlux localization with one y-offset pinhole and pattern. In (*c*)-(*g*), 2000 expected signal photons and 8 expected background photons per pixel were used. Results are evaluated for the scenario where the entire signal photon budget is exhausted after illumination with the pattern (disregarding signal photons blocked by the spinning disk). (*a*) Schematic overview of SpinFlux localization with one pinhole with radius r_p, centred at coordinates $(x_\mathrm{p}, y_\mathrm{p})$. In (*d*)-(*g*), the y-distance $(y_\mathrm{p} - \theta_y)$ between the pinhole and the emitter is varied, where $x_\mathrm{p} = \theta_x$. (*b*) Example of pinhole in the region of interest (650 × 650 nm). The pinhole radius $r_\mathrm{p} = 2\sigma_\mathrm{PSF}$ was used. The pinhole mask was discretized with $N_{\mathrm{M},x}$, $N_{\mathrm{M},y} = 100$ mesh pixels in each direction. (*c*) Example of fluorescent response in the region of interest, resulting from illumination and emission through the pinhole in (*b*). (*d*) CRLB in the x-direction as a function of the emitter-pinhole y-distance. Simulations show SpinFlux with varying pinhole sizes and widefield SMLM. (*e*) Improvement of the SpinFlux CRLB over SMLM as a function of the emitter-pinhole y-distance for varying pinhole sizes. (*f*) Average amount of signal photons after compensation for non-maximum illumination intensity as a function of the emitter-pinhole y-distance, for SpinFlux with varying pinhole sizes and widefield SMLM. (*g*) Average amount of background photons per pixel after compensation for non-maximum illumination intensity as a function of the emitter-pinhole y-distance, for SpinFlux with varying pinhole sizes and widefield SMLM. (*h*) CRLB in the x-direction as a function of the expected signal photon count for varying values of the expected background photon count. The pinhole radius $r_\mathrm{p} = 3\sigma_\mathrm{PSF}$ was used and $(x_\mathrm{p}, y_\mathrm{p}) = (\theta_x, \theta_y)$.

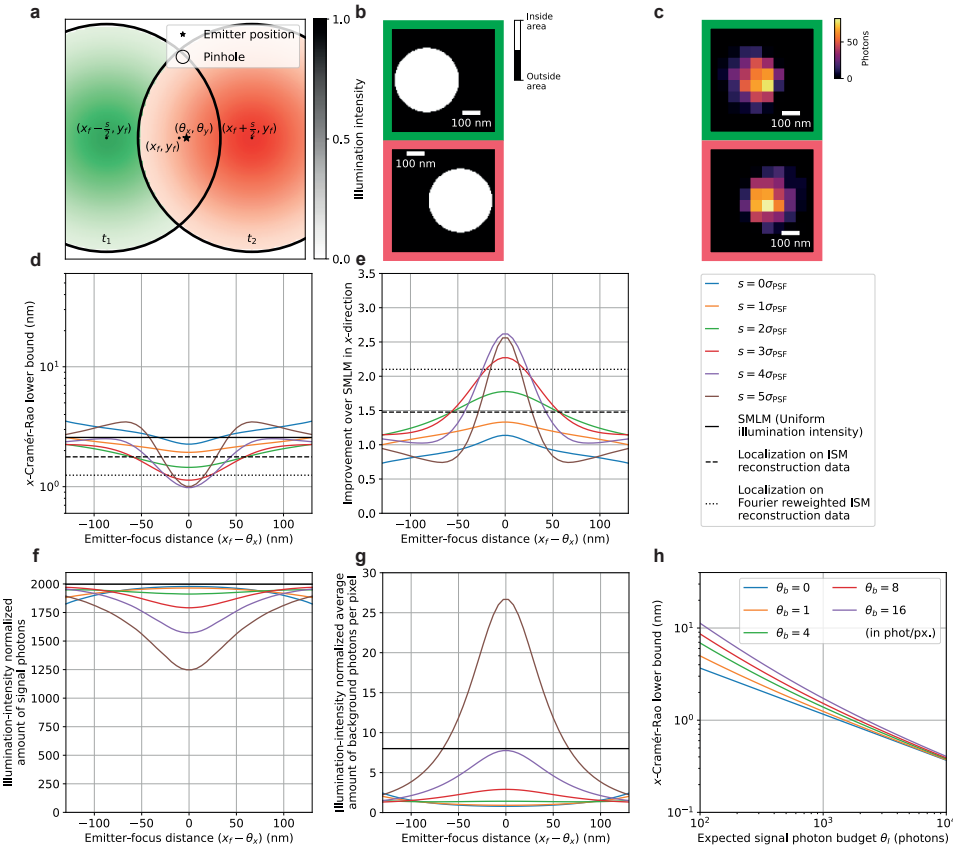

Figure 2.S6: Theoretical minimum localization uncertainty of SpinFlux localization with two pinholes and patterns separated in the x-direction. In (*c*)-(*g*), 2000 expected signal photons and 8 expected background photons per pixel were used, with pinhole radius $r_p = 3\sigma_{PSF}$. Results are evaluated for the scenario where the entire signal photon budget is exhausted after illumination with all patterns (disregarding signal photons blocked by the spinning disk). (*a*) Schematic overview of SpinFlux localization with two pinholes, separated in x and centred around the focus coordinates (x_f, y_f). In (*d*)-(*g*), the x-distance $(x_f - \theta_x)$ between the pattern focus and the emitter is varied, where $y_f = \theta_y$. (*b*) Example of pinholes in the region of interest (650 × 650 nm). The pinhole radius $r_p = 2\sigma_{PSF}$ and pinhole separation $s = 2\sigma_{PSF}$ were used. The pinhole masks were discretized with $N_{M,x}$, $N_{M,y} = 100$ mesh pixels in each direction. (*c*) Example of fluorescent response in the region of interest, resulting from illumination and emission through each pinhole in (*b*). (*d*) CRLB in the x-direction as a function of the emitter-focus x-distance. Simulations show SpinFlux with varying pinhole separations and widefield SMLM. (*e*) Improvement of the SpinFlux CRLB over SMLM as a function of the emitter-focus x-distance for varying pinhole separations. (*f*) Average amount of signal photons after compensation for non-maximum illumination intensity as a function of the emitter-focus x-distance, for SpinFlux with varying pinhole separations and widefield SMLM. (*g*) Average amount of background photons per pixel after compensation for non-maximum illumination intensity as a function of the emitter-focus x-distance, for SpinFlux with varying pinhole separations and widefield SMLM. (*h*) CRLB in the x-direction as a function of expected signal photon count for varying values of the expected background photon count. The pinhole radius $r_p = 3\sigma_{PSF}$ and pinhole separation $s = 4\sigma_{PSF}$ were used and $(x_f, y_f) = (\theta_x, \theta_y)$.

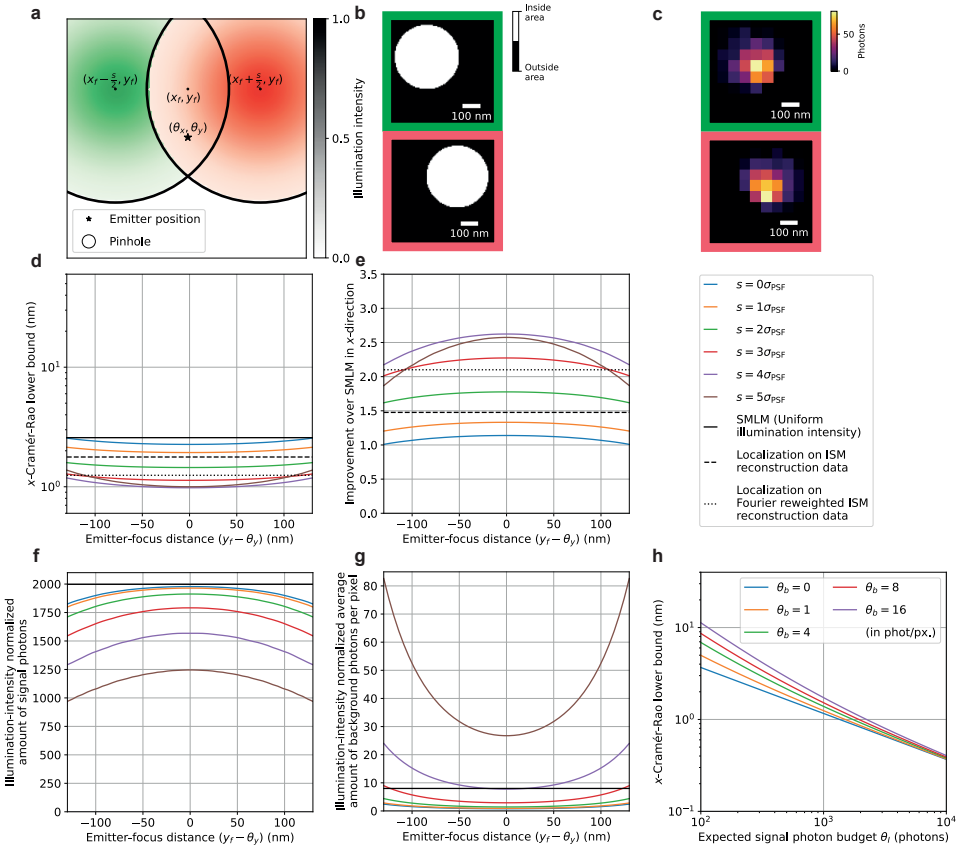

Figure 2.S7: Theoretical minimum localization uncertainty of SpinFlux localization with two y-offset pinholes and patterns separated in the x-direction. In (*c*)-(*g*), 2000 expected signal photons and 8 expected background photons per pixel were used, with pinhole radius $r_\mathrm{p} = 3\sigma_\mathrm{PSF}$. Results are evaluated for the scenario where the entire signal photon budget is exhausted after illumination with all patterns (disregarding signal photons blocked by the spinning disk). (*a*) Schematic overview of SpinFlux localization with two pinholes, separated in x and centred around the focus coordinates $(x_\mathrm{f}, y_\mathrm{f})$. In (*d*)-(*g*), the y-distance $(y_\mathrm{f} - \theta_y)$ between the pattern focus and the emitter is varied, where $x_\mathrm{f} = \theta_x$. (*b*) Example of pinholes in the region of interest (650 × 650 nm). The pinhole radius $r_\mathrm{p} = 2\sigma_\mathrm{PSF}$ and pinhole separation $s = 2\sigma_\mathrm{PSF}$ were used. The pinhole masks were discretized with $N_{\mathrm{M},x}$, $N_{\mathrm{M},y} = 100$ mesh pixels in each direction. (*c*) Example of fluorescent response in the region of interest, resulting from illumination and emission through each pinhole in (*b*). (*d*) CRLB in the x-direction as a function of the emitter-focus y-distance. Simulations show SpinFlux with varying pinhole separations and widefield SMLM. (*e*) Improvement of the SpinFlux CRLB over SMLM as a function of the emitter-focus y-distance for varying pinhole separations. (*f*) Average amount of signal photons after compensation for non-maximum illumination intensity as a function of the emitter-focus y-distance, for SpinFlux with varying pinhole separations and widefield SMLM. (*g*) Average amount of background photons per pixel after compensation for non-maximum illumination intensity as a function of the emitter-focus y-distance, for SpinFlux with varying pinhole separations and widefield SMLM. (*h*) CRLB in the x-direction as a function of expected signal photon count for varying values of the expected background photon count. The pinhole radius $r_\mathrm{p} = 3\sigma_\mathrm{PSF}$ and pinhole separation $s = 4\sigma_\mathrm{PSF}$ were used and $(x_\mathrm{f}, y_\mathrm{f}) = (\theta_x, \theta_y)$.

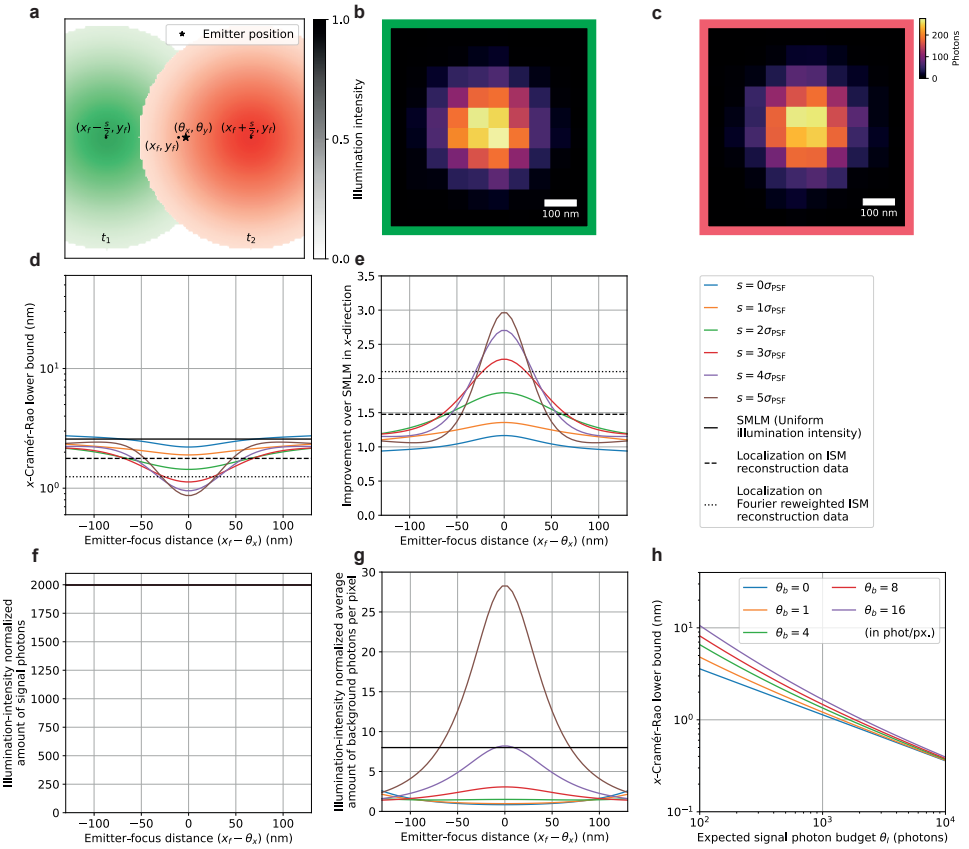

Figure 2.S8: Theoretical minimum localization uncertainty of SpinFlux localization with two patterns without pinholes separated in the x-direction. in (b)-(f), 2000 expected signal photons and 8 expected background photons per pixel were used. Results are evaluated for the scenario where the entire signal photon budget is exhausted after illumination with all patterns. (a) Schematic overview of SpinFlux localization with two pinholes, separated in x and centred around the focus coordinates (x_f, y_f). In (c)-(f), the x-distance $(x_f - \theta_x)$ between the pattern focus and the emitter is varied, where $y_f = \theta_y$. (b) Example of fluorescent response in the region of interest, resulting from illumination and emission by each pattern in (a). (c) CRLB in the x-direction as a function of the emitter-focus x-distance. Simulations show SpinFlux with varying pinhole separations and widefield SMLM. (d) Improvement of the SpinFlux CRLB over SMLM as a function of the emitter-focus x-distance for varying pinhole separations. (e) Average amount of signal photons after compensation for non-maximum illumination intensity as a function of the emitter-focus x-distance, for SpinFlux with varying pinhole separations and widefield SMLM. (f) Average amount of background photons per pixel after compensation for non-maximum illumination intensity as a function of the emitter-focus x-distance, for SpinFlux with varying pinhole separations and widefield SMLM. (g) CRLB in the x-direction as a function of expected signal photon count for varying values of the expected background photon count. The pattern separation $s = 4\sigma_{\mathrm{PSF}}$ was used and $(x_f, y_f) = (\theta_x, \theta_y)$.

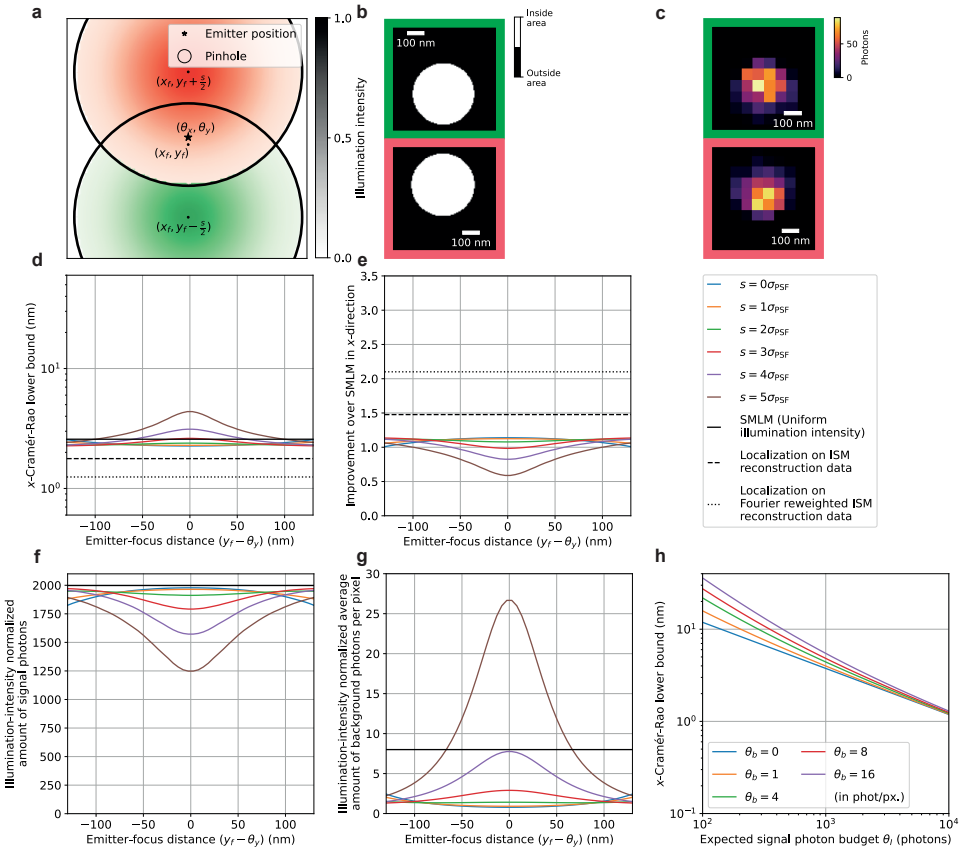

Figure 2.S9: Theoretical minimum localization uncertainty of SpinFlux localization with two pinholes and patterns separated in the y-direction. In (*c*)-(*g*), 2000 expected signal photons and 8 expected background photons per pixel were used, with pinhole radius $r_p = 3\sigma_{PSF}$. Results are evaluated for the scenario where the entire signal photon budget is exhausted after illumination with all patterns (disregarding signal photons blocked by the spinning disk). (*a*) Schematic overview of SpinFlux localization with two pinholes, separated in y and centred around the focus coordinates (x_f, y_f). In (*d*)-(*g*), the y-distance $(y_f - \theta_y)$ between the pattern focus and the emitter is varied, where $x_f = \theta_x$. (*b*) Example of pinholes in the region of interest (650 × 650 nm). The pinhole radius $r_p = 2\sigma_{PSF}$ and pinhole separation $s = 2\sigma_{PSF}$ were used. The pinhole masks were discretized with $N_{M,x}$, $N_{M,y} = 100$ mesh pixels in each direction. (*c*) Example of fluorescent response in the region of interest, resulting from illumination and emission through each pinhole in (*b*). (*d*) CRLB in the x-direction as a function of the emitter-focus y-distance. Simulations show SpinFlux with varying pinhole separations and widefield SMLM. (*e*) Improvement of the SpinFlux CRLB over SMLM as a function of the emitter-focus y-distance for varying pinhole separations. (*f*) Average amount of signal photons after compensation for non-maximum illumination intensity as a function of the emitter-focus y-distance, for SpinFlux with varying pinhole separations and widefield SMLM. (*g*) Average amount of background photons per pixel after compensation for non-maximum illumination intensity as a function of the emitter-focus y-distance, for SpinFlux with varying pinhole separations and widefield SMLM. (*h*) CRLB in the x-direction as a function of expected signal photon count for varying values of the expected background photon count. The pinhole radius $r_p = 3\sigma_{PSF}$ and pinhole separation $s = 4\sigma_{PSF}$ were used and $(x_f, y_f) = (\theta_x, \theta_y)$.

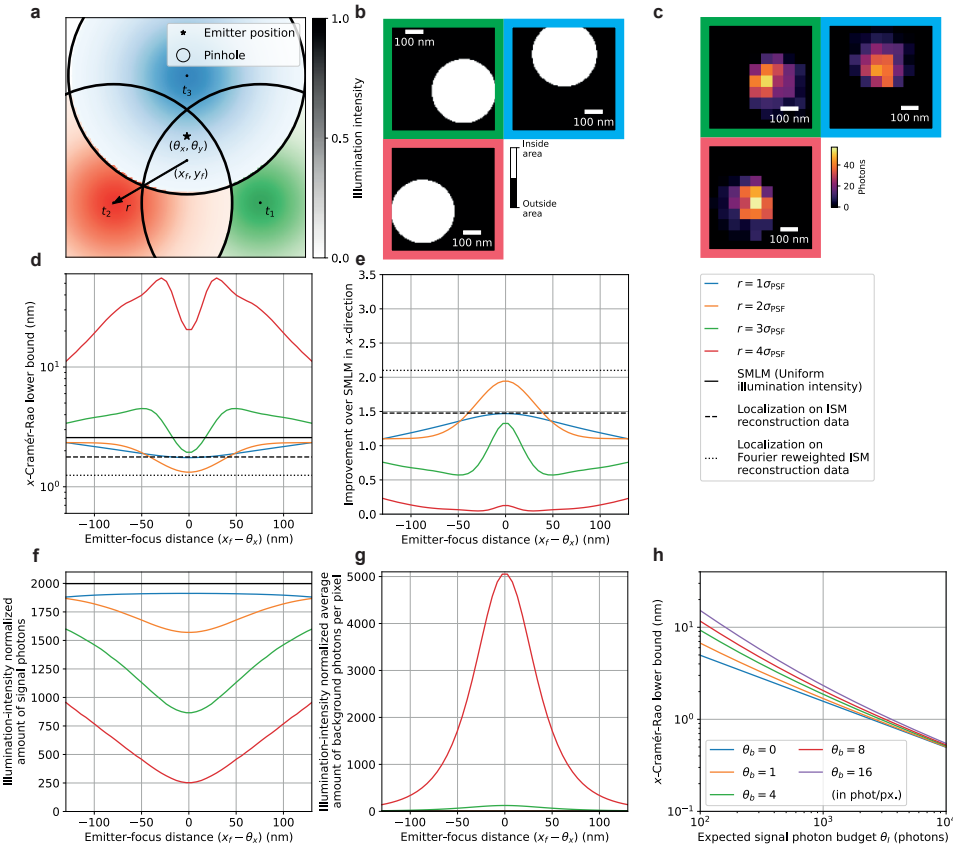

Figure 2.S10: Theoretical minimum localization uncertainty of SpinFlux localization with three pinholes and patterns in an equilateral triangle configuration. In (*c*)-(*g*), we used 2000 expected signal photons and 8 expected background photons per pixel, with pinhole radius $r_p = 3\sigma_{PSF}$. Results are evaluated for the scenario where the entire signal photon budget is exhausted after illumination with all patterns (disregarding signal photons blocked by the spinning disk). (*a*) Schematic overview of SpinFlux localization with a triangle of three pinholes, centred at focus coordinates (x_f, y_f). In (*d*)-(*g*), the x-distance $(x_f - \theta_x)$ between the pattern focus and the emitter is varied, where $y_f = \theta_y$. (*b*) Example of pinholes in the region of interest (650 × 650 nm). The pinhole radius $r_p = 2\sigma_{PSF}$ and pinhole spacing $r = 1.5\sigma_{PSF}$ were used. The pinhole masks were discretized with $N_{M,x}$, $N_{M,y} = 100$ mesh pixels in each direction. (*c*) Example of fluorescent response in the region of interest, resulting from illumination and emission through each pinhole in (*b*). (*d*) CRLB in the x-direction as a function of the emitter-focus x-distance. Simulations show SpinFlux with varying pinhole spacing and widefield SMLM. (*e*) Improvement of the SpinFlux CRLB over SMLM as a function of the emitter-focus x-distance for varying pinhole spacing. (*f*) Average amount of signal photons after compensation for non-maximum illumination intensity as a function of the emitter-focus x-distance, for SpinFlux with varying pinhole spacing and widefield SMLM. (*g*) Average amount of background photons per pixel after compensation for non-maximum illumination intensity as a function of the emitter-focus x-distance, for SpinFlux with varying pinhole spacing and widefield SMLM. (*h*) CRLB in the x-direction as a function of expected signal photon count for varying values of the expected background photon count. The pinhole radius $r_p = 3\sigma_{PSF}$ and pinhole spacing $r = 2\sigma_{PSF}$ were used and $(x_f, y_f) = (\theta_x, \theta_y)$.

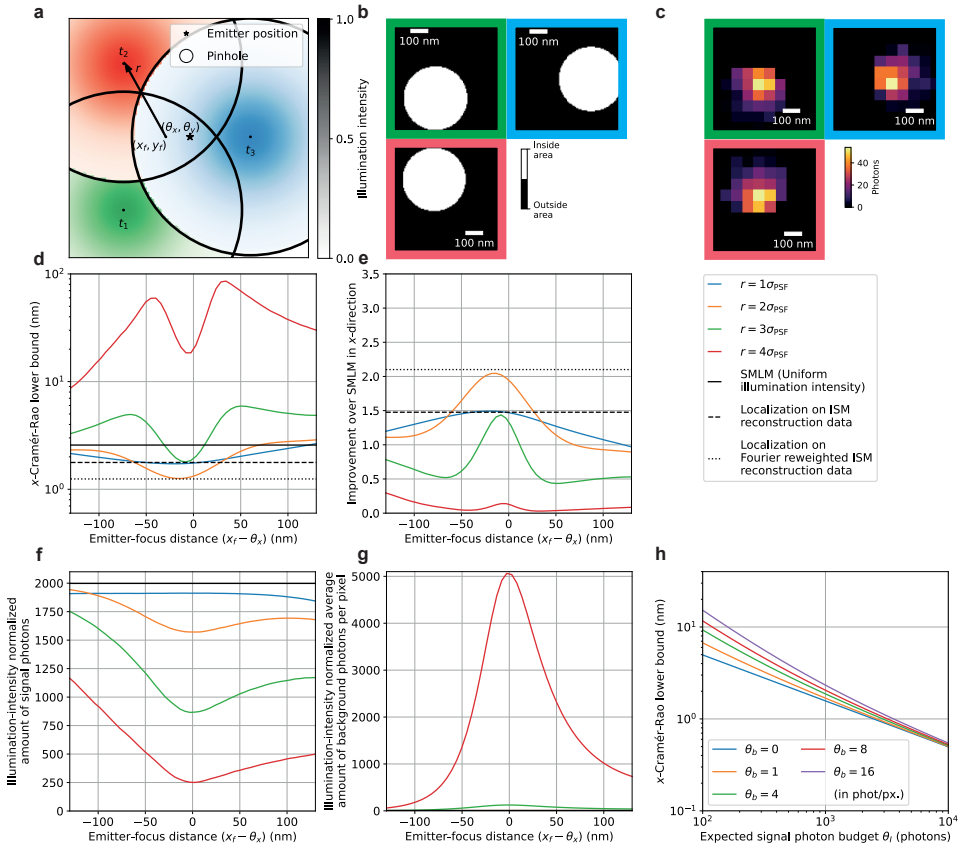

Figure 2.S11: Theoretical minimum localization uncertainty of SpinFlux localization with three pinholes and patterns in a 90° rotated equilateral triangle configuration. The pattern is rotated clockwise by 90 degrees with respect Fig. 2.S10. In (*c*)-(*g*), we used 2000 expected signal photons and 8 expected background photons per pixel, with pinhole radius $r_p = 3\sigma_{PSF}$. Results are evaluated for the scenario where the entire signal photon budget is exhausted after illumination with all patterns (disregarding signal photons blocked by the spinning disk). (*a*) Schematic overview of SpinFlux localization with a triangle of three pinholes, centred at focus coordinates (x_f, y_f). In (*d*)-(*g*), the x-distance $(x_f - \theta_x)$ between the pattern focus and the emitter is varied, where $y_f = \theta_y$. (*b*) Example of pinholes in the region of interest (650 × 650 nm). The pinhole radius $r_p = 2\sigma_{PSF}$ and pinhole spacing $r = 1.5\sigma_{PSF}$ were used. The pinhole masks were discretized with $N_{M,x}$, $N_{M,y} = 100$ mesh pixels in each direction. (*c*) Example of fluorescent response in the region of interest, resulting from illumination and emission through each pinhole in (*b*). (*d*) CRLB in the x-direction as a function of the emitter-focus x-distance. Simulations show SpinFlux with varying pinhole spacing and widefield SMLM. (*e*) Improvement of the SpinFlux CRLB over SMLM as a function of the emitter-focus x-distance for varying pinhole spacing. (*f*) Average amount of signal photons after compensation for non-maximum illumination intensity as a function of the emitter-focus x-distance, for SpinFlux with varying pinhole spacing and widefield SMLM. (*g*) Average amount of background photons per pixel after compensation for non-maximum illumination intensity as a function of the emitter-focus x-distance, for SpinFlux with varying pinhole spacing and widefield SMLM. (*h*) CRLB in the x-direction as a function of expected signal photon count for varying values of the expected background photon count. The pinhole radius $r_p = 3\sigma_{PSF}$ and pinhole spacing $r = 2\sigma_{PSF}$ were used and $(x_f, y_f) = (\theta_x, \theta_y)$.

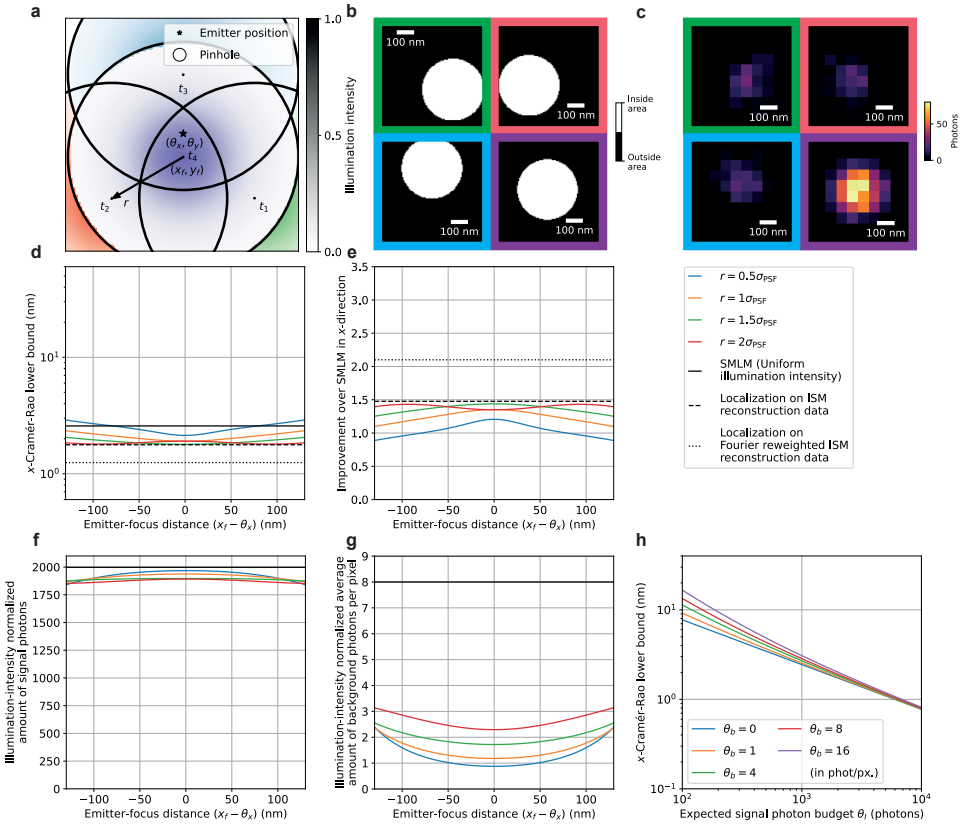

Figure 2.S12: Theoretical minimum localization uncertainty of SpinFlux localization with four pinholes and patterns in an equilateral triangle configuration with a centre pinhole. In (*c*)-(*g*), we used 2000 expected signal photons and 8 expected background photons per pixel, with pinhole radius $r_p = 3\sigma_{PSF}$. Results are evaluated for the scenario where the entire signal photon budget is exhausted after illumination with all patterns (disregarding signal photons blocked by the spinning disk). (*a*) Schematic overview of SpinFlux localization with a triangle of three pinholes with an additional centre pinhole, centred at focus coordinates (x_f, y_f). In (*d*)-(*g*), the x-distance $(x_f - \theta_x)$ between the pattern focus and the emitter is varied, where $y_f = \theta_y$. (*b*) Example of pinholes in the region of interest (650 × 650 nm). The pinhole radius $r_p = 2\sigma_{PSF}$ and pinhole spacing $r = 1.5\sigma_{PSF}$ were used. The pinhole masks were discretized with $N_{M,x}$, $N_{M,y} = 100$ mesh pixels in each direction. (*c*) Example of fluorescent response in the region of interest, resulting from illumination and emission through each pinhole in (*b*). (*d*) CRLB in the x-direction as a function of the emitter-focus x-distance. Simulations show SpinFlux with varying pinhole spacing and widefield SMLM. (*e*) Improvement of the SpinFlux CRLB over SMLM as a function of the emitter-focus x-distance for varying pinhole spacing. (*f*) Average amount of signal photons after compensation for non-maximum illumination intensity as a function of the emitter-focus x-distance, for SpinFlux with varying pinhole spacing and widefield SMLM. (*g*) Average amount of background photons per pixel after compensation for non-maximum illumination intensity as a function of the emitter-focus x-distance, for SpinFlux with varying pinhole spacing and widefield SMLM. (*h*) CRLB in the x-direction as a function of expected signal photon count for varying values of the expected background photon count. The pinhole radius $r_p = 3\sigma_{PSF}$ and pinhole spacing $r = 2\sigma_{PSF}$ were used and $(x_f, y_f) = (\theta_x, \theta_y)$.

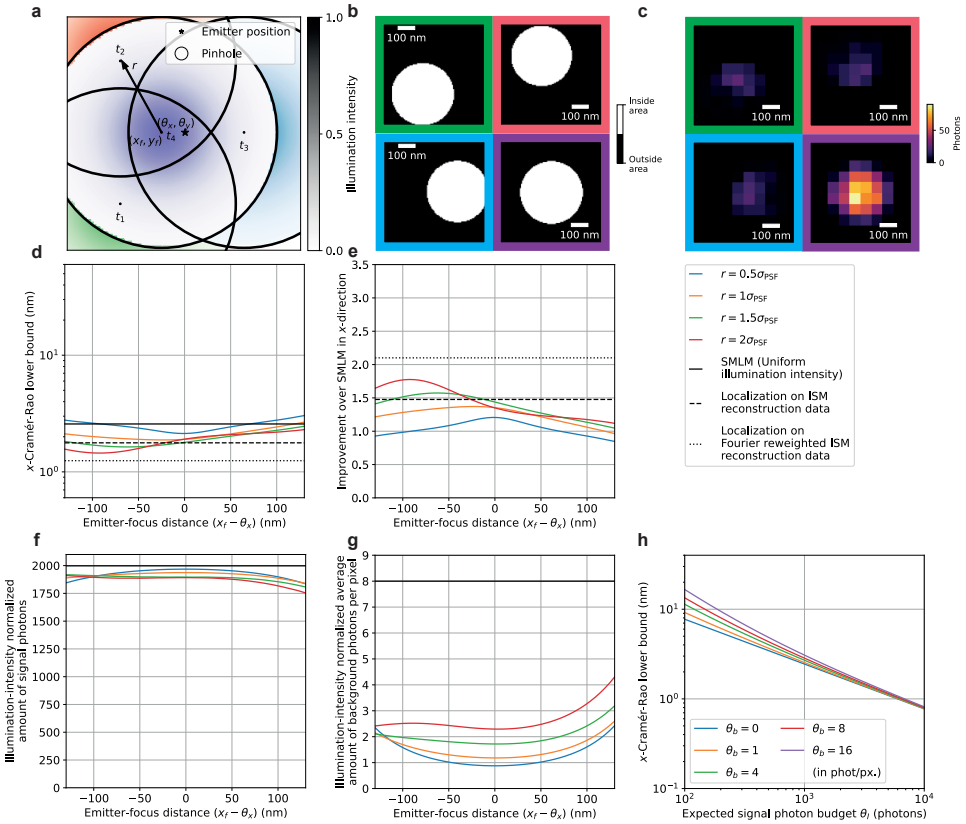

Figure 2.S13: Theoretical minimum localization uncertainty of SpinFlux localization with four pinholes and patterns in a 90° rotated equilateral triangle configuration with a centre pinhole. The pattern is rotated clockwise by 90 degrees with respect to Fig. 2.S12. In (*c*)-(*g*), we used 2000 expected signal photons and 8 expected background photons per pixel, with pinhole radius $r_p = 3\sigma_{PSF}$. Results are evaluated for the scenario where the entire signal photon budget is exhausted after illumination with all patterns (disregarding signal photons blocked by the spinning disk). (*a*) Schematic overview of SpinFlux localization with a triangle of three pinholes with an additional centre pinhole, centred at focus coordinates (x_f, y_f). In (*d*)-(*g*), the *x*-distance $(x_f - \theta_x)$ between the pattern focus and the emitter is varied, where $y_f = \theta_y$. (*b*) Example of pinholes in the region of interest (650 × 650 nm). The pinhole radius $r_p = 2\sigma_{PSF}$ and pinhole spacing $r = 1.5\sigma_{PSF}$ were used. The pinhole masks were discretized with $N_{M,x}$, $N_{M,y} = 100$ mesh pixels in each direction. (*c*) Example of fluorescent response in the region of interest, resulting from illumination and emission through each pinhole in (*b*). (*d*) CRLB in the *x*-direction as a function of the emitter-focus *x*-distance. Simulations show SpinFlux with varying pinhole spacing and widefield SMLM. (*e*) Improvement of the SpinFlux CRLB over SMLM as a function of the emitter-focus *x*-distance for varying pinhole spacing. (*f*) Average amount of signal photons after compensation for non-maximum illumination intensity as a function of the emitter-focus *x*-distance, for SpinFlux with varying pinhole spacing and widefield SMLM. (*g*) Average amount of background photons per pixel after compensation for non-maximum illumination intensity as a function of the emitter-focus *x*-distance, for SpinFlux with varying pinhole spacing and widefield SMLM. (*h*) CRLB in the *x*-direction as a function of expected signal photon count for varying values of the expected background photon count. The pinhole radius $r_p = 3\sigma_{PSF}$ and pinhole spacing $r = 2\sigma_{PSF}$ were used and $(x_f, y_f) = (\theta_x, \theta_y)$.

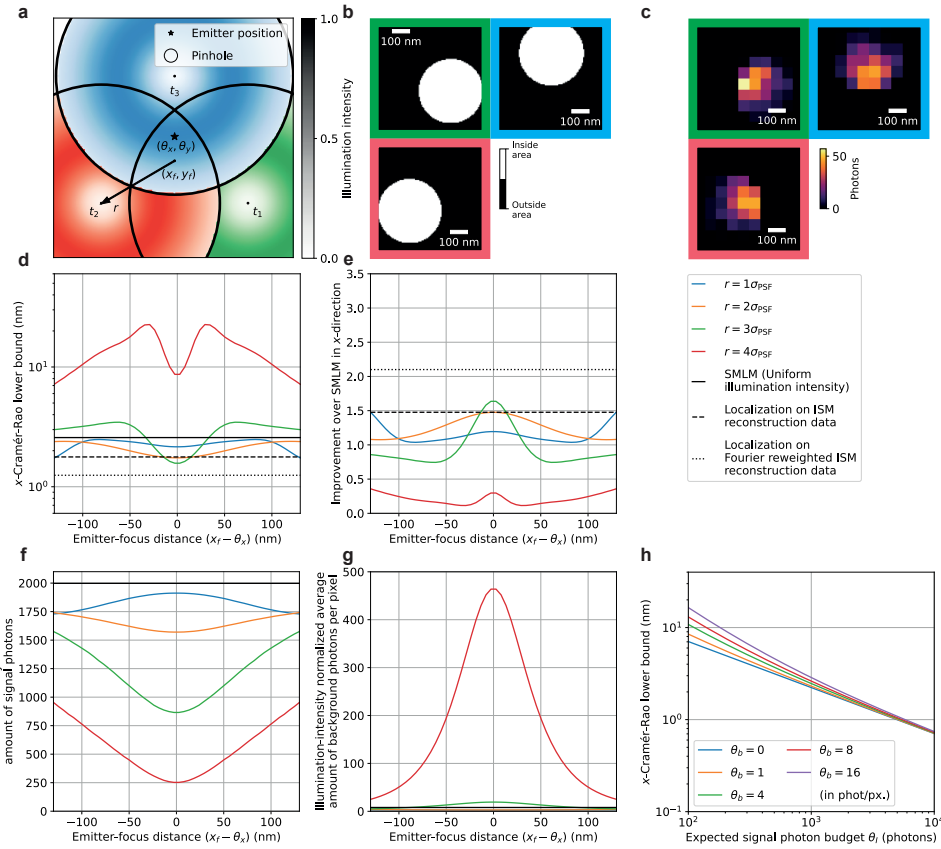

Figure 2.S14: Theoretical minimum localization uncertainty of SpinFlux localization with three pinholes and donut-shaped patterns in an equilateral triangle configuration. In (*c*)-(*g*), we used 2000 expected signal photons and 8 expected background photons per pixel, with pinhole radius $r_p = 3\sigma_{PSF}$. Results are evaluated for the scenario where the entire signal photon budget is exhausted after illumination with all patterns (disregarding signal photons blocked by the spinning disk). (*a*) Schematic overview of SpinFlux localization with a triangle of three pinholes, centred at focus coordinates (x_f, y_f). In (*d*)-(*g*), the x-distance $(x_f - \theta_x)$ between the pattern focus and the emitter is varied, where $y_f = \theta_y$. (*b*) Example of pinholes in the region of interest (650 × 650 nm). The pinhole radius $r_p = 2\sigma_{PSF}$ and pinhole spacing $r = 1.5\sigma_{PSF}$ were used. The pinhole masks were discretized with $N_{M,x}$, $N_{M,y} = 100$ mesh pixels in each direction. (*c*) Example of fluorescent response in the region of interest, resulting from illumination and emission through each pinhole in (*b*). (*d*) CRLB in the x-direction as a function of the emitter-focus x-distance. Simulations show SpinFlux with varying pinhole spacing and widefield SMLM. (*e*) Improvement of the SpinFlux CRLB over SMLM as a function of the emitter-focus x-distance for varying pinhole spacing. (*f*) Average amount of signal photons after compensation for non-maximum illumination intensity as a function of the emitter-focus x-distance, for SpinFlux with varying pinhole spacing and widefield SMLM. (*g*) Average amount of background photons per pixel after compensation for non-maximum illumination intensity as a function of the emitter-focus x-distance, for SpinFlux with varying pinhole spacing and widefield SMLM. (*h*) CRLB in the x-direction as a function of expected signal photon count for varying values of the expected background photon count. The pinhole radius $r_p = 3\sigma_{PSF}$ and pinhole spacing $r = 2\sigma_{PSF}$ were used and $(x_f, y_f) = (\theta_x, \theta_y)$.

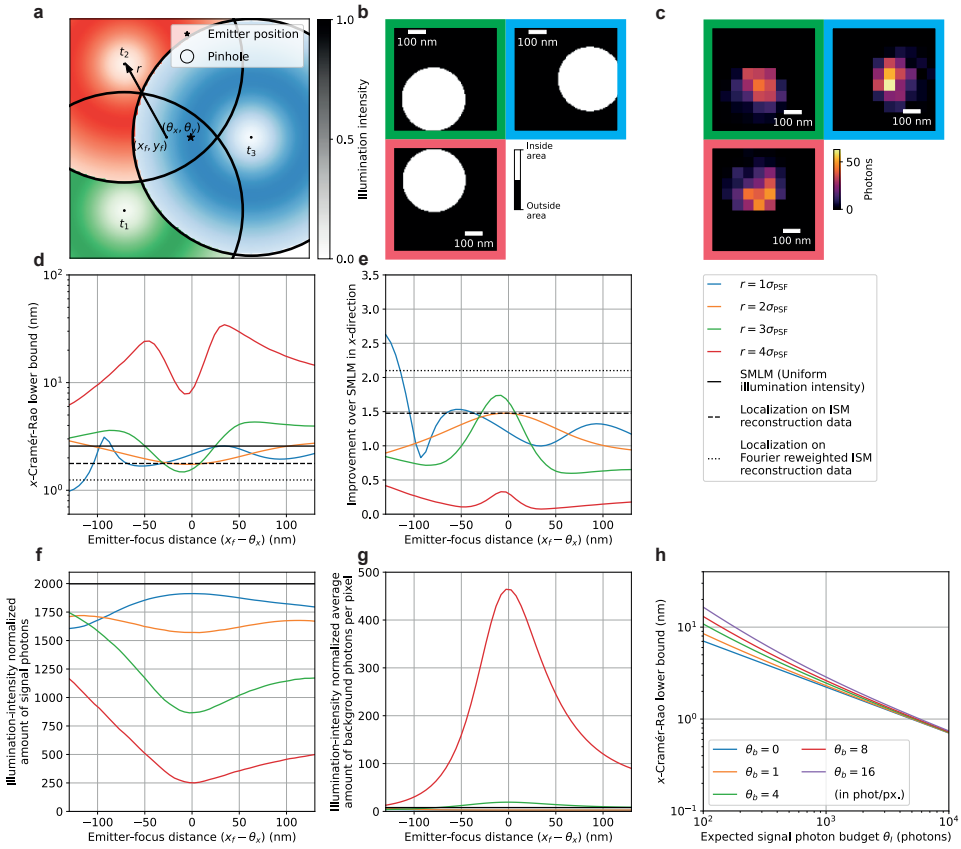

Figure 2.S15: Theoretical minimum localization uncertainty of SpinFlux localization with three pinholes and donut-shaped patterns in a 90° rotated equilateral triangle configuration. The pattern is rotated clockwise by 90 degrees with respect to Fig. 2.4. In (*c*)-(*g*), we used 2000 expected signal photons and 8 expected background photons per pixel, with pinhole radius $r_p = 3\sigma_{PSF}$. Results are evaluated for the scenario where the entire signal photon budget is exhausted after illumination with all patterns (disregarding signal photons blocked by the spinning disk). (*a*) Schematic overview of SpinFlux localization with a triangle of three pinholes, centred at focus coordinates (x_f, y_f). In (*d*)-(*g*), the x-distance $(x_f - \theta_x)$ between the pattern focus and the emitter is varied, where $y_f = \theta_y$. (*b*) Example of pinholes in the region of interest (650 × 650 nm). The pinhole radius $r_p = 2\sigma_{PSF}$ and pinhole spacing $r = 1.5\sigma_{PSF}$ were used. The pinhole masks were discretized with $N_{M,x}$, $N_{M,y} = 100$ mesh pixels in each direction. (*c*) Example of fluorescent response in the region of interest, resulting from illumination and emission through each pinhole in (*b*). (*d*) CRLB in the x-direction as a function of the emitter-focus x-distance. Simulations show SpinFlux with varying pinhole spacing and widefield SMLM. (*e*) Improvement of the SpinFlux CRLB over SMLM as a function of the emitter-focus x-distance for varying pinhole spacing. (*f*) Average amount of signal photons after compensation for non-maximum illumination intensity as a function of the emitter-focus x-distance, for SpinFlux with varying pinhole spacing and widefield SMLM. (*g*) Average amount of background photons per pixel after compensation for non-maximum illumination intensity as a function of the emitter-focus x-distance, for SpinFlux with varying pinhole spacing and widefield SMLM. (*h*) CRLB in the x-direction as a function of expected signal photon count for varying values of the expected background photon count. The pinhole radius $r_p = 3\sigma_{PSF}$ and pinhole spacing $r = 2\sigma_{PSF}$ were used and $(x_f, y_f) = (\theta_x, \theta_y)$.

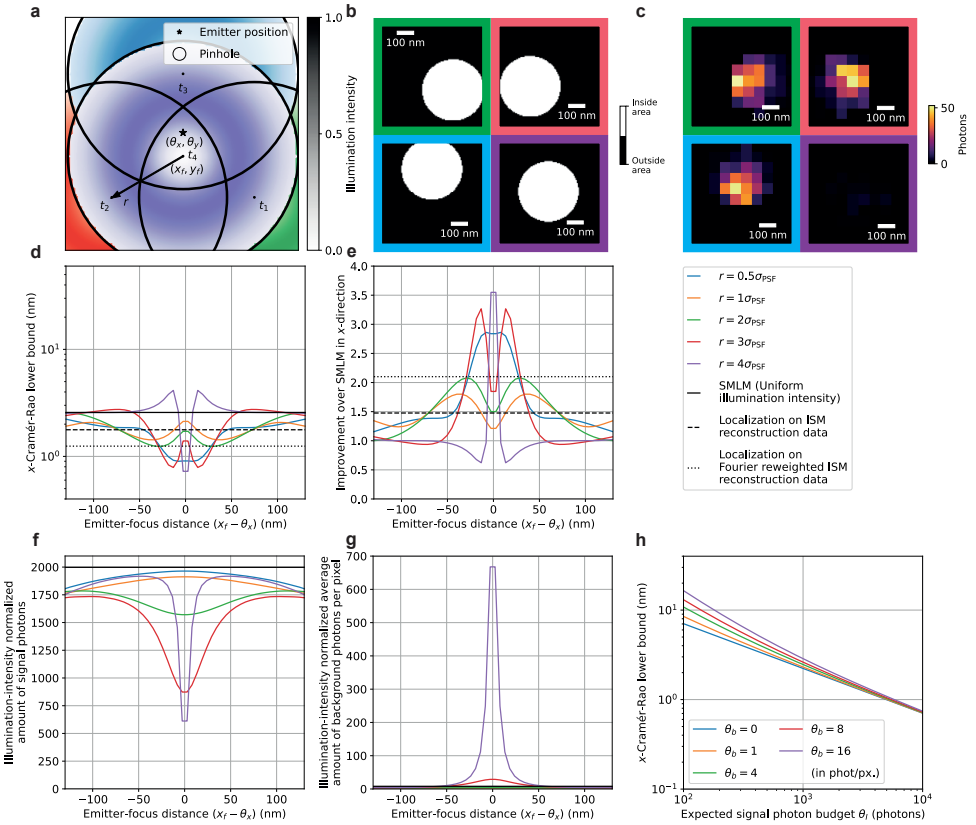

Figure 2.S16: Theoretical minimum localization uncertainty of SpinFlux localization with four pinholes and donut-shaped patterns in an equilateral triangle configuration with a centre pinhole. In (*c*)-(*g*), we used 2000 expected signal photons and 8 expected background photons per pixel, with pinhole radius $r_p = 3\sigma_{PSF}$. Results are evaluated for the scenario where the entire signal photon budget is exhausted after illumination with all patterns (disregarding signal photons blocked by the spinning disk). (*a*) Schematic overview of SpinFlux localization with a triangle of three pinholes with an additional centre pinhole, centred at focus coordinates (x_f, y_f). In (*d*)-(*g*), the *x*-distance $(x_f - \theta_x)$ between the pattern focus and the emitter is varied, where $y_f = \theta_y$. (*b*) Example of pinholes in the region of interest (650 × 650 nm). The pinhole radius $r_p = 2\sigma_{PSF}$ and pinhole spacing $r = 1.5\sigma_{PSF}$ were used. The pinhole masks were discretized with $N_{M,x}$, $N_{M,y} = 100$ mesh pixels in each direction. (*c*) Example of fluorescent response in the region of interest, resulting from illumination and emission through each pinhole in (*b*). (*d*) CRLB in the *x*-direction as a function of the emitter-focus *x*-distance. Simulations show SpinFlux with varying pinhole spacing and widefield SMLM. (*e*) Improvement of the SpinFlux CRLB over SMLM as a function of the emitter-focus *x*-distance for varying pinhole spacing. (*f*) Average amount of signal photons after compensation for non-maximum illumination intensity as a function of the emitter-focus *x*-distance, for SpinFlux with varying pinhole spacing and widefield SMLM. (*g*) Average amount of background photons per pixel after compensation for non-maximum illumination intensity as a function of the emitter-focus *x*-distance, for SpinFlux with varying pinhole spacing and widefield SMLM. (*h*) CRLB in the *x*-direction as a function of expected signal photon count for varying values of the expected background photon count. The pinhole radius $r_p = 3\sigma_{PSF}$ and pinhole spacing $r = 2\sigma_{PSF}$ were used and $(x_f, y_f) = (\theta_x, \theta_y)$.

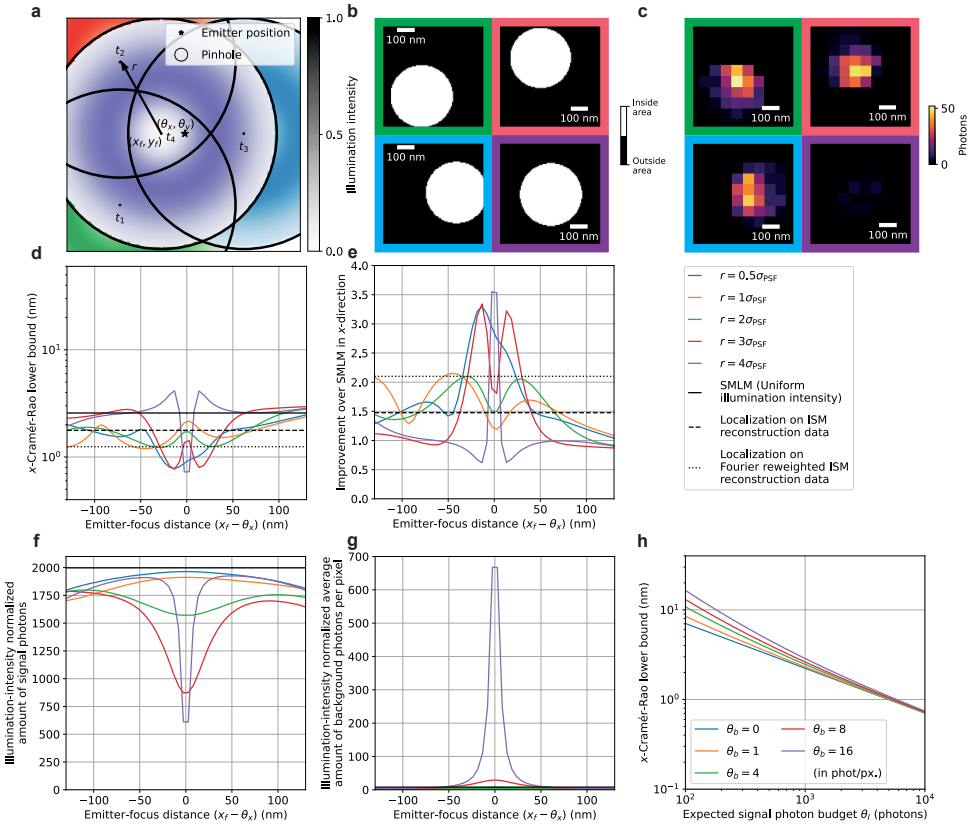

Figure 2.S17: Theoretical minimum localization uncertainty of SpinFlux localization with four pinholes and donut-shaped patterns in a 90° rotated equilateral triangle configuration with a centre pinhole. The pattern is rotated clockwise by 90 degrees with respect to Fig. 2.S12. In (*c*)-(*g*), we used 2000 expected signal photons and 8 expected background photons per pixel, with pinhole radius $r_p = 3\sigma_{PSF}$. Results are evaluated for the scenario where the entire signal photon budget is exhausted after illumination with all patterns (disregarding signal photons blocked by the spinning disk). (*a*) Schematic overview of SpinFlux localization with a triangle of three pinholes with an additional centre pinhole, centred at focus coordinates (x_f, y_f). In (*d*)-(*g*), the *x*-distance $(x_f - \theta_x)$ between the pattern focus and the emitter is varied, where $y_f = \theta_y$. (*b*) Example of pinholes in the region of interest (650 × 650 nm). The pinhole radius $r_p = 2\sigma_{PSF}$ and pinhole spacing $r = 1.5\sigma_{PSF}$ were used. The pinhole masks were discretized with $N_{M,x}$, $N_{M,y} = 100$ mesh pixels in each direction. (*c*) Example of fluorescent response in the region of interest, resulting from illumination and emission through each pinhole in (*b*). (*d*) CRLB in the *x*-direction as a function of the emitter-focus *x*-distance. Simulations show SpinFlux with varying pinhole spacing and widefield SMLM. (*e*) Improvement of the SpinFlux CRLB over SMLM as a function of the emitter-focus *x*-distance for varying pinhole spacing. (*f*) Average amount of signal photons after compensation for non-maximum illumination intensity as a function of the emitter-focus *x*-distance, for SpinFlux with varying pinhole spacing and widefield SMLM. (*g*) Average amount of background photons per pixel after compensation for non-maximum illumination intensity as a function of the emitter-focus *x*-distance, for SpinFlux with varying pinhole spacing and widefield SMLM. (*h*) CRLB in the *x*-direction as a function of expected signal photon count for varying values of the expected background photon count. The pinhole radius $r_p = 3\sigma_{PSF}$ and pinhole spacing $r = 2\sigma_{PSF}$ were used and $(x_f, y_f) = (\theta_x, \theta_y)$.

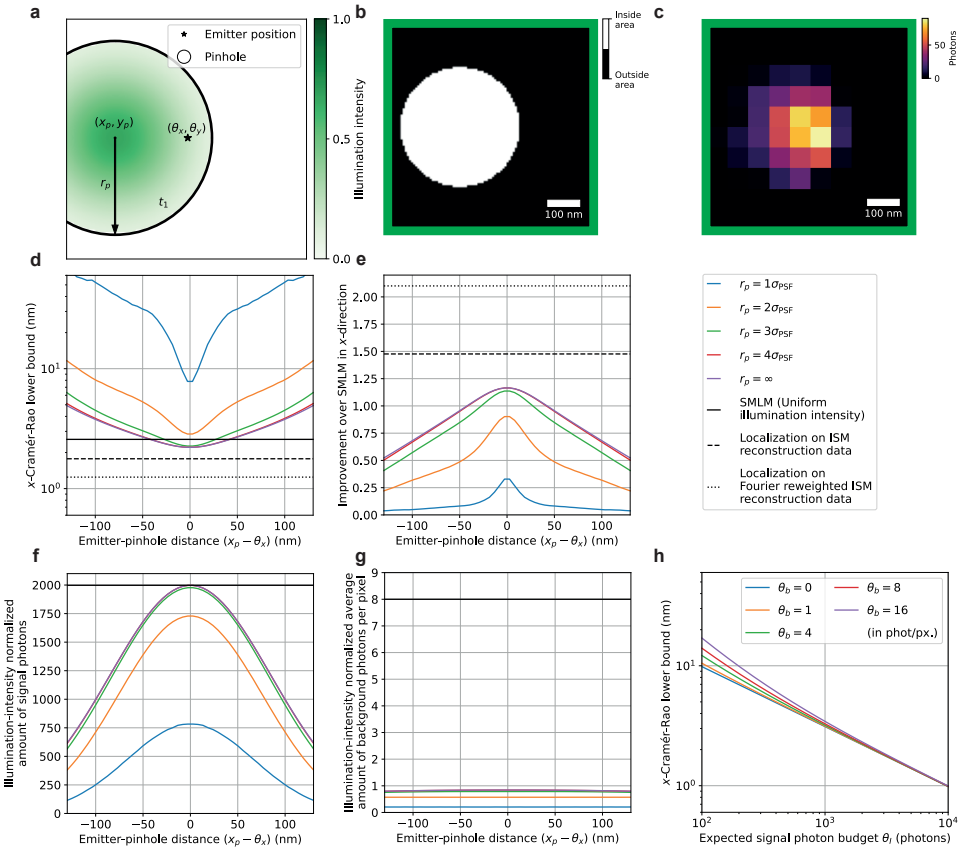

Figure 2.S18: Theoretical minimum localization uncertainty of SpinFlux localization with one x-offset pinhole and pattern. In (*c*)-(*g*), 2000 expected signal photons and 8 expected background photons per pixel were used. Results are evaluated for the scenario where the illumination power and time are constant during illumination with this pattern. (*a*) Schematic overview of SpinFlux localization with one pinhole with radius r_p, centred at coordinates $(x_\mathrm{p}, y_\mathrm{p})$. In (*d*)-(*g*), the x-distance $(x_\mathrm{p} - \theta_x)$ between the pinhole and the emitter is varied, where $y_\mathrm{p} = \theta_y$. (*b*) Example of pinhole in the region of interest (650 × 650 nm). The pinhole radius $r_\mathrm{p} = 2\sigma_\mathrm{PSF}$ was used. The pinhole mask was discretized with $N_{\mathrm{M},x}$, $N_{\mathrm{M},y} = 100$ mesh pixels in each direction. (*c*) Example of fluorescent response in the region of interest, resulting from illumination and emission through the pinhole in (*b*). (*d*) CRLB in the x-direction as a function of the emitter-pinhole x-distance. Simulations show SpinFlux with varying pinhole sizes and widefield SMLM. (*e*) Improvement of the SpinFlux CRLB over SMLM as a function of the emitter-pinhole x-distance for varying pinhole sizes. (*f*) Average amount of signal photons after compensation for non-maximum illumination intensity as a function of the emitter-pinhole x-distance, for SpinFlux with varying pinhole sizes and widefield SMLM. (*g*) Average amount of background photons per pixel after compensation for non-maximum illumination intensity as a function of the emitter-pinhole x-distance, for SpinFlux with varying pinhole sizes and widefield SMLM. (*h*) CRLB in the x-direction as a function of the expected signal photon count for varying values of the expected background photon count. The pinhole radius $r_\mathrm{p} = 3\sigma_\mathrm{PSF}$ was used and $(x_\mathrm{p}, y_\mathrm{p}) = (\theta_x, \theta_y)$.

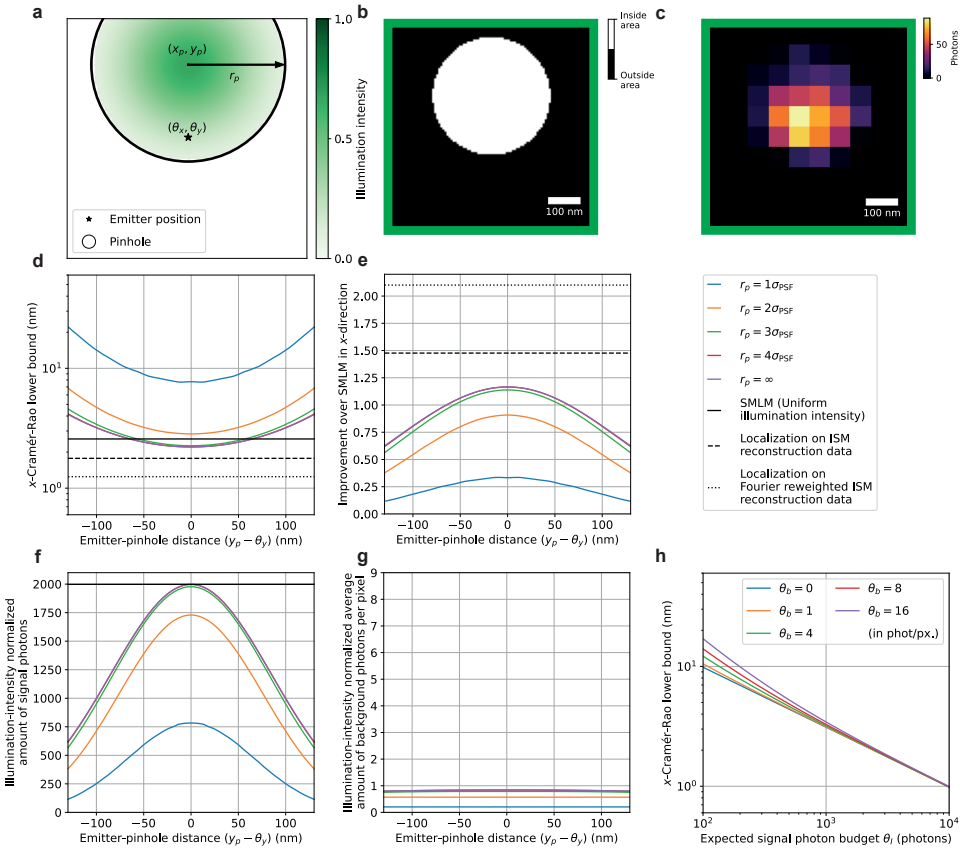

Figure 2.S19: Theoretical minimum localization uncertainty of SpinFlux localization with one y-offset pinhole and pattern. In (*c*)-(*g*), 2000 expected signal photons and 8 expected background photons per pixel were used. Results are evaluated for the scenario where the illumination power and time are constant during illumination with this pattern. (*a*) Schematic overview of SpinFlux localization with one pinhole with radius r_p, centred at coordinates $(x_\mathrm{p}, y_\mathrm{p})$. In (*d*)-(*g*), the y-distance $(y_\mathrm{p} - \theta_y)$ between the pinhole and the emitter is varied, where $x_\mathrm{p} = \theta_x$. (*b*) Example of pinhole in the region of interest (650 × 650 nm). The pinhole radius $r_\mathrm{p} = 2\sigma_\mathrm{PSF}$ was used. The pinhole mask was discretized with $N_{\mathrm{M},x}$, $N_{\mathrm{M},y} = 100$ mesh pixels in each direction. (*c*) Example of fluorescent response in the region of interest, resulting from illumination and emission through the pinhole in (*b*). (*d*) CRLB in the x-direction as a function of the emitter-pinhole y-distance. Simulations show SpinFlux with varying pinhole sizes and widefield SMLM. (*e*) Improvement of the SpinFlux CRLB over SMLM as a function of the emitter-pinhole y-distance for varying pinhole sizes. (*f*) Average amount of signal photons after compensation for non-maximum illumination intensity as a function of the emitter-pinhole y-distance, for SpinFlux with varying pinhole sizes and widefield SMLM. (*g*) Average amount of background photons per pixel after compensation for non-maximum illumination intensity as a function of the emitter-pinhole y-distance, for SpinFlux with varying pinhole sizes and widefield SMLM. (*h*) CRLB in the x-direction as a function of the expected signal photon count for varying values of the expected background photon count. The pinhole radius $r_\mathrm{p} = 3\sigma_\mathrm{PSF}$ was used and $(x_\mathrm{p}, y_\mathrm{p}) = (\theta_x, \theta_y)$.

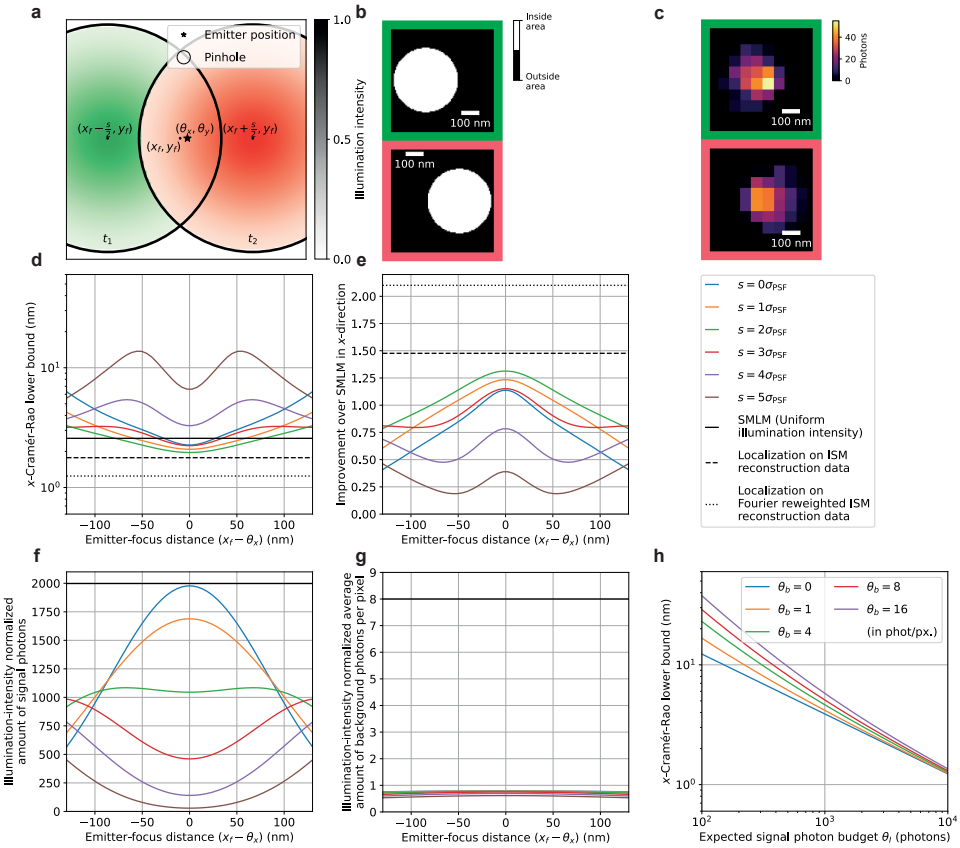

Figure 2.S20: Theoretical minimum localization uncertainty of SpinFlux localization with two pinholes and patterns separated in the x-direction. In (*c*)-(*g*), 2000 expected signal photons and 8 expected background photons per pixel were used, with pinhole radius $r_p = 3\sigma_{PSF}$. Results are evaluated for the scenario where the illumination power and time are constant during illumination with all patterns. (*a*) Schematic overview of SpinFlux localization with two pinholes, separated in x and centred around the focus coordinates (x_f, y_f). In (*d*)-(*g*), the x-distance $(x_f - \theta_x)$ between the pattern focus and the emitter is varied, where $y_f = \theta_y$. (*b*) Example of pinholes in the region of interest (650 × 650 nm). The pinhole radius $r_p = 2\sigma_{PSF}$ and pinhole separation $s = 2\sigma_{PSF}$ were used. The pinhole masks were discretized with $N_{M,x}$, $N_{M,y} = 100$ mesh pixels in each direction. (*c*) Example of fluorescent response in the region of interest, resulting from illumination and emission through each pinhole in (*b*). (*d*) CRLB in the x-direction as a function of the emitter-focus x-distance. Simulations show SpinFlux with varying pinhole separations and widefield SMLM. (*e*) Improvement of the SpinFlux CRLB over SMLM as a function of the emitter-focus x-distance for varying pinhole separations. (*f*) Average amount of signal photons after compensation for non-maximum illumination intensity as a function of the emitter-focus x-distance, for SpinFlux with varying pinhole separations and widefield SMLM. (*g*) Average amount of background photons per pixel after compensation for non-maximum illumination intensity as a function of the emitter-focus x-distance, for SpinFlux with varying pinhole separations and widefield SMLM. (*h*) CRLB in the x-direction as a function of expected signal photon count for varying values of the expected background photon count. The pinhole radius $r_p = 3\sigma_{PSF}$ and pinhole separation $s = 4\sigma_{PSF}$ were used and $(x_f, y_f) = (\theta_x, \theta_y)$.

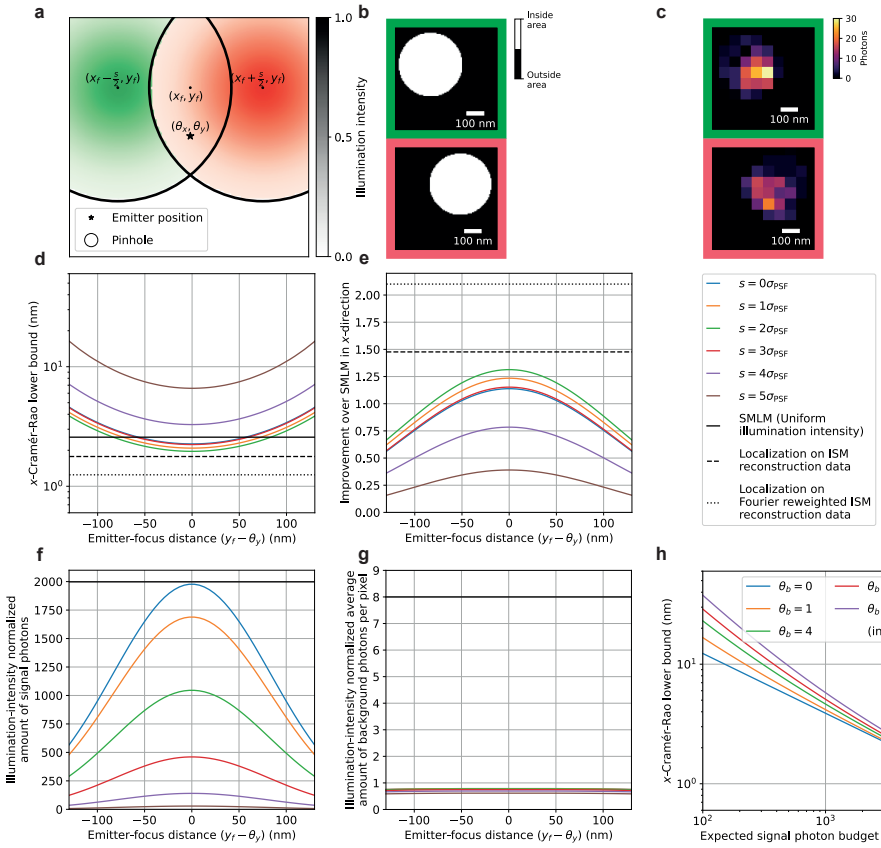

Figure 2.S21: Theoretical minimum localization uncertainty of SpinFlux localization with two y-offset pinholes and patterns separated in the x-direction. In (*c*)-(*g*), 2000 expected signal photons and 8 expected background photons per pixel were used, with pinhole radius $r_p = 3\sigma_{PSF}$. Results are evaluated for the scenario where the illumination power and time are constant during illumination with all patterns. (*a*) Schematic overview of SpinFlux localization with two pinholes, separated in x and centred around the focus coordinates (x_f, y_f). In (*d*)-(*g*), the y-distance $(y_f - \theta_y)$ between the pattern focus and the emitter is varied, where $x_f = \theta_x$. (*b*) Example of pinholes in the region of interest (650 × 650 nm). The pinhole radius $r_p = 2\sigma_{PSF}$ and pinhole separation $s = 2\sigma_{PSF}$ were used. The pinhole masks were discretized with $N_{M,x}$, $N_{M,y} = 100$ mesh pixels in each direction. (*c*) Example of fluorescent response in the region of interest, resulting from illumination and emission through each pinhole in (*b*). (*d*) CRLB in the x-direction as a function of the emitter-focus y-distance. Simulations show SpinFlux with varying pinhole separations and widefield SMLM. (*e*) Improvement of the SpinFlux CRLB over SMLM as a function of the emitter-focus y-distance for varying pinhole separations. (*f*) Average amount of signal photons after compensation for non-maximum illumination intensity as a function of the emitter-focus y-distance, for SpinFlux with varying pinhole separations and widefield SMLM. (*g*) Average amount of background photons per pixel after compensation for non-maximum illumination intensity as a function of the emitter-focus y-distance, for SpinFlux with varying pinhole separations and widefield SMLM. (*h*) CRLB in the x-direction as a function of expected signal photon count for varying values of the expected background photon count. The pinhole radius $r_p = 3\sigma_{PSF}$ and pinhole separation $s = 4\sigma_{PSF}$ were used and $(x_f, y_f) = (\theta_x, \theta_y)$.

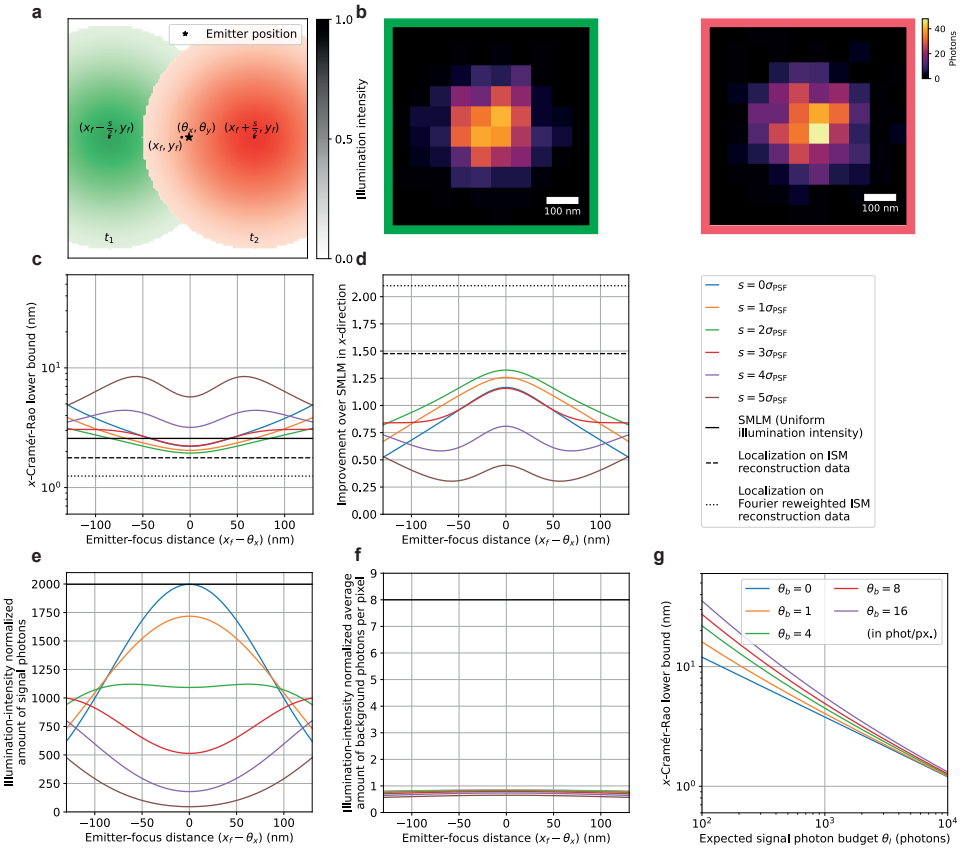

Figure 2.S22: Theoretical minimum localization uncertainty of SpinFlux localization with two patterns without pinholes separated in the x-direction. in (b)-(f), 2000 expected signal photons and 8 expected background photons per pixel were used. Results are evaluated for the scenario where the illumination power and time are constant during illumination with all patterns. (a) Schematic overview of SpinFlux localization with two pinholes, separated in x and centred around the focus coordinates (x_f, y_f). In (c)-(f), the x-distance $(x_f - \theta_x)$ between the pattern focus and the emitter is varied, where $y_f = \theta_y$. (b) Example of fluorescent response in the region of interest, resulting from illumination and emission by each pattern in (a). (c) CRLB in the x-direction as a function of the emitter-focus x-distance. Simulations show SpinFlux with varying pinhole separations and widefield SMLM. (d) Improvement of the SpinFlux CRLB over SMLM as a function of the emitter-focus x-distance for varying pinhole separations. (e) Average amount of signal photons after compensation for non-maximum illumination intensity as a function of the emitter-focus x-distance, for SpinFlux with varying pinhole separations and widefield SMLM. (f) Average amount of background photons per pixel after compensation for non-maximum illumination intensity as a function of the emitter-focus x-distance, for SpinFlux with varying pinhole separations and widefield SMLM. (g) CRLB in the x-direction as a function of expected signal photon count for varying values of the expected background photon count. The pattern separation $s = 4\sigma_{\mathrm{PSF}}$ was used and $(x_f, y_f) = (\theta_x, \theta_y)$.

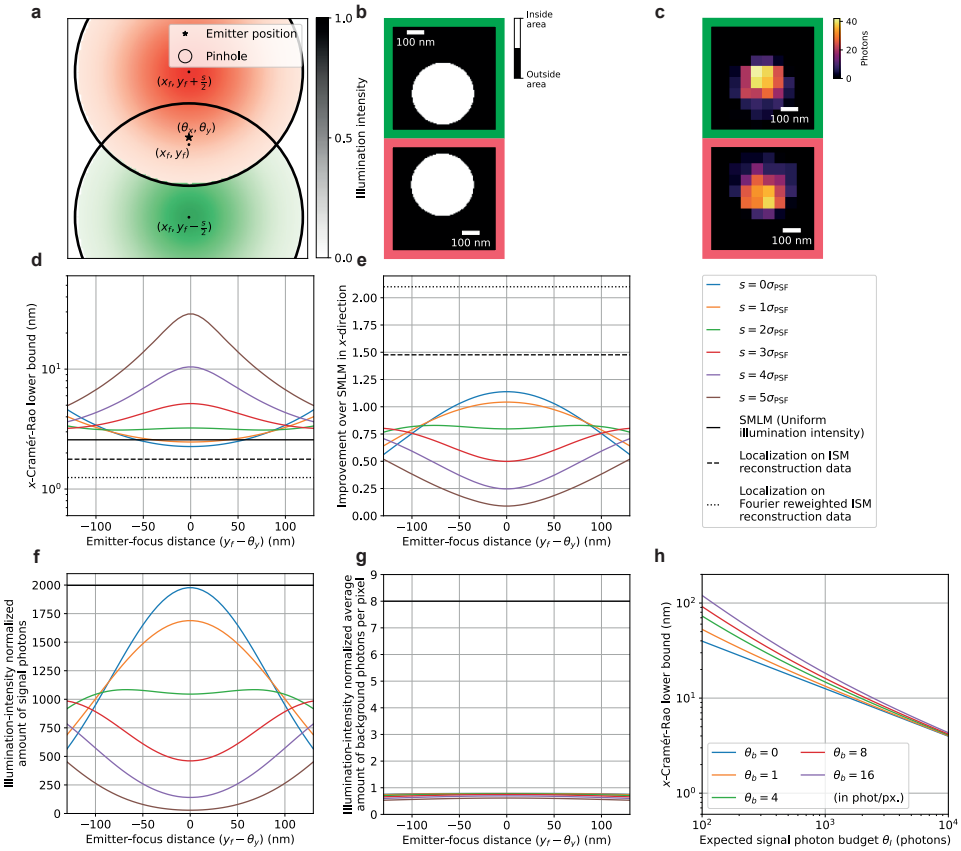

Figure 2.S23: Theoretical minimum localization uncertainty of SpinFlux localization with two pinholes and patterns separated in the y-direction. In (*c*)-(*g*), 2000 expected signal photons and 8 expected background photons per pixel were used, with pinhole radius $r_p = 3\sigma_{PSF}$. Results are evaluated for the scenario where the illumination power and time are constant during illumination with all patterns. (*a*) Schematic overview of SpinFlux localization with two pinholes, separated in y and centred around the focus coordinates (x_f, y_f). In (*d*)-(*g*), the y-distance $(y_f - \theta_y)$ between the pattern focus and the emitter is varied, where $x_f = \theta_x$. (*b*) Example of pinholes in the region of interest (650 × 650 nm). The pinhole radius $r_p = 2\sigma_{PSF}$ and pinhole separation $s = 2\sigma_{PSF}$ were used. The pinhole masks were discretized with $N_{M,x}$, $N_{M,y} = 100$ mesh pixels in each direction. (*c*) Example of fluorescent response in the region of interest, resulting from illumination and emission through each pinhole in (*b*). (*d*) CRLB in the x-direction as a function of the emitter-focus y-distance. Simulations show SpinFlux with varying pinhole separations and widefield SMLM. (*e*) Improvement of the SpinFlux CRLB over SMLM as a function of the emitter-focus y-distance for varying pinhole separations. (*f*) Average amount of signal photons after compensation for non-maximum illumination intensity as a function of the emitter-focus y-distance, for SpinFlux with varying pinhole separations and widefield SMLM. (*g*) Average amount of background photons per pixel after compensation for non-maximum illumination intensity as a function of the emitter-focus y-distance, for SpinFlux with varying pinhole separations and widefield SMLM. (*h*) CRLB in the x-direction as a function of expected signal photon count for varying values of the expected background photon count. The pinhole radius $r_p = 3\sigma_{PSF}$ and pinhole separation $s = 4\sigma_{PSF}$ were used and $(x_f, y_f) = (\theta_x, \theta_y)$.

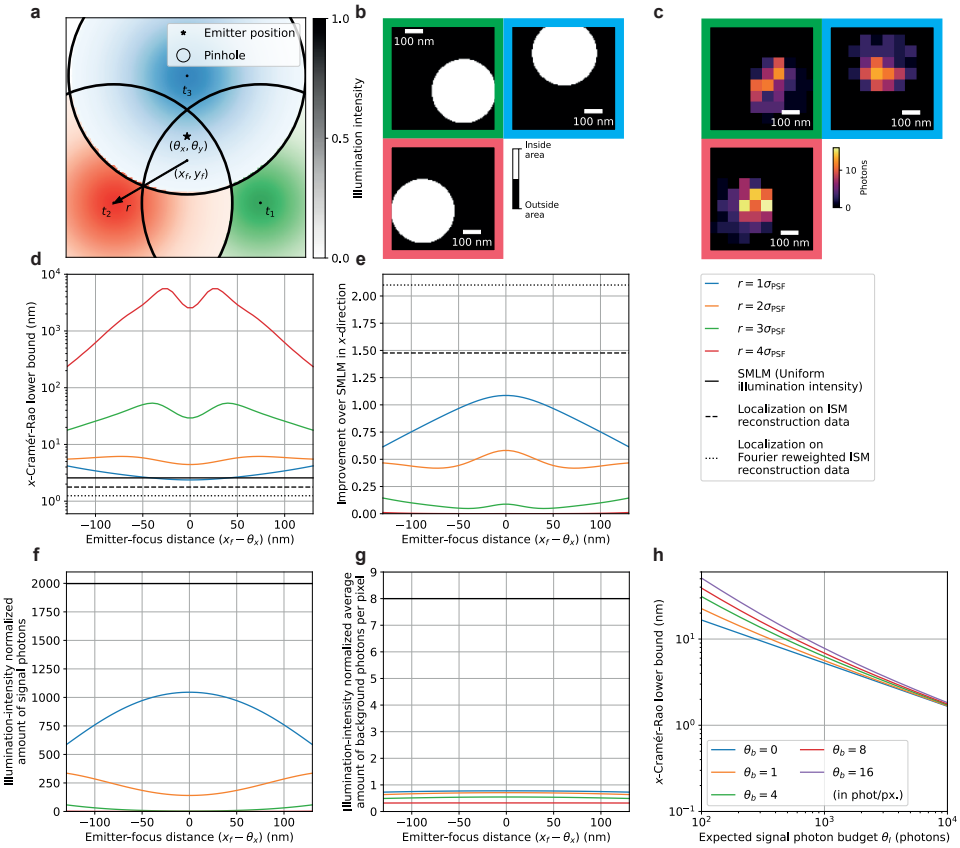

Figure 2.S24: Theoretical minimum localization uncertainty of SpinFlux localization with three pinholes and patterns in an equilateral triangle configuration. In (*c*)-(*g*), we used 2000 expected signal photons and 8 expected background photons per pixel, with pinhole radius $r_p = 3\sigma_{PSF}$. Results are evaluated for the scenario where the illumination power and time are constant during illumination with all patterns. (*a*) Schematic overview of SpinFlux localization with a triangle of three pinholes, centred at focus coordinates (x_f, y_f). In (*d*)-(*g*), the *x*-distance $(x_f - \theta_x)$ between the pattern focus and the emitter is varied, where $y_f = \theta_y$. (*b*) Example of pinholes in the region of interest (650 × 650 nm). The pinhole radius $r_p = 2\sigma_{PSF}$ and pinhole spacing $r = 1.5\sigma_{PSF}$ were used. The pinhole masks were discretized with $N_{M,x}$, $N_{M,y} = 100$ mesh pixels in each direction. (*c*) Example of fluorescent response in the region of interest, resulting from illumination and emission through each pinhole in (*b*). (*d*) CRLB in the *x*-direction as a function of the emitter-focus *x*-distance. Simulations show SpinFlux with varying pinhole spacing and widefield SMLM. (*e*) Improvement of the SpinFlux CRLB over SMLM as a function of the emitter-focus *x*-distance for varying pinhole spacing. (*f*) Average amount of signal photons after compensation for non-maximum illumination intensity as a function of the emitter-focus *x*-distance, for SpinFlux with varying pinhole spacing and widefield SMLM. (*g*) Average amount of background photons per pixel after compensation for non-maximum illumination intensity as a function of the emitter-focus *x*-distance, for SpinFlux with varying pinhole spacing and widefield SMLM. (*h*) CRLB in the *x*-direction as a function of expected signal photon count for varying values of the expected background photon count. The pinhole radius $r_p = 3\sigma_{PSF}$ and pinhole spacing $r = 2\sigma_{PSF}$ were used and $(x_f, y_f) = (\theta_x, \theta_y)$.

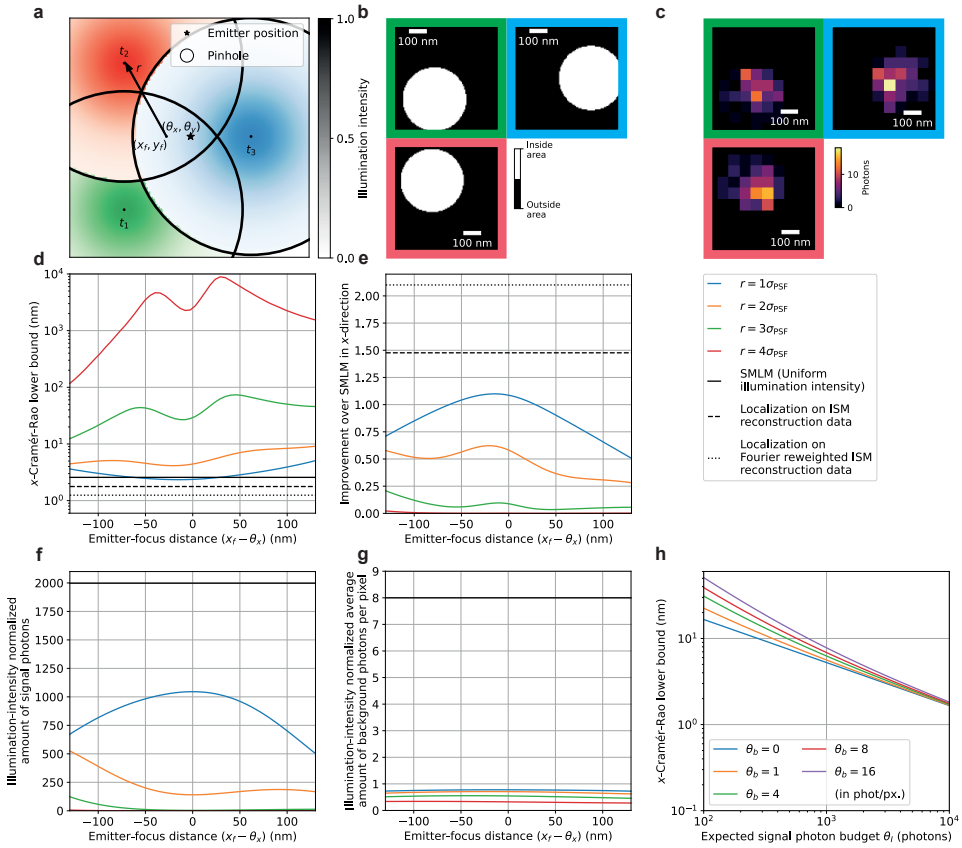

Figure 2.S25: Theoretical minimum localization uncertainty of SpinFlux localization with three pinholes and patterns in a 90° rotated equilateral triangle configuration. The pattern is rotated clockwise by 90 degrees with respect to Fig. 2.S24. In (*c*)-(*g*), we used 2000 expected signal photons and 8 expected background photons per pixel, with pinhole radius $r_p = 3\sigma_{PSF}$. Results are evaluated for the scenario where the illumination power and time are constant during illumination with all patterns. (*a*) Schematic overview of SpinFlux localization with a triangle of three pinholes, centred at focus coordinates (x_f, y_f). In (*d*)-(*g*), the *x*-distance $(x_f - \theta_x)$ between the pattern focus and the emitter is varied, where $y_f = \theta_y$. (*b*) Example of pinholes in the region of interest (650 × 650 nm). The pinhole radius $r_p = 2\sigma_{PSF}$ and pinhole spacing $r = 1.5\sigma_{PSF}$ were used. The pinhole masks were discretized with $N_{M,x}$, $N_{M,y} = 100$ mesh pixels in each direction. (*c*) Example of fluorescent response in the region of interest, resulting from illumination and emission through each pinhole in (*b*). (*d*) CRLB in the *x*-direction as a function of the emitter-focus *x*-distance. Simulations show SpinFlux with varying pinhole spacing and widefield SMLM. (*e*) Improvement of the SpinFlux CRLB over SMLM as a function of the emitter-focus *x*-distance for varying pinhole spacing. (*f*) Average amount of signal photons after compensation for non-maximum illumination intensity as a function of the emitter-focus *x*-distance, for SpinFlux with varying pinhole spacing and widefield SMLM. (*g*) Average amount of background photons per pixel after compensation for non-maximum illumination intensity as a function of the emitter-focus *x*-distance, for SpinFlux with varying pinhole spacing and widefield SMLM. (*h*) CRLB in the *x*-direction as a function of expected signal photon count for varying values of the expected background photon count. The pinhole radius $r_p = 3\sigma_{PSF}$ and pinhole spacing $r = 2\sigma_{PSF}$ were used and $(x_f, y_f) = (\theta_x, \theta_y)$.

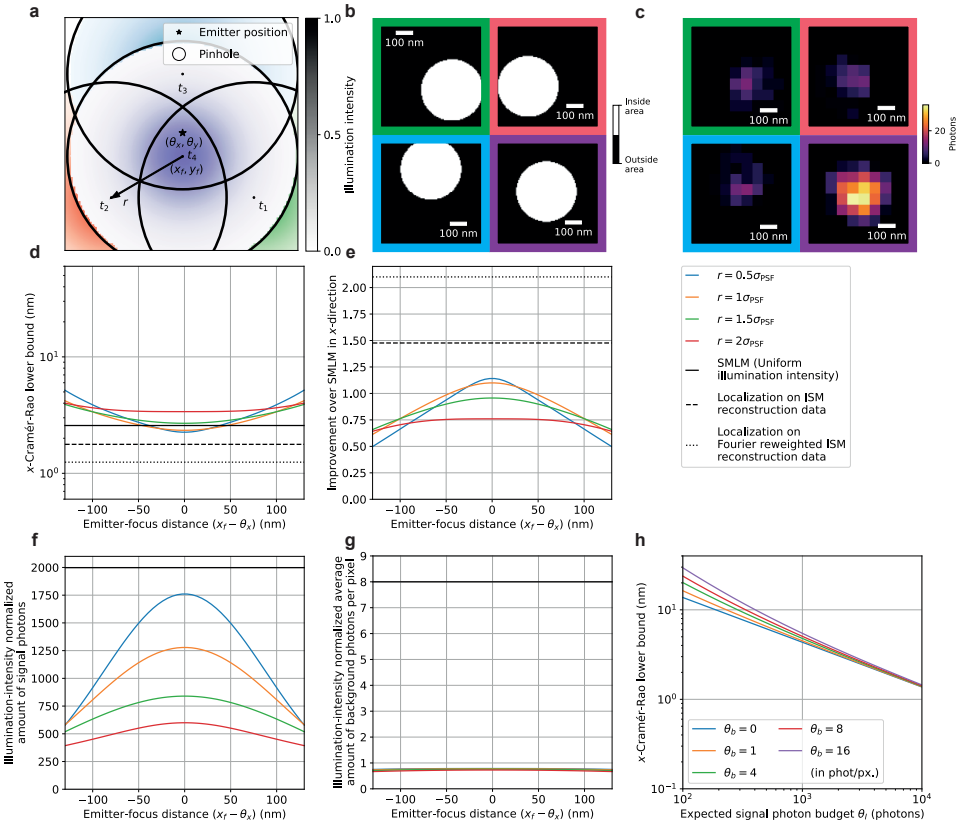

Figure 2.S26: Theoretical minimum localization uncertainty of SpinFlux localization with four pinholes and patterns in an equilateral triangle configuration with a centre pinhole. In (*c*)-(*g*), we used 2000 expected signal photons and 8 expected background photons per pixel, with pinhole radius $r_p = 3\sigma_{PSF}$. Results are evaluated for the scenario where the illumination power and time are constant during illumination with all patterns. (*a*) Schematic overview of SpinFlux localization with a triangle of three pinholes with an additional centre pinhole, centred at focus coordinates (x_f, y_f). In (*d*)-(*g*), the x-distance $(x_f - \theta_x)$ between the pattern focus and the emitter is varied, where $y_f = \theta_y$. (*b*) Example of pinholes in the region of interest (650 × 650 nm). The pinhole radius $r_p = 2\sigma_{PSF}$ and pinhole spacing $r = 1.5\sigma_{PSF}$ were used. The pinhole masks were discretized with $N_{M,x}$, $N_{M,y} = 100$ mesh pixels in each direction. (*c*) Example of fluorescent response in the region of interest, resulting from illumination and emission through each pinhole in (*b*). (*d*) CRLB in the x-direction as a function of the emitter-focus x-distance. Simulations show SpinFlux with varying pinhole spacing and widefield SMLM. (*e*) Improvement of the SpinFlux CRLB over SMLM as a function of the emitter-focus x-distance for varying pinhole spacing. (*f*) Average amount of signal photons after compensation for non-maximum illumination intensity as a function of the emitter-focus x-distance, for SpinFlux with varying pinhole spacing and widefield SMLM. (*g*) Average amount of background photons per pixel after compensation for non-maximum illumination intensity as a function of the emitter-focus x-distance, for SpinFlux with varying pinhole spacing and widefield SMLM. (*h*) CRLB in the x-direction as a function of expected signal photon count for varying values of the expected background photon count. The pinhole radius $r_p = 3\sigma_{PSF}$ and pinhole spacing $r = 2\sigma_{PSF}$ were used and $(x_f, y_f) = (\theta_x, \theta_y)$.

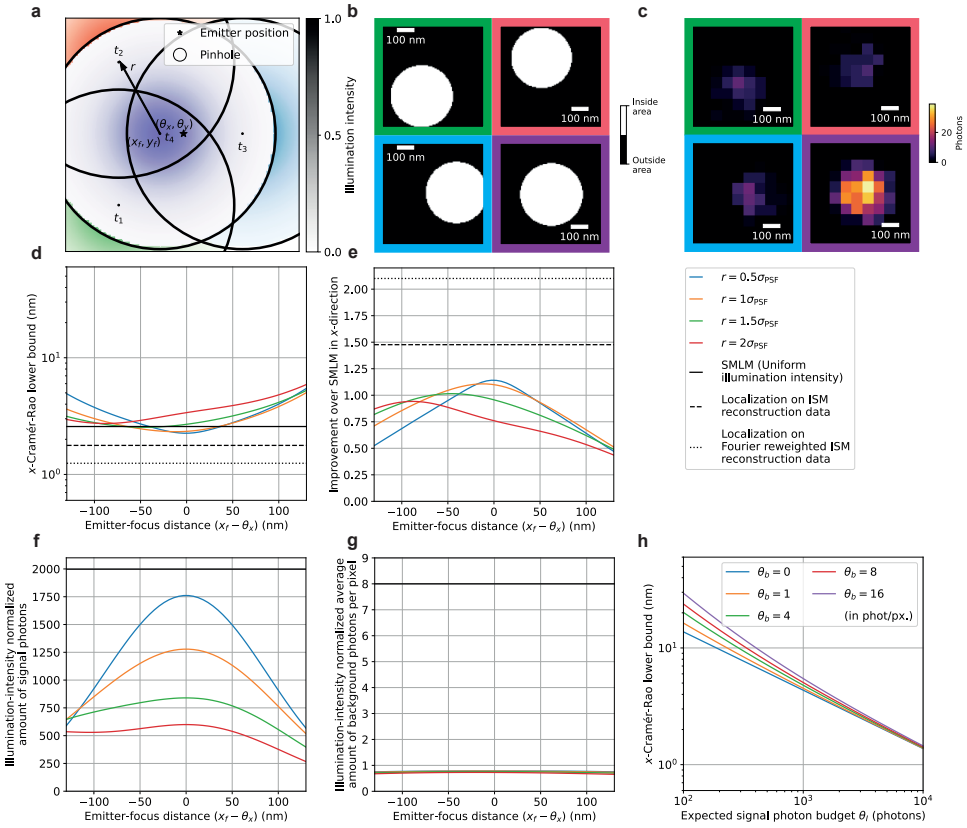

Figure 2.S27: Theoretical minimum localization uncertainty of SpinFlux localization with four pinholes and patterns in a 90° rotated equilateral triangle configuration with a centre pinhole. The pattern is rotated clockwise by 90 degrees with respect to Fig. 2.S26. In (*c*)-(*g*), we used 2000 expected signal photons and 8 expected background photons per pixel, with pinhole radius $r_p = 3\sigma_{PSF}$. Results are evaluated for the scenario where the illumination power and time are constant during illumination with all patterns. (*a*) Schematic overview of SpinFlux localization with a triangle of three pinholes with an additional centre pinhole, centred at focus coordinates (x_f, y_f). In (*d*)-(*g*), the x-distance $(x_f - \theta_x)$ between the pattern focus and the emitter is varied, where $y_f = \theta_y$. (*b*) Example of pinholes in the region of interest (650 × 650 nm). The pinhole radius $r_p = 2\sigma_{PSF}$ and pinhole spacing $r = 1.5\sigma_{PSF}$ were used. The pinhole masks were discretized with $N_{M,x}$, $N_{M,y} = 100$ mesh pixels in each direction. (*c*) Example of fluorescent response in the region of interest, resulting from illumination and emission through each pinhole in (*b*). (*d*) CRLB in the x-direction as a function of the emitter-focus x-distance. Simulations show SpinFlux with varying pinhole spacing and widefield SMLM. (*e*) Improvement of the SpinFlux CRLB over SMLM as a function of the emitter-focus x-distance for varying pinhole spacing. (*f*) Average amount of signal photons after compensation for non-maximum illumination intensity as a function of the emitter-focus x-distance, for SpinFlux with varying pinhole spacing and widefield SMLM. (*g*) Average amount of background photons per pixel after compensation for non-maximum illumination intensity as a function of the emitter-focus x-distance, for SpinFlux with varying pinhole spacing and widefield SMLM. (*h*) CRLB in the x-direction as a function of expected signal photon count for varying values of the expected background photon count. The pinhole radius $r_p = 3\sigma_{PSF}$ and pinhole spacing $r = 2\sigma_{PSF}$ were used and $(x_f, y_f) = (\theta_x, \theta_y)$.

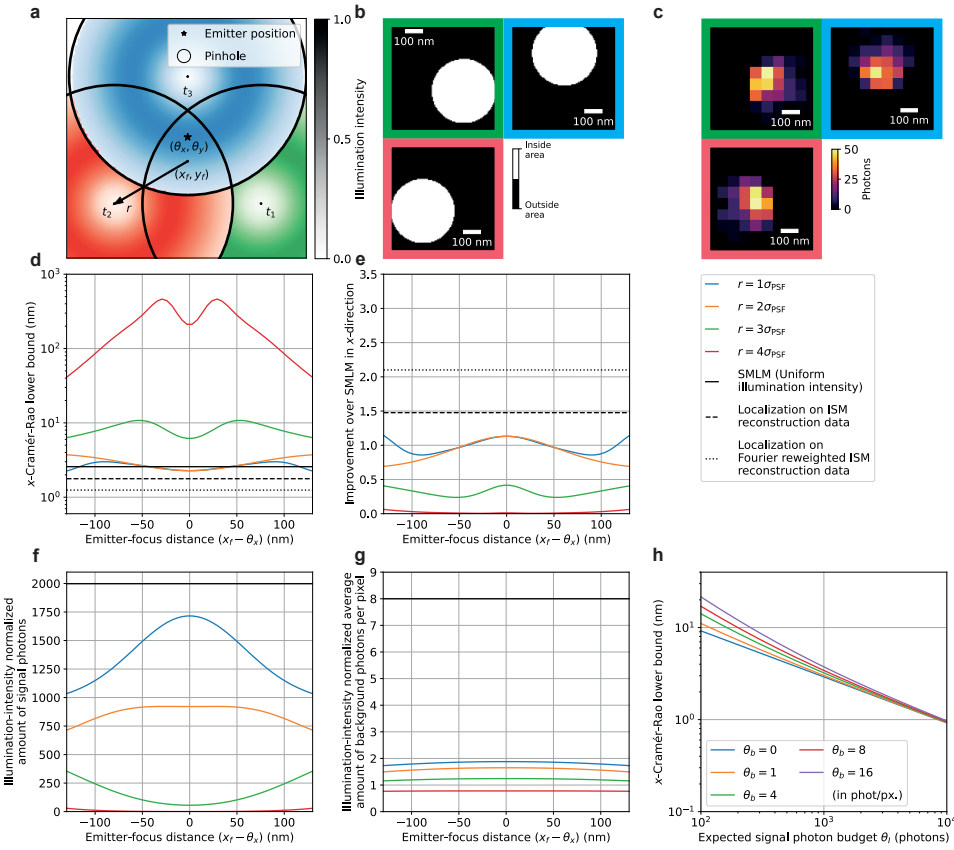

Figure 2.S28: Theoretical minimum localization uncertainty of SpinFlux localization with three pinholes and donut-shaped patterns in an equilateral triangle configuration. In (*c*)-(*g*), we used 2000 expected signal photons and 8 expected background photons per pixel, with pinhole radius $r_p = 3\sigma_{PSF}$. Results are evaluated for the scenario where the illumination power and time are constant during illumination with all patterns. (*a*) Schematic overview of SpinFlux localization with a triangle of three pinholes, centred at focus coordinates (x_f, y_f). In (*d*)-(*g*), the *x*-distance $(x_f - \theta_x)$ between the pattern focus and the emitter is varied, where $y_f = \theta_y$. (*b*) Example of pinholes in the region of interest (650 × 650 nm). The pinhole radius $r_p = 2\sigma_{PSF}$ and pinhole spacing $r = 1.5\sigma_{PSF}$ were used. The pinhole masks were discretized with $N_{M,x}$, $N_{M,y} = 100$ mesh pixels in each direction. (*c*) Example of fluorescent response in the region of interest, resulting from illumination and emission through each pinhole in (*b*). (*d*) CRLB in the *x*-direction as a function of the emitter-focus *x*-distance. Simulations show SpinFlux with varying pinhole spacing and widefield SMLM. (*e*) Improvement of the SpinFlux CRLB over SMLM as a function of the emitter-focus *x*-distance for varying pinhole spacing. (*f*) Average amount of signal photons after compensation for non-maximum illumination intensity as a function of the emitter-focus *x*-distance, for SpinFlux with varying pinhole spacing and widefield SMLM. (*g*) Average amount of background photons per pixel after compensation for non-maximum illumination intensity as a function of the emitter-focus *x*-distance, for SpinFlux with varying pinhole spacing and widefield SMLM. (*h*) CRLB in the *x*-direction as a function of expected signal photon count for varying values of the expected background photon count. The pinhole radius $r_p = 3\sigma_{PSF}$ and pinhole spacing $r = 2\sigma_{PSF}$ were used and $(x_f, y_f) = (\theta_x, \theta_y)$.

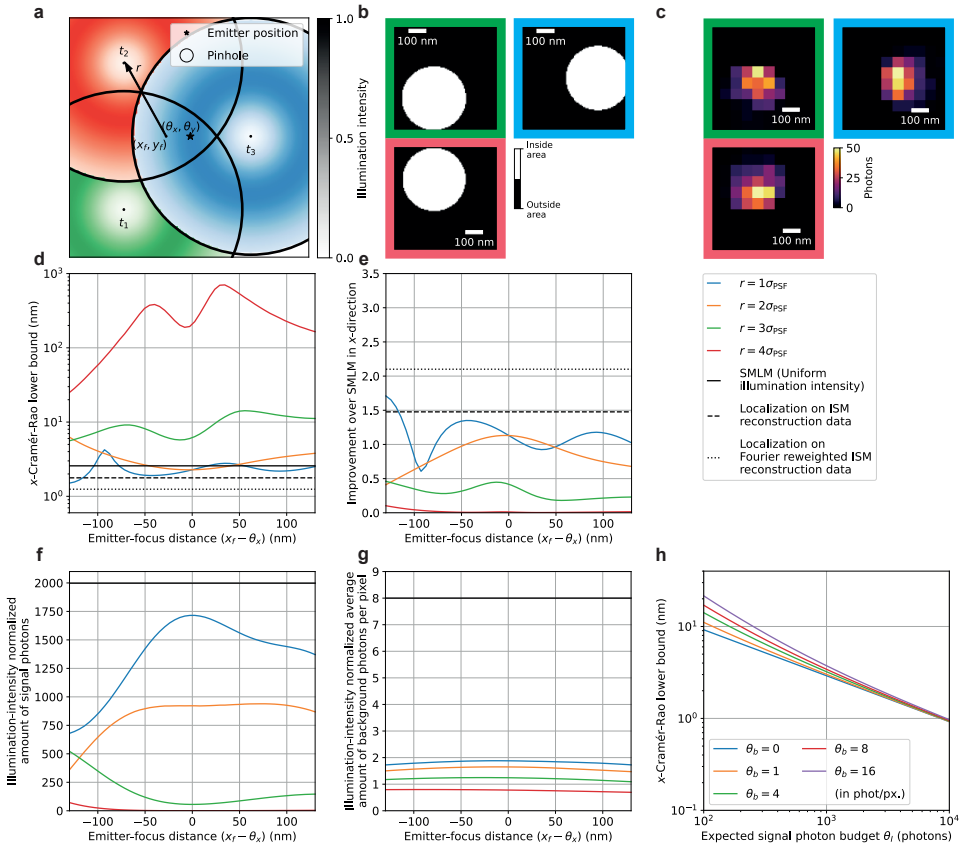

Figure 2.S29: Theoretical minimum localization uncertainty of SpinFlux localization with three pinholes and donut-shaped patterns in a 90° rotated equilateral triangle configuration. The pattern is rotated clockwise by 90 degrees with respect to Fig. 2.S24. In (*c*)-(*g*), we used 2000 expected signal photons and 8 expected background photons per pixel, with pinhole radius $r_p = 3\sigma_{PSF}$. Results are evaluated for the scenario where the illumination power and time are constant during illumination with all patterns. (*a*) Schematic overview of SpinFlux localization with a triangle of three pinholes, centred at focus coordinates (x_f, y_f). In (*d*)-(*g*), the x-distance $(x_f - \theta_x)$ between the pattern focus and the emitter is varied, where $y_f = \theta_y$. (*b*) Example of pinholes in the region of interest (650 × 650 nm). The pinhole radius $r_p = 2\sigma_{PSF}$ and pinhole spacing $r = 1.5\sigma_{PSF}$ were used. The pinhole masks were discretized with $N_{M,x}$, $N_{M,y} = 100$ mesh pixels in each direction. (*c*) Example of fluorescent response in the region of interest, resulting from illumination and emission through each pinhole in (*b*). (*d*) CRLB in the x-direction as a function of the emitter-focus x-distance. Simulations show SpinFlux with varying pinhole spacing and widefield SMLM. (*e*) Improvement of the SpinFlux CRLB over SMLM as a function of the emitter-focus x-distance for varying pinhole spacing. (*f*) Average amount of signal photons after compensation for non-maximum illumination intensity as a function of the emitter-focus x-distance, for SpinFlux with varying pinhole spacing and widefield SMLM. (*g*) Average amount of background photons per pixel after compensation for non-maximum illumination intensity as a function of the emitter-focus x-distance, for SpinFlux with varying pinhole spacing and widefield SMLM. (*h*) CRLB in the x-direction as a function of expected signal photon count for varying values of the expected background photon count. The pinhole radius $r_p = 3\sigma_{PSF}$ and pinhole spacing $r = 2\sigma_{PSF}$ were used and $(x_f, y_f) = (\theta_x, \theta_y)$.

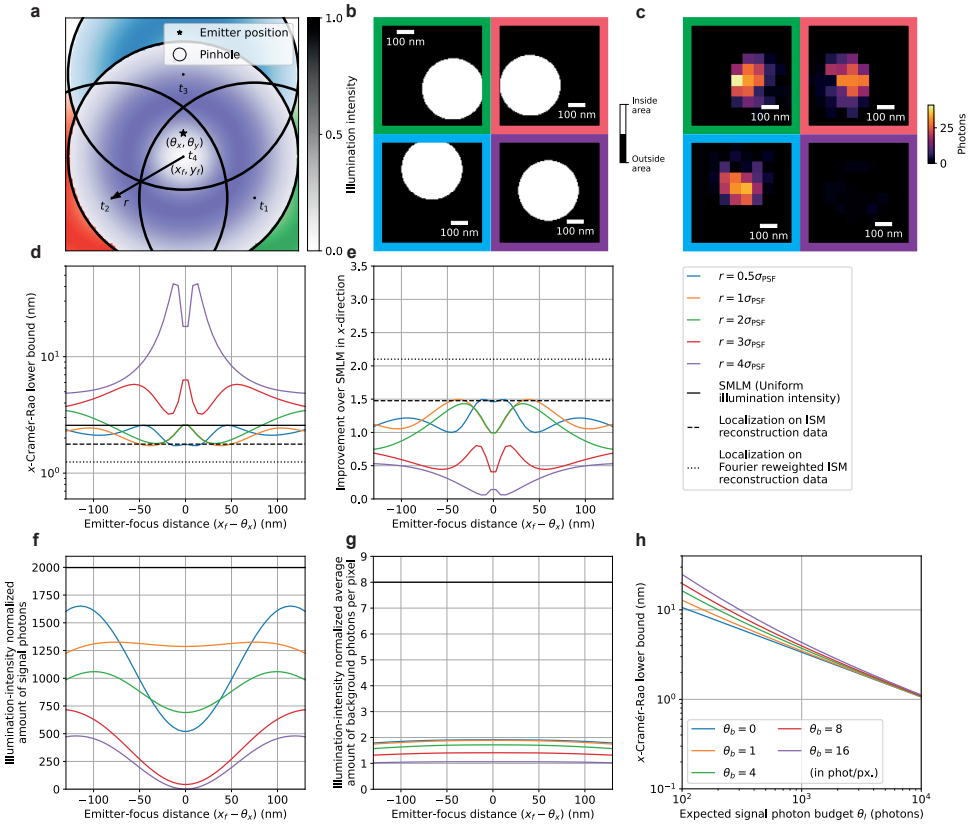

Figure 2.S30: Theoretical minimum localization uncertainty of SpinFlux localization with four pinholes and donut-shaped patterns in an equilateral triangle configuration with a centre pinhole. In (*c*)-(*g*), we used 2000 expected signal photons and 8 expected background photons per pixel, with pinhole radius $r_p = 3\sigma_{PSF}$. Results are evaluated for the scenario where the illumination power and time are constant during illumination with all patterns. (*a*) Schematic overview of SpinFlux localization with a triangle of three pinholes with an additional centre pinhole, centred at focus coordinates (x_f, y_f). In (*d*)-(*g*), the *x*-distance $(x_f - \theta_x)$ between the pattern focus and the emitter is varied, where $y_f = \theta_y$. (*b*) Example of pinholes in the region of interest (650 × 650 nm). The pinhole radius $r_p = 2\sigma_{PSF}$ and pinhole spacing $r = 1.5\sigma_{PSF}$ were used. The pinhole masks were discretized with $N_{M,x}$, $N_{M,y} = 100$ mesh pixels in each direction. (*c*) Example of fluorescent response in the region of interest, resulting from illumination and emission through each pinhole in (*b*). (*d*) CRLB in the *x*-direction as a function of the emitter-focus *x*-distance. Simulations show SpinFlux with varying pinhole spacing and widefield SMLM. (*e*) Improvement of the SpinFlux CRLB over SMLM as a function of the emitter-focus *x*-distance for varying pinhole spacing. (*f*) Average amount of signal photons after compensation for non-maximum illumination intensity as a function of the emitter-focus *x*-distance, for SpinFlux with varying pinhole spacing and widefield SMLM. (*g*) Average amount of background photons per pixel after compensation for non-maximum illumination intensity as a function of the emitter-focus *x*-distance, for SpinFlux with varying pinhole spacing and widefield SMLM. (*h*) CRLB in the *x*-direction as a function of expected signal photon count for varying values of the expected background photon count. The pinhole radius $r_p = 3\sigma_{PSF}$ and pinhole spacing $r = 2\sigma_{PSF}$ were used and $(x_f, y_f) = (\theta_x, \theta_y)$.

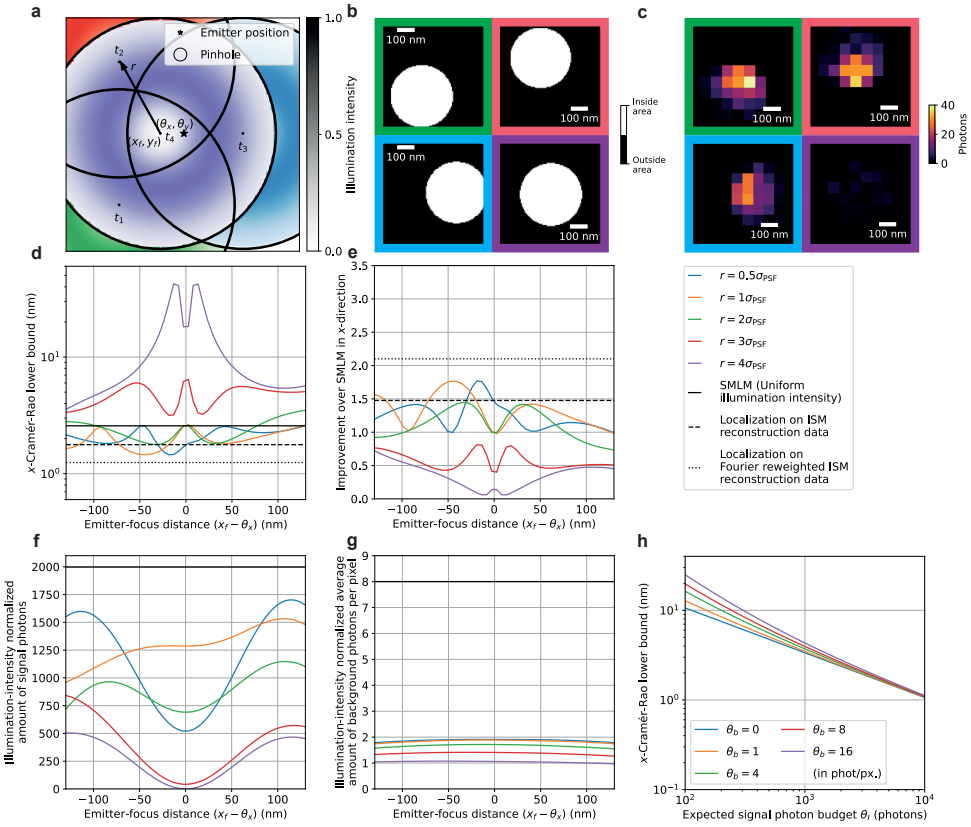

Figure 2.S31: Theoretical minimum localization uncertainty of SpinFlux localization with four pinholes and donut-shaped patterns in a 90° rotated equilateral triangle configuration with a centre pinhole. The pattern is rotated clockwise by 90 degrees with respect to Fig. 2.S26. In (*c*)-(*g*), we used 2000 expected signal photons and 8 expected background photons per pixel, with pinhole radius $r_p = 3\sigma_{PSF}$. Results are evaluated for the scenario where the illumination power and time are constant during illumination with all patterns. (*a*) Schematic overview of SpinFlux localization with a triangle of three pinholes with an additional centre pinhole, centred at focus coordinates (x_f, y_f). In (*d*)-(*g*), the *x*-distance $(x_f - \theta_x)$ between the pattern focus and the emitter is varied, where $y_f = \theta_y$. (*b*) Example of pinholes in the region of interest (650 × 650 nm). The pinhole radius $r_p = 2\sigma_{PSF}$ and pinhole spacing $r = 1.5\sigma_{PSF}$ were used. The pinhole masks were discretized with $N_{M,x}$, $N_{M,y} = 100$ mesh pixels in each direction. (*c*) Example of fluorescent response in the region of interest, resulting from illumination and emission through each pinhole in (*b*). (*d*) CRLB in the *x*-direction as a function of the emitter-focus *x*-distance. Simulations show SpinFlux with varying pinhole spacing and widefield SMLM. (*e*) Improvement of the SpinFlux CRLB over SMLM as a function of the emitter-focus *x*-distance for varying pinhole spacing. (*f*) Average amount of signal photons after compensation for non-maximum illumination intensity as a function of the emitter-focus *x*-distance, for SpinFlux with varying pinhole spacing and widefield SMLM. (*g*) Average amount of background photons per pixel after compensation for non-maximum illumination intensity as a function of the emitter-focus *x*-distance, for SpinFlux with varying pinhole spacing and widefield SMLM. (*h*) CRLB in the *x*-direction as a function of expected signal photon count for varying values of the expected background photon count. The pinhole radius $r_p = 3\sigma_{PSF}$ and pinhole spacing $r = 2\sigma_{PSF}$ were used and $(x_f, y_f) = (\theta_x, \theta_y)$.

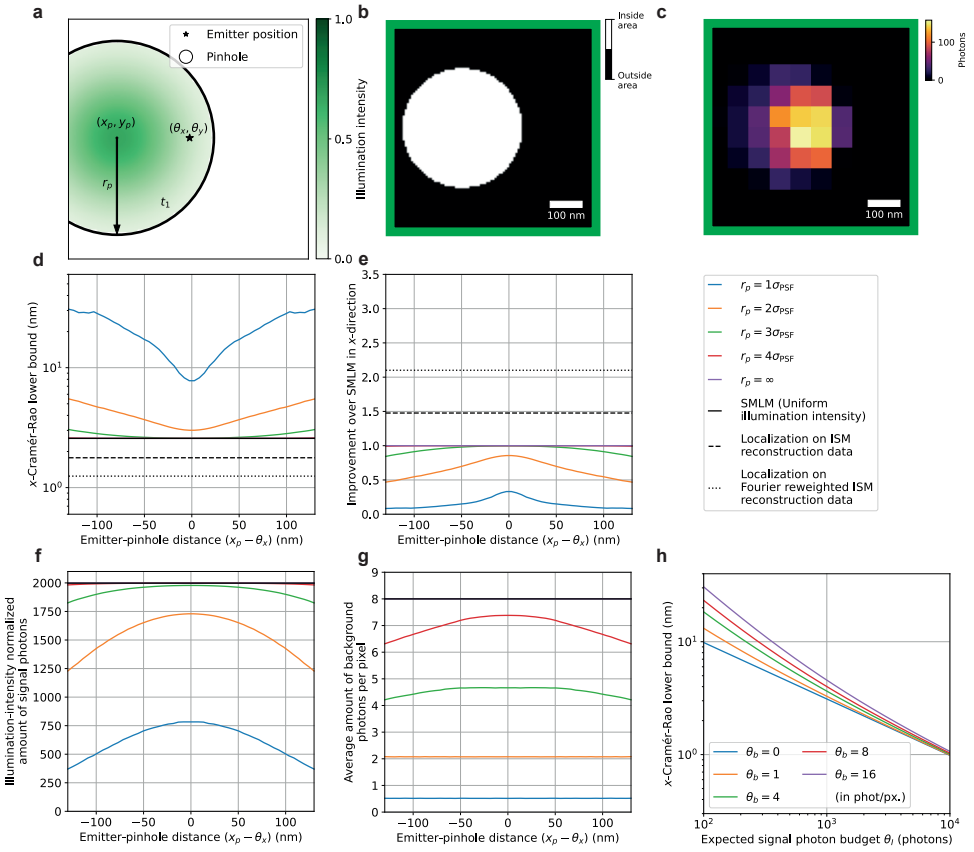

Figure 2.S32: Theoretical minimum localization uncertainty of SpinFlux localization with one x-offset pinhole and pattern. In (*c*)-(*g*), 2000 expected signal photons and 8 expected background photons per pixel were used. Results are evaluated for the scenario where the entire signal photon budget is exhausted after illumination with the pattern (disregarding signal photons blocked by the spinning disk), neglecting the effects of pattern-dependent background. (*a*) Schematic overview of SpinFlux localization with one pinhole with radius r_p, centred at coordinates $(x_\mathrm{p}, y_\mathrm{p})$. In (*d*)-(*g*), the x-distance $(x_\mathrm{p} - \theta_x)$ between the pinhole and the emitter is varied, where $y_\mathrm{p} = \theta_y$. (*b*) Example of pinhole in the region of interest (650 × 650 nm). The pinhole radius $r_\mathrm{p} = 2\sigma_\mathrm{PSF}$ was used. The pinhole mask was discretized with $N_{\mathrm{M},x}$, $N_{\mathrm{M},y} = 100$ mesh pixels in each direction. (*c*) Example of fluorescent response in the region of interest, resulting from illumination and emission through the pinhole in (*b*). (*d*) CRLB in the x-direction as a function of the emitter-pinhole x-distance. Simulations show SpinFlux with varying pinhole sizes and widefield SMLM. (*e*) Improvement of the SpinFlux CRLB over SMLM as a function of the emitter-pinhole x-distance for varying pinhole sizes. (*f*) Average amount of signal photons after compensation for non-maximum illumination intensity as a function of the emitter-pinhole x-distance, for SpinFlux with varying pinhole sizes and widefield SMLM. (*g*) Average amount of background photons per pixel as a function of the emitter-pinhole x-distance, for SpinFlux with varying pinhole sizes and widefield SMLM. (*h*) CRLB in the x-direction as a function of the expected signal photon count for varying values of the expected background photon count. The pinhole radius $r_\mathrm{p} = 3\sigma_\mathrm{PSF}$ was used and $(x_\mathrm{p}, y_\mathrm{p}) = (\theta_x, \theta_y)$.

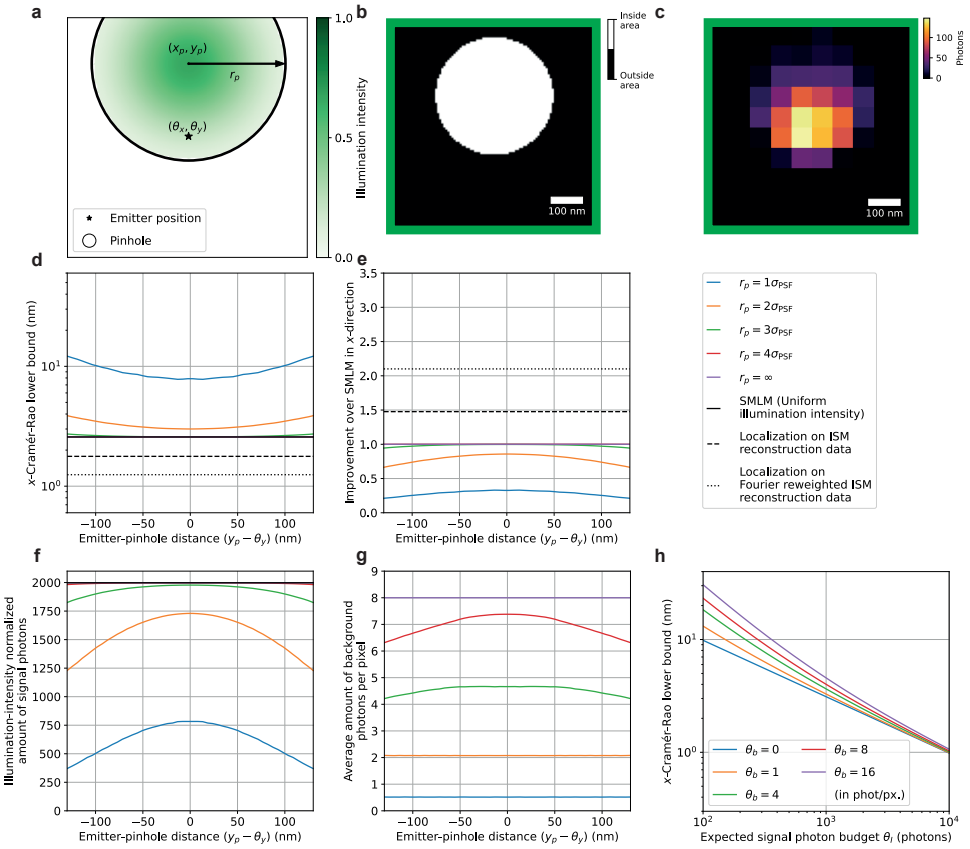

Figure 2.S33: Theoretical minimum localization uncertainty of SpinFlux localization with one y-offset pinhole and pattern. In (*c*)-(*g*), 2000 expected signal photons and 8 expected background photons per pixel were used. Results are evaluated for the scenario where the entire signal photon budget is exhausted after illumination with the pattern (disregarding signal photons blocked by the spinning disk), neglecting the effects of pattern-dependent background. (*a*) Schematic overview of SpinFlux localization with one pinhole with radius r_p, centred at coordinates $(x_\mathrm{p}, y_\mathrm{p})$. In (*d*)-(*g*), the y-distance $(y_\mathrm{p} - \theta_y)$ between the pinhole and the emitter is varied, where $x_\mathrm{p} = \theta_x$. (*b*) Example of pinhole in the region of interest (650 × 650 nm). The pinhole radius $r_\mathrm{p} = 2\sigma_\mathrm{PSF}$ was used. The pinhole mask was discretized with $N_{\mathrm{M},x}$, $N_{\mathrm{M},y} = 100$ mesh pixels in each direction. (*c*) Example of fluorescent response in the region of interest, resulting from illumination and emission through the pinhole in (*b*). (*d*) CRLB in the x-direction as a function of the emitter-pinhole y-distance. Simulations show SpinFlux with varying pinhole sizes and widefield SMLM. (*e*) Improvement of the SpinFlux CRLB over SMLM as a function of the emitter-pinhole y-distance for varying pinhole sizes. (*f*) Average amount of signal photons after compensation for non-maximum illumination intensity as a function of the emitter-pinhole y-distance, for SpinFlux with varying pinhole sizes and widefield SMLM. (*g*) Average amount of background photons per pixel as a function of the emitter-pinhole y-distance, for SpinFlux with varying pinhole sizes and widefield SMLM. (*h*) CRLB in the x-direction as a function of the expected signal photon count for varying values of the expected background photon count. The pinhole radius $r_\mathrm{p} = 3\sigma_\mathrm{PSF}$ was used and $(x_\mathrm{p}, y_\mathrm{p}) = (\theta_x, \theta_y)$.

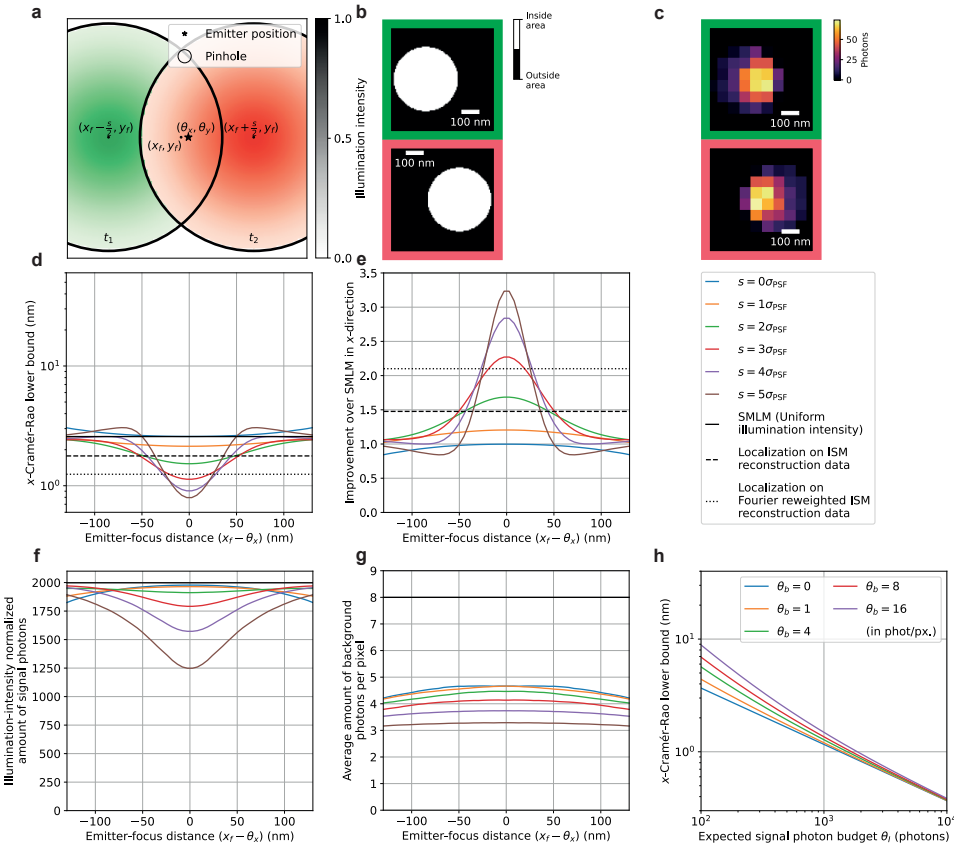

Figure 2.S34: Theoretical minimum localization uncertainty of SpinFlux localization with two pinholes and patterns separated in the x-direction. In (*c*)-(*g*), 2000 expected signal photons and 8 expected background photons per pixel were used, with pinhole radius $r_p = 3\sigma_{PSF}$. Results are evaluated for the scenario where the entire signal photon budget is exhausted after illumination with all patterns (disregarding signal photons blocked by the spinning disk), neglecting the effects of pattern-dependent background. (*a*) Schematic overview of SpinFlux localization with two pinholes, separated in x and centred around the focus coordinates (x_f, y_f). In (*d*)-(*g*), the x-distance $(x_f-\theta_x)$ between the pattern focus and the emitter is varied, where $y_f = \theta_y$. (*b*) Example of pinholes in the region of interest (650 × 650 nm). The pinhole radius $r_p = 2\sigma_{PSF}$ and pinhole separation $s = 2\sigma_{PSF}$ were used. The pinhole masks were discretized with $N_{M,x}$, $N_{M,y} = 100$ mesh pixels in each direction. (*c*) Example of fluorescent response in the region of interest, resulting from illumination and emission through each pinhole in (*b*). (*d*) CRLB in the x-direction as a function of the emitter-focus x-distance. Simulations show SpinFlux with varying pinhole separations and widefield SMLM. (*e*) Improvement of the SpinFlux CRLB over SMLM as a function of the emitter-focus x-distance for varying pinhole separations. (*f*) Average amount of signal photons after compensation for non-maximum illumination intensity as a function of the emitter-focus x-distance, for SpinFlux with varying pinhole separations and widefield SMLM. (*g*) Average amount of background photons per pixel as a function of the emitter-focus x-distance, for SpinFlux with varying pinhole separations and widefield SMLM. (*h*) CRLB in the x-direction as a function of expected signal photon count for varying values of the expected background photon count. The pinhole radius $r_p = 3\sigma_{PSF}$ and pinhole separation $s = 4\sigma_{PSF}$ were used and $(x_f, y_f) = (\theta_x, \theta_y)$.

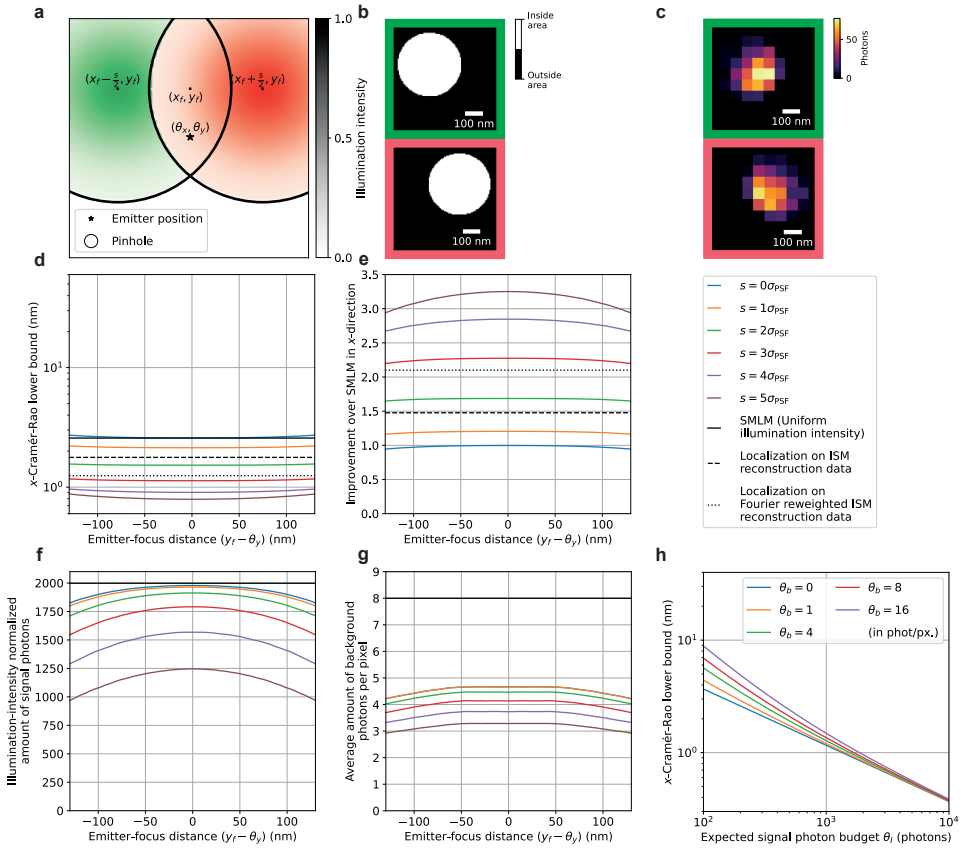

Figure 2.S35: Theoretical minimum localization uncertainty of SpinFlux localization with two y-offset pinholes and patterns separated in the x-direction. In (*c*)-(*g*), 2000 expected signal photons and 8 expected background photons per pixel were used, with pinhole radius $r_p = 3\sigma_{PSF}$. Results are evaluated for the scenario where the entire signal photon budget is exhausted after illumination with all patterns (disregarding signal photons blocked by the spinning disk), neglecting the effects of pattern-dependent background. (*a*) Schematic overview of SpinFlux localization with two pinholes, separated in x and centred around the focus coordinates (x_f, y_f). In (*d*)-(*g*), the y-distance $(y_f - \theta_y)$ between the pattern focus and the emitter is varied, where $x_f = \theta_x$. (*b*) Example of pinholes in the region of interest (650 × 650 nm). The pinhole radius $r_p = 2\sigma_{PSF}$ and pinhole separation $s = 2\sigma_{PSF}$ were used. The pinhole masks were discretized with $N_{M,x}$, $N_{M,y} = 100$ mesh pixels in each direction. (*c*) Example of fluorescent response in the region of interest, resulting from illumination and emission through each pinhole in (*b*). (*d*) CRLB in the x-direction as a function of the emitter-focus y-distance. Simulations show SpinFlux with varying pinhole separations and widefield SMLM. (*e*) Improvement of the SpinFlux CRLB over SMLM as a function of the emitter-focus y-distance for varying pinhole separations. (*f*) Average amount of signal photons after compensation for non-maximum illumination intensity as a function of the emitter-focus y-distance, for SpinFlux with varying pinhole separations and widefield SMLM. (*g*) Average amount of background photons per pixel as a function of the emitter-focus y-distance, for SpinFlux with varying pinhole separations and widefield SMLM. (*h*) CRLB in the x-direction as a function of expected signal photon count for varying values of the expected background photon count. The pinhole radius $r_p = 3\sigma_{PSF}$ and pinhole separation $s = 4\sigma_{PSF}$ were used and $(x_f, y_f) = (\theta_x, \theta_y)$.

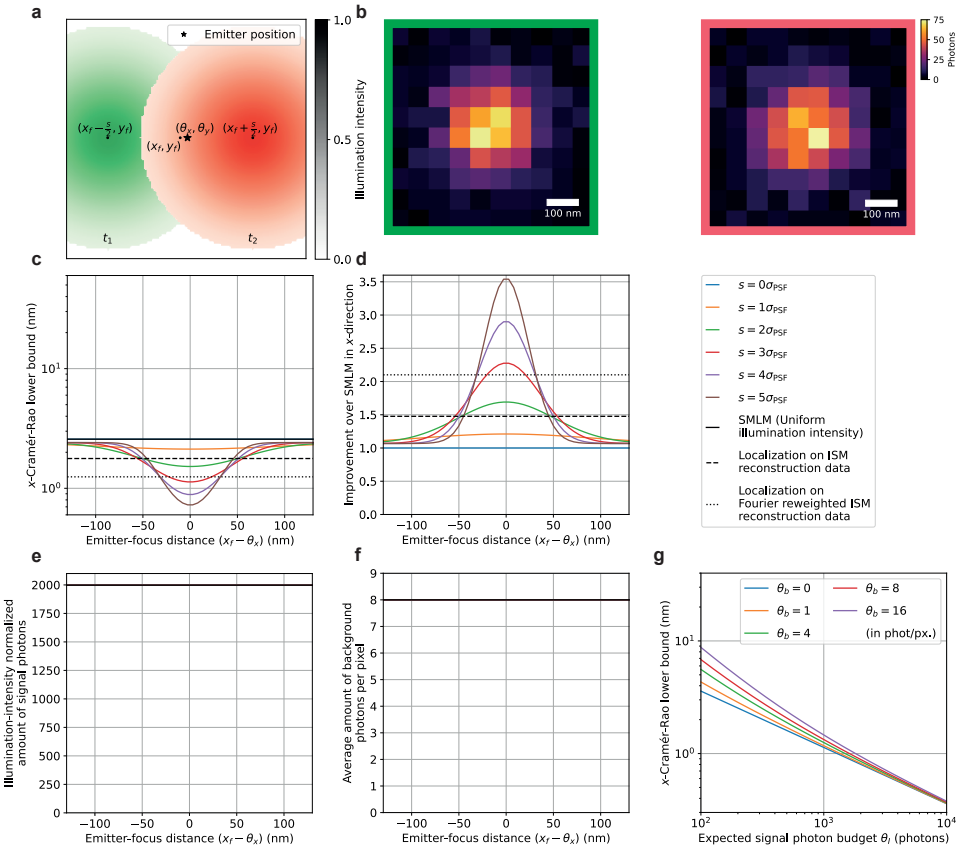

Figure 2.S36: Theoretical minimum localization uncertainty of SpinFlux localization with two patterns without pinholes separated in the x-direction. in (b)-(f), 2000 expected signal photons and 8 expected background photons per pixel were used. Results are evaluated for the scenario where the entire signal photon budget is exhausted after illumination with all patterns, neglecting the effects of pattern-dependent background. (a) Schematic overview of SpinFlux localization with two pinholes, separated in x and centred around the focus coordinates (x_f, y_f). In (c)-(f), the x-distance $(x_f - \theta_x)$ between the pattern focus and the emitter is varied, where $y_f = \theta_y$. (b) Example of fluorescent response in the region of interest, resulting from illumination and emission by each pattern in (a). (c) CRLB in the x-direction as a function of the emitter-focus x-distance. Simulations show SpinFlux with varying pinhole separations and widefield SMLM. (d) Improvement of the SpinFlux CRLB over SMLM as a function of the emitter-focus x-distance for varying pinhole separations. (e) Average amount of signal photons after compensation for non-maximum illumination intensity as a function of the emitter-focus x-distance, for SpinFlux with varying pinhole separations and widefield SMLM. (f) Average amount of background photons per pixel as a function of the emitter-focus x-distance, for SpinFlux with varying pinhole separations and widefield SMLM. (g) CRLB in the x-direction as a function of expected signal photon count for varying values of the expected background photon count. The pattern separation $s = 4\sigma_{\mathrm{PSF}}$ was used and $(x_f, y_f) = (\theta_x, \theta_y)$.

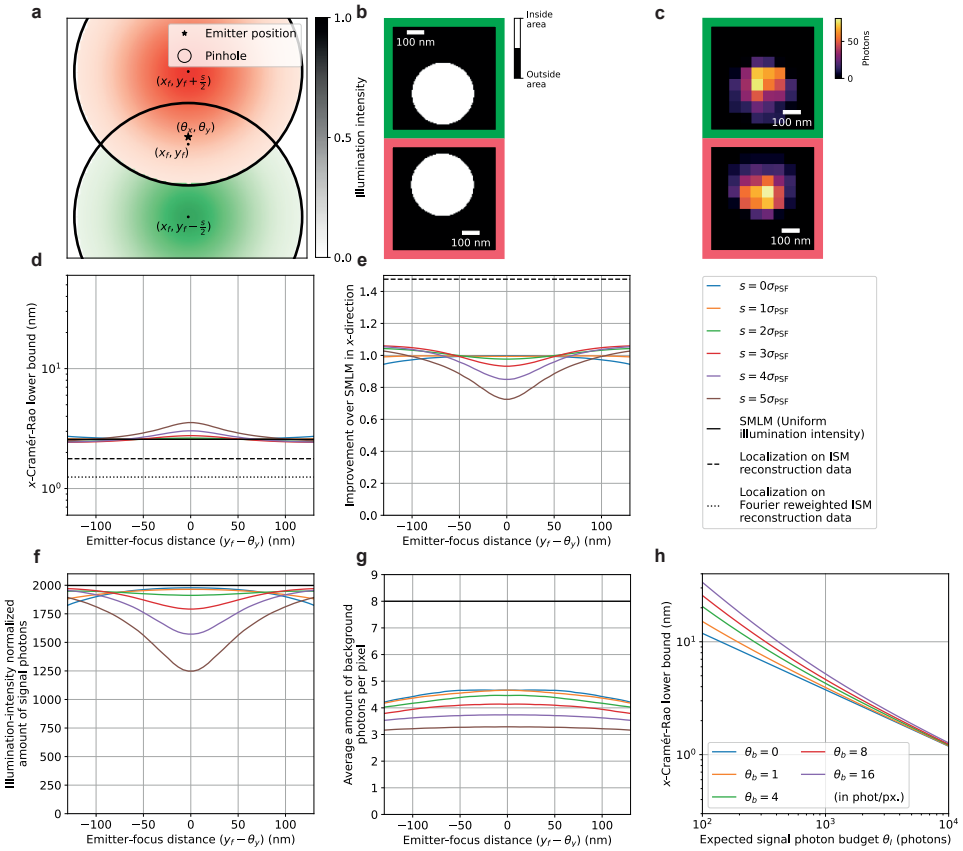

Figure 2.S37: Theoretical minimum localization uncertainty of SpinFlux localization with two pinholes and patterns separated in the y-direction. In (*c*)-(*g*), 2000 expected signal photons and 8 expected background photons per pixel were used, with pinhole radius $r_p = 3\sigma_{PSF}$. Results are evaluated for the scenario where the entire signal photon budget is exhausted after illumination with all patterns (disregarding signal photons blocked by the spinning disk), neglecting the effects of pattern-dependent background. (*a*) Schematic overview of SpinFlux localization with two pinholes, separated in y and centred around the focus coordinates (x_f, y_f). In (*d*)-(*g*), the y-distance $(y_f - \theta_y)$ between the pattern focus and the emitter is varied, where $x_f = \theta_x$. (*b*) Example of pinholes in the region of interest (650 × 650 nm). The pinhole radius $r_p = 2\sigma_{PSF}$ and pinhole separation $s = 2\sigma_{PSF}$ were used. The pinhole masks were discretized with $N_{M,x}$, $N_{M,y} = 100$ mesh pixels in each direction. (*c*) Example of fluorescent response in the region of interest, resulting from illumination and emission through each pinhole in (*b*). (*d*) CRLB in the x-direction as a function of the emitter-focus y-distance. Simulations show SpinFlux with varying pinhole separations and widefield SMLM. (*e*) Improvement of the SpinFlux CRLB over SMLM as a function of the emitter-focus y-distance for varying pinhole separations. (*f*) Average amount of signal photons after compensation for non-maximum illumination intensity as a function of the emitter-focus y-distance, for SpinFlux with varying pinhole separations and widefield SMLM. (*g*) Average amount of background photons per pixel as a function of the emitter-focus y-distance, for SpinFlux with varying pinhole separations and widefield SMLM. (*h*) CRLB in the x-direction as a function of expected signal photon count for varying values of the expected background photon count. The pinhole radius $r_p = 3\sigma_{PSF}$ and pinhole separation $s = 4\sigma_{PSF}$ were used and $(x_f, y_f) = (\theta_x, \theta_y)$.

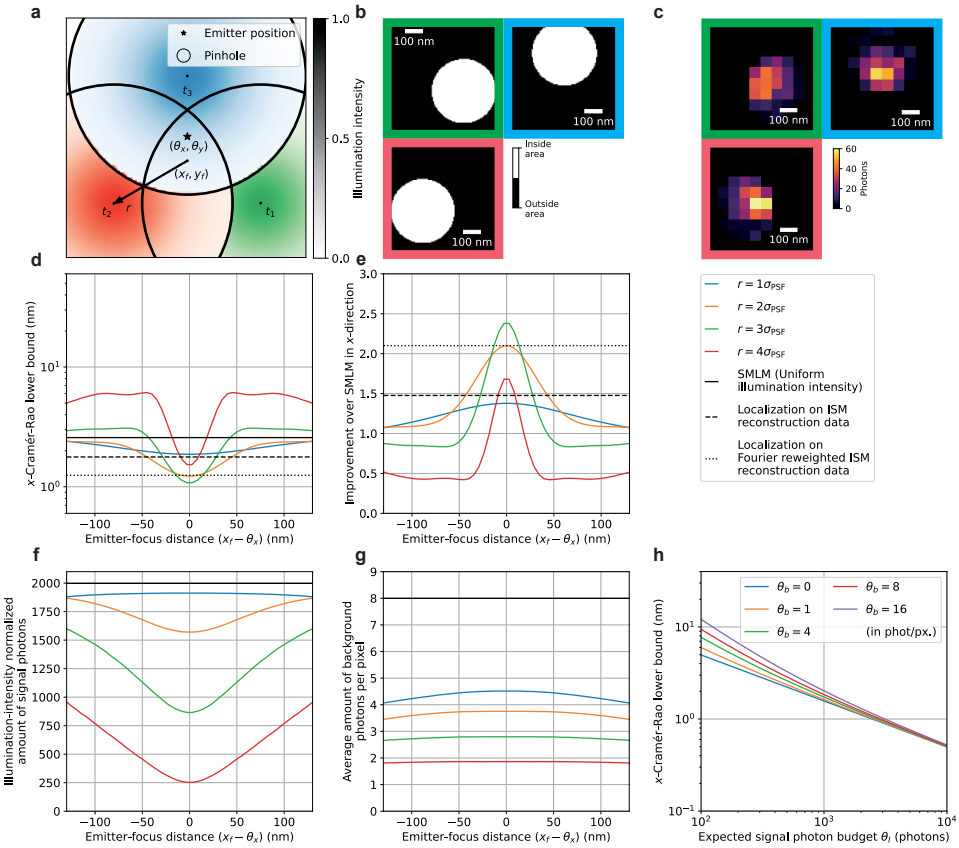

Figure 2.S38: Theoretical minimum localization uncertainty of SpinFlux localization with three pinholes and patterns in an equilateral triangle configuration. In (*c*)-(*g*), we used 2000 expected signal photons and 8 expected background photons per pixel, with pinhole radius $r_p = 3\sigma_{PSF}$. Results are evaluated for the scenario where the entire signal photon budget is exhausted after illumination with all patterns (disregarding signal photons blocked by the spinning disk), neglecting the effects of pattern-dependent background. (*a*) Schematic overview of SpinFlux localization with a triangle of three pinholes, centred at focus coordinates (x_f, y_f). In (*d*)-(*g*), the *x*-distance $(x_f - \theta_x)$ between the pattern focus and the emitter is varied, where $y_f = \theta_y$. (*b*) Example of pinholes in the region of interest (650 × 650 nm). The pinhole radius $r_p = 2\sigma_{PSF}$ and pinhole spacing $r = 1.5\sigma_{PSF}$ were used. The pinhole masks were discretized with $N_{M,x}$, $N_{M,y} = 100$ mesh pixels in each direction. (*c*) Example of fluorescent response in the region of interest, resulting from illumination and emission through each pinhole in (*b*). (*d*) CRLB in the *x*-direction as a function of the emitter-focus *x*-distance. Simulations show SpinFlux with varying pinhole spacing and widefield SMLM. (*e*) Improvement of the SpinFlux CRLB over SMLM as a function of the emitter-focus *x*-distance for varying pinhole spacing. (*f*) Average amount of signal photons after compensation for non-maximum illumination intensity as a function of the emitter-focus *x*-distance, for SpinFlux with varying pinhole spacing and widefield SMLM. (*g*) Average amount of background photons per pixel as a function of the emitter-focus *x*-distance, for SpinFlux with varying pinhole spacing and widefield SMLM. (*h*) CRLB in the *x*-direction as a function of expected signal photon count for varying values of the expected background photon count. The pinhole radius $r_p = 3\sigma_{PSF}$ and pinhole spacing $r = 2\sigma_{PSF}$ were used and $(x_f, y_f) = (\theta_x, \theta_y)$.

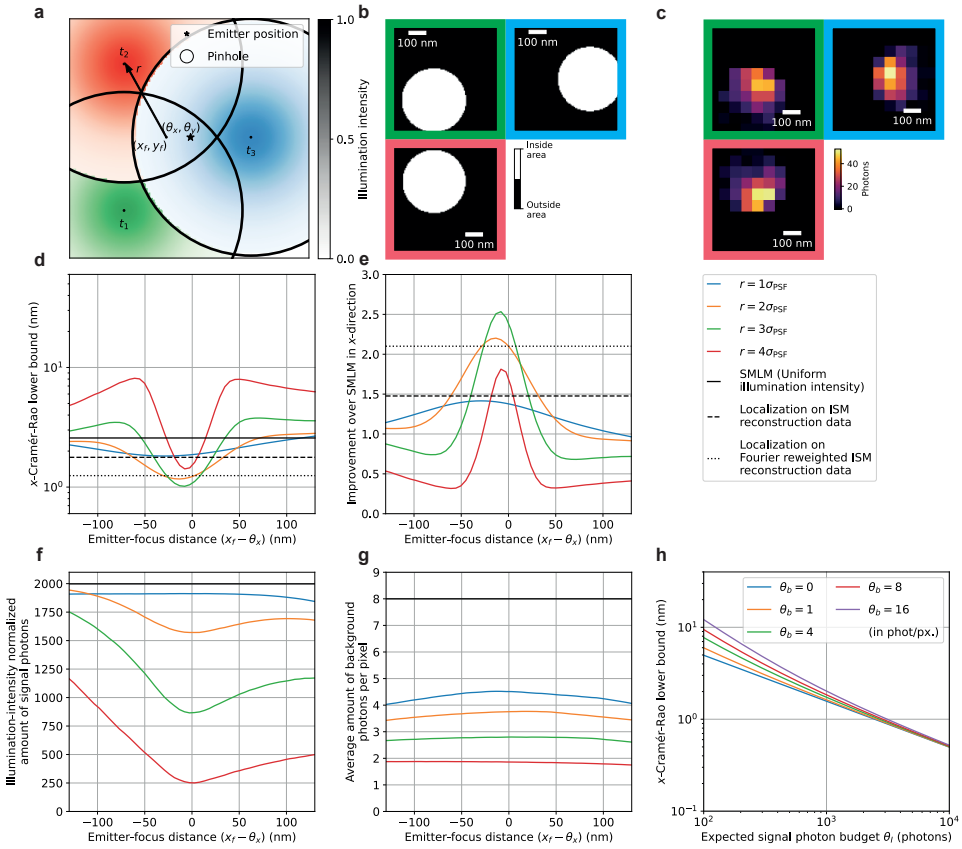

Figure 2.S39: Theoretical minimum localization uncertainty of SpinFlux localization with three pinholes and patterns in a 90° rotated equilateral triangle configuration. The pattern is rotated clockwise by 90 degrees with respect to Fig. 2.S38. In (*c*)-(*g*), we used 2000 expected signal photons and 8 expected background photons per pixel, with pinhole radius $r_p = 3\sigma_{PSF}$. Results are evaluated for the scenario where the entire signal photon budget is exhausted after illumination with all patterns (disregarding signal photons blocked by the spinning disk), neglecting the effects of pattern-dependent background. (*a*) Schematic overview of SpinFlux localization with a triangle of three pinholes, centred at focus coordinates (x_f, y_f). In (*d*)-(*g*), the x-distance $(x_f - \theta_x)$ between the pattern focus and the emitter is varied, where $y_f = \theta_y$. (*b*) Example of pinholes in the region of interest (650 × 650 nm). The pinhole radius $r_p = 2\sigma_{PSF}$ and pinhole spacing $r = 1.5\sigma_{PSF}$ were used. The pinhole masks were discretized with $N_{M,x}$, $N_{M,y} = 100$ mesh pixels in each direction. (*c*) Example of fluorescent response in the region of interest, resulting from illumination and emission through each pinhole in (*b*). (*d*) CRLB in the x-direction as a function of the emitter-focus x-distance. Simulations show SpinFlux with varying pinhole spacing and widefield SMLM. (*e*) Improvement of the SpinFlux CRLB over SMLM as a function of the emitter-focus x-distance for varying pinhole spacing. (*f*) Average amount of signal photons after compensation for non-maximum illumination intensity as a function of the emitter-focus x-distance, for SpinFlux with varying pinhole spacing and widefield SMLM. (*g*) Average amount of background photons per pixel as a function of the emitter-focus x-distance, for SpinFlux with varying pinhole spacing and widefield SMLM. (*h*) CRLB in the x-direction as a function of expected signal photon count for varying values of the expected background photon count. The pinhole radius $r_p = 3\sigma_{PSF}$ and pinhole spacing $r = 2\sigma_{PSF}$ were used and $(x_f, y_f) = (\theta_x, \theta_y)$.

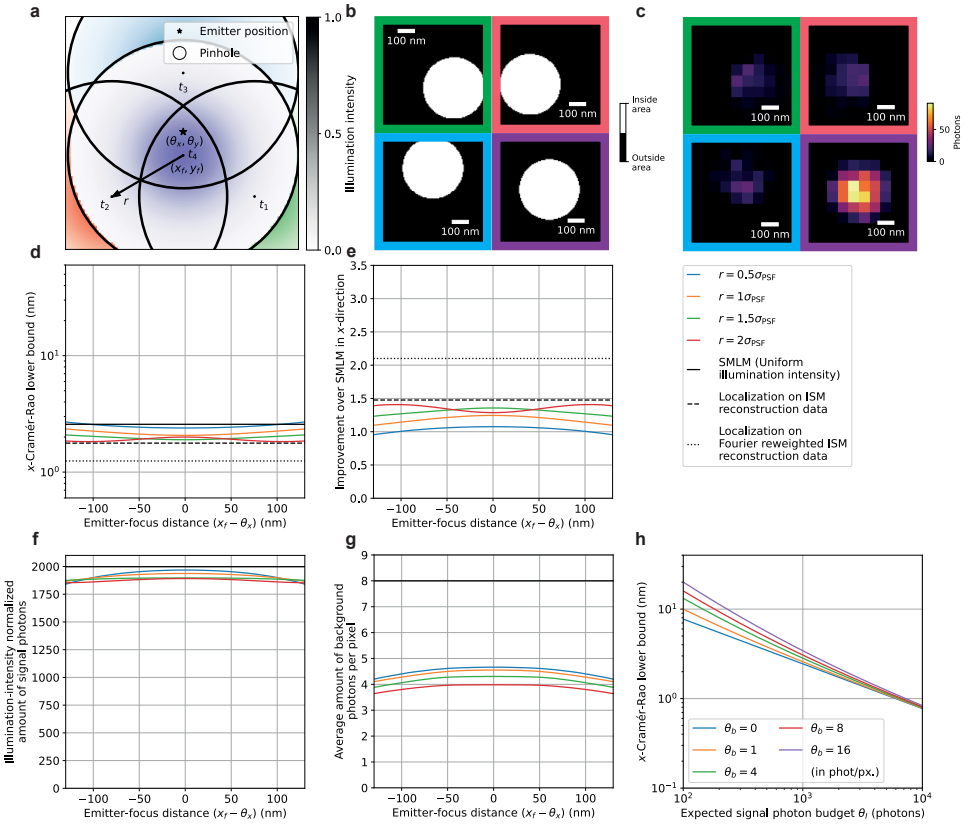

Figure 2.S40: Theoretical minimum localization uncertainty of SpinFlux localization with four pinholes and patterns in an equilateral triangle configuration with a centre pinhole. In (*c*)-(*g*), we used 2000 expected signal photons and 8 expected background photons per pixel, with pinhole radius $r_p = 3\sigma_{PSF}$. Results are evaluated for the scenario where the entire signal photon budget is exhausted after illumination with all patterns (disregarding signal photons blocked by the spinning disk), neglecting the effects of pattern-dependent background. (*a*) Schematic overview of SpinFlux localization with a triangle of three pinholes with an additional centre pinhole, centred at focus coordinates (x_f, y_f). In (*d*)-(*g*), the x-distance $(x_f - \theta_x)$ between the pattern focus and the emitter is varied, where $y_f = \theta_y$. (*b*) Example of pinholes in the region of interest (650 × 650 nm). The pinhole radius $r_p = 2\sigma_{PSF}$ and pinhole spacing $r = 1.5\sigma_{PSF}$ were used. The pinhole masks were discretized with $N_{M,x}$, $N_{M,y} = 100$ mesh pixels in each direction. (*c*) Example of fluorescent response in the region of interest, resulting from illumination and emission through each pinhole in (*b*). (*d*) CRLB in the x-direction as a function of the emitter-focus x-distance. Simulations show SpinFlux with varying pinhole spacing and widefield SMLM. (*e*) Improvement of the SpinFlux CRLB over SMLM as a function of the emitter-focus x-distance for varying pinhole spacing. (*f*) Average amount of signal photons after compensation for non-maximum illumination intensity as a function of the emitter-focus x-distance, for SpinFlux with varying pinhole spacing and widefield SMLM. (*g*) Average amount of background photons per pixel as a function of the emitter-focus x-distance, for SpinFlux with varying pinhole spacing and widefield SMLM. (*h*) CRLB in the x-direction as a function of expected signal photon count for varying values of the expected background photon count. The pinhole radius $r_p = 3\sigma_{PSF}$ and pinhole spacing $r = 2\sigma_{PSF}$ were used and $(x_f, y_f) = (\theta_x, \theta_y)$.

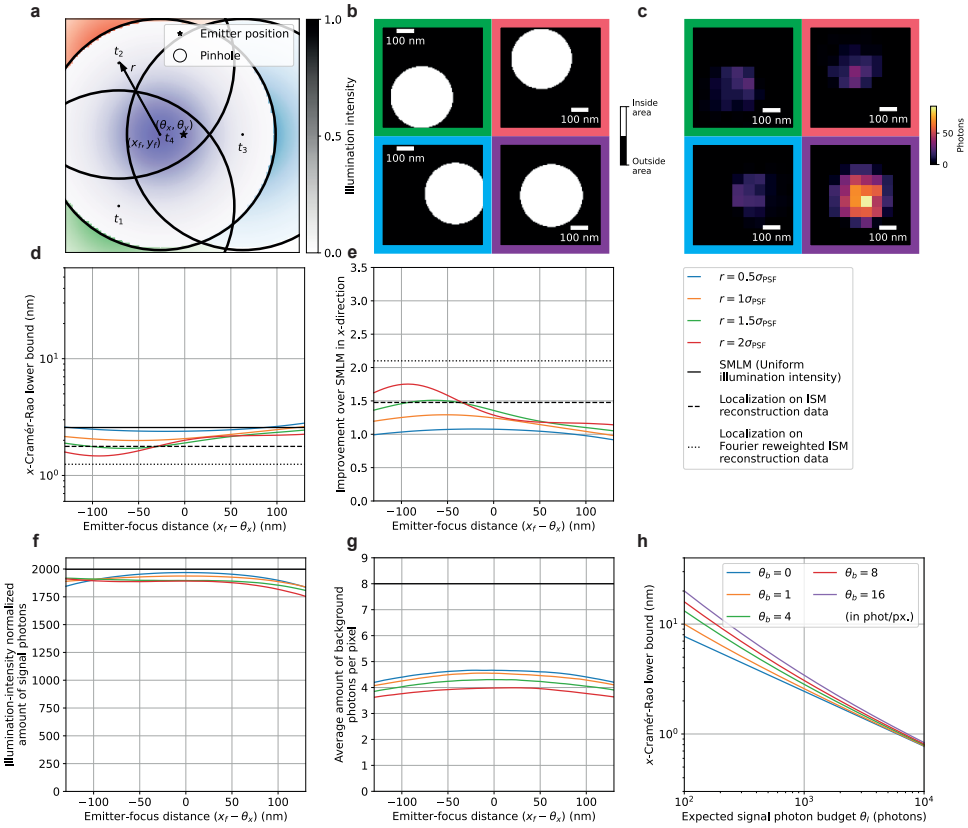

Figure 2.S41: Theoretical minimum localization uncertainty of SpinFlux localization with four pinholes and patterns in a 90° rotated equilateral triangle configuration with a centre pinhole. The pattern is rotated clockwise by 90 degrees with respect to Fig. 2.S40. In (*c*)-(*g*), we used 2000 expected signal photons and 8 expected background photons per pixel, with pinhole radius $r_p = 3\sigma_{PSF}$. Results are evaluated for the scenario where the entire signal photon budget is exhausted after illumination with all patterns (disregarding signal photons blocked by the spinning disk), neglecting the effects of pattern-dependent background. (*a*) Schematic overview of SpinFlux localization with a triangle of three pinholes with an additional centre pinhole, centred at focus coordinates (x_f, y_f). In (*d*)-(*g*), the x-distance $(x_f - \theta_x)$ between the pattern focus and the emitter is varied, where $y_f = \theta_y$. (*b*) Example of pinholes in the region of interest (650 × 650 nm). The pinhole radius $r_p = 2\sigma_{PSF}$ and pinhole spacing $r = 1.5\sigma_{PSF}$ were used. The pinhole masks were discretized with $N_{M,x}$, $N_{M,y} = 100$ mesh pixels in each direction. (*c*) Example of fluorescent response in the region of interest, resulting from illumination and emission through each pinhole in (*b*). (*d*) CRLB in the x-direction as a function of the emitter-focus x-distance. Simulations show SpinFlux with varying pinhole spacing and widefield SMLM. (*e*) Improvement of the SpinFlux CRLB over SMLM as a function of the emitter-focus x-distance for varying pinhole spacing. (*f*) Average amount of signal photons after compensation for non-maximum illumination intensity as a function of the emitter-focus x-distance, for SpinFlux with varying pinhole spacing and widefield SMLM. (*g*) Average amount of background photons per pixel as a function of the emitter-focus x-distance, for SpinFlux with varying pinhole spacing and widefield SMLM. (*h*) CRLB in the x-direction as a function of expected signal photon count for varying values of the expected background photon count. The pinhole radius $r_p = 3\sigma_{PSF}$ and pinhole spacing $r = 2\sigma_{PSF}$ were used and $(x_f, y_f) = (\theta_x, \theta_y)$.

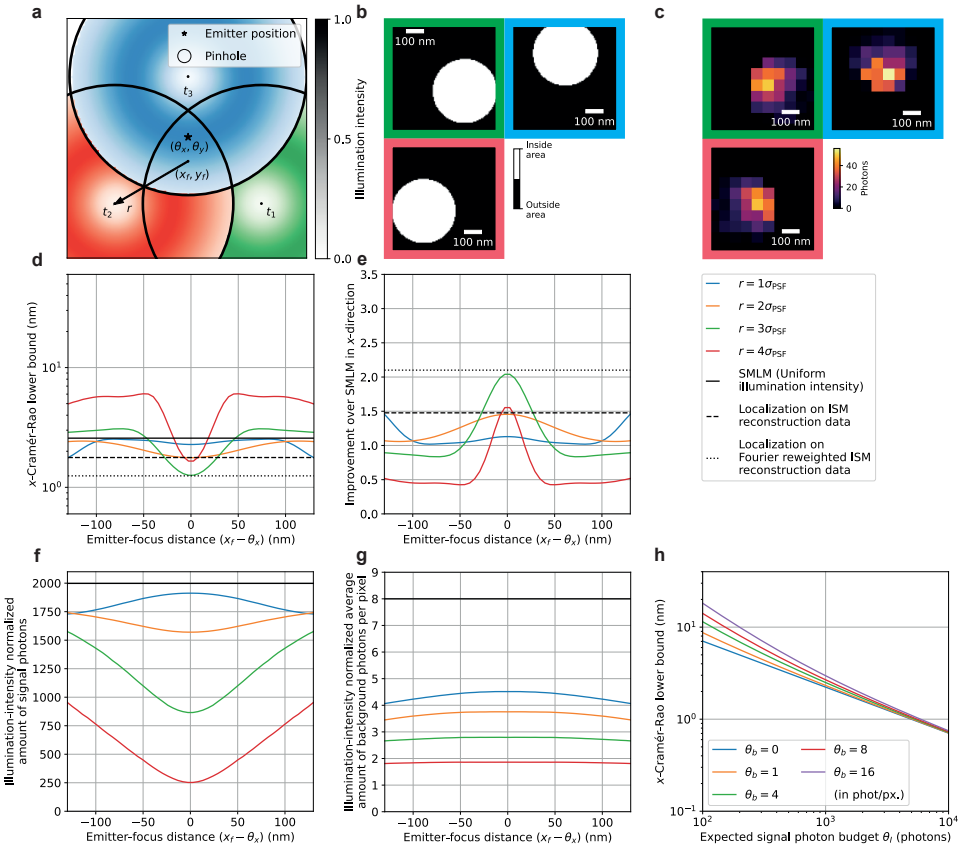

Figure 2.S42: Theoretical minimum localization uncertainty of SpinFlux localization with three pinholes and donut-shaped patterns in an equilateral triangle configuration. In (*c*)-(*g*), we used 2000 expected signal photons and 8 expected background photons per pixel, with pinhole radius $r_p = 3\sigma_{PSF}$. Results are evaluated for the scenario where the entire signal photon budget is exhausted after illumination with all patterns (disregarding signal photons blocked by the spinning disk), neglecting the effects of pattern-dependent background. (*a*) Schematic overview of SpinFlux localization with a triangle of three pinholes, centred at focus coordinates (x_f, y_f). In (*d*)-(*g*), the *x*-distance $(x_f - \theta_x)$ between the pattern focus and the emitter is varied, where $y_f = \theta_y$. (*b*) Example of pinholes in the region of interest (650 × 650 nm). The pinhole radius $r_p = 2\sigma_{PSF}$ and pinhole spacing $r = 1.5\sigma_{PSF}$ were used. The pinhole masks were discretized with $N_{M,x}$, $N_{M,y} = 100$ mesh pixels in each direction. (*c*) Example of fluorescent response in the region of interest, resulting from illumination and emission through each pinhole in (*b*). (*d*) CRLB in the *x*-direction as a function of the emitter-focus *x*-distance. Simulations show SpinFlux with varying pinhole spacing and widefield SMLM. (*e*) Improvement of the SpinFlux CRLB over SMLM as a function of the emitter-focus *x*-distance for varying pinhole spacing. (*f*) Average amount of signal photons after compensation for non-maximum illumination intensity as a function of the emitter-focus *x*-distance, for SpinFlux with varying pinhole spacing and widefield SMLM. (*g*) Average amount of background photons per pixel as a function of the emitter-focus *x*-distance, for SpinFlux with varying pinhole spacing and widefield SMLM. (*h*) CRLB in the *x*-direction as a function of expected signal photon count for varying values of the expected background photon count. The pinhole radius $r_p = 3\sigma_{PSF}$ and pinhole spacing $r = 2\sigma_{PSF}$ were used and $(x_f, y_f) = (\theta_x, \theta_y)$.

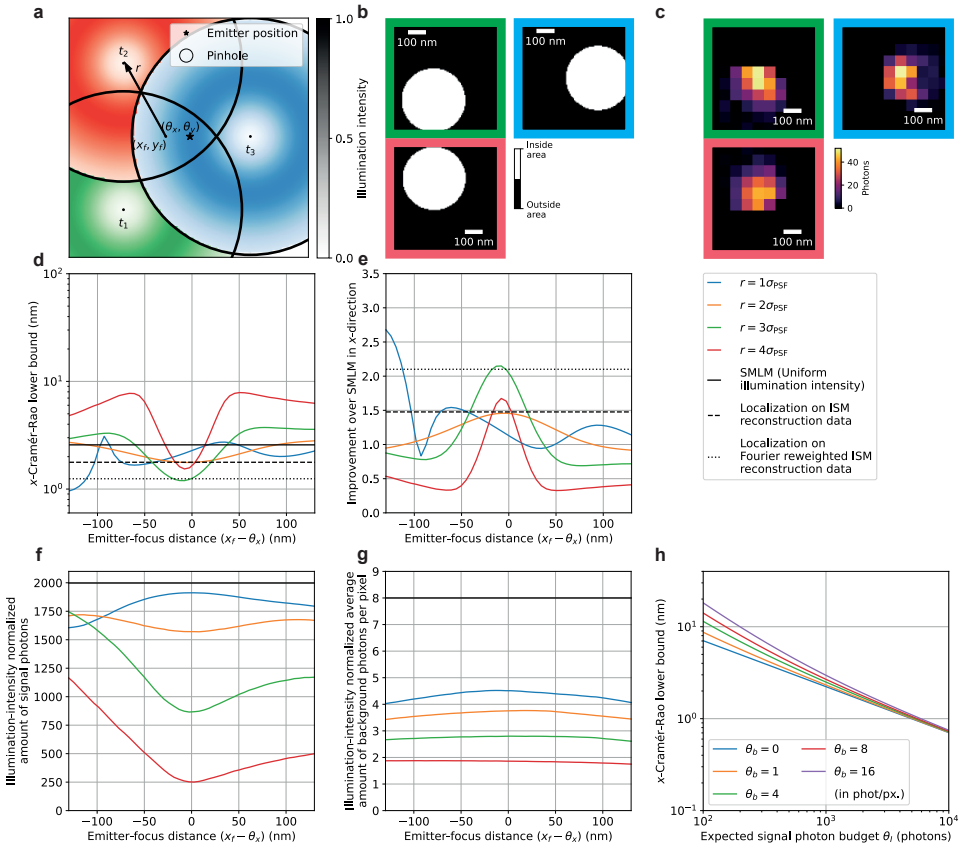

Figure 2.S43: Theoretical minimum localization uncertainty of SpinFlux localization with three pinholes and donut-shaped patterns in a 90° rotated equilateral triangle configuration. The pattern is rotated clockwise by 90 degrees with respect to Fig. 2.S38. In (*c*)-(*g*), we used 2000 expected signal photons and 8 expected background photons per pixel, with pinhole radius $r_p = 3\sigma_{PSF}$. Results are evaluated for the scenario where the entire signal photon budget is exhausted after illumination with all patterns (disregarding signal photons blocked by the spinning disk), neglecting the effects of pattern-dependent background. (*a*) Schematic overview of SpinFlux localization with a triangle of three pinholes, centred at focus coordinates (x_f, y_f). In (*d*)-(*g*), the x-distance $(x_f - \theta_x)$ between the pattern focus and the emitter is varied, where $y_f = \theta_y$. (*b*) Example of pinholes in the region of interest (650 × 650 nm). The pinhole radius $r_p = 2\sigma_{PSF}$ and pinhole spacing $r = 1.5\sigma_{PSF}$ were used. The pinhole masks were discretized with $N_{M,x}$, $N_{M,y} = 100$ mesh pixels in each direction. (*c*) Example of fluorescent response in the region of interest, resulting from illumination and emission through each pinhole in (*b*). (*d*) CRLB in the x-direction as a function of the emitter-focus x-distance. Simulations show SpinFlux with varying pinhole spacing and widefield SMLM. (*e*) Improvement of the SpinFlux CRLB over SMLM as a function of the emitter-focus x-distance for varying pinhole spacing. (*f*) Average amount of signal photons after compensation for non-maximum illumination intensity as a function of the emitter-focus x-distance, for SpinFlux with varying pinhole spacing and widefield SMLM. (*g*) Average amount of background photons per pixel as a function of the emitter-focus x-distance, for SpinFlux with varying pinhole spacing and widefield SMLM. (*h*) CRLB in the x-direction as a function of expected signal photon count for varying values of the expected background photon count. The pinhole radius $r_p = 3\sigma_{PSF}$ and pinhole spacing $r = 2\sigma_{PSF}$ were used and $(x_f, y_f) = (\theta_x, \theta_y)$.

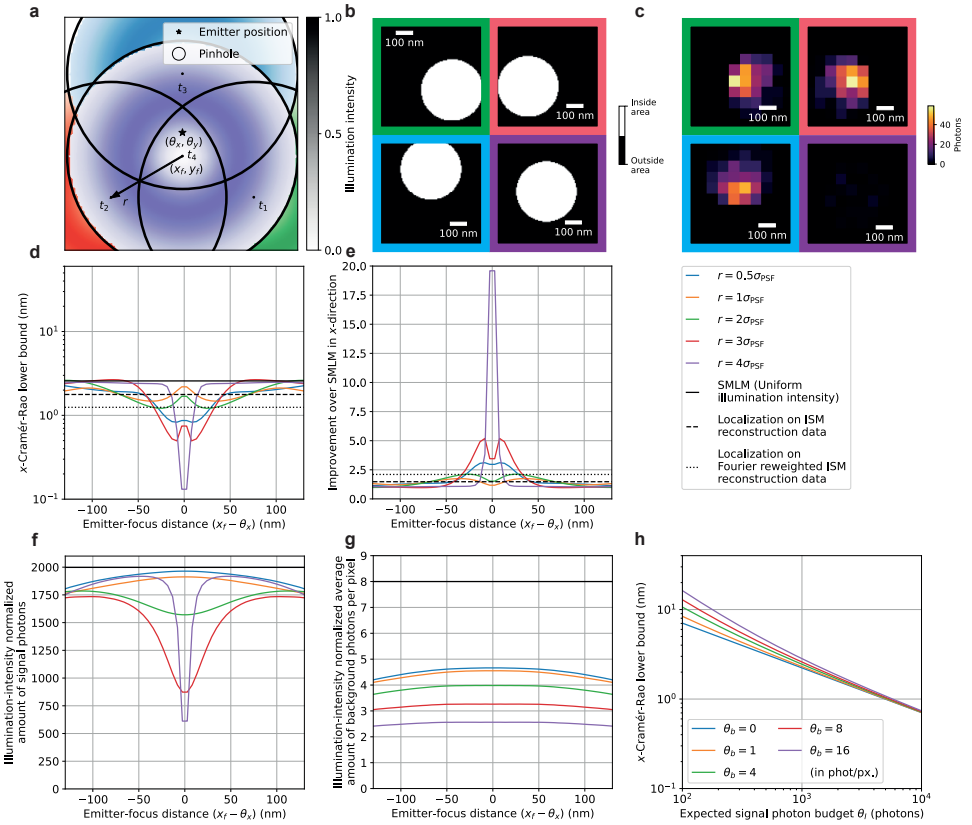

Figure 2.S44: Theoretical minimum localization uncertainty of SpinFlux localization with four pinholes and donut-shaped patterns in an equilateral triangle configuration with a centre pinhole. In (*c*)-(*g*), we used 2000 expected signal photons and 8 expected background photons per pixel, with pinhole radius $r_p = 3\sigma_{PSF}$. Results are evaluated for the scenario where the entire signal photon budget is exhausted after illumination with all patterns (disregarding signal photons blocked by the spinning disk), neglecting the effects of pattern-dependent background. (*a*) Schematic overview of SpinFlux localization with a triangle of three pinholes with an additional centre pinhole, centred at focus coordinates (x_f, y_f). In (*d*)-(*g*), the *x*-distance $(x_f - \theta_x)$ between the pattern focus and the emitter is varied, where $y_f = \theta_y$. (*b*) Example of pinholes in the region of interest (650 × 650 nm). The pinhole radius $r_p = 2\sigma_{PSF}$ and pinhole spacing $r = 1.5\sigma_{PSF}$ were used. The pinhole masks were discretized with $N_{M,x}$, $N_{M,y} = 100$ mesh pixels in each direction. (*c*) Example of fluorescent response in the region of interest, resulting from illumination and emission through each pinhole in (*b*). (*d*) CRLB in the *x*-direction as a function of the emitter-focus *x*-distance. Simulations show SpinFlux with varying pinhole spacing and widefield SMLM. (*e*) Improvement of the SpinFlux CRLB over SMLM as a function of the emitter-focus *x*-distance for varying pinhole spacing. (*f*) Average amount of signal photons after compensation for non-maximum illumination intensity as a function of the emitter-focus *x*-distance, for SpinFlux with varying pinhole spacing and widefield SMLM. (*g*) Average amount of background photons per pixel as a function of the emitter-focus *x*-distance, for SpinFlux with varying pinhole spacing and widefield SMLM. (*h*) CRLB in the *x*-direction as a function of expected signal photon count for varying values of the expected background photon count. The pinhole radius $r_p = 3\sigma_{PSF}$ and pinhole spacing $r = 2\sigma_{PSF}$ were used and $(x_f, y_f) = (\theta_x, \theta_y)$.

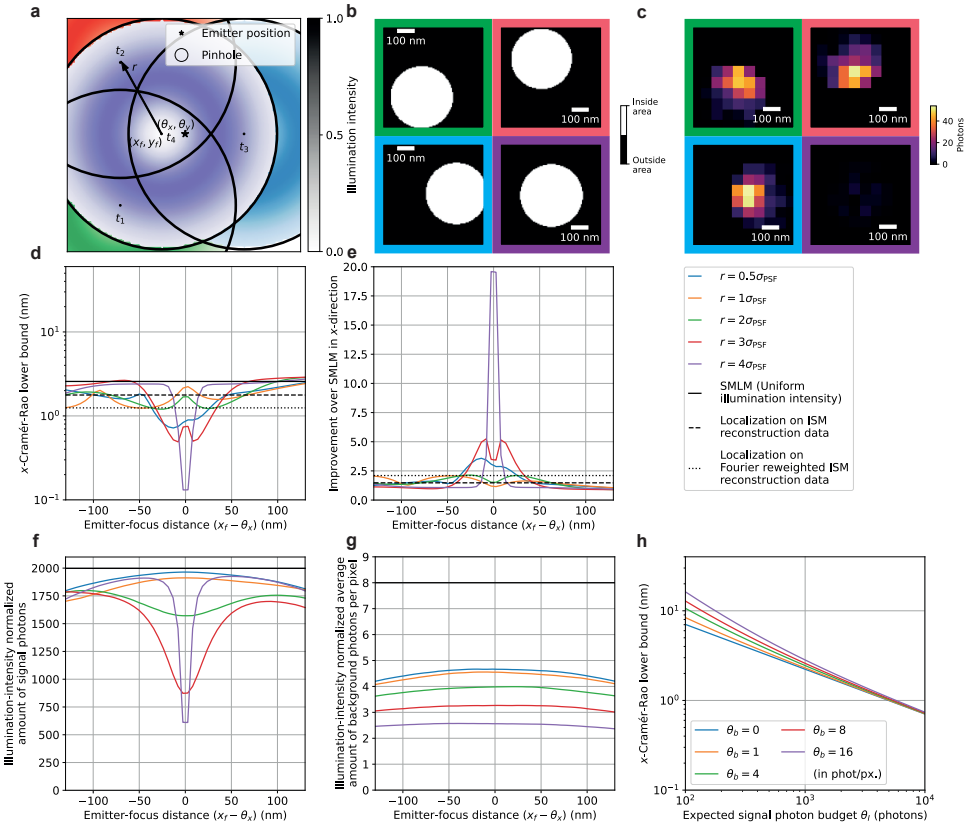

Figure 2.S45: Theoretical minimum localization uncertainty of SpinFlux localization with four pinholes and donut-shaped patterns in a 90° rotated equilateral triangle configuration with a centre pinhole. The pattern is rotated clockwise by 90 degrees with respect to Fig. 2.S40. In (*c*)-(*g*), we used 2000 expected signal photons and 8 expected background photons per pixel, with pinhole radius $r_p = 3\sigma_{PSF}$. Results are evaluated for the scenario where the entire signal photon budget is exhausted after illumination with all patterns (disregarding signal photons blocked by the spinning disk), neglecting the effects of pattern-dependent background. (*a*) Schematic overview of SpinFlux localization with a triangle of three pinholes with an additional centre pinhole, centred at focus coordinates (x_f, y_f). In (*d*)-(*g*), the *x*-distance $(x_f - \theta_x)$ between the pattern focus and the emitter is varied, where $y_f = \theta_y$. (*b*) Example of pinholes in the region of interest (650 × 650 nm). The pinhole radius $r_p = 2\sigma_{PSF}$ and pinhole spacing $r = 1.5\sigma_{PSF}$ were used. The pinhole masks were discretized with $N_{M,x}$, $N_{M,y} = 100$ mesh pixels in each direction. (*c*) Example of fluorescent response in the region of interest, resulting from illumination and emission through each pinhole in (*b*). (*d*) CRLB in the *x*-direction as a function of the emitter-focus *x*-distance. Simulations show SpinFlux with varying pinhole spacing and widefield SMLM. (*e*) Improvement of the SpinFlux CRLB over SMLM as a function of the emitter-focus *x*-distance for varying pinhole spacing. (*f*) Average amount of signal photons after compensation for non-maximum illumination intensity as a function of the emitter-focus *x*-distance, for SpinFlux with varying pinhole spacing and widefield SMLM. (*g*) Average amount of background photons per pixel as a function of the emitter-focus *x*-distance, for SpinFlux with varying pinhole spacing and widefield SMLM. (*h*) CRLB in the *x*-direction as a function of expected signal photon count for varying values of the expected background photon count. The pinhole radius $r_p = 3\sigma_{PSF}$ and pinhole spacing $r = 2\sigma_{PSF}$ were used and $(x_f, y_f) = (\theta_x, \theta_y)$.

Table 2.S1: Model parameters used in the SpinFlux localization precision simulations with Gaussian illumination patterns and with a Gaussian emission point spread function.

Quantity	Symbol	Value
Wavelength of excitation light	λ_{ex}	546 nm
Wavelength of emission light	λ_{em}	600 nm
Amount of pixels in x- and y-direction	N_x, N_y	10 pixels
Total amount of pixels	N_{pixels}	$N_x N_y = 100$ pixels
Pixel size (x- and y-direction)	Δx, Δy	65 nm
Emitter x-position	θ_x	$\frac{N_{\text{pixels}}}{2}\Delta x = 325$ nm
Emitter y-position	θ_y	$\frac{N_{\text{pixels}}}{2}\Delta y = 325$ nm
Expected signal photon budget	θ_I	2000 photons
Expected background photon count	θ_b	8 photons/pixel
Numerical aperture	NA	1.35
Standard deviation of illumination PSF in x- and y-directions	σ_{illum}	$0.21\frac{\lambda_{\text{ex}}}{\text{NA}} = 84.9$ nm
Standard deviation of emission PSF in x- and y-directions	σ_{PSF}	$0.21\frac{\lambda_{\text{em}}}{\text{NA}} = 93.3$ nm
Amount of discretization mesh pixels in x- and y-direction	$N_{x,M}$, $N_{y,M}$	100 pixels
Total amount of discretization mesh pixels	N_{M}	$N_{\text{M},x} N_{\text{M},y} = 10000$ pixels
Discretization mesh pixel size (x-direction)	Δx_{M}	$\frac{N_x}{N_{\text{M},x}} \cdot \Delta x = 6.5$ nm
Discretization mesh pixel size (y-direction)	Δy_{M}	$\frac{N_y}{N_{\text{M},y}} \cdot \Delta y = 6.5$ nm

References

[1] O. Schulz, C. Pieper, M. Clever, J. Pfaff, A. Ruhlandt, R. H. Kehlenbach, F. S. Wouters, J. Großhans, G. Bunt, and J. Enderlein. “Resolution doubling in fluorescence microscopy with confocal spinning-disk image scanning microscopy”. In: *Proceedings of the National Academy of Sciences* 110.52 (2013), pp. 21000–21005.

[2] S. Qin, S. Isbaner, I. Gregor, and J. Enderlein. “Doubling the resolution of a confocal spinning-disk microscope using image scanning microscopy”. In: *Nature Protocols* 16.1 (2020), pp. 164–181.

[3] S. Stallinga and B. Rieger. “The effect of background on localization uncertainty in single emitter imaging”. In: *2012 9th IEEE International Symposium on Biomedical Imaging (ISBI)*. IEEE, 2012, pp. 988–991.

[4] B. Rieger and S. Stallinga. “The Lateral and Axial Localization Uncertainty in Super-Resolution Light Microscopy”. In: *ChemPhysChem* 15.4 (2013), pp. 664–670.

[5] C. S. Smith, N. Joseph, B. Rieger, and K. A. Lidke. “Fast, single-molecule localization that achieves theoretically minimum uncertainty”. In: *Nature Methods* 7.5 (2010), pp. 373–375.

[6] J. Cnossen, T. Hinsdale, R. Ø. Thorsen, M. Siemons, F. Schueder, R. Jungmann, C. S. Smith, B. Rieger, and S. Stallinga. “Localization microscopy at doubled precision with patterned illumination”. In: *Nature Methods* 17.1 (2019), pp. 59–63.

[7] Q. Houwink, D. Kalisvaart, S. Hung, J. Cnossen, D. Fan, P. Mos, A. Can Ülkü, C. Bruschini, E. Charbon, and C. S. Smith. “Theoretical minimum uncertainty of single-molecule localizations using a single-photon avalanche diode array”. In: *Optics Express* 29.24 (2021), p. 39920.

[8] D. Kalisvaart, J. Cnossen, S. Hung, S. Stallinga, M. Verhaegen, and C. S. Smith. “Precision in iterative modulation enhanced single-molecule localization microscopy”. In: *Biophysical Journal* 121.12 (2022), pp. 2279–2289.

[9] G. M. De Luca, R. M. Breedijk, R. A. Brandt, C. H. Zeelenberg, B. E. de Jong, W. Timmermans, L. N. Azar, R. A. Hoebe, S. Stallinga, and E. M. Manders. “Re-scan confocal microscopy: scanning twice for better resolution”. In: *Biomedical Optics Express* 4.11 (2013), p. 2644.

[10] J. Mertz. *Introduction to Optical Microscopy*. 2nd ed. Cambridge, England: Cambridge University Press, 2019.

[11] J. Pawley, ed. *Handbook of Biological Confocal Microscopy*. 3rd ed. New York, NY: Springer, 2006.

[12] E. Slenders and G. Vicidomini. “ISM-FLUX: MINFLUX with an array detector”. In: *Physical Review Research* 5.2 (2023).

[13] F. Balzarotti, Y. Eilers, K. C. Gwosch, A. H. Gynnå, V. Westphal, F. D. Stefani, J. Elf, and S. W. Hell. “Nanometer resolution imaging and tracking of fluorescent molecules with minimal photon fluxes”. In: *Science* 355.6325 (2017), pp. 606–612.

[14] G. Sirinakis, E. S. Allgeyer, J. Cheng, and D. St Johnston. “Quantitative comparison of spinning disk geometries for PAINT based super-resolution microscopy”. In: *Biomedical Optics Express* 13.7 (2022), p. 3773.

[15] A. R. Halpern, M. Y. Lee, M. D. Howard, M. A. Woodworth, P. R. Nicovich, and J. C. Vaughan. “Versatile, do-it-yourself, low-cost spinning disk confocal microscope”. In: *Biomedical Optics Express* 13.2 (2022), p. 1102.

[16] S. M. Kay. *Fundamentals of Statistical Signal Processing: Estimation Theory*. Prentice Hall international editions. London, England: Prentice Hall, 1993.

[17] R. J. Ober, S. Ram, and E. S. Ward. “Localization Accuracy in Single-Molecule Microscopy”. In: *Biophysical Journal* 86.2 (2004), pp. 1185–1200.

3

Bayesian Posterior Density Estimation Reveals Degeneracy in Three-Dimensional Multiple Emitter Localization

Is it not a strange fate that we should suffer so much fear and doubt for so small a thing?
So small a thing! And I have seen it only for an instant in the house of Elrond.
Could I not have a sight of it again?

John Ronald Reuel Tolkien, *The Fellowship of the Ring*

Raymond van Dijk†
Dylan Kalisvaart†
Jelmer Cnossen
Carlas S. Smith

Scientific Reports, vol. 13, (2023), Article 22372

† These authors contributed equally to this work.

3

Abstract

Single-molecule localization microscopy requires sparse activation of emitters to circumvent the diffraction limit. In densely labelled or thick samples, overlap of emitter images is inevitable. Single-molecule localization of these samples results in a biased parameter estimate with a wrong model of the number of emitters. On the other hand, multiple emitter fitting suffers from point spread function degeneracy, which increases model and parameter uncertainty. To better estimate the model, parameters and uncertainties, a three-dimensional Bayesian multiple emitter fitting algorithm was constructed using reversible jump Markov chain Monte Carlo. It reconstructs the posterior density of both the model and the parameters, namely the three-dimensional position and photon intensity, of overlapping emitters. The ability of the algorithm to separate two emitters at varying distance was evaluated using an astigmatic point spread function. We found that for astigmatic imaging, the posterior distribution of the emitter positions is multimodal when emitters are within two times the in-focus standard deviation of the point spread function. This multimodality describes the ambiguity in position that astigmatism introduces in localization microscopy. Biplane imaging was also tested, proving capable of separating emitters up to 0.75 times the in-focus standard deviation of the point spread function while staying free of multimodality. The posteriors seen in astigmatic and biplane imaging demonstrate how the algorithm can identify point spread function degeneracy and evaluate imaging techniques for three-dimensional multiple-emitter fitting performance.

Significance

This chapter addresses the fundamental challenge of degeneracy in three-dimensional multiple emitter fitting. Degeneracy occurs when different spatial configurations of fluorophores produce nearly indistinguishable image data, making it impossible to uniquely identify their true positions. By applying Bayesian posterior density estimation, we reveal the conditions in which such ambiguities appear, for example in astigmatic imaging. Our method reconstructs the full posterior distribution of the emitter position estimates, making it possible to identify cases where point estimates may provide misleadingly confident results. With this, we show the necessity of using probabilistic frameworks that can capture degeneracy in three-dimensional multiple emitter localization.

3.1. Introduction

Single-molecule localization microscopy (SMLM) [1, 2] circumvents the diffraction limit through localization of sparsely activated emitters and reaches theoretical minimum uncertainty [3]. For localization, SMLM assumes a single molecule is contained in a region of interest (ROI). Overlap of emitter signal is inevitable in densely labelled samples and thick samples for 3D imaging. In SMLM, denser ROIs result in inaccurate estimates that have to be discarded.

Multiple emitter fitting [4–8] mitigates this problem by extending the model to account for more than one emitter in the ROI. For two-dimensional localization, various high density localization methods exists, including temporal correlation [4], compressed sensing [5, 6], deep learning [7], and posterior density reconstruction [8]. These methods work by simultaneously estimating the model and parameters, or by making a model-free reconstruction. In [8], reversible jump Markov chain Monte Carlo (RJMCMC) is used, which is a Bayesian method to sample directly from the posterior distribution, reconstructing the posterior by making a histogram of the samples. Bayesian approaches have the added advantages of including prior information and more accurately representing the uncertainty of model and parameter estimates. The RJMCMC sampler also makes model space jumps, changing the number of parameters while estimating the model.

However, PSF degeneracy [9] complicates multiple emitter fitting in three-dimensional localization. Fig. 3.1, *b-d*, illustrates these problems with high density imaging and PSF degeneracy. As the PSF changes over depth, the image of an emitter at a given depth may match that of a sum of emitters at different depths. Fig. 3.1*e* shows how an astigmatic and tetrapod PSF change over depth. This ambiguity increases model and parameter uncertainty, where a k-emitter model can be represented by a different number of emitters at different positions. It thus complicates the use of most 2D multiple emitter fitting methods for 3D, as they misrepresent these uncertainties.

In this chapter, we use Bayesian posterior density estimation to identify the PSF degeneracy in 3D multiple emitter fitting. To do so, we construct a 3D Bayesian localization algorithm using RJMCMC [10]. The algorithm is described in detail in Section 3.S1 and extends the approach from [8] to 3D. It provides an accurate reconstruction of the estimation uncertainty through posterior density sampling, constructing probability distributions for the number of emitters and their parameters. The reconstructed posteriors are used to quantify the circumstances in which 3D PSF degeneracy occurs in multiple emitter imaging.

Using this method, we show that multiple emitter fitting on two emitters with an astigmatic PSF results in degeneracy when the separation between the emitters is smaller than 2 standard deviations of the in-focus PSF (σ_{PSF}). Between $2\sigma_{\text{PSF}}$ and $1\sigma_{\text{PSF}}$, the multiple emitter fitting problem has two statistically equivalent solutions. Below $1\sigma_{\text{PSF}}$, the emitters are no longer individually identifiable. Additionally, we show that degeneracy in three-dimensional multiple emitter fitting can be avoided using biplane imaging.

Fig. 3.1*a* shows a schematic of the algorithm. After gathering the frames and correcting for the camera gain, the user sets priors and hyperparameters that are appropriate for the imaging conditions. Then, an RJMCMC localization algorithm is ran on each of the frames, finding the posterior of the parameters and number of emitters given the data.

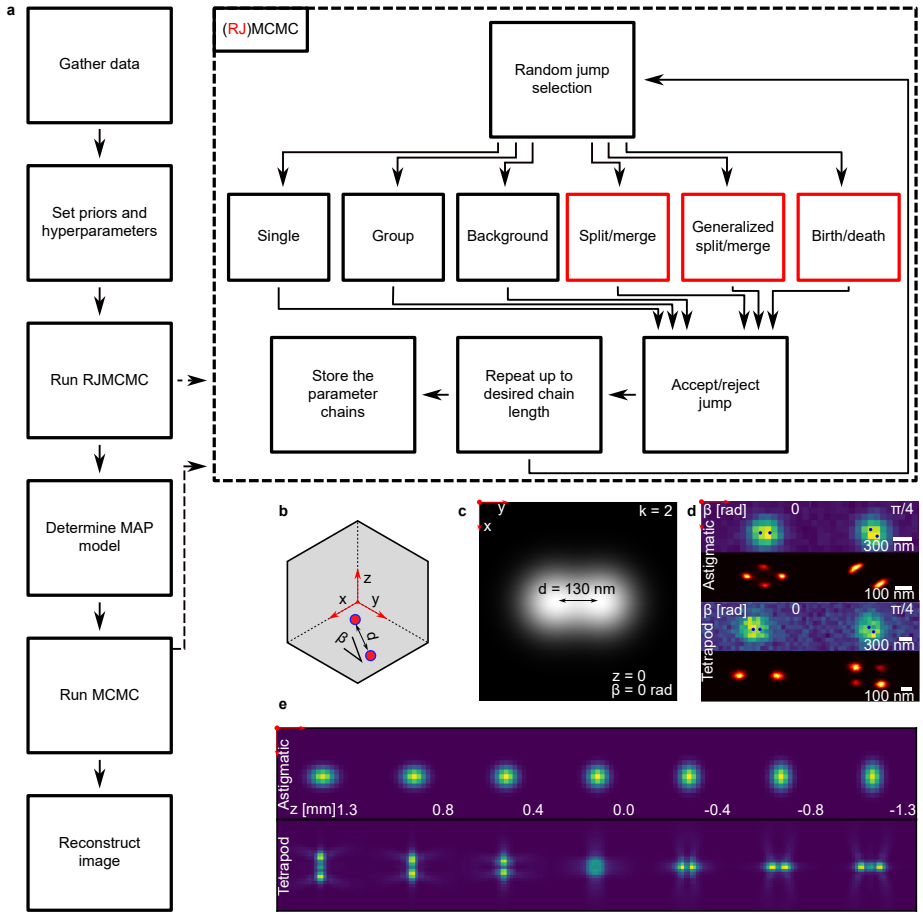

Figure 3.1: Schematic of the algorithm and problem description. (*a*) 3D RJMCMC localization flowchart. Frames are gathered and converted to photon counts. Then, priors and hyperparameters are set. An initial run of RJMCMC samples from the joint posterior of the parameters and model, from which the MAP number of emitters is determined. Using this MAP model, another MCMC run is used to condition the parameter distribution on the estimated model. Finally, the image is reconstructed by plotting histograms of the MCMC chains. The dashed rectangle demonstrates the (RJ)MCMC algorithm. Each loop, a move is randomly selected (RJMCMC moves that act on model space are highlighted in red) and used to propose a new set of parameters. This jump in parameters is accepted or rejected based on the ratio of posteriors. The algorithm repeats this loop, storing the parameters at each iteration to finally output the chain of iterations. (*b*) Diagram of two overlapping emitters separated by distance d and under angle β. (*c*) Ideal image of two nearby emitters. (*d*) Simulated data and reconstruction using astigmatic and tetrapod PSFs. Frames are shown in rows 1 and 3, while the reconstructed posterior distribution is shown in rows 2 and 4. (*e*) Z-scan of the PSFs used in (*d*) to generate and reconstruct the data.

Using the posterior, the maximum a posteriori (MAP) number of emitters is selected, and the estimates within this model are used to start a Markov chain Monte Carlo (MCMC) localization run. The MCMC output is used to form the histogram that reconstructs the object.

3.2. Results

3.2.1. Two emitter separability for astigmatic imaging

We first evaluate the posterior distribution of multiple emitter fitting using an astigmatic PSF, as it is the most commonly used PSF for 3D localization. Two emitters were simulated at varying distance to one another, from 3.0 σ_{PSF} to 0.75 σ_{PSF}, to analyse the ability to separate emitters. This is shown in Fig. 3.2. As MCMC generates samples from the posterior distribution, the reconstructions are made by plotting histograms of the MCMC chains for all of the 100 simulated frames.

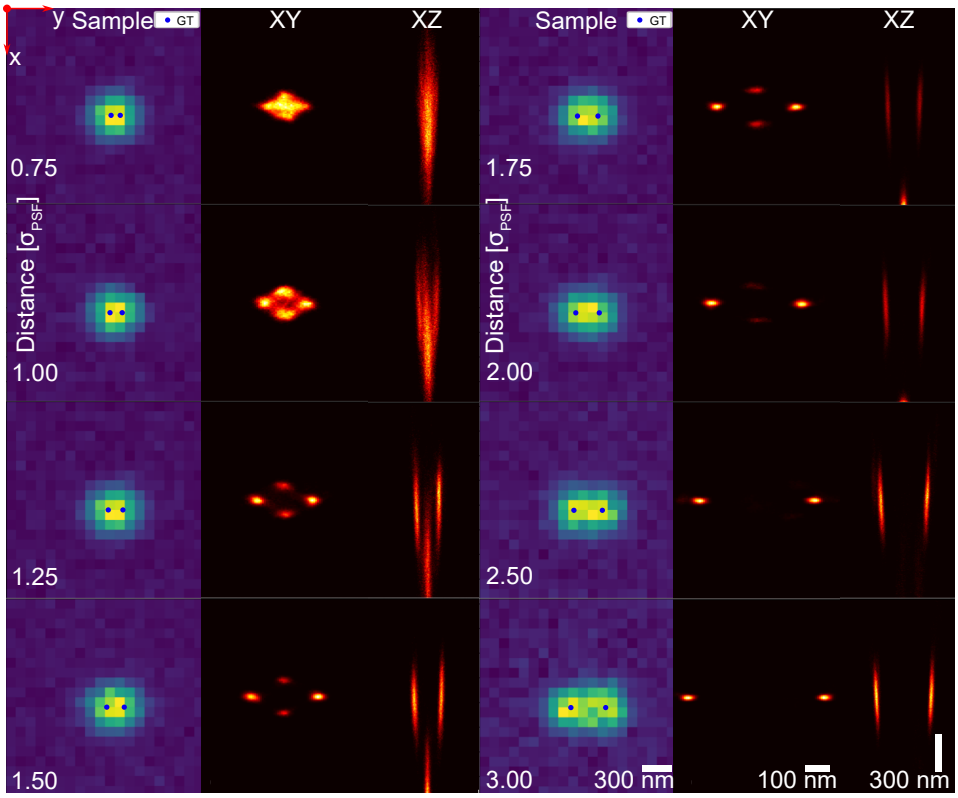

Figure 3.2: Two emitter separability using an astigmatic PSF, collecting 100 simulated frames into one reconstruction while varying emitter distance. (*Columns 1 and 4*) Example frames. (*Columns 2 and 5*) Zoomed in XY plane reconstruction. (*Columns 3 and 6*) Zoomed in XZ plane reconstruction. Emitters were placed in focal plane, with an intensity of 2000 photons each and a background of 20 photons. The ROI is 20 by 20 pixels, scalebars assume an effective pixel size of 100 nm. The reconstructed image consists of histograms from MCMC chains which used the MAP number of emitters as model.

From Fig. 3.2, we see that the algorithm can separate the two emitters up to a distance of 2.5 σ_{PSF}, as the histogram of the reconstructed posterior distribution shows two isolated peaks. For separations between 2 σ_{PSF} and 1 σ_{PSF}, four peaks can be distinguished in the reconstructed posterior distribution, despite the MAP model finding two emitters. At a distance less than 1 σ_{PSF}, the four individual peaks collapse into one clus-

ter. Running a k-means clustering algorithm on the chain outputs for two clusters finds both clusters at the same position, in the middle of the frame. This shows the emitters can no longer be separated at distances lower than 1 σ_{PSF}.

We further investigate the multimodal posterior distribution between 2 σ_{PSF} and 1 σ_{PSF}. To investigate the multimodality, a single frame with four peaks in the reconstruction was analysed as shown in Fig. 3.S12. The four peaks formed two pairs of possible modes, one at the true positions and one perpendicular to those. A chi-squared test was done to determine if either mode was representative of the frame. Interestingly, the chi-square values of 408 and 407 showed that both modes are representative for the frame, as the chi-square value at the 95% confidence interval is 456. We tested the probability of selecting the correct mode under both of these hypotheses. The probability of error was found to be 49.8%, making the modes indistinguishable in terms of likelihood. This confirms that the posterior distribution of the emitter position is indeed multimodal.

While the true mode localizations find the ground truth, the alternate mode localizations (at least for this particular astigmatic PSF model) are placed not just perpendicular to the ground truth, but also at a greater depth. At a separation of 0.75 σ_{PSF}, the alternate mode is found at a depth of -600 nm. This can be explained by the astigmatic PSF characteristics. When moving below the focal plane, the astigmatic PSF stretches along the same axis that separates the emitters. Thus, two emitters in the focal plane separated along the x axis can be represented by a pair on the y axis far below focal plane. This same problem occurs when emitters are separated along the y axis, resulting in an alternative pair along the x axis above the focal plane. These results show that posterior density reconstruction can be used to analyse 3D PSF suitability for high density localization microscopy. Specifically, these two special cases in which degeneracy occurs increase the maximum error that can be expected from 3D localization. This allows us to bound the worst-case localization error. Note that with randomly oriented emitters, only a subset of emitter pairs will be separated along a vector close to the x or y axis, so the impact on the mean squared error over all localizations will be limited.

From the XZ plots in Fig. 3.2, it can be seen that as the separation increases, the alternative mode starts to fall outside the provided PSF range of [-1.3, 1.3] μm, disappearing at large emitter separation. As the PSF range gets constrained further, this alternative mode disappears faster. This is consistent with the multimodality we found as a result of the PSF degeneracy, as constraining the PSF range decreases the solution space, thereby excluding ambiguous solutions.

3.2.2. Influence of priors on multimodality

In [8], it is identified that the intensity prior plays a critical role in multiple emitter fitting using RJMCMC. We therefore study the dependency of the multimodality on the intensity prior, as shown in Fig. 3.3. The image data from Fig. 3.2 was used for localization with four different intensity priors, $P_0(I)$ to $P_3(I)$. $P_0(I)$ and $P_1(I)$ combine a sloped and uniform probability at lower intensities with a Gaussian distribution around the expected count of 2000 photons, similar to what is done in [8]. The intention of this prior is to increase the convergence speed of 3D RJMCMC by improving the ability to escape from local minima and to increase inter-model jumps. Priors $P_2(I)$ and $P_3(I)$ are strictly Gaussian. The standard deviation of the Gaussian peak in the intensity prior was var-

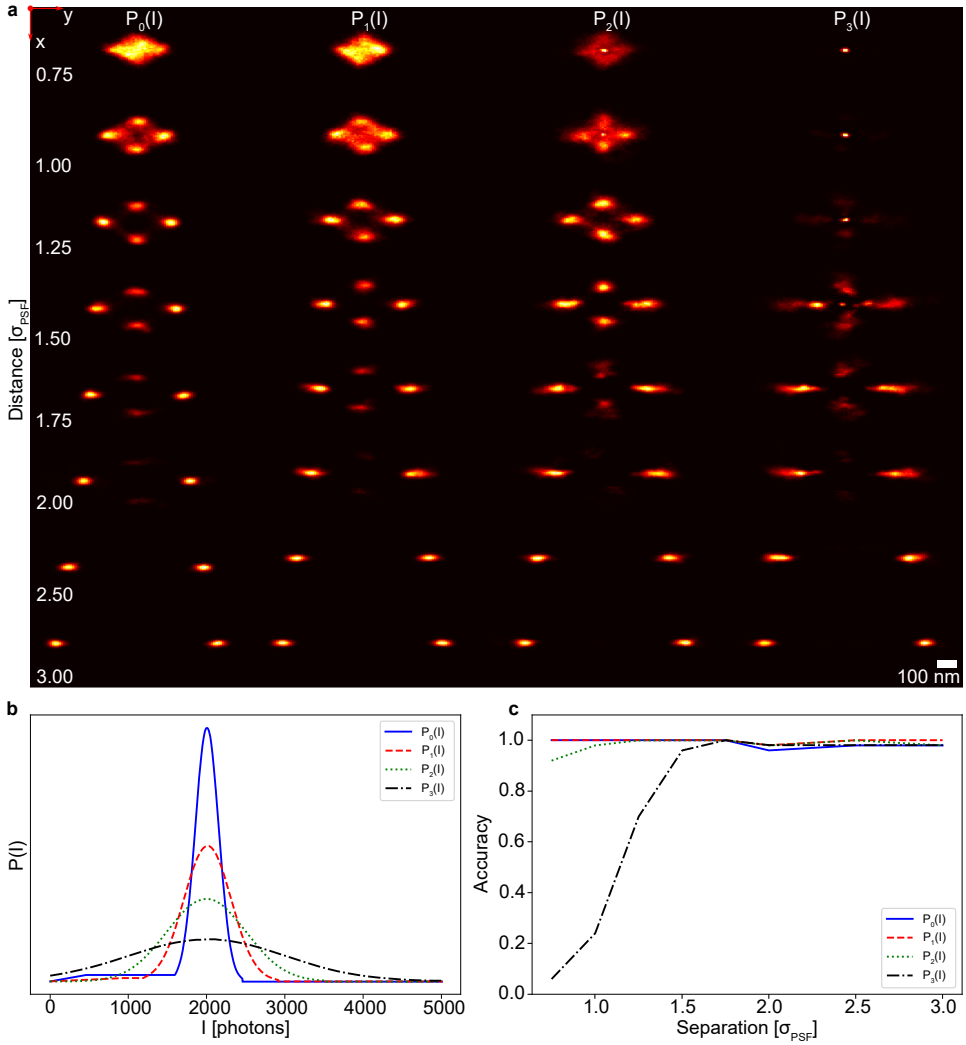

Figure 3.3: Two emitter separability using an astigmatic PSF, varying the width of the intensity prior, using the same frames as shown in Fig. 3.2. (*a*) XY plane reconstructions, each column using a different intensity prior. Images were formed by constructing histograms of the MCMC chains. (*b*) Plots of the respective intensity priors used in each column in (*a*). (*c*) Accuracy of the found model as a function of the emitter separation plotted for each intensity prior used. Accuracy is found using $N_{\text{frames},\hat{k}=k}/N_{\text{frames}}$ with $N_{\text{frames},\hat{k}=k}$ the frames where the estimated model matches the ground truth and N_{frames} the total frame count. The widths of the Gaussian peaks in the priors are 150, 300, 500, and 1000 photons, for $P_0(I)$ up to $P_3(I)$, respectively. $P_0(I)$ and $P_1(I)$ additionally use a uniform and sloped probability at lower intensities to facilitate model space moves. Priors were set to 0 at intensities beyond $2000 + 3\sigma_{\text{prior}}$.

ied from 150 up to 1000 photons, as shown in Fig. 3.3*b*. The first column of Fig. 3.3*a* matches the results of Fig. 3.2, as it uses the same priors and data. The algorithm separates emitters up to 2.5 σ_{PSF}, multimodality is present from 2 σ_{PSF} down to 1 σ_{PSF}, and

emitters are no longer separable within 1 σ_{PSF}. Using $P_1(I)$, column 2 again shows multimodality from 2 down to 1 σ_{PSF}, with failure to separate emitters within 1 σ_{PSF}. Using $P_2(I)$, multimodality is now observed at distances from 2 down to 1.25 σ_{PSF}, failing to separate emitters within 1.25 σ_{PSF}. Finally, using $P_3(I)$, multimodal reconstructions are found from 2 σ_{PSF} down to 1.5 σ_{PSF}. Within this distance, the correct number of emitters is not found consistently. Fig. 3.3*c* plots the accuracy of the estimated model for the priors used, calculated by counting the number of correct estimates and dividing by the frame count. For $P_0(I)$ and $P_1(I)$, the model accuracy is greater than 98% over the range of tested distances. For $P_2(I)$, model accuracy only goes below 95% at a distance of 0.75 σ_{PSF}. Prior $P_3(I)$ decreases in model accuracy from a distance of 1.5 σ_{PSF}, going from 94% down to 5% at a distance of 0.75 σ_{PSF}. This shows that Gaussian intensity priors wider than 500 photons cannot consistently separate emitters within 1.5 σ_{PSF} of one another. While three out of four used priors can retrieve the model over 3 σ_{PSF} down to 0.75 σ_{PSF} distance, all of the used priors returned multimodal posterior densities within the range of 2 σ_{PSF} down to 1.5 σ_{PSF}.

3.2.3. Two emitter separability using biplane imaging

Biplane imaging was tested for its ability to separate emitters and the multimodalities that may occur when doing so. For biplane imaging, the PSF can be approximated by a Gaussian. Unlike the astigmatic PSF, the 3D Gaussian PSF stays radially symmetrical over its range. It can therefore be expected that the same multimodality shown in astigmatic imaging will not be present here. Fig. 3.4 shows that is indeed the case. As the emitter distance varies over the same range of 0.75 to 3 σ_{PSF}, the algorithm consistently finds a model of two emitters while the reconstruction also consists of just two peaks. Under these conditions, biplane imaging can separate two emitters up to a distance of 0.75 σ_{PSF}, entirely free of multimodality. This not only validates the idea that multimodality is caused by 3D PSF degeneracy, it also demonstrates how the algorithm can be used to determine which PSFs suffer the least from this problem and which are best used in dense 3D imaging.

3.3. Conclusion

3D localization microscopy suffers from overlapping emitter images, often not being able to determine the number of active emitters in the ROI and leading to inaccurate position estimates. Multiple emitter fitting algorithms can find the number of emitters, but the added complexity of 3D PSF degeneracy means that these algorithms often misrepresent the uncertainty of their estimates.

We constructed 3D RJMCMC to identify PSF degeneracy in multi-emitter fitting problems, by using the reconstructed posterior density of emitter positions. For astigmatic and biplane imaging, 3D RJMCMC is capable of separating emitters up to a distance of 1 σ_{PSF} and 0.75 σ_{PSF}, respectively, localizing emitters in 3D where SMLM methods would fail. However, astigmatic imaging at these densities will result in multimodal reconstructions. This is an accurate representation of the posterior and a consequence of the 3D PSF structure. Therefore, posterior density reconstruction is the tool of choice to identify potential PSF degeneracy problems in dense 3D localization.

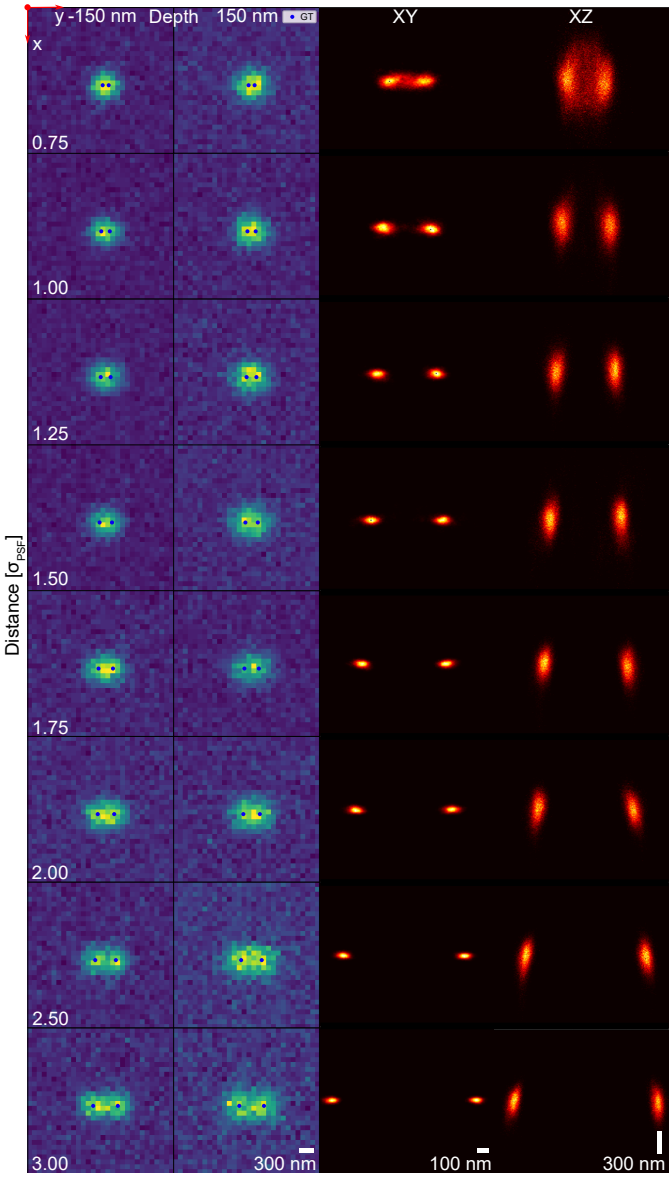

Figure 3.4: Two emitter separability using biplane imaging with planes separated by 300 nm. 100 pairs of frames were simulated and used to make one reconstruction. As photons are split evenly among the planes, the intensity prior was changed to be a Gaussian with mean 1000 photons and width 150 photons. (*Columns 1 and 2*) Example frames at both the positive and negative depth. (*Column 3*) XY plane reconstruction. (*Column 4*) XZ plane reconstruction. Emitters were placed in focal plane, with an intensity of 2000 photons each and a background of 20 photons. The ROI is 30 by 30 pixels, scalebars assume an effective pixel size of 100 nm. The reconstructed image consists of histograms from MCMC chains which used the MAP-estimated number of emitters.

3.4. Discussion

As a main result of our 3D RJMCMC analysis, we found that single-frame astigmatic multiple emitter fitting can result in a multimodal posterior distribution. Due to the practicality of astigmatic imaging and its ability to acquire high-density data, this should serve as an important warning when using it for multiple emitter localization.

Fortunately, the multimodality in multiple emitter fitting using astigmatic imaging can be reduced by analysing a larger time window or by limiting the PSF depth range. Constraining the range reduces the variety of shapes the PSF can take on, limiting PSF degeneracy. Multimodality may also be reduced by encoding the axial position in intensity. Modifying the algorithm to work with total internal reflection fluorescence (TIRF) [11, 12] is therefore a promising method to image without multimodality. Modulation enhanced localization microscopy (meLM) [13] techniques such as ModLoc [14], SIMFLUX [15], and ROSE [16] could all be decoded with 3D RJMCMC localization and a position-dependent intensity prior. A combination of these techniques with RJMCMC may result in a posterior distribution free of multimodality.

With our analysis, we show the importance of including the localization uncertainty in localization algorithms. In multiple emitter fitting, 3D RJMCMC reveals the multimodality of the posterior. This allows us to reveal degeneracy, whereas traditional point estimates would have resulted in overconfident position estimates. Furthermore, 3D RJMCMC also shows that the position uncertainty for individual emitters is not well-represented by Gaussian uncertainty ellipses with a diagonal covariance matrix. Future research should therefore look at incorporating the full uncertainty covariance matrix into the localization algorithm.

The 3D RJMCMC algorithm is best used to analyse imaging techniques for their effectiveness in 3D multiple emitter fitting. Though no multimodality was revealed when testing biplane imaging with 3D RJMCMC localization, orientations of emitter pairs were not exhaustively tested. Furthermore, 3D RJMCMC assumes the PSF model to be accurately known during localization. In the case of PSF uncertainty, we expect this results in an increase in the localization uncertainty contained in the posterior. Within the current methodological framework of 3D RJMCMC, there is however no obvious way to incorporate a PSF mismatch. This combined with the slow and memory intensive nature of RJMCMC means we do not recommend using the algorithm for localization.

However, it should be used to analyse PSFs for possible multimodality in dense samples. Specifically, it remains an open question which PSF allows for both the evasion of degeneracy and an accessible implementation. Additionally, we recommend studying the occurrence of multimodality of the tetrapod PSF, as it is a popular choice for 3D imaging. Our initial study (see Section 3.S6) suggests that multimodality occurs for multiple emitter localization with the tetrapod PSF at 45-degree angles with respect to the x axis. Further study is needed into the conditions, such as the emitter separation, in which this multimodality occurs. 3D RJMCMC is the method of choice to study this. Testing imaging techniques that would require a position dependent intensity prior, such as TIRF or meLM techniques, is also a topic of great interest.

3.5. Methods

3.5.1. Image formation model and key probabilities

For multiple emitter fitting, the expected photon count per camera pixel can be described as:

$$\mu_i = \sum_{j=1}^{k} \theta_{I,j} \int_{A_k} H(\theta_{x,j}, \theta_{y,j}, \theta_{z,j}) \mathrm{d}x\mathrm{d}y + \theta_b, \tag{3.1}$$

with μ_i the photon count in pixel i, $\theta_{I,j}$ the intensity of the j^{th} emitter in the frame, k the amount of emitters in the frame, A_k the pixel area, $H(x,y,z)$ the PSF, $\theta_{x,j}$, $\theta_{y,j}$, $\theta_{z,j}$ the 3D position of the j^{th} emitter, and θ_b the background photon count.

For a high gain camera, such as an electron multiplying charge coupled device (EMCCD), the readout noise is negligible and thus the likelihood function has a Poisson distribution:

$$P(D_i|\theta,k) = \frac{\mu_i^{D_i} \exp\left(-\mu_i\right)}{D_i!}, \tag{3.2}$$

with $P(D_i|\theta,k)$ the likelihood of observing measured data D on the i^{th} pixel as function of parameter vector
$\theta = \begin{bmatrix}\theta_{x,0} & \theta_{y,0} & \theta_{z,0} & \theta_{I,0} & \dots & \theta_{x,k} & \theta_{y,k} & \theta_{z,k} & \theta_{I,k} & \theta_b\end{bmatrix}$ and number of emitters k. Given the pixels are independent, the likelihood of one frame becomes:

$$P(D|\theta,k) = \prod_{i=1}^{N_\mathrm{p}} \frac{\mu_i^{D_i} \exp\left(-\mu_i\right)}{D_i!}, \tag{3.3}$$

with N_p the pixel count. The joint posterior distribution of the parameters and model can then be found using Bayes' rule:

$$P(\theta,k|D) = \frac{P(D|\theta,k)P(\theta|k)P(k)}{P(D)}, \tag{3.4}$$

with $P(k)$ the model prior, $P(\theta|k)$ the parameter prior given the model, and $P(D)$ the evidence. The priors can be formulated from earlier attained knowledge of labelling density or emitter intensity, however the evidence term, $P(D) = \int P(D|\theta,k)P(\theta|k)P(k)\mathrm{d}\theta\mathrm{d}k$, only has a closed form solution when the prior distribution is conjugate to the posterior. This is often not the case [17], therefore RJMCMC [10] is employed to asymptotically sample from the posterior.

After attaining samples from $P(\theta,k|D)$, the MAP number of emitters, $\hat{k}$, is used as the true model to condition the parameter estimate on, running a MCMC algorithm to find $P(\theta|\hat{k},D)$. This is done to avoid introducing bias in the parameter estimates coming from models of different dimension.

3.5.2. Priors and hyperparameters

The algorithm takes in priors for 3D position, emitter intensity, background intensity, and emitter count. Throughout the tests, the prior on the lateral emitter position is kept uniform over the ROI plus four extra pixels, to account for the influence of emitters outside the ROI. The axial position prior is uniform over the presumed depth range of the

PSF. Emitter intensity was set as a Gaussian distribution, enabling the algorithm to separate the emitters. In practice, it is recommended [8] to estimate the intensity prior using kernel density estimation on intensity data of a previous SMLM run. Finally, the emitter count prior is also kept uniform. Although it is possible estimate the emitter count within a sample given the label density, it can still vary widely on a local scale, thus we keep the prior uniform for smaller ROIs.

Each iteration, the move was randomly selected using user-determined selection probabilities [P_{single}, P_{group}, $P_{\text{background}}$, P_{split}, P_{merge}, $P_{\text{g-split}}$, $P_{\text{g-merge}}$, P_{birth}, P_{death}]. Throughout the tests, the RJMCMC burn-in portion uses [1/5, 1/5, 1/5, 1/15, 1/15, 1/15, 1/15, 1/15, 1/15], while post burn-in [1/4, 1/4, 1/4, 0, 0, 3/32, 3/32, 1/32, 1/32] are used. The burn-in portion uses higher model space move probabilities to ensure more model space mixing, while post burn-in focuses more on parameter space moves. The MCMC portion uses [2/5, 2/5, 1/5, 0, 0, 0, 0, 0, 0], focusing mainly on emitter parameters. Each test runs for 30,000 RJMCMC iterations, using 10,000 of those as burn-in and following them up with 5000 MCMC iterations. The parameter space moves use random walk samplers, leaving jump sizes [σ_x, σ_y, σ_z, σ_I, σ_b] as parameters for tuning. For good mixing, lateral jump size may vary from 0.05 to 0.1 pixels, axial jump size from 0.07 up to 0.12 μm, emitter intensity between 10 and 40 photons, and background intensity of 1 to 3 photons.

3.5.3. Convergence and precision

To verify convergence of the algorithm, 100 frames with a single active emitter were localized. Emitters in the centre of the ROI sampled their intensity randomly from the matching prior and were given a random sub-pixel displacement. Figs. 3.S3 and 3.S5 show the model and parameter autocorrelation as well as the time series and histogram of the model, for a high and low signal to background, respectively. The algorithm manages to converge to the correct model 100% of the time, while also converging in parameter space. By using only uniform priors, the algorithm yields an unbiased estimate that can be compared to the Cramér-Rao lower bound (CRLB) [3] to verify the precision. For non-uniform priors, the Van Trees inequality (VTI) [18, 19] can be used as a Bayesian Cramér-Rao bound to find the theoretically minimum localization error. Fig. 3.S8 shows a violin plot of the precisions found with 3D RJMCMC localization compared to the CRLB over varying emitter intensity. It can be seen that the localization precision matches the CRLB over the plotted intensity range. Fig. 3.S9 shows violin plots for the root mean squared error (RMSE) of the same data. The results show that the algorithm reaches the minimum theoretical uncertainty for low emitter density.

3.5.4. Synthetic data and results

For Fig. 3.2, two emitters were placed in focus and simulated using an astigmatic PSF, their centre of mass in the middle of the ROI. The PSF was evaluated using a 3D Gaussian approximation [3], with parameters [$s_{0,x}$, γ_x, d_x, A_x] and [$s_{0,y}$, γ_y, d_y, A_y] of [σ_{PSF}, 2, 3, 0] and [σ_{PSF}, -2, 3, 0], respectively. Here σ_{PSF} is the width in focal plane, set at 1.2 pixels. The PSF range was set at [-1.3, 1.3] μm, with a ROI size of 20 by 20 pixels. Emitter intensity was fixed at 2000 photons, with a background intensity of 20 photons. A total of 100 frames were simulated and their 5000 iteration MCMC chains were merged to

finally form the histogram reconstructions of the XY and XZ planes. The histograms were magnified in x and y direction by a factor 2.5 with respect to the sample frames. Move selection probabilities were as in Subsection Priors and hyperparameters, while the jump size hyperparameters were set to [0.1, 0.1, 0.08, 15, 1]. All priors were kept uniform except the emitter intensity, using a Gaussian around 2000 photons with a width of 150 and a small uniform probability between 0 and 1500 that slopes down to 0, as shown in Fig. 3.3*b*. The prior is set to 0 for intensities greater than 2450 photons. The number of emitters ranges from 0 to 6 and lateral position estimates may exceed the ROI by four pixels. Background intensity was limited to a range of 1 to 40 photons.

Fig. 3.3 uses the same data and settings as Fig. 3.2, only changing the random number generator seed and the emitter intensity priors used. Priors $P_0(I)$ to $P_3(I)$ all use Gaussian distributions centred around 2000 photons, with a width of 150, 300, 500, and 1000 photons, respectively. Again, $P_0(I)$ and $P_1(I)$ keep a uniform probability sloping to 0 at lower intensities to help facilitate splitting of emitters.

Fig. 3.4 uses 100 frames simulated with biplane imaging, splitting the response of a Gaussian PSF between planes at +150 and -150 nm depth relative to the focal plane. A depth range of [-1, 1] μm was used. Again, the PSF was evaluated with a 3D Gaussian approximation [3] of an experimentally measured astigmatic PSF on the setup described in [20], with [1.70, −4.64, 8.34, 0.00] for the x and y parameters. Emitter intensities and background photons were split evenly across the planes. The ROI is now expanded to 30 by 30 pixels. All hyperparameters and priors used were identical to the previous experiments, except the emitter intensity prior, which is a Gaussian with mean 1000 and width 150 photons. The intensity prior is set to 0 for intensities greater than 1450 photons and again is uniform between 200 and 500 photons, sloping upwards from 0 to 200 photons.

Data and Code Availability

The data and code that support the findings of this study are openly available on GitHub [21].

References

[1] E. Betzig, G. H. Patterson, R. Sougrat, O. W. Lindwasser, S. Olenych, J. S. Bonifacino, M. W. Davidson, J. Lippincott-Schwartz, and H. F. Hess. "Imaging Intracellular Fluorescent Proteins at Nanometer Resolution". In: *Science* 313.5793 (2006), pp. 1642–1645.

[2] M. J. Rust, M. Bates, and X. Zhuang. "Sub-diffraction-limit imaging by stochastic optical reconstruction microscopy (STORM)". In: *Nature Methods* 3.10 (2006), pp. 793–796.

[3] C. S. Smith, N. Joseph, B. Rieger, and K. A. Lidke. "Fast, single-molecule localization that achieves theoretically minimum uncertainty". In: *Nature Methods* 7.5 (2010), pp. 373–375.

[4] T. Dertinger, R. Colyer, G. Iyer, S. Weiss, and J. Enderlein. "Fast, background-free, 3D super-resolution optical fluctuation imaging (SOFI)". In: *Proceedings of the National Academy of Sciences* 106.52 (2009), pp. 22287–22292.

[5] L. Zhu, W. Zhang, D. Elnatan, and B. Huang. "Faster STORM using compressed sensing". In: *Nature Methods* 9.7 (2012), pp. 721–723.

[6] J. Min, C. Vonesch, H. Kirshner, L. Carlini, N. Olivier, S. Holden, S. Manley, J. C. Ye, and M. Unser. "FALCON: fast and unbiased reconstruction of high-density super-resolution microscopy data". In: *Scientific Reports* 4.1 (2014).

[7] E. Nehme, L. E. Weiss, T. Michaeli, and Y. Shechtman. "Deep-STORM: super-resolution single-molecule microscopy by deep learning". In: *Optica* 5.4 (2018), p. 458.

[8] M. Fazel, M. J. Wester, H. Mazloom-Farsibaf, M. B. M. Meddens, A. S. Eklund, T. Schlichthaerle, F. Schueder, R. Jungmann, and K. A. Lidke. "Bayesian Multiple Emitter Fitting using Reversible Jump Markov Chain Monte Carlo". In: *Scientific Reports* 9.1 (2019).

[9] H. P. Babcock and X. Zhuang. "Analyzing Single Molecule Localization Microscopy Data Using Cubic Splines". In: *Scientific Reports* 7.1 (2017).

[10] P. J. Green. "Reversible Jump Markov Chain Monte Carlo Computation and Bayesian Model Determination". In: *Biometrika* 82.4 (1995), pp. 711–732.

[11] D. Axelrod. "Total Internal Reflection Fluorescence Microscopy". In: *Fluorescence Microscopy of Living Cells in Culture Part B. Quantitative Fluorescence Microscopy—Imaging and Spectroscopy*. Elsevier, 1989, pp. 245–270.

[12] N. Bourg, C. Mayet, G. Dupuis, T. Barroca, P. Bon, S. Lécart, E. Fort, and S. Lévêque-Fort. "Direct optical nanoscopy with axially localized detection". In: *Nature Photonics* 9.9 (2015), pp. 587–593.

[13] L. Reymond, T. Huser, V. Ruprecht, and S. Wieser. "Modulation-enhanced localization microscopy". In: *Journal of Physics: Photonics* 2.4 (2020), p. 041001.

[14] P. Jouchet, C. Cabriel, N. Bourg, M. Bardou, C. Poüs, E. Fort, and S. Lévêque-Fort. "Nanometric axial localization of single fluorescent molecules with modulated excitation". In: *Nature Photonics* 15.4 (2021), pp. 297–304.

[15] J. Cnossen, T. Hinsdale, R. Ø. Thorsen, M. Siemons, F. Schueder, R. Jungmann, C. S. Smith, B. Rieger, and S. Stallinga. "Localization microscopy at doubled precision with patterned illumination". In: *Nature Methods* 17.1 (2019), pp. 59–63.

[16] L. Gu, Y. Li, S. Zhang, M. Zhou, Y. Xue, W. Li, T. Xu, and W. Ji. "Molecular-scale axial localization by repetitive optical selective exposure". In: *Nature Methods* 18.4 (2021), pp. 369–373.

[17] N. Metropolis, A. W. Rosenbluth, M. N. Rosenbluth, A. H. Teller, and E. Teller. “Equation of State Calculations by Fast Computing Machines”. In: *The Journal of Chemical Physics* 21.6 (1953), pp. 1087–1092.

[18] R. D. Gill and B. Y. Levit. “Applications of the van Trees Inequality: A Bayesian Cramér-Rao Bound”. In: *Bernoulli* 1.1/2 (1995), p. 59.

[19] D. Kalisvaart, J. Cnossen, S. Hung, S. Stallinga, M. Verhaegen, and C. S. Smith. “Precision in iterative modulation enhanced single-molecule localization microscopy”. In: *Biophysical Journal* 121.12 (2022), pp. 2279–2289.

[20] T. A. Hinsdale, S. Stallinga, and B. Rieger. “High-speed multicolor structured illumination microscopy using a hexagonal single mode fiber array”. In: *Biomedical Optics Express* 12.2 (2021), p. 1181.

[21] R. van Dijk, D. Kalisvaart, J. Cnossen, and C. S. Smith. *Data and software underlying: Bayesian posterior density estimation reveals degeneracy in three-dimensional multiple emitter localization*. 2023.

Supporting Information for: Bayesian Posterior Density Estimation Reveals Degeneracy in Three-Dimensional Multiple Emitter Localization

3.S1. Reversible jump Markov chain Monte Carlo localization algorithm

To both estimate the model and find the parameters, reversible jump Markov chain Monte Carlo (RJMCMC) is employed. The RJMCMC algorithm makes jumps in model space, making it possible to recover a distribution of possible model and parameter pairings. For 3D localization, the model only varies in number of emitters active per frame, in which we try to estimate the parameters of the emitters, that being the x, y, and z positions as well as the intensity I, and the background photons present in the frame, b. With the use of smart priors, 3D RJMCMC localization can retrieve the correct model and localize the emitters.

Localization in 3D using RJMCMC is done as follows:

1. An emitter is initialized randomly;
2. RJMCMC is run with the burn-in move probabilities;
3. The move probabilities are adjusted for the fraction of the chain that follows the burn-in;
4. From the post burn-in RJMCMC chain, the MAP model is selected from the distribution to be used with MCMC;
5. MCMC is initialized using the last element from the RJMCMC chain in which the model corresponds to the MAP model;
6. MCMC is run with the parameter space move list;
7. K-means clustering is used to perform label switching and retrieve the localizations from the chains, setting the cluster count to the MAP model.

The RJMCMC and MCMC runs undergo the following steps internally:

1. A move is randomly selected from the move list;
2. The move is executed on each frame, generating new parameters and models (if the move is not valid for the frame, the parameters stay fixed);
3. The acceptance rate is calculated and the jump is either accepted or rejected, updating the chain;
4. Steps 1 to 3 are repeated until the desired chain length is achieved.

3.S1.1. Priors

The algorithm takes in priors for the emitter position, emitter intensity, background intensity, and the number of emitters present. Though the prior for number of emitters can be set as a Poisson distribution if the user has knowledge of the labelling density, we keep the prior $P(k)$ uniform as the local density when evaluating small regions of interest (ROIs) can differ greatly:

$$P(k) \sim \mathcal{U}(0, k_{\max}), \tag{3.S1}$$

with $k_{\max}$ the user defined maximum number of emitters expected in the ROI.

For the emitter position, the priors are set to be uniform to avoid bias:

$$P(\theta_{x,i}|k) \sim \mathcal{U}(-w_{\text{border}}, x_{\text{ROI}} + w_{\text{border}}), \tag{3.S2}$$

$$P(\theta_{y,i}|k) \sim \mathcal{U}(-w_{\text{border}}, y_{\text{ROI}} + w_{\text{border}}), \tag{3.S3}$$

$$P(\theta_{z,i}|k) \sim \mathcal{U}(z_{\min}, z_{\max}), \tag{3.S4}$$

with $\theta_{x,i}$, $\theta_{y,i}$, $\theta_{z,i}$ the 3D position of the i^{th} found emitter, x_{ROI}, y_{ROI} the x- and y-dimensions of the ROI, w_{border} some additional pixels outside the ROI to account for influence of external emitters, and $z_{\min}$, $z_{\max}$ the admissible range of z-positions.
The prior on background intensity is kept as a simple uniform distribution:

$$P(\theta_b) \sim \mathcal{U}(b_{\min}, b_{\max}), \tag{3.S5}$$

with $b_{\min}$, $b_{\max}$ the user defined minimum and maximum expected background values for the experiment.

Finally, the prior for the intensity should be either determined experimentally by kernel density fitting SMLM results, or directly defined by the user given sufficient knowledge of the emission response. For the testing on synthetic data, often a Gaussian prior around the expected emitter intensity is used [1], with an additional flat shoulder at lower intensities to facilitate model jumps if necessary, such as:

$$P(\theta_{I,i}|k) = \begin{cases} \frac{1}{150\sqrt{2\pi}} \exp\left[-\frac{1}{2}\left(\frac{\theta_I - 2000}{150}\right)^2\right] & \text{if } 1600 < \theta_I < 2500, \\ 6 \cdot 10^{-5} & \text{if } 500 < \theta_I < 1600, \\ 6 \cdot 10^{-5} \frac{\theta_I}{500} & \text{if } 1 < \theta_I < 500, \\ 0 & \text{otherwise.} \end{cases} \tag{3.S6}$$

The prior on intensity is assumed to be unchanging over depth.

3.S1.2. Moves

In RJMCMC, the design of the moves is crucial for exploring the model space. The moves used in 3D RJMCMC localization are:

- A single emitter move, varying the 3D position and intensity of a single emitter;
- A group move, varying the 3D position and intensity of a cluster of emitters;
- A background move, changing the offset background estimate;
- A split move, splitting one emitter into two;
- A merge move, merging two emitters into one;
- A generalized split move, splitting a cluster of N emitters into $N+1$;
- A generalized merge move, merging a cluster of N emitters into $N-1$;
- A birth move, spawning an emitter where the difference between measured and expected intensity is high;
- A death move, removing an emitter at random.

The single emitter, group, and background move work in parameter space while leaving the model space identical. The rest of the moves come in pairs to retain detailed balance and change both the model and the parameters of the estimate. Fig. 3.S1 shows schematically how each move changes the parameters or model.

Move proposal At every iteration of the algorithm, a move is selected according to fixed probabilities defined by the user. Move probabilities can be set separately for the MCMC portion, as well as both the burn-in phase and the post burn-in phase of the RJMCMC portion.

An appropriate setting of the move probabilities results in sufficient mixing between chains. As a result of chain mixing, the algorithm makes jumps between multiple solution modes, which allows exploration of the full posterior density. Specifically for our problem, this allows us to explore ambiguous localization solutions due to PSF degeneracy.

To facilitate sufficient mixing, the following procedure was used to determine the move probabilities in Table 3.S1. To choose the probabilities related to 2D moves, the parameters from [1] were initially chosen. For the 3D probabilities, the starting point was based on our presumed depth of view. Given the increased complexity when moving from 2D RJMCMC to 3D RJMCMC, we identified that these parameters needed to be tuned. As such, these parameters were tuned until sufficient mixing between the chains was observed. For testing on synthetic data, the move probabilities in Table 3.S1 were found to work well.

3.S1.3. Single emitter move

The single emitter, group, and background move moves will act on the parameter space only and their acceptance rates can be determined from the Metropolis-Hastings algorithm for the MCMC case.

Metropolis-Hastings acceptance rate for parameter space jumps The probability of accepting parameter space jumps is given as:

$$\alpha = \min\left[1, \frac{P(\theta', k, D)}{P(\theta, k, D)}\left|\frac{\partial(\theta')}{\partial(\theta, u)}\right|\right], \tag{3.S7}$$

with α the acceptance rate, using the joint probability $P(\theta, k, D) = P(D|\theta, k)P(\theta|k)P(k)$ to calculate the posterior ratio (ignoring evidence term $P(D)$ as it gets cancelled in the division) and the final fraction as the determinant of the Jacobian of the function $\theta'(\theta, u)$ that generates the new parameters. Here,

$$\theta = \begin{bmatrix}\theta_{x,0} & \theta_{y,0} & \theta_{z,0} & \theta_{I,0} & \dots & \theta_{x,i} & \theta_{y,i} & \theta_{z,i} & \theta_{I,i} & \theta_b\end{bmatrix}$$

is the parameter vector, containing the positions and intensities of the i emitters used in the current model along with the background parameter θ_b. Using a random walk sampler for the parameter space moves and cancelling the model prior, the acceptance rate reduces to:

$$\alpha = \min\left[1, \frac{P(\theta', k, D)}{P(\theta, k, D)}\right] = \min\left[1, \frac{P(D|\theta', k)P(\theta'|k)}{P(D|\theta, k)P(\theta|k)}\right]. \tag{3.S8}$$

The single emitter move randomly selects one of the i current emitters and generates a new estimate out of its previous parameters as follows:

$$\theta'_{x,j} = \theta_{x,j} + u_x, \tag{3.S9}$$
$$\theta'_{y,j} = \theta_{y,j} + u_y, \tag{3.S10}$$
$$\theta'_{z,j} = \theta_{z,j} + u_z, \tag{3.S11}$$
$$\theta'_{I,j} = \theta_{I,j} + u_I, \tag{3.S12}$$

with u drawn from the following normal distributions:

$$P(u_x) \sim \mathcal{N}(0, \sigma_x), \tag{3.S13}$$
$$P(u_y) \sim \mathcal{N}(0, \sigma_y), \tag{3.S14}$$
$$P(u_z) \sim \mathcal{N}(0, \sigma_z), \tag{3.S15}$$
$$P(u_I) \sim \mathcal{N}(0, \sigma_I), \tag{3.S16}$$

and σ_x, σ_y, σ_z, σ_I some user determined hyperparameters to vary the jump size. The posterior ratio in Eq. (3.S8) can now be simplified to:

$$\frac{P(D|\theta', k)P(\theta'|k)}{P(D|\theta, k)P(\theta|k)} = \left[\prod_{k_\mathrm{p}} \exp\left(\mu_{k_\mathrm{p}} - \mu'_{k_\mathrm{p}}\right)\left(\frac{\mu'_{k_\mathrm{p}}}{\mu_{k_\mathrm{p}}}\right)^{n_{k_\mathrm{p}}}\left(\prod_{k}^{k_\mathrm{max}} \frac{P(\theta'_{I,k})}{P(\theta_{I,k})}\right)\right]. \tag{3.S17}$$

Assuming the estimated parameters stay within the bounds of the priors, the uniform position priors cancel out and only the likelihood ratio and intensity prior ratio are left.

3.S1.4. Group move

The group move first finds a cluster of nearby emitters, and then executes a single emitter move on each of them. It randomly picks one emitter, then searches for emitters within a $2\sigma_{\text{PSF}}$ sphere around it to form a cluster. This radius can be treated as a hyperparameter and tuned, though for Gaussian and astigmatic PSFs it works well when set to the PSF width in focal plane. More complex 3D PSFs may require a fairly large radius for clustering.

After finding an eligible cluster and executing the moves, the acceptance rate can be calculated using the same equations as in the single move, namely as in Eqs. (3.S8) and (3.S17). If a cluster cannot be found, the move fails.

3.S1.5. Background move

The background move is not coupled to any emitter. It updates a flat offset background intensity with a random walk sampler as follows:

$$\theta_b' = \theta_b + u_b, \tag{3.S18}$$

$$P(u_b) \sim \mathcal{N}(0, \sigma_b), \tag{3.S19}$$

with σ_b another hyperparameter for tuning the background jump size. The acceptance rate from Eq. (3.S17) can now be reduced even further, assuming the background jump stays within the bounds of its uniform prior:

$$\frac{P(D|\theta', k)P(\theta'|k)}{P(D|\theta, k)P(\theta|k)} = \left[\prod_{k_\text{p}} \exp\left(\mu_{k_\text{p}} - \mu'_{k_\text{p}}\right)\left(\frac{\mu'_{k_\text{p}}}{\mu_{k_\text{p}}}\right)^{n_{k_\text{p}}}\right], \tag{3.S20}$$

which is just the likelihood ratio of the parameters before and after the jump.

3.S1.6. Split and Merge pair

The (generalized) split, merge, birth and death moves come in pairs and may act on both the parameter and the model space. Their acceptance rates can be determined from the general acceptance rate used in RJMCMC.

Metropolis-Hastings acceptance rate for model space jumps The probability of accepting model space jumps in the general case is given as:

$$\alpha = \min\left\{1, \frac{P(\theta', k', D)\, r_\text{m}(\theta')}{P(\theta, k, D)\, r_\text{m}(\theta)\, q(u)} \left|\frac{\partial(\theta')}{\partial(\theta, u)}\right|\right\}, \tag{3.S21}$$

with $r_\text{m}(\theta)$ the probability of choosing the move type (selecting either split or merge) and $q(u)$ the probability density function of the draws from u used to generate the split weights, means, and standard deviations.

The split and merge move turn one emitter into two and vice versa. By using this move pair, the algorithm has a move that allows it to distinguish emitters that are in

close proximity to one another. Split and merge will uphold the following constraints:

$$\theta_{I,j^*} = \theta_{I,j_1} + \theta_{I,j_2}, \tag{3.S22}$$
$$\theta_{I,j^*}\theta_{x,j^*} = \theta_{I,j_1}\theta_{x,j_1} + \theta_{I,j_2}\theta_{x,j_2}, \tag{3.S23}$$
$$\theta_{I,j^*}\theta_{y,j^*} = \theta_{I,j_1}\theta_{y,j_1} + \theta_{I,j_2}\theta_{y,j_2}, \tag{3.S24}$$
$$\theta_{I,j^*}\theta_{z,j^*} = \theta_{I,j_1}\theta_{z,j_1} + \theta_{I,j_2}\theta_{z,j_2}. \tag{3.S25}$$

Split For a split, θ' is generated from a randomly selected emitter with index j^* as follows:

$$u_1 \sim \mathcal{U}(0,1), \tag{3.S26}$$
$$u_2 \sim \mathcal{N}(0,\sigma_{\mathrm{PSF}}), \tag{3.S27}$$
$$u_3 \sim \mathcal{N}(0,\sigma_{\mathrm{PSF}}), \tag{3.S28}$$
$$u_4 \sim \mathcal{N}(0,\sigma_{\mathrm{PSF}}), \tag{3.S29}$$
$$\theta_{I,j_1} = \theta_{I,j^*}u_1, \tag{3.S30}$$
$$\theta_{I,j_2} = \theta_{I,j^*}(1-u_1), \tag{3.S31}$$
$$\theta_{x,j_1} = \theta_{x,j^*} + u_2, \tag{3.S32}$$
$$\theta_{y,j_1} = \theta_{y,j^*} + u_3, \tag{3.S33}$$
$$\theta_{z,j_1} = \theta_{z,j^*} + u_4, \tag{3.S34}$$
$$\theta_{x,j^*}\theta_{I,j^*} = \theta_{x,j_1}\theta_{I,j_1} + \theta_{x,j_2}\theta_{I,j_2}, \tag{3.S35}$$
$$\theta_{x,j_2} = \theta_{x,j^*} - \frac{u_1 u_2}{1-u_1}, \tag{3.S36}$$
$$\theta_{y,j^*}\theta_{I,j^*} = \theta_{y,j_1}\theta_{I,j_1} + \theta_{y,j_2}\theta_{I,j_2}, \tag{3.S37}$$
$$\theta_{y,j_2} = \theta_{y,j^*} - \frac{u_1 u_3}{1-u_1}, \tag{3.S38}$$
$$\theta_{z,j^*}\theta_{I,j^*} = \theta_{z,j_1}\theta_{I,j_1} + \theta_{z,j_2}\theta_{I,j_2}, \tag{3.S39}$$
$$\theta_{z,j_2} = \theta_{z,j^*} - \frac{u_1 u_4}{1-u_1}, \tag{3.S40}$$

with the two new emitters retaining the 3D centre of mass and total intensity of the emitter they split from. Indices j_1 and j_2 are used to indicate the emitters resulting from a split, or those used in a merge, whereas index j^* is used for the result of a merge or the target of a split.

The ratio of selecting the move types then becomes:

$$\frac{r_{\mathrm{m}}(\theta')}{r_{\mathrm{m}}(\theta)} = \frac{P_{\mathrm{split}}}{P_{\mathrm{merge}}}, \tag{3.S41}$$

and $q(u)$ is:

$$q(u) = P(u_1)P(u_2)P(u_3)P(u_4). \tag{3.S42}$$

Knowing the split move only influences these parameters and leaves the other emitters and background untouched, the emitter to be split and the resulting emitters after the

split can be moved to the back for both θ' and (θ, u) vectors. The resulting vectors then become:

$$\theta' = \begin{bmatrix} \dots & \theta_{I,j_1} & \theta_{x,j_1} & \theta_{y,j_1} & \theta_{z,j_1} & \theta_{I,j_2} & \theta_{x,j_2} & \theta_{y,j_2} & \theta_{z,j_2} \end{bmatrix}, \tag{3.S43}$$

$$(\theta, u) = \begin{bmatrix} \dots & \theta_{I,j^*} & u_1 & \theta_{x,j^*} & u_2 & \theta_{y,j^*} & u_3 & \theta_{z,j^*} & u_4 \end{bmatrix}. \tag{3.S44}$$

The Jacobian can then be constructed as:

$$\frac{\partial(\theta')}{\partial(\theta, u)} = \begin{bmatrix} I_{k-1} & \mathbf{0}_{k-1,1} & & & & \dots & & & \mathbf{0}_{k-1,1} \\ \mathbf{0}_{1,k-1} & u_1 & 0 & 0 & 0 & -\theta_{I,j^*} & 0 & 0 & 0 \\ & 0 & 0 & 1 & 1 & 0 & 0 & 0 & 0 \\ & 0 & 0 & 0 & 0 & 1 & 1 & 0 & 0 \\ & 0 & 0 & 0 & 0 & 0 & 0 & 1 & 1 \\ \vdots & 1-u_1 & 0 & 0 & 0 & -\theta_{I,j^*} & 0 & 0 & 0 \\ & 0 & \frac{-u_2}{(1-u_1)^2} & 1 & \frac{-u_1}{1-u_1} & 0 & 0 & 0 & 0 \\ & 0 & \frac{-u_3}{(1-u_1)^2} & 0 & 0 & 1 & \frac{-u_1}{1-u_1} & 0 & 0 \\ \mathbf{0}_{1,k-1} & 0 & \frac{-u_4}{(1-u_1)^2} & 0 & 0 & 0 & 0 & 1 & \frac{-u_1}{1-u_1} \end{bmatrix},$$

with identity matrix I_{k-1} of dimension $k-1$ for all the unchanged parameters and $\mathbf{0}_{k-1,1}$, $\mathbf{0}_{1,k-1}$ column and row vectors containing zeros. This yields the determinant:

$$\left| \frac{\partial(\theta')}{\partial(\theta, u)} \right| = \frac{\theta_{I,j^*}}{(1-u_1)^3}. \tag{3.S45}$$

Setting $P_{\text{split}} = P_{\text{merge}}$, the final result is then:

$$\alpha = \min\{1, A_{\text{split}}\}, \tag{3.S46}$$

$$A_{\text{split}} = \frac{P(\theta'|D) r_{\text{m}}(\theta')}{P(\theta|D) r_{\text{m}}(\theta) q(u)} \left| \frac{\partial(\theta')}{\partial(\theta, u)} \right| = \frac{P(\theta', k', D)}{P(\theta, k, D)} \frac{\theta_{I,j^*}}{P(u_1, u_2, u_3, u_4)(1-u_1)^3}. \tag{3.S47}$$

Merge For a merge move, an emitter is selected at random, after which it is randomly paired with another emitter within 2 σ_{PSF} of itself. If no emitter can be found within this distance, the move fails. The emitters combine their intensity and centre of mass. The acceptance rate can be set to the inverse of that for the split move, finding u_1, u_2, u_3 and u_4 deterministically from Eqs. (3.S30), (3.S32), (3.S33), and (3.S34):

$$u_1 = \frac{\theta_{I,j_1}}{\theta_{I,j^*}}, \tag{3.S48}$$

$$u_2 = \theta_{x,j_1} - \theta_{x,j^*}, \tag{3.S49}$$

$$u_3 = \theta_{y,j_1} - \theta_{y,j^*}, \tag{3.S50}$$

$$u_4 = \theta_{z,j_1} - \theta_{z,j^*}. \tag{3.S51}$$

This gives the the acceptance rate:

$$\alpha = \min\{1, A_{\text{merge}}\}, \tag{3.S52}$$

$$A_{\text{merge}} = A_{\text{split}}^{-1} = \frac{P(\theta, k, D)}{P(\theta', k', D)} \frac{P(u_1, u_2, u_3, u_4)(1-u_1)^3}{\theta_{I,j^*}}, \tag{3.S53}$$

with θ previously being the parameters before the split and now thus the parameters after the merge and vice versa for θ'.

3.S1.7. Generalized Split and Merge

Whereas split and merge work on a single emitter, their generalized versions are helpful for very densely packed frames, allowing the splitting and merging of emitters within clusters of N emitters. Generalized split jumps from N to $N+1$ emitters, while generalized merge does the opposite. These moves use the same clustering as was used for the group move, picking one random emitter and forming an eligible cluster within $2\sigma_{\mathrm{PSF}}$ of itself.

Generalized Split Now, instead of distributing the intensity of one emitter to two, the combined intensity of N emitters is distributed over $N+1$, again retaining the centre of mass:

$$\sum_{j=1}^{N} \theta_{I,j} = \sum_{j=1}^{N+1} \theta'_{I,j}, \tag{3.S54}$$

$$\sum_{j=1}^{N} \theta_{I,j}\theta_{x,j} = \sum_{j=1}^{N+1} \theta'_{I,j}\theta'_{x,j}, \tag{3.S55}$$

$$\sum_{j=1}^{N} \theta_{I,j}\theta_{y,j} = \sum_{j=1}^{N+1} \theta'_{I,j}\theta'_{y,j}, \tag{3.S56}$$

$$\sum_{j=1}^{N} \theta_{I,j}\theta_{z,j} = \sum_{j=1}^{N+1} \theta'_{I,j}\theta'_{z,j}. \tag{3.S57}$$

Putting up some additional constraints to remove the same fraction of intensity for each emitter in the cluster and to let the new emitter be formed close to the centre of mass of the cluster:

$$\theta'_{I,j} = (1-u_1)\theta_{I,j}, \tag{3.S58}$$

$$\theta'_{x,j} = \frac{\theta_{x,j} - u_1\left(\frac{1}{N}\sum_{j=1}^{N}\theta_{x,j} + u_2\right)}{1-u_1}, \tag{3.S59}$$

$$\theta'_{y,j} = \frac{\theta_{x,j} - u_1\left(\frac{1}{N}\sum_{j=1}^{N}\theta_{x,j} + u_3\right)}{1-u_1}, \tag{3.S60}$$

$$\theta'_{z,j} = \frac{\theta_{y,j} - u_1\left(\frac{1}{N}\sum_{j=1}^{N}\theta_{z,j} + u_4\right)}{1-u_1}. \tag{3.S61}$$

The new emitter is then generated as follows:

$$\theta'_{I,N+1} = u_1 \sum_{j=1}^{N} \theta_{I,j}, \tag{3.S62}$$

$$\theta'_{x,N+1} = \frac{1}{N} \sum_{j=1}^{N} \theta_{x,j} + u_2, \tag{3.S63}$$

$$\theta'_{y,N+1} = \frac{1}{N} \sum_{j=1}^{N} \theta_{y,j} + u_3, \tag{3.S64}$$

$$\theta'_{z,N+1} = \frac{1}{N} \sum_{j=1}^{N} \theta_{z,j} + u_4. \tag{3.S65}$$

Applying the general acceptance rate from Eq. (3.S21), the result is similar to Eq. (3.S47) except the Jacobian now expands to:

$$\left| \frac{\partial(\theta')}{\partial(\theta, u)} \right| = \frac{\sum_{j=1}^{N} \theta_{I,j}}{(1-u_1)^{2N+1}}. \tag{3.S66}$$

The acceptance rate then becomes:

$$A_{\text{g-split}} = \frac{P(\theta', k', D)}{P(\theta, k, D)} \frac{\sum_{j=1}^{N} \theta_{I,j}}{P(u_1, u_2, u_3, u_4)((1-u_1)^{2N+1}}. \tag{3.S67}$$

Generalized Merge The generalized merge selects an emitter and then distributes its intensity evenly over the N emitters in the corresponding cluster. As with the merge, the randomly sampled parameters can now be found deterministically:

$$u_1 = \frac{\theta'_{I,N+1}}{\sum_{j=1}^{N} \theta_j}, \tag{3.S68}$$

$$u_2 = \theta'_{x,N+1} - \frac{1}{N} \sum_{j=1}^{N} \theta_{x,j}, \tag{3.S69}$$

$$u_3 = \theta'_{y,N+1} - \frac{1}{N} \sum_{j=1}^{N} \theta_{y,j}, \tag{3.S70}$$

$$u_4 = \theta'_{z,N+1} - \frac{1}{N} \sum_{j=1}^{N} \theta_{z,j}. \tag{3.S71}$$

The new parameters become:

$$\theta_{I,j} = \frac{\theta'_{I,j}}{1-u_1}, \tag{3.S72}$$

$$\theta_{x,j} = u_1 \theta'_{x,N+1} + (1-u_1)\theta'_{x,j}, \tag{3.S73}$$

$$\theta_{y,j} = u_1 \theta'_{x,N+1} + (1-u_1)\theta'_{y,j}, \tag{3.S74}$$

$$\theta_{z,j} = u_1 \theta'_{x,N+1} + (1-u_1)\theta'_{z,j}. \tag{3.S75}$$

$$\tag{3.S76}$$

Inverting the acceptance rate of the generalized split yields:

$$A_{\text{g-merge}} = \frac{P(\theta, k, D)}{P(\theta', k', D)} \frac{P(u_1, u_2, u_3, u_4)((1-u_1)^{2N+1}}{\sum_{j=1}^{N} \theta_{I,j}}. \tag{3.S77}$$

3.S1.8. Birth and Death pair

The birth and death pair can increase and decrease the number of emitters independent of the positions of the currently found emitters. Birth will generate an emitter anywhere in the volume covered by the support of the position priors, using the residual of the frame and the expected image as the probability distribution for selecting the new lateral emitter position. Death randomly chooses any of the current emitters and removes it.

Birth The first task of the birth move is finding probable locations for yet unmodelled emitters. It calculates the expected image from the current model and parameters and subtracts this from the ROI. Any negative values are fixed to zero, and the values are normalized to give a per pixel probability of an undetected emitter:

$$P(k_{\text{new},k_\text{p}}) = \frac{n_{k_\text{p}} - \mu_{k_\text{p}}}{\sum_{k_\text{p}=1}^{N_\text{p}} n_{k_\text{p}} - \mu_{k_\text{p}}}, \qquad \{k_\text{p} : n_{k_\text{p}} - \mu_{k_\text{p}} \geq 0\}, \tag{3.S78}$$

with $P(k_{\text{new},k_\text{p}})$ the pixel probability of a yet undiscovered emitter residing in pixel p_k. After randomly selecting a pixel, a subpixel position is generated from a uniform distribution and the z-position is uniformly sampled from the entire depth range. The intensity of the new emitter is sampled directly from the intensity prior distribution.

This sampling of the z-position may result in a lot of ineffective proposals, however there are little effective alternatives to effectively finding the z-position that do not also impact calculation times or convergence. Some tests have been run where the residual image was filtered with the 3D PSF to return a probability distribution for pairs of x-, y- and z-position. It unfortunately resulted in some chains getting stuck, while only marginally improving convergence speed overall.

Fixing the birth and death selection probabilities to be equal, just as for the (generalized) split and merge moves, yields the acceptance rate:

$$A_{\text{birth}} = \frac{P(\theta', k', D)}{P(\theta, k, D)} \frac{z_{\max} - z_{\min}}{P(k^*_{\text{new},k_\text{p}})}, \tag{3.S79}$$

with $P(k^*_{\text{new},k_\text{p}})$ the probability of sampling from pixel k^*_p and $z_{\max}$, $z_{\min}$ the depth range from which the z-position is sampled. Note that since birth and death work independently from the current emitters, the determinant of the Jacobian $\partial\theta'/\partial(\theta, u)$ is 1.

Death Death is the most straightforward move of them all, simply removing one emitter from the model at random. This move helps remove unnecessary emitters that may have a low intensity or contribute little to a cluster of emitters. It also helps remove emitters spawned by birth that do not necessarily fit the data, but went through despite a low

acceptance rate. The acceptance rate for death is:

$$A_{\text{death}} = \frac{P(\theta', k', D)}{P(\theta, k, D)} = \frac{P(\theta'|D)}{P(\theta|D)}, \tag{3.S80}$$

where the second simplification holds as long as the model prior is kept uniform.

3.S2. Single emitter localization convergence for an astigmatic PSF

To verify if the algorithm works correctly, it is first tested on frames where only a single emitter is active. Synthetic data is generated for an emitter in focal plane of a 20 by 20 pixel ROI, assuming an effective pixel size of 100 nm. Simulated emitters are placed in the centre of the ROI, generating 50 frames, each with a random subpixel shift in x and y drawn from a uniform distribution and intensities drawn from a normal distribution:

$$\theta_x \sim \mathcal{U}(9.5, 10.5), \tag{3.S81}$$
$$\theta_y \sim \mathcal{U}(9.5, 10.5), \tag{3.S82}$$
$$\theta_I \sim \mathcal{N}(I_{\text{sim}}, 150), \tag{3.S83}$$

with the position in pixels, and I_{sim} the mean intensity for the synthetic dataset. The background photon count is fixed at 20 photons. The algorithm is tested on data with $I_{\text{sim}} = 2000$ and $I_{\text{sim}} = 500$ to demonstrate convergence at varying SBR.

The hyperparameters used for localization are as follows. The RJMCMC portion ran for 20000 burn-in iterations, followed by another 10000 iterations from which the model is determined. MCMC is then run for another 5000 iterations, from which the final positions of the emitters are determined. The parameters for the random walk samplers within the RJMCMC and MCMC portions are detailed in Table 3.S2, while the move probabilities were taken from Table 3.S1. The depth was constrained to a range of $[-1, \quad 1]$ μm.

The priors for position and background are uniform, with a custom prior used for intensity. The number of emitters was constrained to $k_{\text{max}} = 6$. The algorithm was initialized randomly with k_{max} active emitters drawn from the priors, ensuring the initial model is incorrect and allowing for meaningful conclusions from the model time series and autocorrelation.

High SBR results

For $I_{\text{sim}} = 2000$, the prior on intensity is given as follows:

$$P(I) = \begin{cases} 0, & \text{if } I > 2500, \\ \frac{1}{150\sqrt{2\pi}} \exp\left\{-\frac{1}{2}\left(\frac{I-2000}{150}\right)^2\right\}/1.08, & \text{if } 1600 < I < 2500, \\ 6.6 \cdot 10^{-5}, & \text{if } 500 < I < 1600, \\ (\frac{I}{500}) \cdot 6.6 \cdot 10^{-5}, & \text{if } I > 500. \end{cases} \tag{3.S84}$$

The prior is plotted in Fig. 3.S2.

Model convergence To verify the model has converged, the time series of the models over all frames as well as the average autocorrelation of the model is studied.

In Fig. 3.S3, the model time series and autocorrelation are plotted. From the time series, we can see that from the initialization at $k_{\max} = 6$ emitters, the estimated model rapidly reduces to a two or one emitter model. There is notably little mixing in the model chain. This may be due to the simplicity of localizing a single emitter, the algorithm therefore having infinitesimal probabilities of jumping to models with 3 emitters or more. Note that after the burn-in fraction, the split and merge move are turned off and there is no more change in the model found. With split and merge disabled, and G-split and G-merge failing since no clusters can be made out of one emitter, the only moves capable of changing the model are birth and death. At this point, the RJMCMC seems to have converged strongly. Evaluating the average model chain autocorrelation, it is clear that after 2000 RJMCMC iterations, the autocorrelation has gone to zero. This gives an idea of the chain length required to estimate the model distribution under these conditions. Some multiple of 2000, say 6000 RJMCMC iterations, may already be sufficient for model convergence on this problem. From the histogram in Fig. 3.S3*d* it is clear that on average, the estimates spend nearly all their time in a model with one active emitter.

Parameter convergence Again, we look to the autocorrelation of the parameters to assess convergence. In Fig. 3.S3*b*, the average autocorrelations of all parameters for their MCMC chains are plotted. Note that the MCMC chain was initialized from the last RJMCMC iteration that had the correct model, therefore the parameters can be expected to converge quickly and there is no need to discard the initial part of the chain. The autocorrelations of the lateral position and background decrease almost immediately to zero. Note that while the autocorrelation for axial position drops to zero in the same time, there are some slower transients visible in the plot. The same holds for the autocorrelation of intensity, which also takes significantly longer to reach zero. The acceptance rates for the moves are

$$\left[0, \quad 0.47 \pm 0.02, \quad 0.28 \pm 0.01\right]$$

for the group move, single emitter move, and background move, respectively. The group move cannot find a cluster and is therefore never executed, meanwhile the single emitter move has a good acceptance rate ensuring proper mixing. The background move has low acceptance, though it should still be enough for proper mixing.

Calculating the lateral and axial RMSE results in 0.05 pixels and 120 nm errors, respectively, giving us an accurate estimate of the emitter position.

It can be concluded that the initial position found from RJMCMC was sufficiently close to the optimum and the chosen hyperparameters and chain length were appropriate, though the sampling of intensity still shows correlation and σ_I may need to be tuned more.

Low SBR results

For $I_{\text{sim}} = 500$, the prior on intensity is given as follows:

$$P(I) = \begin{cases} 0, & \text{if } I > 950, \\ \frac{1}{150\sqrt{2\pi}} \exp\left\{-\frac{1}{2}\left(\frac{I-500}{150}\right)^2\right\}, & \text{if } I < 950. \end{cases} \tag{3.S85}$$

The prior is plotted in Fig. 3.S4. This dataset samples intensities from $\mathcal{N}(500, 150)$ photons, with a background of 20 photons.

Model convergence In Fig. 3.S5, *a* and *c*, the model time series and autocorrelation are plotted. Again, from the incorrect initialization the estimated model rapidly reduces to a two or one emitter model. There is less mixing and faster convergence compared to the simulations with $I_{\text{sim}} = 2000$. The lower SBR results in more uncertainty when determining the model. Even after the burn-in, some frames still make jumps in model space. Looking at the average autocorrelation, it reaches zero with a lag of just 250. This is in line with the increased mixing in the first 3000 steps. After a lag of about 1250, the autocorrelation seems to settle at zero. Again, this indicates that the 30000 RJMCMC iterations are more than sufficient for determining the model. The histogram in Fig. 3.S5*d* again shows that the chain spends virtually all its time in a single emitter model.

Parameter convergence In Fig. 3.S5*b*, the average parameter autocorrelation for the 50 frames is shown. The autocorrelations of the position chains take longer to reach zero compared to the high SBR case. This time, the axial chain is actually slower than the intensity chain, and now even the lateral chain displays some slow transient behaviour. The background converges first, followed by intensity and lateral position, and finally axial position. Under these conditions, convergence is limited by the sampling of the z-position instead of the intensity. The acceptance rates for the moves are

$$\left[0, \quad 0.73 \pm 0.04, \quad 0.270 \pm 0.009\right].$$

The single emitter move has a high acceptance rate and the corresponding random walk hyperparameters may be increased for better mixing and less correlation between samples.

Calculating the lateral and axial RMSE results in 2 pixels and 360 nm errors, respectively, which is a lot less accurate especially in lateral direction compared to the high SBR case. This is due to some of the outliers in the sampled intensity, for instance frames 18 and 45 having an intensity less than 100 photons (79 and 83, respectively). Not considering these two frames, intensities still range from 200 to 700 photons (covering about 85% of the interval), and the lateral and axial RMSE become 0.14 pixels and 340 nm each.

This test has shown that though the chain length is sufficient, tuning of the single emitter move may lead to faster convergence.

Finally, it can be concluded that the hyperparameters provided here generally result in convergence, though it is best practice to adjust them to the imaging conditions of your system, ideally making use of autocorrelation plots to identify sub-optimal behaviour.

3.S3. Single emitter localization convergence for a tetrapod PSF

The same test is run for a tetrapod PSF, under similar conditions, simulating 50 frames of in-focus emitters in the centre of the ROI with some subpixel shift, for varying SBR. The size of the ROI was set to 28 by 28 pixels, to account for the wider PSF. The same move probabilities were used, while adjusting the hyperparameters and PSF width, which was estimated from a Gaussian fit of the width in focal plane. The hyperparameters can be found in Table 3.S3.

High SBR results

For $I_{\text{sim}} = 2000$, using the intensity prior shown in Fig. 3.S2, the results are as follows.

Model convergence Studying the autocorrelation in Fig. 3.S6*a*, it appears that model convergence is slightly slower with the tetrapod PSF. This may be related to use of a fixed clustering radius, after all the tetrapod PSF greatly changes in width over depth. There is a lot more mixing in the chain of Fig. 3.S6*c* this time, with two or three emitter models existing up to around 3000 iterations into the run.

Beyond 5000 iterations, the RJMCMC run seems to have converged strongly. Evaluating the average model chain autocorrelation suggests that a minimum of 2600 RJMCMC iterations is needed. Some multiple of 2600, say 7800 RJMCMC iterations, should be sufficient for model convergence on this problem. From the histogram in Fig. 3.S6*d* it is clear that on average, the estimates spend nearly all their time in a model with one active emitter.

Parameter convergence Fig. 3.S6*b* plots the average parameter autocorrelation for the 50 frames. The lateral, axial, and background autocorrelation converge rapidly. The intensity chain takes the longest to reach zero after a lag of 500 and still shows some more slow transient behaviour. The acceptance rates for the moves are

$$\begin{bmatrix} 0, & 0.18 \pm 0.02, & 0.205 \pm 0.009 \end{bmatrix}$$

for the group move, single emitter move, and background move, respectively. The single emitter move has a low acceptance rate, possibly due to poor intensity sampling. The background move performs similarly to the runs on astigmatic data.

Calculating the lateral and axial RMSE results in 0.09 pixels and 20 nm errors.

It can be concluded that the chosen hyperparameters and chain length can converge, though the sampling of intensity still shows correlation and σ_I may need to be tuned more.

Low SBR results

For $I_{\text{sim}} = 500$, the prior in Fig. 3.S4 was used. The results are as follows.

Model convergence In Fig. 3.S7, *a* and *c*, the model time series and autocorrelation are plotted. Again, from the incorrect initialization the estimated model rapidly reduces

to a two or one emitter model. More mixing seems to be happening in the first 10000 iterations compared to the simulations with $I_{\text{sim}} = 2000$. The lower SBR gives more uncertainty when determining the model. The average model autocorrelation reaches zero at a lag of about 200, as expected from the increase in mixing. This again indicates that the 30000 iterations used were more than sufficient. The histogram in Fig. 3.S7*d* shows that the chains generally stay in a single emitter model.

Parameter convergence In Fig. 3.S7*b*, the average parameter autocorrelation for the 50 frames is shown. This time, the lateral and axial position chains are slowest to converge, around a lag of 1500, while the background and intensity chains still reach zero in about 400 steps. Under these conditions, convergence is limited by the emitter position sampling instead of the intensity. The acceptance rates for the moves are

$$\left[0, \quad 0.55 \pm 0.08, \quad 0.198 \pm 0.009\right].$$

Both the single emitter and background move show appropriate acceptance rates, the single emitter move even on the higher side. The high acceptance rates in combination with the strong correlation in parameter jumps suggests σ_x, σ_y, and σ_z may be increased to reduce sample correlation and get faster convergence.

The lateral and axial RMSE are in 1.6 pixels and 200 nm errors, respectively. Again, removing some outliers with intensities less than 200 returns precisions of 0.3 pixels and 70 nm, which is appropriate for these conditions.

Again, these tests have shown that extensive tuning of the single emitter move may lead to faster convergence in both scenarios.

Finally, the hyperparameters used for imaging with the tetrapod PSF will converge to an accurate estimate, though not as rapidly as astigmatic imaging with its respective hyperparameters.

3.S4. Single emitter precision and accuracy for an astigmatic PSF

To further verify the accuracy and precision of the algorithm, another set of synthetic data was generated using the same PSFs from the convergence test. Again, single emitters with random subpixel shifts were simulated with a background of 20 photons and intensities ranging from 600 to 3000 photons, in steps of 100. 50 emitters were simulated at each intensity. Move probabilities were the same as in the convergence tests, while the hyperparameters can be found in Table 3.S4.

The intensity prior is now set to be uniform, fixing the range of the intensity prior from 100 to 4000 photons. This makes all the priors uniform, effectively only serving as loose constraints. It is now possible to compare our results to the CRLB, as the algorithm is virtually unbiased. Fig. 3.S8 plots the CRLB against the localization precision found directly on individual frames, calculated from the MCMC chain under a Gaussian assumption. This indicates that for the astigmatic PSF, the histograms from individual frames give an accurate representation of the achievable precision. Fig. 3.S9 plots the resampled RMSE for the same results. The RMSE roughly matches the CRLB from Fig.

3.S8, showing that the algorithm can find a precise and accurate estimate under these conditions.

3.S5. Single emitter precision and accuracy for a tetrapod PSF

The same testing was done for a tetrapod PSF, using the same hyperparameters as in Table 3.S4 but with a PSF width of 2.1 pixels. At emitter intensities less than 1000 photons, some frames failed to converge, showcasing the difficulty of using a complex PSF at a low SBR. This may be due to the flat intensity prior yielding poor initializations and difficulty escaping local minima. The accuracy and precision are thus plotted over a range of 1000 to 3000 photons. Fig. 3.S10 shows the CRLB and localization precision found as above. Note that the found precision for intensity breaks the CRLB, especially at higher intensity, despite the other parameter precisions tracking the CRLB well. The precision found when assuming a Gaussian distribution is thus not representative of the information present in the frame, at least not for the emitter intensity. Fig. 3.S11 again shows the resampled RMSE for the same data. This time, all estimates behave as expected, broadly tracking the CRLB.

3.S6. Multimodality in two emitter imaging

During testing of two emitter separability, under some conditions four peaks were found in the reconstruction of the emitter position. This occurred despite the chains in those situations converging to the correct MAP number of emitters. This phenomenon was observed at smaller distances between emitters, using the astigmatic PSF under relative angles of 0 and 90 degrees with respect to the x-axis, and for the tetrapod PSF under angles of 45 degrees. To understand if this was due to pseudo-convergence or if this was representative of the underlying posterior, a multimodal frame was analysed, shown in Fig. 3.S12. K-means clustering was used to find four potential localizations, shown together with the ground truth in Fig. 3.S12*a*. Then, by picking fixing one of these emitters and moving the other around the ROI at the same depth and intensity, the log likelihood was mapped, shown in Fig. 3.S12*c*. Fixing the rightmost emitter finds the global optimum to be a pair of emitters near the ground truth, while fixing the bottom emitter finds an alternate mode of the solution, a pair perpendicular to the ground truth. Note that this local optimum has virtually the same likelihood. To investigate if either mode could be representative of the data, a χ-squared test was done on a 95% confidence interval. The χ^2 value is calculated as follows:

$$\chi^2 = \sum_{i=1}^{N_\mathrm{p}} \frac{(D_i - \mu_i)^2}{\mu_i}, \tag{3.S86}$$

with N_p the number of pixels, D_i the measurement of the i^{th} pixel, and μ_i the expected value. As the frames are subject to Poisson noise, the χ^2 threshold for a 95% confidence

interval can be found with:

$$\chi^2_{\text{threshold}} = N_\text{p} + 1.96\sqrt{2N_\text{p} + \sum_{i=1}^{N_\text{p}} \frac{1}{\mu_i}}. \tag{3.S87}$$

Applying it to this frame results in $\chi^2_{\text{threshold}} = 456$, with the true and alternate modes returning a χ^2 of 407 and 408, respectively. Both modes thus are well within the 95% confidence interval and are representative of the frame.

To test whether it is possible to select the true mode from these hypotheses, the log likelihood ratios of the hypotheses are used to calculate the probability of error. This log likelihood ratio can be approximated by a Gaussian distribution:

$$\text{LLR}_{q,r} = \ln\left(\frac{P(D|H_q)}{P(D|H_r)}\right), \tag{3.S88}$$

$$\mu_{q,r,s} = \sum_i^{N_\text{p}} \mu_i^s \ln\left(\frac{\mu_i^q}{\mu_i^r}\right) - \mu_i^q + \mu_i^r, \tag{3.S89}$$

$$\sigma_{q,r,s} = \sum_i^{N_\text{p}} \mu_i^s \ln\left(\frac{\mu_i^q}{\mu_i^r}\right)^2, \tag{3.S90}$$

with $\text{LLR}_{q,r}$ the log likelihood ratio of hypothesis q over hypothesis r, $\mu_{q,r,s}$ the mean of $\text{LLR}_{q,r}$ assuming hypothesis s is true, and $\sigma_{q,r,s}$ the corresponding width. For the two hypotheses H_0 and H_1, $P(\text{LLR}_{0,1}|H_0)$ and $P\text{LLR}_{0,1}|H_1)$ can now be calculated, as shown in Fig. 3.S12*b*. To retrieve the probability of error, we now use the probability of making a correct selection:

$$P_\text{c} = P(\text{LLR}_{0,1} > 0|H_0) - P(\text{LLR}_{0,1} < 0|H_1), \tag{3.S91}$$

$$P_\text{e} = (1 - P_\text{c})/2, \tag{3.S92}$$

with P_c the probability of being correct and P_e the probability of error. Applying this to the two modes from Fig. 3.S12 results in a probability of error of 0.498. It is therefore not possible to select the right mode solely given the data.

Testing the multimodal reconstructions found under different angles for the astigmatic and tetrapod PSF yielded similar results, where both pairs of emitter locations pass the chi-squared test and have greater than 49.5% probability of error.

In conclusion, while both modes are representative of the data, there is no distinction to be made based on their likelihood. This indicates that pseudo-convergence is not the case and the posterior distribution in this scenario is multimodal. As both PSFs show this multimodality under different conditions, this indicates PSF degeneracy.

3.S7. Supporting figures and tables

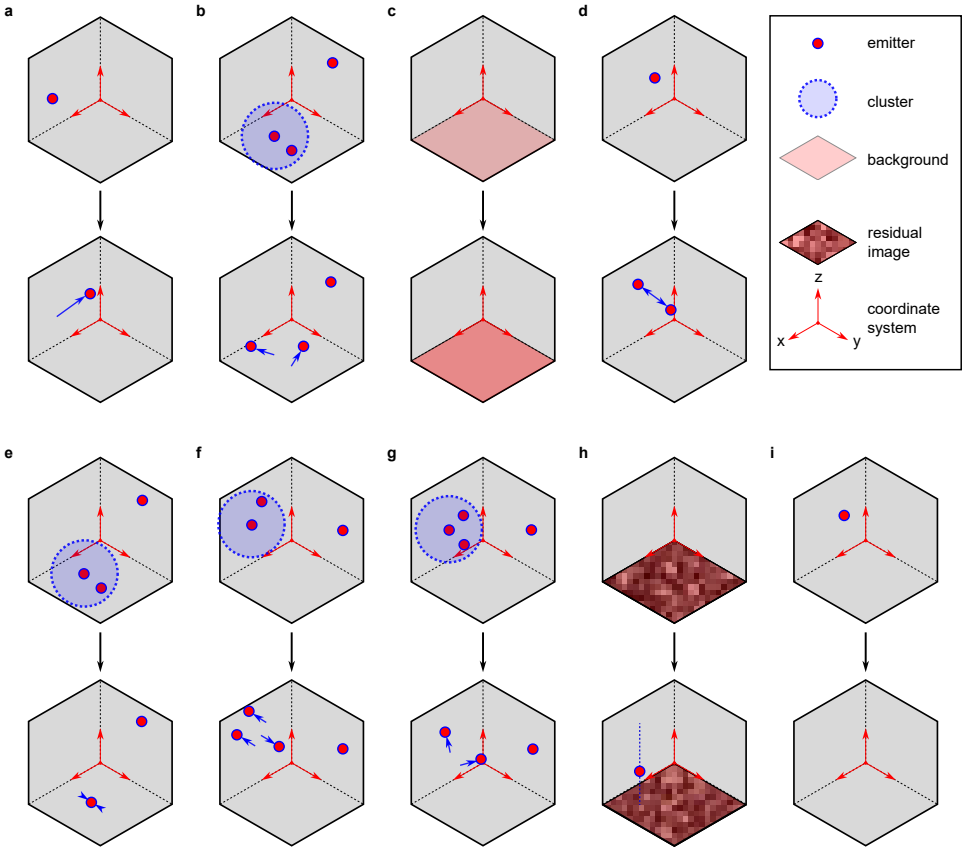

Figure 3.S1: A collection of diagrams visualising the proposals that each move makes. (*a*) The single emitter move changes the 3D position of an emitter, as well as its intensity. (*b*) The group move finds a cluster of emitters and randomly and independently changes their positions and intensities. (*c*) The background move changes the estimated background photon count. (*d*) Split distributes the intensity of a random emitter over two new emitters. (*e*) Merge randomly selects an emitter and searches within a given radius for an emitter to merge it with, combining intensities. (*f*) Generalized split finds a cluster of N emitters and splits them off into $N+1$ emitters. (*g*) Generalized merge finds a cluster of $N+1$ emitters to merge into N emitters. (*h*) Birth constructs a residual image to use as a probability distribution for possible undetected emitter positions, generating a new emitter with a random position. (*i*) Death removes a randomly selected emitter from the model.

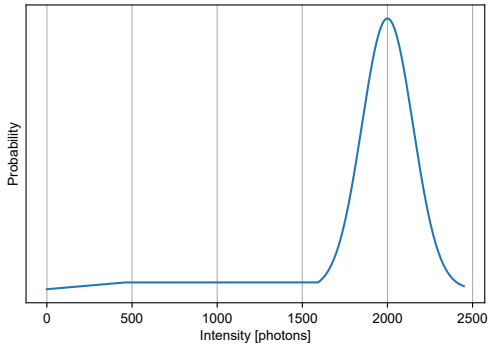

Figure 3.S2: Prior on intensity. Used for synthetic data with intensities drawn from $\mathcal{N}(2000, 150)$.

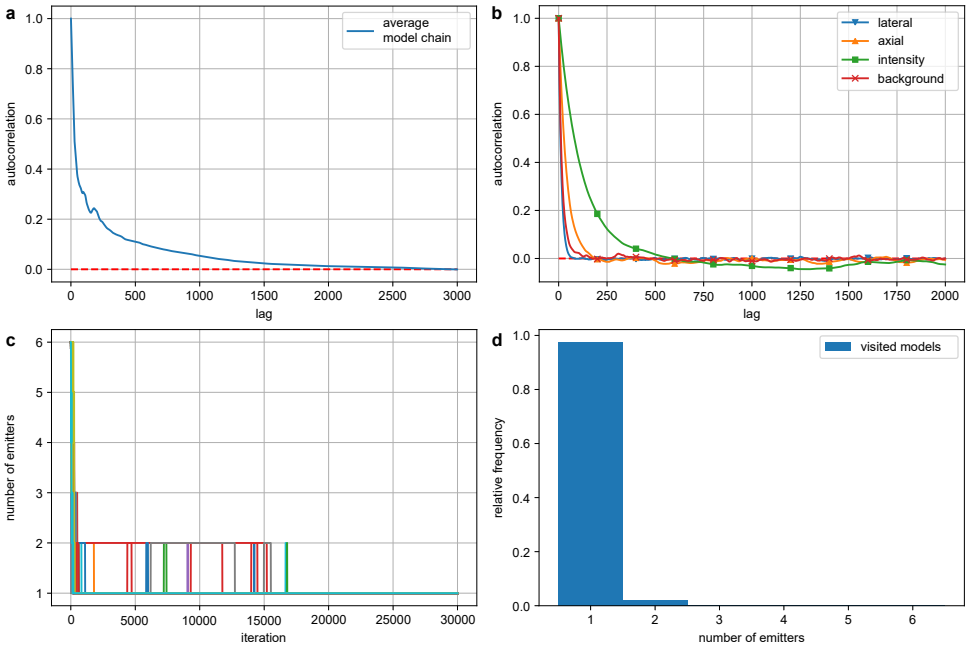

Figure 3.S3: Model and parameter space convergence of the algorithm for high SBR frames. (*a*) Autocorrelation of the model chain. (*b*) Autocorrelation of the parameters. (*c*) Time series plot of the model for all frames. (*d*) Histogram of all visited models across all frames. Emitter intensities were sampled from $\mathcal{N}(2000, 150)$, background was set to 20 photons. Emitters were placed in focal plane at the centre of the region of interest (ROI) and given a sub-pixel shift drawn from $\mathcal{U}(-0.5, 0.5)$. 100 frames were used.

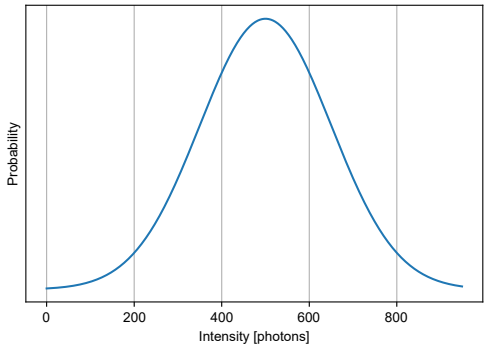

Figure 3.S4: Prior on intensity for low SBR. Used for synthetic data with intensities drawn from $\mathcal{N}(500, 150)$.

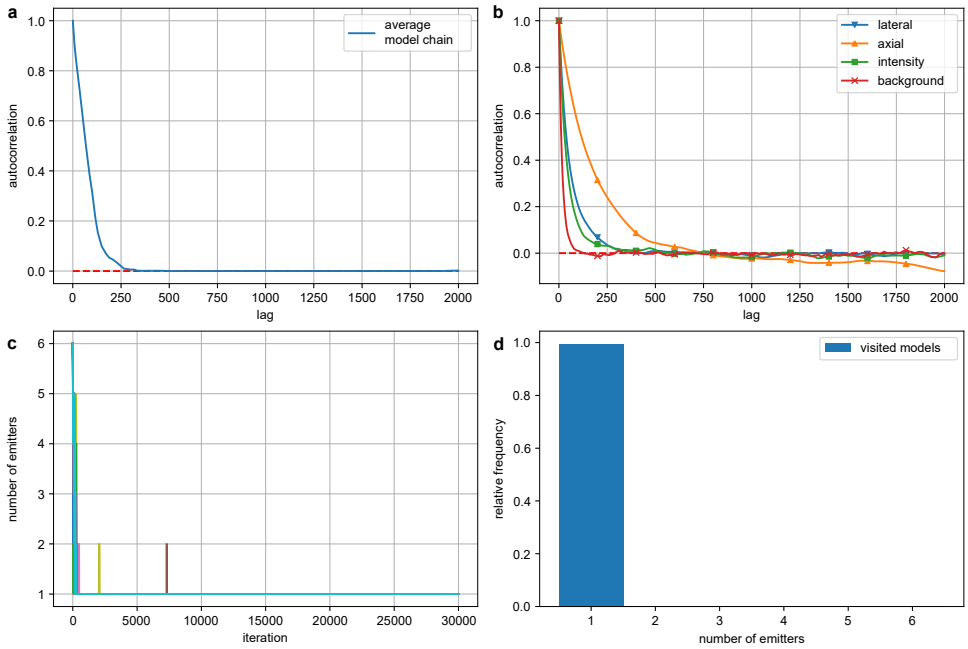

Figure 3.S5: Model and parameter space convergence of the algorithm for low SBR frames. (*a*) Autocorrelation of the model chain. (*b*) Autocorrelation of the parameters. (*c*) Time series plot of the model for all frames. (*d*) Histogram of all visited models across all frames. Emitter intensities were sampled from $\mathcal{N}(500, 150)$, background was set to 20 photons. Emitters were placed in focal plane at the centre of the ROI and given a sub-pixel shift drawn from $\mathcal{U}(-0.5, 0.5)$. 100 frames were used.

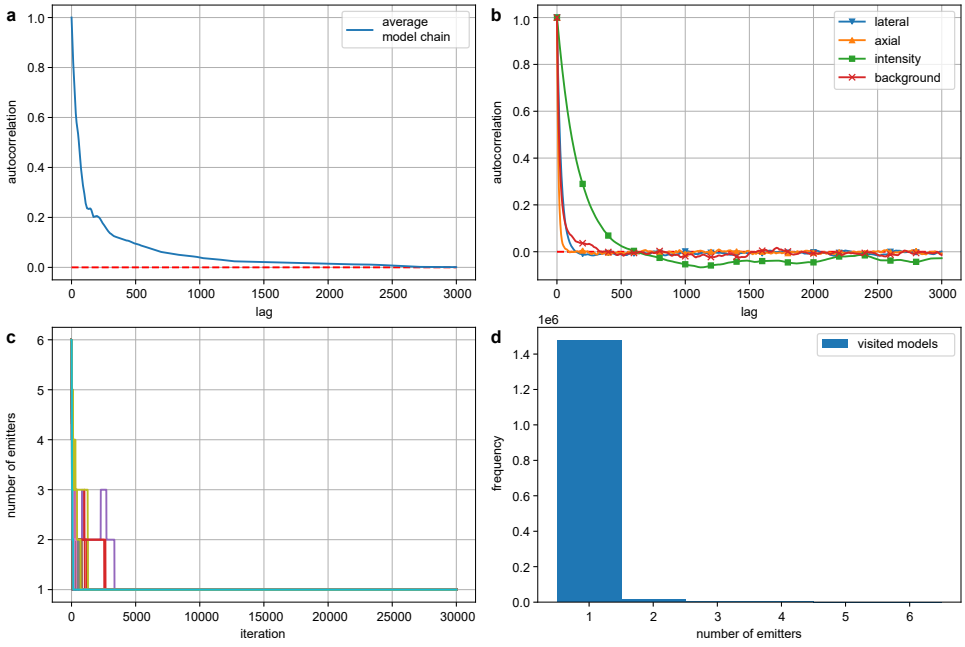

Figure 3.S6: Model and parameter space convergence of the algorithm for high SBR frames. (*a*) Autocorrelation of the model chain. (*b*) Autocorrelation of the parameters. (*c*) Time series plot of the model for all frames. (*d*) Histogram of all visited models across all frames. Emitter intensities were sampled from $\mathcal{N}(2000, 150)$, background was set to 20 photons. Emitters were placed in focal plane at the centre of the ROI and given a sub-pixel shift drawn from $\mathcal{U}(-0.5, 0.5)$. 100 frames were used.

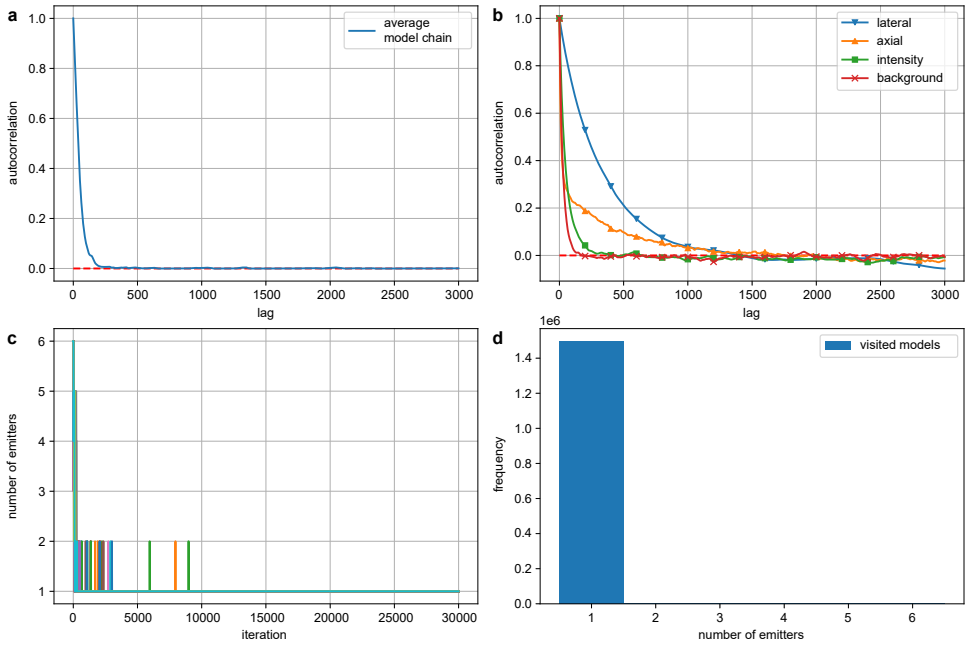

Figure 3.S7: Model and parameter space convergence of the algorithm for low SBR frames. (*a*) Autocorrelation of the model chain. (*b*) Autocorrelation of the parameters. (*c*) Time series plot of the model for all frames. (*d*) Histogram of all visited models across all frames. Emitter intensities were sampled from $\mathcal{N}(500, 150)$, background was set to 20 photons. Emitters were placed in focal plane at the centre of the ROI and given a sub-pixel shift drawn from $\mathcal{U}(-0.5, 0.5)$. 100 frames were used.

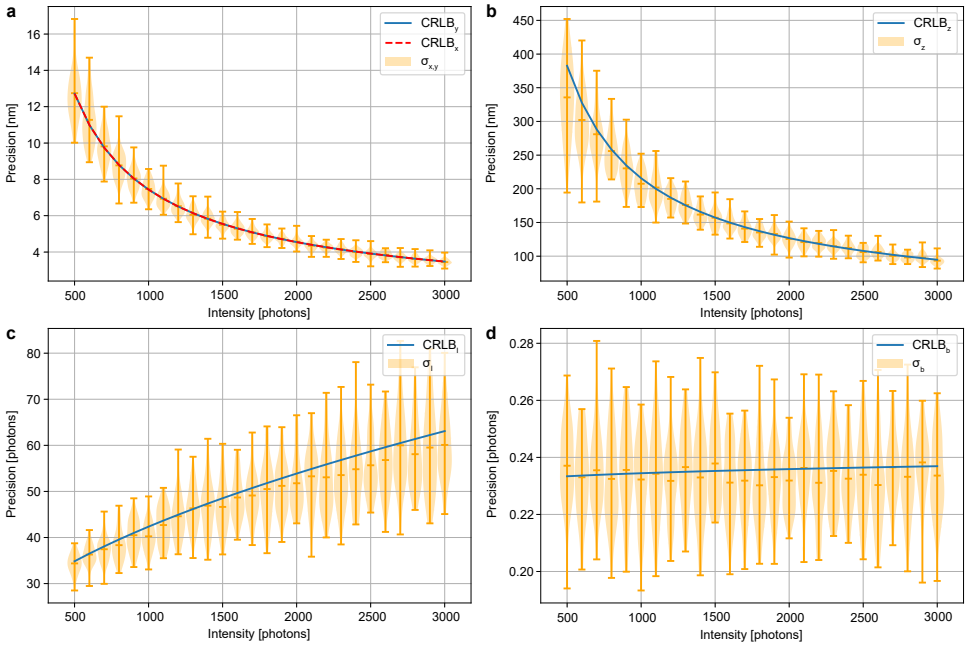

Figure 3.S8: Violin plots of parameter estimates over intensity using astigmatic imaging, compared to the CRLB. (*a*) Lateral precision violin plot, using an effective pixel size of 100 nm. (*b*) Axial precision violin plot. (*c*) Violin plot of the emitter intensity precision. (*d*) Violin plot of the background intensity precision. Precisions were calculated from the MCMC chain of individual frames, assuming a Gaussian distribution. With a background of 20 photons, 50 frames were used per datapoint from 500 to 3000 emitter intensity photons. Emitters were placed in focal plane at the centre of the ROI and given a sub-pixel shift drawn from $\mathcal{U}(-0.5, 0.5)$.

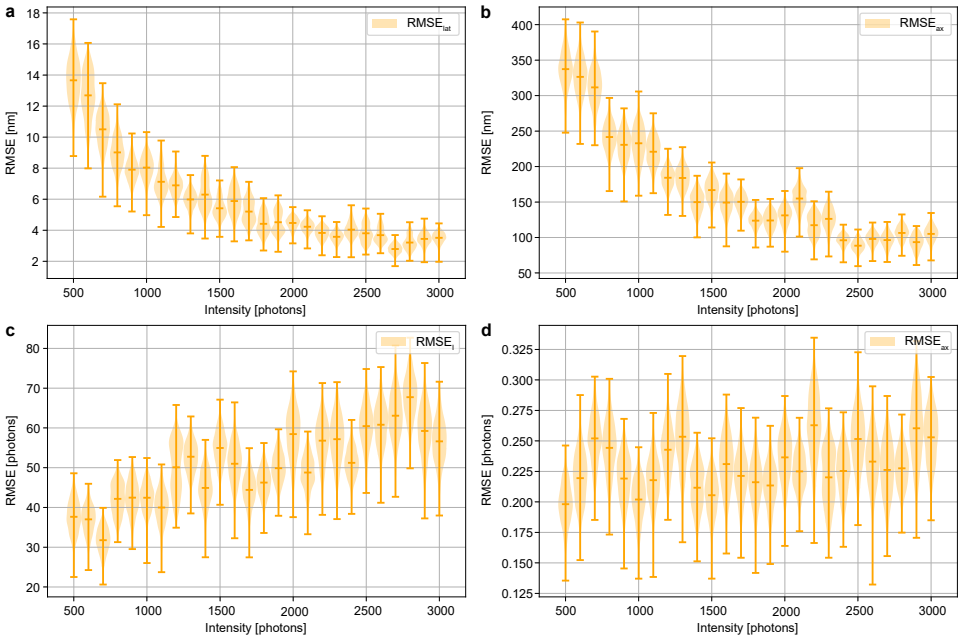

Figure 3.S9: Bootstrap resampled RMSE results for the parameter estimates plotted over intensity using astigmatic imaging. (*a*) Violin plot of the lateral RMSE. (*b*) Violin plot of the axial RMSE. (*c*) Violin plot of the emitter intensity RMSE. (*d*) Violin plot of the background intensity RMSE. Results were resampled using 50% of the available data and 1000 runs. With a background of 20 photons, 50 frames were used per datapoint from 500 to 3000 emitter intensity photons. Emitters were placed in focal plane at the centre of the ROI and given a sub-pixel shift drawn from $\mathscr{U}(-0.5, 0.5)$.

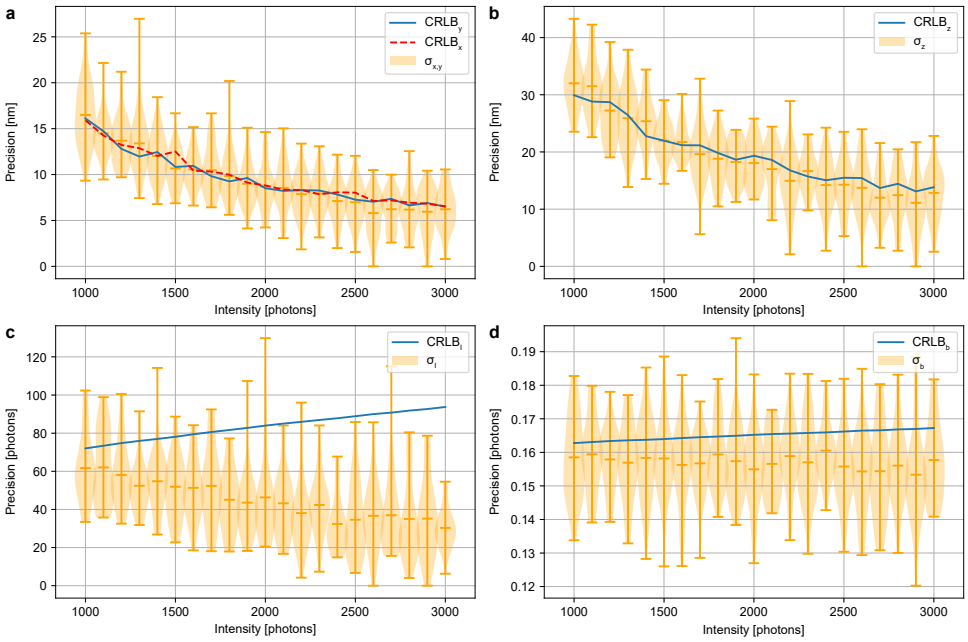

Figure 3.S10: Violin plots of the parameter estimates over intensity using a tetrapod PSF, compared to the CRLB. (*a*) Lateral precision violin plot, using an effective pixel size of 100 nm. (*b*) Axial precision violin plot. (*c*) Violin plot of the emitter intensity precision. (*d*) Violin plot of the background intensity precision. Precisions were calculated from the MCMC chain of individual frames, assuming a Gaussian distribution. With a background of 20 photons, 50 frames were used per datapoint from 500 to 3000 emitter intensity photons. Emitters were placed in focal plane at the centre of the ROI and given a sub-pixel shift drawn from $\mathcal{U}(-0.5, 0.5)$.

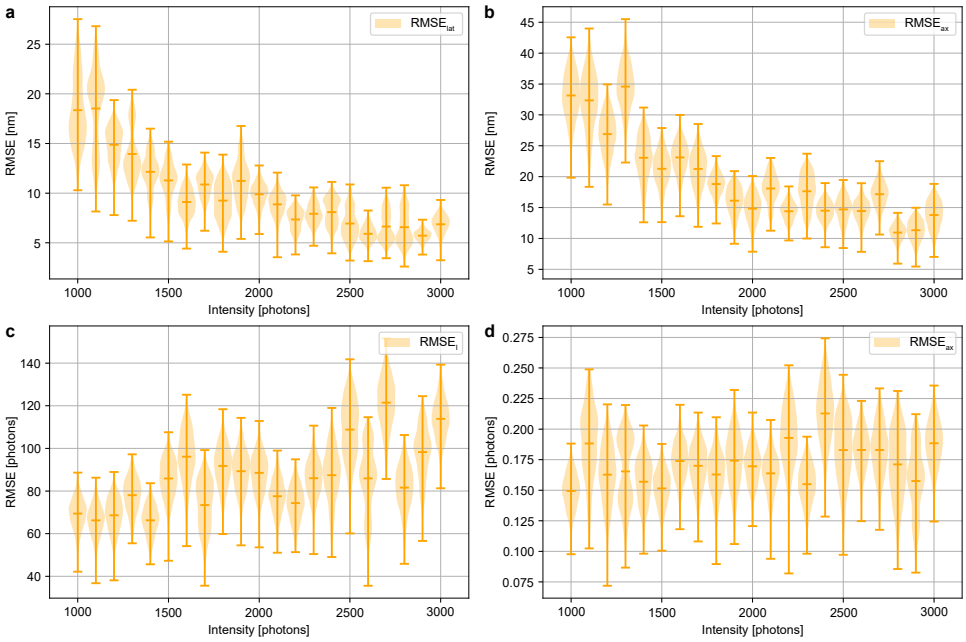

Figure 3.S11: Bootstrap resampled RMSE results for the parameter estimates using a tetrapod PSF, plotted over intensity. (*a*) Violin plot of the lateral RMSE. (*b*) Violin plot of the axial RMSE. (*c*) Violin plot of the emitter intensity RMSE. (*d*) Violin plot of the background intensity RMSE. Results were resampled using 50% of the available data and 1000 runs. With a background of 20 photons, 50 frames were used per datapoint from 500 to 3000 emitter intensity photons. Emitters were placed in focal plane at the centre of the ROI and given a sub-pixel shift drawn from $\mathscr{U}(-0.5, 0.5)$.

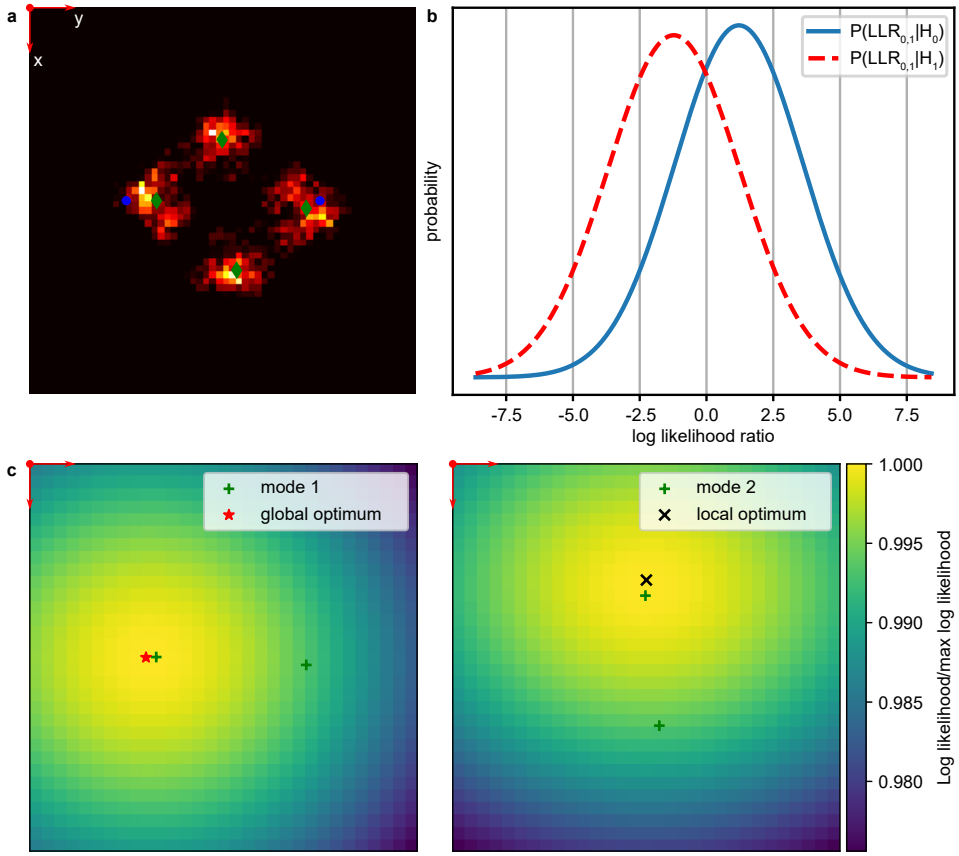

Figure 3.S12: Analysis of multimodality in astigmatic PSF 3D reconstructions for the two emitter problem. Ground truth positions are marked with blue dots, while localizations are marked with green crosses. (*a*) Single frame reconstruction for the two emitter problem. (*b*) Plots of the log likelihood ratios between the hypothesised modes of the reconstruction in a), using a Gaussian approximation. (*c*) Left: fixing the rightmost localization, an emitter is shifted over the ROI, imaging the log likelihood and marking the maximum (red star). Right: the bottom emitter is fixed, and a local optimum is found in the black cross. This finds the pair of modes used in b), one on the ground truth and one perpendicular to it. Calculating the probability of error yields a 49.8% chance of selecting the wrong hypothesis. The expected value of either mode passes a chi-squared test on a 95% confidence interval.

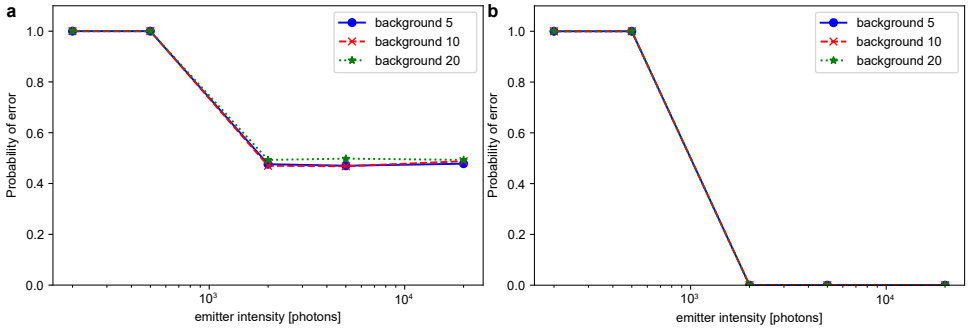

Figure 3.S13: Probability of error between modes for the two emitter problem using astigmatic and biplane imaging. Plotted for varying emitter and background intensities. (*a*) Probability of error when selecting modes with astigmatic imaging. (*b*) Probability of error when selecting modes using biplane imaging. Emitters were placed in focal plane, separated by $5/4\ \sigma_{\mathrm{PSF}}$ along the x-axis. All uniform priors except for emitter intensity, which used $\mathcal{N}(I_{\mathrm{sample}}, 3.5\sqrt{I_{\mathrm{sample}}})$. Probability of error was calculated using the same methods as for Fig. 3.S12 described in Section 3.S6. Reconstructions without alternate mode used a probability of error of 0, while reconstructions that could not separate emitters used a probability of error of 1.

Table 3.S1: Move proposal probabilities.

Move type	Probability		
	$\text{RJMCMC}_{\text{burn}}$	RJMCMC	MCMC
Single Emitter	$\frac{1}{5}$	$\frac{1}{4}$	$\frac{2}{5}$
Group Move	$\frac{1}{5}$	$\frac{1}{4}$	$\frac{2}{5}$
Background	$\frac{1}{5}$	$\frac{1}{4}$	$\frac{1}{5}$
Split	$\frac{1}{15}$	0	0
Merge	$\frac{1}{15}$	0	0
Generalized Split	$\frac{1}{15}$	$\frac{3}{32}$	0
Generalized Merge	$\frac{1}{15}$	$\frac{3}{32}$	0
Birth	$\frac{1}{15}$	$\frac{1}{32}$	0
Death	$\frac{1}{15}$	$\frac{1}{32}$	0

Table 3.S2: RJMCMC hyperparameters for astigmatic PSF, single emitter convergence test.

Parameter	RJMCMC	MCMC	Units
σ_x	0.05	0.05	pixels
σ_y	0.05	0.05	pixels
σ_z	0.08	0.07	μm
σ_I	18	15	photons
σ_b	1	1	photons
σ_{PSF}	1.3	1.3	pixels

Table 3.S3: RJMCMC hyperparameters for tetrapod PSF, single emitter convergence test.

Parameter	RJMCMC	MCMC	Units
σ_x	0.1	0.1	pixels
σ_y	0.1	0.1	pixels
σ_z	0.08	0.08	μm
σ_I	30	30	photons
σ_b	1	1	photons
σ_{PSF}	2.1	2.1	pixels

Table 3.S4: RJMCMC hyperparameters for astigmatic PSF, single emitter precision test.

Parameter	RJMCMC	MCMC	Units
σ_x	0.08	0.08	pixels
σ_y	0.08	0.08	pixels
σ_z	0.08	0.08	μm
σ_I	30	30	photons
σ_b	1	1	photons
σ_{PSF}	1.3	1.3	pixels

References

[1] M. Fazel, M. J. Wester, H. Mazloom-Farsibaf, M. B. M. Meddens, A. S. Eklund, T. Schlichthaerle, F. Schueder, R. Jungmann, and K. A. Lidke. “Bayesian Multiple Emitter Fitting using Reversible Jump Markov Chain Monte Carlo”. In: *Scientific Reports* 9.1 (2019).

4

Precision in Iterative Modulation Enhanced Single-Molecule Localization Microscopy

Light thinks it travels faster than anything but it is wrong. No matter how fast light travels, it finds the darkness has always got there first, and is waiting for it.

Sir Terence David John Pratchett, *Reaper Man*

Dylan Kalisvaart
Jelmer Cnossen
Shih-Te Hung
Sjoerd Stallinga
Michel Verhaegen
Carlas S. Smith

Biophysical Journal, vol. 121, no. 12, (2022), pp. 2279-2289

Abstract

Modulation enhanced single-molecule localization microscopy (meSMLM) methods improve the localization precision by using patterned illumination to encode additional position information. Iterative meSMLM (imeSMLM) methods iteratively generate prior information on emitter positions, used to locally improve the localization precision during subsequent iterations. The Cramér-Rao lower bound cannot incorporate prior information to bound the best achievable localization precision because it requires estimators to be unbiased. By treating estimands as random variables with a known prior distribution, the Van Trees inequality (VTI) can be used to bound the best possible localization precision of imeSMLM methods. An imeSMLM method is considered, where the positions of in-plane standing-wave illumination patterns are controlled over the course of multiple iterations. Using the VTI, we analytically approximate a lower bound on the maximum localization precision of imeSMLM methods that make use of standing-wave illumination patterns. In addition, we evaluate the maximally achievable localization precision for different illumination pattern placement strategies using Monte Carlo simulations. We show that in the absence of background and under perfect modulation, the information content of signal photons increases exponentially as a function of the iteration count. However, the information increase is no longer exponential as a function of the iteration count under non-zero background, imperfect modulation, or limited mechanical resolution of the illumination positioning system. As a result, imeSMLM with two iterations reaches at most a fivefold improvement over SMLM at 8 expected background photons per pixel and 95% modulation contrast. Moreover, the information increase from imeSMLM is balanced by a reduced signal photon rate. Therefore, SMLM outperforms imeSMLM when considering an equal measurement time and illumination power per iteration. Finally, the VTI is an excellent tool for the assessment of the performance of illumination control and is therefore the method of choice for optimal design and control of imeSMLM methods.

Significance

One of the fundamental questions in single-molecule localization microscopy is at what precision the position of a single molecule can be determined. In this chapter, we show that iterative localization microscopy obtains its precision improvement through incorporation of prior information, thereby reducing the number of photons needed for precise localization. In this situation, the Van Trees inequality quantifies the best possible localization precision that can be achieved. The approach presented here can be generalized to evaluate the best possible localization precision obtainable for different imaging tasks and with different illumination patterns, point spread functions, and/or control strategies.

4.1. Introduction

In single-molecule localization microscopy (SMLM), sparsely activated fluorescent emitters are localized sequentially to obtain a resolution higher than the diffraction limit [1–3]. Modulation enhanced SMLM (meSMLM) increases the localization precision using patterned illumination to sparsely activate emitters in a sample, after which emitter positions are estimated from the sparsity in the emission light [4]. Methods such as SIMFLUX [5], SIMPLE [6] and repetitive optical selective exposure [7] use a standing-wave intensity pattern for the illumination, while MINFLUX [8] uses a doughnut-shaped intensity pattern. Axial resolution was also increased through modulated localization [9, 10] and axial localization with repetitive optical selective exposure [11], which use patterns with structure in lateral and axial directions.

Localization precision can be increased locally around the emitter by iteratively adapting meSMLM methods through using prior information on the emitter position that was generated from previous measurements, which we call iterative meSMLM (imeSMLM). In [12], an iterative variant of MINFLUX is discussed, where the position of an emitter is estimated through triangulation with doughnut-shaped illumination patterns. This estimate and its localization uncertainty are used as prior information to reposition and shrink the region of triangulation, after which the emitter position is estimated again. This procedure locally improves precision in the neighbourhood of the emitter. Furthermore, it is argued that distributing the limited signal photon budget over many iterations is preferred over increasing the amount of signal photons per iteration, as the information content of signal photons increases over the course of iterations.

To characterize the localization precision of (me)SMLM methods, the Cramér-Rao lower bound (CRLB) is often used [13]. Under mild assumptions (see [14]) on the likelihood function of the acquired data, it holds for any unbiased estimator $\hat{\boldsymbol{\theta}}$ of the parameter vector $\boldsymbol{\theta}$ that $\left(C_{\hat{\boldsymbol{\theta}}} - I^{-1}(\boldsymbol{\theta})\right)$ is positive semi-definite. Here, $C_{\hat{\boldsymbol{\theta}}}$ denotes the estimator covariance, $I(\boldsymbol{\theta})$ is the Fisher information, and $I^{-1}(\boldsymbol{\theta})$ is the CRLB. In particular, the CRLB thus bounds the estimator variance from below. It is shown in [15] that in SMLM, the covariance of the maximum likelihood estimator (MLE) converges to the CRLB for increasing signal photon counts. As MLEs attain the CRLB asymptotically, the CRLB can be used to quantify the best possible localization precision that can be obtained through (me)SMLM.

imeSMLM methods iteratively update prior information on emitter positions. This prior information locally improves the localization precision during subsequent iterations. Additional prior information can be gained from photoactivation, as is done in iterative MINFLUX [12] or MINSTED [16], as only a pool of molecules is activated. To quantify the best possible improvement of the localization precision in imeSMLM, a suitable error bound should be able to incorporate prior information. The CRLB requires estimators to be unbiased, which means that it is not able to incorporate a prior distribution on the estimands into the localization precision.

In this chapter, we use the Van Trees inequality (VTI) as a Bayesian alternative to the CRLB because prior information on the estimands, such as the emitter position, is available. We use the VTI to develop a fundamental limit on the localization precision of imeSMLM methods, for example, where standing-wave illumination patterns are used for the localization. Furthermore, we simulate the effects of illumination pattern posi-

tioning on the localization precision. We show that in the absence of background and under perfect modulation, the information content of signal photons increases exponentially as a function of the iteration count. Under non-ideal conditions such as non-zero background or imperfect modulation, this favourable scaling is lost, which shows that optimal design of an imeSMLM method is a complex problem, requiring knowledge of the practical imaging conditions. The VTI is the performance metric of choice to design optimal control strategies in silico.

4.2. Methods

In this section, we describe the VTI as a lower bound on the precision of arbitrary estimators in case prior information is available. We describe how to apply the VTI on an imeSMLM method with sinusoidal intensity patterns. Furthermore, we describe the maximum a posteriori (MAP) estimator as a method to iteratively fuse prior information with measurements from the current iteration (see Fig. 4.S1).

4.2.1. Van Trees inequality

The VTI [17–19] is a Bayesian variant of the CRLB. By treating the estimand vector $\boldsymbol{\theta}$ as a random variable with a known prior distribution, it can incorporate prior information into the localization precision bound. Because of this, the VTI can bound the localization precision of biased and unbiased estimators from below, while the CRLB only bounds the localization precision of unbiased estimators.

The VTI can be used to bound the localization precision of any estimator $\hat{\boldsymbol{\theta}}$ of the parameter vector $\boldsymbol{\theta}$ from below. For this, the measurements $\boldsymbol{x} \in \mathbb{R}^n$ are modelled as independent realizations from a model distribution, which depends on the parameter vector $\boldsymbol{\theta}$ through the likelihood function $L(\boldsymbol{\theta}|\boldsymbol{x})$. Additionally, a prior distribution $\lambda_{k-1}(\boldsymbol{\theta})$ on the parameter vector is available in each iteration k of the localization procedure [17, 18]. Under regularity conditions on the likelihood function $L(\boldsymbol{\theta}|\boldsymbol{x})$ and the prior distribution $\lambda_{k-1}(\boldsymbol{\theta})$ (see Section 4.S2), the mean squared error matrix

$$\mathrm{MSE}\left(\hat{\boldsymbol{\theta}}_k\right) = \mathbb{E}_{\lambda_{k-1}}\left[\int_{\mathbb{R}^n} (\hat{\boldsymbol{\theta}}_k - \boldsymbol{\theta})(\hat{\boldsymbol{\theta}}_k - \boldsymbol{\theta})^T L(\boldsymbol{\theta}|\boldsymbol{x}) \mathrm{d}\boldsymbol{x}\right] \tag{4.1}$$

of any estimator $\hat{\boldsymbol{\theta}}_k$ of $\boldsymbol{\theta}$ during iteration k satisfies:

$$\mathrm{MSE}\left(\hat{\boldsymbol{\theta}}_k\right) - (J_{D,k} + J_{P,k})^{-1} \succeq 0. \tag{4.2}$$

Here, $J_k = J_{D,k} + J_{P,k}$ is called the Bayesian information matrix, which is the Bayesian equivalent of the Fisher information matrix. The data information matrix $J_{D,k}$ describes the Fisher information of the data, averaged over the prior. It is given by:

$$[J_{D,k}]_{i,j} = \mathbb{E}_{\lambda_{k-1}}\left[[I_k(\boldsymbol{\theta})]_{i,j}\right]. \tag{4.3}$$

Here, $I_k(\boldsymbol{\theta})$ denotes the Fisher information in iteration k (see Section 4.S1).

The prior information matrix $J_{P,k}$ describes the information contained in the distribution of the prior information. It is given by:

$$[J_{P,k}]_{i,j} = \mathbb{E}_{\lambda_{k-1}}\left[\frac{\partial \log(\lambda_{k-1}(\boldsymbol{\theta}))}{\partial \boldsymbol{\theta}_i} \frac{\partial \log(\lambda_{k-1}(\boldsymbol{\theta}))}{\partial \boldsymbol{\theta}_j}\right]. \tag{4.4}$$

In many practical scenarios, the data information matrix in Eq. (4.3) is difficult to compute analytically. Aside from certain special cases (see Subsection 4.3.1), one generally resorts to numerical methods to evaluate the VTI [20, 21].

4.2.2. Localization precision for iterative modulation enhanced single-molecule localization microscopy

In imeSMLM, prior information on the emitter position that was generated during previous iterations is used to maximize the information content of signal photons in the next iteration. The CRLB cannot incorporate prior information on estimand vector $\boldsymbol{\theta}$ and therefore the Bayesian VTI is needed.

To be able to formulate the VTI for the described imeSMLM method, a prior distribution on the parameter vector $\boldsymbol{\theta}$ needs to be chosen during each iteration. Here, $\boldsymbol{\theta}$ consists of the emitter position (θ_x, θ_y), the expected signal photon count θ_I and the expected background photon count per pattern θ_b.

We choose the asymptotic Gaussian distribution of the MLE as a prior. It is shown in [17, 22] that the MLE asymptotically follows a multivariate normal distribution, with mean $\boldsymbol{\theta}$ and with the covariance given by the CRLB $I^{-1}(\boldsymbol{\theta})$. Alternatively, one can say that for an increasing amount of signal photons, the MLE becomes unbiased and attains minimum covariance given by the CRLB. As a result of this choice, the VTI for imeSMLM is approximately equal to the CRLB, computed over all iterations (see Fig. 4.S2). This shows that the information increase in imeSMLM is derived from Gaussian prior information.

Using this prior, we iteratively compute the best localization precision as follows (see Fig. 4.S3). In the first iteration, the CRLB $I_1^{-1}(\boldsymbol{\theta})$ is evaluated. The corresponding MLE $\hat{\boldsymbol{\theta}}_1$ will approximately be Gaussian distributed, with mean $\boldsymbol{\theta}$ and covariance $I_1^{-1}(\boldsymbol{\theta})$.

We use this distribution as prior information on the next iteration. In iteration 1, we take the prior distribution $\lambda_1(\boldsymbol{\theta})$ to be the probability density function of a multivariate Gaussian distribution. To simulate the best possible localization precision, ignoring the effects of estimation errors made during earlier iterations, the true estimand vector $\boldsymbol{\theta}$ is used as the mean of the Gaussian prior. We then evaluate $J_{D,2}$ and $J_{P,2}$. The new prior $\lambda_2(\boldsymbol{\theta})$ is chosen to be Gaussian, with mean $\boldsymbol{\theta}$ and covariance $(J_{D,2} + J_{P,2})^{-1}$.

In each new iteration k, we take the prior distribution $\lambda_{k-1}(\boldsymbol{\theta})$ to be the probability density function of a multivariate Gaussian distribution, with mean $\boldsymbol{\theta}$ and covariance $(J_{D,k-1} + J_{P,k-1})^{-1}$. We then evaluate $J_{D,k}$ and $J_{P,k}$. The new prior $\lambda_k(\boldsymbol{\theta})$ is chosen to be Gaussian, with mean $\boldsymbol{\theta}$ and covariance $(J_{D,k} + J_{P,k})^{-1}$. This continues until M iterations are completed.

4.2.3. Choice of pattern positions

We consider standing-wave intensity patterns with controllable spatial phase shifts $\phi_{x,k}^{\pm}$, $\phi_{y,k}^{\pm}$ in two orthogonal orientations. In each iteration of the localization procedure, two x-oriented pattern phases, $\phi_{x,k}^{+}$, $\phi_{x,k}^{-}$, and two y-oriented pattern phases, $\phi_{y,k}^{+}$, $\phi_{y,k}^{-}$, are used to illuminate the sample. The superscripts $+$, $-$ describe the pattern placement with respect to the emitter position. Using prior information on the emitter position, the pattern positions can be selected to maximize the information content of signal photons.

In the initialization step, no prior information is available. Therefore, the pattern positions are chosen to be $\phi^{\pm}_{x,1} = \phi^{\pm}_{y,1} = 0$ by default. A parameter estimate $\hat{\boldsymbol{\theta}}_1$ is obtained, and the CRLB can now be computed, which results in a $\mathcal{N}(\boldsymbol{\theta}, I_1^{-1}(\boldsymbol{\theta}))$ prior distribution for the next iteration.

If the modulation contrast of the pattern is perfect, the intensity minima of the standing-wave patterns should ideally be placed on the true emitter position (θ_x, θ_y) during subsequent iterations k for the information content of signal photons to be maximal. A similar result was found for iterative MINFLUX, where a doughnut-shaped illumination pattern was used [8, 12]. This result can be explained intuitively using a thought experiment, as was done in [4]. If we assume that the modulation contrast $m = 1$, the intensity minimum has true zero intensity. Suppose that the pattern positions are chosen such that each intensity minimum is placed exactly on the emitter position. As the emitter is illuminated with zero-intensity light, it will not emit any photons. We therefore need to wait infinitely long to receive any non-zero amount of signal photons.

For this to happen, two scenarios are possible. Either the emitter is located perfectly in the intensity minimum or nothing is located in the intensity minimum. The prior information expresses confidence that there is indeed an emitter located in this position, resulting in a decrease of the mean squared error. The prior information thus adds information to signal photons in case an emitter is illuminated with (near-)zero intensity light.

In practice, the true emitter positions have to be estimated, so this pattern placement cannot be implemented. An implementable pattern placement strategy could replace the true emitter positions with their currently known estimates $\hat{\theta}_{x,k-1}$ and $\hat{\theta}_{y,k-1}$. However, this can cause the localization precision to become sensitive to estimation errors. If the current position estimate is imprecise, intensity minima will be placed away from the true emitter position, and the newly obtained prior distribution will add little information.

To decrease the sensitivity to estimation errors of the iterative localization method, the intensity minima of two patterns, ϕ^{+}_{k} and ϕ^{-}_{k}, can be placed symmetrically around the current estimate of the emitter position, as shown in Fig. 4.1 (also see Fig. 4.S4). In each iteration, the distance between the intensity minima is decreased, thereby locally improving the localization precision around the current estimate of the emitter position.

In this chapter, we consider a pattern position control strategy where illumination minima are placed symmetrically around the current estimate of the emitter position, in which the distance between the emitter position and an intensity minimum scales with the localization precision of the previous iteration. This control strategy is given by

$$\begin{cases} \phi^{\pm}_{x,k} = & \omega\left(\hat{\theta}_{x,k-1} \pm \alpha\sigma_{x,k-1}\right) - \pi, \\ \phi^{\pm}_{y,k} = & \omega\left(\hat{\theta}_{y,k-1} \pm \alpha\sigma_{y,k-1}\right) - \pi. \end{cases} \tag{4.5}$$

Here, ω denotes the spatial pattern frequency. As the illumination pattern is at best diffraction limited, it must hold that $\omega \leq 2\pi \cdot \frac{2\mathrm{NA}}{\lambda_{\mathrm{ex}}}$, where λ_{ex} is the excitation wavelength and NA is the numerical aperture. The localization precisions $\sigma_{x,k-1}$ and $\sigma_{y,k-1}$ are the square roots of the first and second diagonal elements of J^{-1}_{k-1}, respectively. The aggressiveness parameter α determines how close the pattern minima are placed to the estimated emitter position.

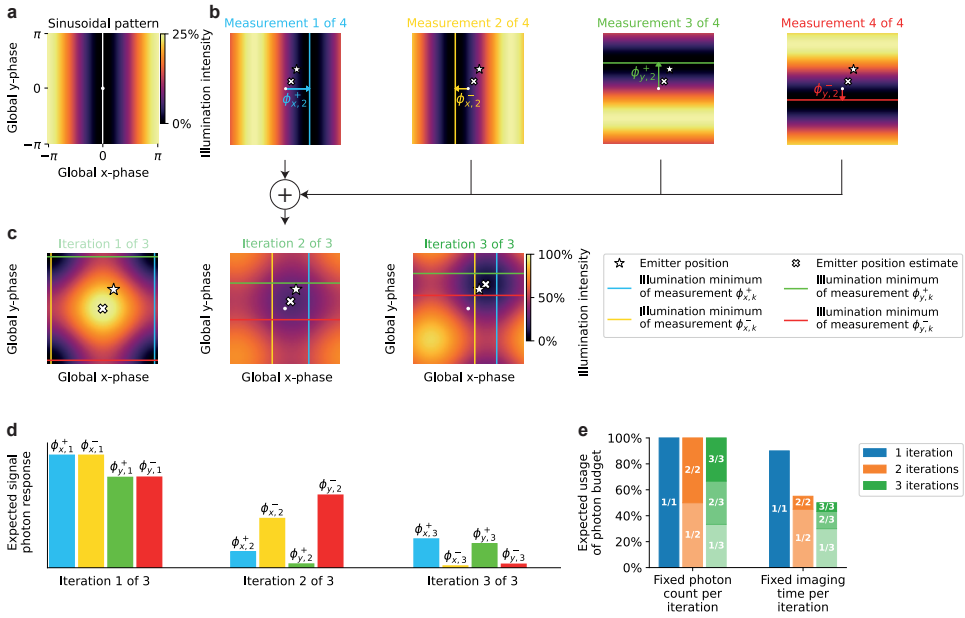

Figure 4.1: Pattern position control strategy (see Eq. (4.5)) to iteratively increase information content of signal photons. (*a*) Example of one period of a sinusoidal intensity pattern in the x-direction, with the intensity minimum centred at a global phase zero. (*b*) Individual illumination patterns placed during iteration 2. In each iteration, four sinusoidal illumination patterns are placed, such that current estimate of the emitter position is enclosed between the illumination minima of the patterns. (*c*) Summed illumination patterns over the course of three iterations. The distance between the intensity minimum of the summed patterns and the emitter position reduces iteratively as a result of adjusting the search region based on prior information about the achieved precision in the previous iteration. (*d*) Expected signal photon response from the emitter in (*b*) and (*c*) over the course of three iterations, using the illumination placement from (*c*). (*e*) Illustration of the expected signal photon budget for one, two, and three iterations. Two scenarios are considered in this chapter, namely the case where the signal photon count is kept constant over the course of all iterations and the case where the imaging time and illumination intensity are kept constant over the course of all iterations. In the latter case, the signal photon budget is only exhausted by imeSMLM in case the single emitter is illuminated with maximum intensity during all iterations. If the intensity pattern minima are placed close to the emitter, a reduced number of photons is recorded within the same time window.

4.2.4. Maximum a posteriori estimation

Estimators used for iterative localization microscopy should be able to recursively fuse measurements with prior knowledge on estimands that was obtained during earlier iterations. In each iteration k, we compute the MAP estimator $\hat{\boldsymbol{\theta}}_k$, which is given by the maximizing argument of the posterior distribution $p(\boldsymbol{\theta}|\boldsymbol{x}_1,\dots,\boldsymbol{x}_k)$. As the measurements $\boldsymbol{x}_1,\dots,\boldsymbol{x}_k$ are independent, the posterior satisfies the following recursion:

$$\begin{aligned} p(\boldsymbol{\theta}|\boldsymbol{x}_1,\dots,\boldsymbol{x}_k) &\overset{\boldsymbol{\theta}}{\propto} p(\boldsymbol{x}_k|\boldsymbol{\theta})\,p(\boldsymbol{\theta}|\boldsymbol{x}_1,\dots,\boldsymbol{x}_{k-1}) \\ &\overset{\boldsymbol{\theta}}{\propto} p(\boldsymbol{x}_k|\boldsymbol{\theta})\,p(\boldsymbol{x}_1,\dots,\boldsymbol{x}_{k-1}|\boldsymbol{\theta})\,p(\boldsymbol{\theta}). \end{aligned} \tag{4.6}$$

Here, $p(\boldsymbol{\theta}|\boldsymbol{x}_1,\dots,\boldsymbol{x}_k)$ denotes the posterior from the previous iteration, $p(\boldsymbol{x}_k|\boldsymbol{\theta})$ represents the likelihood of the measurements from the current iteration, and $p(\boldsymbol{x}_1,\dots,\boldsymbol{x}_{k-1}|\boldsymbol{\theta})$

represents the likelihood of the accumulated measurements from previous iterations. If prior information is available, such as in photoactivation [12, 16], it can be included in $p(\boldsymbol{\theta})$. To keep the analysis as general as possible, we choose $p(\boldsymbol{\theta})$ to be a uniform (improper) prior over $\mathbb{R}^4$ to represent the lack of prior information on $\boldsymbol{\theta}$ before measurements are done. For this choice, the estimation error of the MAP estimator is guaranteed to converge to the VTI if the likelihood reflects the underlying distribution of the data. The MAP estimate can then be computed as follows:

$$\hat{\boldsymbol{\theta}}_k = \arg\max_{\boldsymbol{\theta}} \left[\log(p(\boldsymbol{x}_1, \ldots, \boldsymbol{x}_{k-1}|\boldsymbol{\theta})) + \log(p(\boldsymbol{x}_k|\boldsymbol{\theta})) \right]. \tag{4.7}$$

4.2.5. Simulations and parameter values

The VTI and MAP estimates for the described imeSMLM method were obtained using representative in silico experiments. The VTI was evaluated using simple Monte Carlo integration (see Section 4.S3), where 50,000 Monte Carlo samples were used for convergence. 50,000 realizations of regions of interest were simulated by realizing the image formation model (see Section 4.S1), where the emitter was located in the centre of the camera pixel array and where its subpixel position was uniformly randomized. MAP estimates were obtained from Eq. (4.7) using Levenberg-Marquardt optimization [23, 24]. The model parameters (see Table 4.S1) are considered to be representative of an imeSMLM experiment where standing-wave intensity patterns are used to illuminate the sample. We choose the pattern frequency ω and the standard deviation of the Gaussian point spread function (PSF) to be diffraction limited. This maximizes the information contained in the illumination pattern. For the chosen parameters, the pattern pitch is approximately equal to twice the standard deviation of the Gaussian PSF. This is consistent with earlier work on modulation enhanced localization microscopy with sinusoidal illumination [5].

4.3. Results and Discussion

In this section, we present the theoretical and numerical results of this study. We describe a closed-form expression of the VTI, assuming one-dimensional localization, no image discretization by the camera, and zero background. Simulations explore the effects of the number of iterations and the choice of pattern positioning on the localization precision. In Figs. 4.2 and 4.3, the effects of the iteration count and pattern positioning on the localization precision are simulated, respectively assuming a fixed photon count per iteration and a fixed imaging time and illumination power per iteration.

4.3.1. Analytical approximation of Bayesian lower bound on the localization precision

Under some assumptions on the image formation model, analytical expressions for the localization precision can be derived using the VTI. We derive an analytical approximation of the Bayesian VTI on the localization precision of an imeSMLM method where sinusoidal intensity patterns are used, given a Gaussian PSF and a sequence of pattern positions.

We limit ourselves to one-dimensional localization where we disregard the effect of

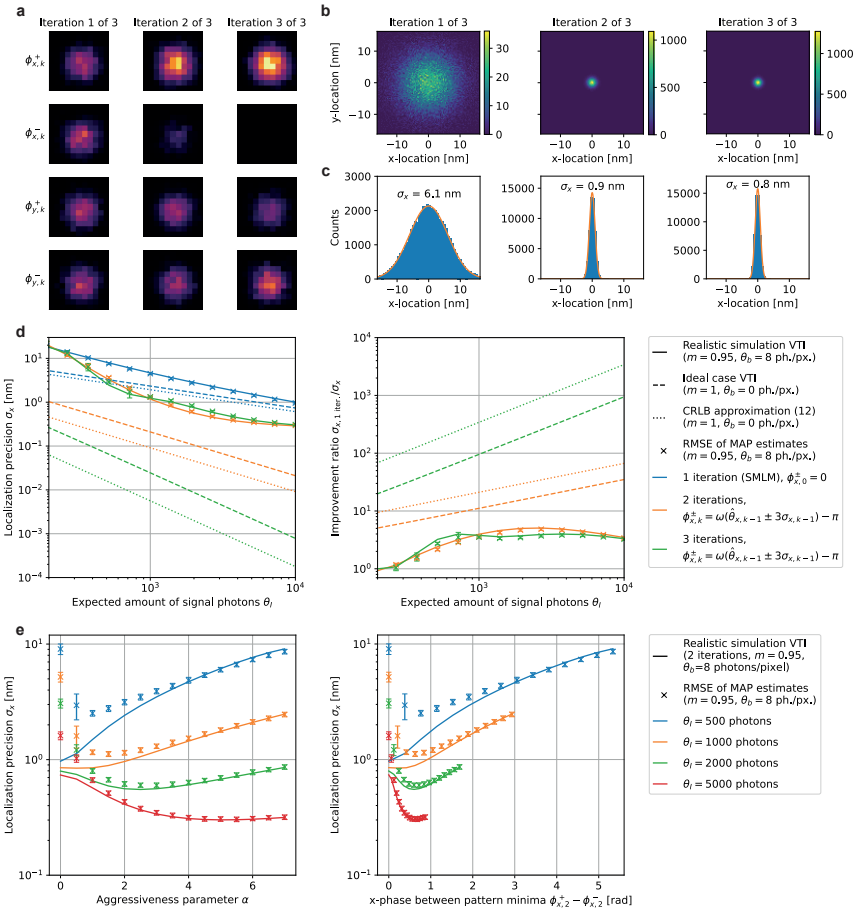

Figure 4.2: Simulated iterative localization and precision bound using a fixed expected signal photon budget per iteration. In (*a*)-(*d*), the pattern positioning of Eq. (4.5) was used with aggressiveness parameter $\alpha = 3$. In (*d*) and (*e*), the results are compared with the theoretical limit of Eq. (4.9) and the precision approximation of Eq. (4.10), which assume perfect modulation and zero background. Error bars denote the standard deviation of the root-mean-square error, obtained by comparing 200 batches of 250 MAP estimates. (*a*) Example of simulated regions of interest during three iterations of an iterative localization experiment. Contrast was enhanced for visualization purposes. The divergence in emitter intensity from iteration 1 to iteration 3 is the result of shrinking the distance between pattern minima while enforcing a fixed expected signal photon budget per iteration in simulation. As a result, the pattern minima that are placed furthest from the emitter position (due to position estimation errors in the previous iteration) will use a larger share of the signal photon budget. (*b*) Two-dimensional histogram of MAP localizations on 50,000 simulated regions of interest during three iterations of an iterative localization experiment at an expected signal photon count of $\theta_I = 2000$ photons. (*c*) Histogram of MAP localizations projected on the x-direction. A Gaussian with standard deviation σ_x is fitted on the histogram. (*d*) Simulated localization precision in x-direction as a function of the expected signal photon count when one, two, or three iterations are used. (*e*) Simulated localization precision in x-direction as a function of the aggressiveness parameter α, and the distance between the pattern minima using the same values of the aggressiveness parameter α, for different expected signal photon counts and assuming a constant signal photon count per iteration.

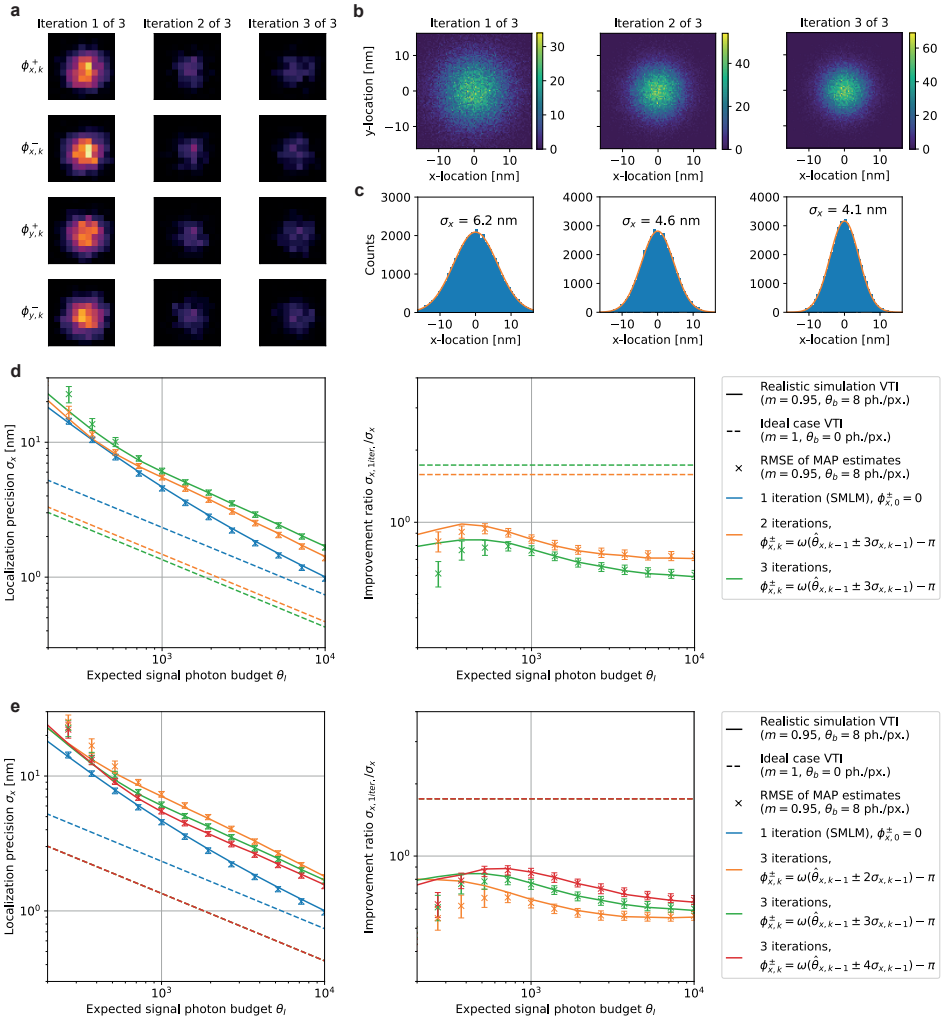

Figure 4.3: Simulated iterative localization and precision bound using a fixed imaging time and illumination power per iteration. In (*a*)-(*d*), the pattern positioning of Eq. (4.5) was used with aggressiveness parameter $\alpha = 3$. In (*d*) and (*e*), results are compared with the theoretical limit of Eq. (4.9), which assumes perfect modulation and zero background. Error bars denote the standard deviation of the root-mean-square error, obtained by comparing 200 batches of 250 MAP estimates. (*a*) Example of simulated regions of interest during three iterations of an iterative localization experiment. Contrast was enhanced for visualization purposes. (*b*) Two-dimensional histogram of MAP localizations on 50,000 simulated regions of interest during three iterations of an iterative localization experiment at an expected signal photon budget of $\theta_I = 2000$ photons. (*c*) Histogram of MAP localizations projected on the x-direction. A Gaussian with standard deviation σ_x is fitted on the histogram. (*d*) Simulated localization precision in x-direction as a function of the expected signal photon budget θ_I, when one, two, or three iterations are used. (*e*) Simulated localization precision in x-direction as a function of the expected signal photon budget for different pattern positioning strategies.

discretization of the image due to the finite size of camera pixels. In addition, we do not estimate the expected signal photon count θ_I and we ignore background such that $\theta_b = 0$. Under these assumptions, the derived analytical approximation serves as a fundamental limit on the localization precision. That is, the localization precision of the described imeSMLM method for two-dimensional localization, under the effects of image discretization, estimation uncertainty on θ_I and θ_b, and non-zero background, can only be worse than the analytical approximation.

The approximation of the best possible localization precision is given by (see Section 4.S4):

$$\sigma_{x,k} \geq (J_k)^{-\frac{1}{2}} \geq \frac{\sigma_{x,k-1}}{\sqrt{1+\sigma_{x,k-1}^2 (F_{\text{PSF}} + F_{\text{illum}})}}, \tag{4.8a}$$

$$F_{\text{PSF}} = \frac{\theta_I c_k}{\sigma_{\text{PSF}}^2} \left(2 + \left(m \cos\left(\omega \hat{\theta}_{x,k-1} - \phi_{x,k}^+\right) + m \cos\left(\omega \hat{\theta}_{x,k-1} - \phi_{x,k}^-\right)\right) \exp\left(-\frac{\omega^2 \sigma_{x,k-1}^2}{2}\right)\right), \tag{4.8b}$$

$$F_{\text{illum}} = \theta_I c_k \omega^2 \left(2 - \left(m \cos\left(\omega \hat{\theta}_{x,k-1} - \phi_{x,k}^+\right) + m \cos\left(\omega \hat{\theta}_{x,k-1} - \phi_{x,k}^-\right)\right) \exp\left(-\frac{\omega^2 \sigma_{x,k-1}^2}{2}\right)\right). \tag{4.8c}$$

Here, c_k models the expected photon count per iteration under imperfect illumination (see Section 4.S1). Furthermore, σ_{PSF} denotes the standard deviation of a Gaussian PSF, and m denotes the modulation contrast of the illumination pattern. In the denominator, the term "1" accounts for the prior information. The terms F_{PSF} and F_{illum} describe the information derived from the spot centre estimation and the information derived from the illumination pattern modulation, respectively. Note that Eq. (4.8) is an exact representation of the VTI for $m = 1$ and $\phi_{x,k}^+ = \phi_{x,k}^-$ and a lower bound on the VTI for $m < 1$ or $\phi_{x,k}^+ \neq \phi_{x,k}^-$.

If the pattern positions of Eq. (4.5) are substituted into Eq. (4.8), we obtain:

$$\sigma_{x,k} \geq (J_k)^{-\frac{1}{2}} \geq \frac{\sigma_{x,k-1}}{\sqrt{1+\sigma_{x,k-1}^2 (F_{\text{PSF}} + F_{\text{illum}})}}, \tag{4.9a}$$

$$F_{\text{PSF}} = \frac{\theta_I c_k}{\sigma_{\text{PSF}}^2} \left(2 - 2m \cos\left(\omega \alpha \sigma_{x,k-1}\right) \exp\left(-\frac{\omega^2 \sigma_{x,k-1}^2}{2}\right)\right), \tag{4.9b}$$

$$F_{\text{illum}} = \theta_I c_k \omega^2 \left(2 + 2m \cos\left(\omega \alpha \sigma_{x,k-1}\right) \exp\left(-\frac{\omega^2 \sigma_{x,k-1}^2}{2}\right)\right). \tag{4.9c}$$

Assuming that the modulation contrast is perfect and that zero background photons are recorded, Eq. (4.9) can be used to derive the optimal distribution of the signal photon budget (see Section 4.S5). This proves that it is optimal to isotopically distribute the signal photon budget over the number of iterations from iteration 2 onwards.

From Eq. (4.9) with $m = 1$, it can be seen that the contribution of the expected signal photon count θ_I to the localization precision grows exponentially as $\sigma_{x,k-1}$ decreases.

This implies that the information content per signal photon grows as the number of iterations increases. Assuming that the modulation contrast is perfect and that zero background photons are recorded, it is thus favourable to increase the number of iterations as much as possible within the limited photon budget.

However, increasing the number of iterations results in a lower amount of signal photons per iteration, lowering the signal-to-background ratio in each iteration. The exponential scaling is therefore destroyed by background. Furthermore, we assume here that the mechanical resolution of the illumination positioning system is not limiting, such that every illumination-pattern position between $-\pi$ and π can be reached. In practice, this becomes increasingly difficult for small $\sigma_{x,k-1}$, preventing the exponential limit to be reached for high amounts of iterations. Because of these factors, it makes sense to limit the number of iterations in practical applications.

4.3.2. Effect of iterations on localization precision

From the theoretical limit of Eq. (4.8) it was found that illumination pattern control can exponentially increase the information content of signal photons under perfect modulation and zero background, making an increase in the iteration count preferable over an increase in the number of photons per iteration. The effect of the iteration count and pattern positioning on the localization precision for imperfect modulation and zero background will be simulated in this subsection.

In Fig. 4.2, the effect of the iteration count on the localization precision is simulated assuming a fixed expected signal photon count per iteration. The aggressiveness parameter α was set to 3 for these simulations. For each simulation, the VTI was evaluated, and MAP estimates were computed for 50,000 randomly generated regions of interest (see Section 4.S1). These results are compared with the theoretical limit of Eq. (4.8), where we assume perfect modulation to reflect the best achievable localization precision. We also compute the CRLB reported in [12], where the illumination minimum is approximated by a quadratic profile. Assuming that N signal photons are collected during each iteration, this approximation of the CRLB is given by

$$\sigma_{x,k} \gtrsim \frac{\left|\phi^{+}_{x,k} - \phi^{-}_{x,k}\right|}{4\omega N^{1/2}} = \frac{2\alpha\sigma_{x,k-1}}{4N^{1/2}}. \tag{4.10}$$

In Fig. 4.2*a*, examples of simulated regions of interest are shown assuming a fixed expected signal photon count per iteration. From iterations 1 to 3, the emitter intensity appears to diverge. This effect is caused by enforcing a fixed expected signal photon budget per iteration in simulation. Due to this assumption, the emitter intensities represent the share of the expected signal photon budget used during each measurement. As the distance between pattern minima shrinks over the course of iterations, the signal photon budget is distributed increasingly unevenly over the measurements.

In iteration 1, pattern minima are placed far from the true emitter position, so the emitter is illuminated with high intensity from all patterns. As such, the illumination patterns will use an approximately equal share of the signal photon budget.

In subsequent iterations, pattern minima are placed increasingly close to the estimated emitter position. Because we make an estimation error, pattern minima are

placed asymmetrically around the true emitter position. As a result, the pattern minima that are placed furthest from the emitter position will use a larger share of the signal photon budget. As the expected signal photon budget is constant over the iterations, the emitter intensities appear to diverge.

From Fig. 4.2*d*, it can be seen that iterative localization using the pattern placement of Eq. (4.5) results in improved localization precision over SMLM. For eight background photons per pixel and 95% modulation, we found that around a fivefold improvement over SMLM can be reached by doing two iterations at a signal photon count of 644 signal photons per iteration. When doing three iterations, the maximum improvement over SMLM is around four, reached at 240 signal photons per iteration.

These findings are in contrast with the results under perfect modulation and zero background, as described by the analytical approximation. As expected from the earlier analysis, we find that the localization precision is proportional to θ_I^{-1} when doing two iterations and $\theta_I^{-3/2}$ when doing three iterations. This difference is explained by the fact that the precision loss due to background, imperfect modulation, and discretization accumulates as the number of iterations increases, as the lowered precision $\sigma_{x,k-1}$ in a previous iteration is carried over to the next iteration. In practice, the favourable exponential increase in information over the course of the iterative procedure is thus lost.

When recording 315 or more photons per iteration, using two iterations rather than three results in a better localization precision. To investigate the cause, Fig. 4.S5 shows the localization precision as a function of the cumulative signal photon count at a total signal photon count of 2000 photons. For eight background photons per pixel and 95% modulation, we see that using three iterations is still preferred when the second out of three iterations ends at 1333 signal photons. At this moment, using three iterations results in a 4.5-fold precision increase over using SMLM. During the third out of three iterations, the localization precision improves only marginally, resulting in a decrease of the precision improvement to 3.7 with respect to SMLM. This is not expected from the analytical approximation under perfect modulation and zero background, where the localization precision improvement over SMLM increases from 13 to 190 during the third iteration.

Simulations show similar results for different settings of the modulation contrast and the background count. Specifically, we find a stagnation of the localization precision during the third iteration for 80% and 90% modulation contrast (see Fig. 4.S6) and background counts of 1, 4, and 12 photons per pixel (see Fig. 4.S7), in contrast to the results for perfect modulation and zero background.

We can conclude that imperfect modulation and non-zero background limit the best possible localization precision when the illumination pattern minima are placed closer to the emitter position. When distributing photons equally over the iterations, increasing the number of iterations indefinitely does not necessarily lead to increasingly informative signal photons.

Additionally, we see an ill-convergence of the MAP estimator at perfect modulation when patterns are placed close to the true emitter position (see Figs. 4.S6 and 4.S10). This is caused by a (near-)zero signal photon response under perfect modulation. For pattern minima that are close to the true emitter position, the signal photon response is low or zero for perfect modulation. This causes low signal-to-background ratios, which

means that the shape of the PSF is poorly represented in the data. Analogous to existing results on the MLE [15], the MAP estimator fails to consistently estimate the emitter position with minimum uncertainty. For 95% modulation, we do not see ill-convergence for expected background counts of one or more photons per pixel, although the maximum localization precision is not reached for $\alpha < 2$ due to the low signal-to-background ratio (see Fig. 4.S11).

In the simulations of Fig. 4.2*d*, the aggressiveness parameter α was kept constant at three. For zero background and perfect modulation, it is expected that reducing the aggressiveness improves the localization precision independently from the expected signal photon budget (see Fig. 4.S8). For eight background photons per pixel and 95% modulation, we see that $\alpha = 2$ improves the localization precision fourfold over SMLM when recording 518 signal photons.

The optimal choice of the aggressiveness parameter depends on the expected background photon count, the modulation contrast, and the expected signal photon count. Fig. 4.2*e* shows that the optimal α decreases for a decreasing signal photon count. For 95% modulation and eight background photons per pixel, $\alpha = 2.5$ is optimal at a signal photon budget of 2000 photons, while $\alpha = 5.5$ is optimal at a signal photon budget of 5000 photons. We also see that the optimal α decreases for increasing background (see Fig. 4.S11). That is, as the signal-to-background ratio increases, the optimal α increases as well.

For perfect modulation, we have already argued that the localization precision can be optimized by placing pattern minima directly on the emitter. However, this optimum shifts when the modulation contrast is imperfect (see Fig. 4.S10). Specifically, this shows that the localization precision does not improve from infinitely reducing the distance between pattern minima in case the pattern modulation is imperfect. This indicates that the prediction from [8] does not hold for imperfect modulation.

Therefore, a practical way of choosing α is needed to optimize imeSMLM. If prior knowledge about the signal photon count, the background, and the modulation contrast is available, the theoretically optimal α should be found by optimizing the VTI. It remains an open question how to do this systematically. A practical solution could be to choose α from a lookup table, constructed in silico from optimizing the VTI under a range of practical experimental conditions.

In Fig. 4.3, the effect of the iteration count and pattern positioning on the localization precision is simulated, assuming a fixed imaging time and illumination power per iteration. As a consequence of using patterned illumination, the use of the available signal photon budget varies between iterations (see Fig. 4.1*e*). Identically to the previous simulations, the aggressiveness parameter α was set to three and the MAP estimates were computed for 50,000 regions of interest.

From Fig. 4.3, *d* and *e*, we see that SMLM outperforms imeSMLM over a range of signal photon budgets and for different pattern positioning strategies. For eight background photons per pixel and 95% modulation, SMLM outperforms imeSMLM with three iterations by a factor 1.2 at a signal photon budget of 518 signal photons.

To investigate the cause of this performance loss, we simulate the localization precision per recorded photon under the illumination strategy of Eq. (4.5) (see Fig. 4.S9, *a* and *c*). It can be seen that imeSMLM still enables an increase in the information content

per recorded signal photon. For eight background photons per pixel and 95% modulation, the localization precision is improved 1.4-fold over SMLM when the first 411 signal photons are recorded using two iterations. When doing three iterations, the maximum improvement over SMLM is 1.5, reached after 422 signal photons.

However, SMLM uses more of the available signal photon budget within the same time span, ultimately resulting in a better localization precision over imeSMLM (see Fig. 4.S9, *b* and *d*). For SMLM, all 2000 signal photons within the budget are collected. For imeSMLM, all signal photons available in first iteration are collected, as the illumination intensity equals that of SMLM. In subsequent iterations, pattern minima are placed closer to the emitter position, resulting in a reduced signal photon response. When doing three iterations in total, 60 signal photons are collected on average during the second iteration, and 40 signal photons are collected on average during the third iteration. While these photons are more informative than those obtained with SMLM, the total amount of information is not enough to outperform SMLM.

These effects are further exemplified by the analytical approximation, as pattern minima are placed even closer to the emitter position when the effects of background and imperfect modulation are removed. For three iterations with a photon budget of 2000 photons, eight signal photons are collected on average during the second iteration, and one signal photon is collected on average during the third iteration. As the amount of signal photons with increased information is so limited, the localization precision approximately scales with $\theta_I^{-1/2}$ for imeSMLM, with a constant improvement factor of 1.6 over SMLM when doing two iterations and 1.7 when doing three iterations.

In the simulations of Fig. 4.3*d*, the aggressiveness parameter α was kept constant at three. Fig. 4.3*e* shows that for zero background and perfect modulation, it is expected that the aggressiveness does not significantly influence the maximum localization precision, as on average less than 15 signal photons are collected during the second and third iterations for $\alpha = 2$, 3, or 4. As such, the precision improvement from aggressive localization is balanced by a reduction of the signal photon count. For eight background photons per pixel and 95% modulation, we see that aggressive localization with $\alpha = 2$ results in a 1.3- to 1.8-fold reduction in localization precision for signal photon budgets θ_I between 200 and 10,000 photons.

4.4. Conclusion

In imeSMLM, resolution is improved locally around an emitter position by using prior information that was derived from measurements in earlier iterations. The CRLB cannot incorporate prior information, as it requires estimators to be unbiased. By treating estimands as random variables with a known prior distribution, the Bayesian VTI can be used to bound the maximally achievable localization precision from below. The VTI is useful for bounding the localization precision in imeSMLM as it is able to account for the effect of prior information that is generated over the course of iterations.

We derived an analytical approximation of the Bayesian lower bound on the localization precision of imeSMLM methods that make use of standing-wave illumination patterns in the absence of image discretization by the camera, estimation uncertainty on the signal photon count, and background fluorescence. This fundamental limit cannot be surpassed, as relaxing the aforementioned assumptions can only worsen the localization

precision of imeSMLM methods. Using this limit, we have shown that the information content of signal photons increases exponentially as a function of the iteration count when the modulation contrast is 100%. Additionally, we prove that for perfect modulation, it is optimal to isotopically distribute the single-molecule's photon budget over the number of iterations from iteration 2 onwards.

We demonstrate a practical imeSMLM pattern control strategy using the VTI. The VTI was simulated to assess the performance of imeSMLM under eight photons per pixel background and 95% modulation contrast. By using two iterations in total, imeSMLM reaches at most a fivefold improvement over SMLM. This indicates that the exponential localization improvement as a function of the iteration count cannot be achieved in most experiments, as it breaks down for slight imperfections in the modulation contrast.

Moreover, SMLM is able to outperform imeSMLM in case the imaging time and illumination laser power are kept constant between iterations. imeSMLM results in signal photons with increased information content. However, placing pattern minima close to the emitter position reduces the signal photon response, while SMLM is able to collect more signal photons within the same time frame. At a signal photon budget of 2000 photons, we find that SMLM is around 1.2 times better than three iterations of imeSMLM at eight expected background photons per pixel and 95% modulation contrast. We conclude that imeSMLM is able to increase the information content per signal photon but that this information increase does not necessarily outweigh the reduced signal photon response.

From this, we find that the optimal selection of pattern placement, the number of iterations, and the time spent per iteration in imeSMLM depends on many factors, such as the photon budget, imperfections in the illumination system, and the expected background count. Specifically, we show that the smallest step size is most likely not the best one and that the optimal step size depends on the molecule intensity, modulation contrast, and background fluorescence. Furthermore, we demonstrate that the localization precision only scales with the step size over a small set of experimental conditions.

The VTI can be used to quantify the best possible performance of illumination pattern control strategies and is therefore a promising performance metric in optimal control of imeSMLM methods. In this chapter, we chose to analyse imeSMLM with four sinusoidal illumination patterns. This is the most straightforward approach using sinusoidal illumination. It remains an open question if other arrangements of sinusoidal illumination patterns could lead to further imeSMLM improvements. Other illumination pattern shapes, such as the doughnut-shaped pattern from MINFLUX [8, 12], could also lead to improvements in imeSMLM. When designing imeSMLM experiments, the VTI is the preferred tool to tailor the pattern placement strategy to different imaging conditions.

Data and Code Availability

The data that support the findings of this study are openly available in 4TU.ResearchData [25]. The code that supports the findings of this study is openly available on GitHub [26].

Supporting Citations

The following references appear in the supporting information: [27, 28].

References

[1] E. Betzig, G. H. Patterson, R. Sougrat, O. W. Lindwasser, S. Olenych, J. S. Bonifacino, M. W. Davidson, J. Lippincott-Schwartz, and H. F. Hess. “Imaging Intracellular Fluorescent Proteins at Nanometer Resolution”. In: *Science* 313.5793 (2006), pp. 1642–1645.

[2] M. J. Rust, M. Bates, and X. Zhuang. “Sub-diffraction-limit imaging by stochastic optical reconstruction microscopy (STORM)”. In: *Nature Methods* 3.10 (2006), pp. 793–796.

[3] B. Huang, M. Bates, and X. Zhuang. “Super-Resolution Fluorescence Microscopy”. In: *Annual Review of Biochemistry* 78.1 (2009), pp. 993–1016.

[4] L. Reymond, T. Huser, V. Ruprecht, and S. Wieser. “Modulation-enhanced localization microscopy”. In: *Journal of Physics: Photonics* 2.4 (2020), p. 041001.

[5] J. Cnossen, T. Hinsdale, R. Ø. Thorsen, M. Siemons, F. Schueder, R. Jungmann, C. S. Smith, B. Rieger, and S. Stallinga. “Localization microscopy at doubled precision with patterned illumination”. In: *Nature Methods* 17.1 (2019), pp. 59–63.

[6] L. Reymond, J. Ziegler, C. Knapp, F.-C. Wang, T. Huser, V. Ruprecht, and S. Wieser. “SIMPLE: Structured illumination based point localization estimator with enhanced precision”. In: *Optics Express* 27.17 (2019), p. 24578.

[7] L. Gu, Y. Li, S. Zhang, Y. Xue, W. Li, D. Li, T. Xu, and W. Ji. “Molecular resolution imaging by repetitive optical selective exposure”. In: *Nature Methods* 16.11 (2019), pp. 1114–1118.

[8] F. Balzarotti, Y. Eilers, K. C. Gwosch, A. H. Gynnå, V. Westphal, F. D. Stefani, J. Elf, and S. W. Hell. “Nanometer resolution imaging and tracking of fluorescent molecules with minimal photon fluxes”. In: *Science* 355.6325 (2017), pp. 606–612.

[9] P. Jouchet, C. Cabriel, N. Bourg, M. Bardou, C. Poüs, E. Fort, and S. Lévêque-Fort. “Nanometric axial localization of single fluorescent molecules with modulated excitation”. In: *Nature Photonics* 15.4 (2021), pp. 297–304.

[10] P. Jouchet, C. Cabriel, N. Bourg, M. Bardou, C. Poüs, E. Fort, and S. Lévêque-Fort. “In Depth 3D Single Molecule Localization Microscopy with Time Modulated Excitation”. In: *Biophysical Journal* 118.3 (2020), 149a.

[11] L. Gu, Y. Li, S. Zhang, M. Zhou, Y. Xue, W. Li, T. Xu, and W. Ji. “Molecular-scale axial localization by repetitive optical selective exposure”. In: *Nature Methods* 18.4 (2021), pp. 369–373.

[12] K. C. Gwosch, J. K. Pape, F. Balzarotti, P. Hoess, J. Ellenberg, J. Ries, and S. W. Hell. “MINFLUX nanoscopy delivers 3D multicolor nanometer resolution in cells”. In: *Nature Methods* 17.2 (2020), pp. 217–224.

[13] R. J. Ober, S. Ram, and E. S. Ward. “Localization Accuracy in Single-Molecule Microscopy”. In: *Biophysical Journal* 86.2 (2004), pp. 1185–1200.

[14] S. M. Kay. *Fundamentals of Statistical Signal Processing: Estimation Theory*. Prentice Hall international editions. London, England: Prentice Hall, 1993.

[15] C. S. Smith, N. Joseph, B. Rieger, and K. A. Lidke. “Fast, single-molecule localization that achieves theoretically minimum uncertainty”. In: *Nature Methods* 7.5 (2010), pp. 373–375.

[16] M. Weber, M. Leutenegger, S. Stoldt, S. Jakobs, T. S. Mihaila, A. N. Butkevich, and S. W. Hell. “MINSTED fluorescence localization and nanoscopy”. In: *Nature Photonics* 15.5 (2021), pp. 361–366.

[17] H. L. Van Trees. *Detection, Estimation and Modulation Theory: Part 1*. Detection, Estimation, and Modulation Theory. Set (Volumes: I,II, III,IV). Nashville, TN: John Wiley & Sons, 2001.

[18] R. D. Gill and B. Y. Levit. "Applications of the van Trees Inequality: A Bayesian Cramér-Rao Bound". In: *Bernoulli* 1.1/2 (1995), p. 59.

[19] L. A. Masullo, L. F. Lopez, and F. D. Stefani. "A common framework for single-molecule localization using sequential structured illumination". In: *Biophysical Reports* 2.1 (2022), p. 100036.

[20] C. Fritsche, E. Özkan, L. Svensson, and F. Gustafsson. "A fresh look at Bayesian Cramér-Rao bounds for discrete-time nonlinear filtering". In: *17th International Conference on Information Fusion (FUSION)*. 2014, pp. 1–8.

[21] S. Bay, C. Herzet, J.-M. Brossier, J.-P. Barbot, and B. Geller. "Analytic and Asymptotic Analysis of Bayesian Cramér–Rao Bound for Dynamical Phase Offset Estimation". In: *IEEE Transactions on Signal Processing* 56.1 (2008), pp. 61–70.

[22] C. S. Smith, K. Jouravleva, M. Huisman, S. M. Jolly, P. D. Zamore, and D. Grunwald. "An automated Bayesian pipeline for rapid analysis of single-molecule binding data". In: *Nature Communications* 10.1 (2019).

[23] K. Levenberg. "A method for the solution of certain non-linear problems in least squares". In: *Quarterly of Applied Mathematics* 2.2 (1944), pp. 164–168.

[24] D. W. Marquardt. "An Algorithm for Least-Squares Estimation of Nonlinear Parameters". In: *Journal of the Society for Industrial and Applied Mathematics* 11.2 (1963), pp. 431–441.

[25] D. Kalisvaart, J. Cnossen, S. Hung, S. Stallinga, M. Verhaegen, and C. S. Smith. *Data underlying: Precision in iterative modulation enhanced single-molecule localization microscopy*. 2022.

[26] D. Kalisvaart, J. Cnossen, S. Hung, S. Stallinga, M. Verhaegen, and C. S. Smith. *Software underlying: Precision in iterative modulation enhanced single-molecule localization microscopy*. 2022.

[27] C. Robert and G. Casella. *Monte Carlo Statistical Methods*. 2nd ed. Springer Texts in Statistics. New York, NY: Springer, 2005.

[28] J. M. Hammersley and D. C. Handscomb. *Monte Carlo Methods*. Monographs on Statistics & Applied Probability. London, England: Chapman and Hall, 1964.

Supporting Information for: Precision in Iterative Modulation Enhanced Single-Molecule Localization Microscopy

4.S1. Image formation model

Here, we discuss the image formation model under consideration in Chapter 4.

We consider an total internal reflection fluorescence (TIRF) microscopy setup, where a single emitter is illuminated with patterned intensity profiles during M iterations and for which read-out noise is assumed to be negligible. As in [1], we consider standing-wave intensity patterns with controllable spatial phase shifts $\phi^{\pm}_{x,k}$, $\phi^{\pm}_{y,k}$ in two orthogonal orientations. The superscripts $+$, $-$ describe the pattern placement with respect to the emitter position (see Section 4.2.3).

In each iteration $k \in \{1,2,\cdots,M\}$ of the localization procedure, two x-oriented patterns $p^{+}_{x,k}(x,y,\phi^{+}_{x,k})$, $p^{-}_{x,k}(x,y,\phi^{-}_{x,k})$ and two y-oriented patterns $p^{+}_{y,k}(x,y,\phi^{+}_{y,k})$, $p^{-}_{y,k}(x,y,\phi^{-}_{y,k})$ are used to illuminate the sample. For the sum of the patterns, we denote:

$$p_k(x,y,\phi^{\pm}_{x,k},\phi^{\pm}_{y,k}) = p^{+}_{x,k}(x,y,\phi^{+}_{x,k}) + p^{-}_{x,k}(x,y,\phi^{-}_{x,k}) + p^{+}_{y,k}(x,y,\phi^{+}_{y,k}) + p^{-}_{y,k}(x,y,\phi^{-}_{y,k}), \tag{4.S1}$$

where the patterns can be described by:

$$\begin{cases} p^{\pm}_{x,k}(x,y,\phi^{\pm}_{x,k}) = & c_k\left[1+m\cos\left(\omega x-\phi^{\pm}_{x,k}\right)\right], \\ p^{\pm}_{y,k}(x,y,\phi^{\pm}_{y,k}) = & c_k\left[1+m\cos\left(\omega y-\phi^{\pm}_{y,k}\right)\right]. \end{cases} \tag{4.S2}$$

Here, $m \in [0,1]$ denotes the modulation contrast of the pattern and ω denotes the spatial frequency of the pattern (in rad/m). As the illumination pattern is at best diffraction limited, it must hold that $\omega \leq 2\pi \cdot \frac{2\mathrm{NA}}{\lambda_{\mathrm{ex}}}$, where λ_{ex} is the excitation wavelength (in m) and NA is the numerical aperture. We choose ω to be diffraction limited (see Table 4.S1), as this maximizes the information contained in the illumination pattern and as it is consistent with earlier work on modulation enhanced localization microscopy with sinusoidal illumination [1].

The normalization coefficient c_k controls the ratio of expected signal photons that are collected per iteration under imperfect illumination. We consider two choices of c_k. First, we consider a scenario where we distribute a fixed signal photon budget equally over all iterations. Note that without normalization, the illumination patterns used during each iteration do not necessarily sum to $1/M$ on the position of the emitter, as the

pattern phases are arbitrary. The normalization coefficient c_k compensates for this effect, to guarantee an emitter is illuminated with a fraction of $1/M$ signal photons during each iteration:

$$\begin{aligned} S_k(x,y,\phi^{\pm}_{x,k},\phi^{\pm}_{y,k}) = 4 &+ m\cos\left(\omega x - \phi^{+}_{x,k}\right) + m\cos\left(\omega x - \phi^{-}_{x,k}\right) \\ &+ m\cos\left(\omega y - \phi^{+}_{y,k}\right) + m\cos\left(\omega y - \phi^{-}_{y,k}\right), \end{aligned} \tag{4.S3}$$

$$c_{k,\text{fixed signal photon count}} = \frac{1}{MS_k(x,y,\phi^{\pm}_{x,k},\phi^{\pm}_{y,k})}. \tag{4.S4}$$

In the second scenario, we keep the imaging time and illumination intensity per iteration constant for all iterations. The normalization constant c_k should be chosen as the largest number for which the sum of the patterns in an iteration equals $1/M$, independent of the chosen pattern phases. This results in the following expression for c_k:

$$c_{k,\text{fixed time}} = \frac{1}{2M(1+m)}. \tag{4.S5}$$

The PSF $h(x,y)^2$ is assumed to be Gaussian with standard deviation σ_{PSF} (in m):

$$h(x,y)^2 = \frac{1}{2\pi\sigma^2_{\text{PSF}}}\exp\left(\frac{-x^2-y^2}{2\sigma^2_{\text{PSF}}}\right). \tag{4.S6}$$

To maximize the information contained in the Gaussian PSF, we choose the standard deviation to be diffraction limited. For a diffraction limited PSF, we define $\sigma_{\text{PSF}} = \frac{\lambda_{\text{em}}}{4\text{NA}}$ as was done in [1], where λ_{em} is the emission wavelength (in m). For the chosen parameters (see Table 4.S1), the pattern pitch is approximately equal to twice the standard deviation of the Gaussian PSF.

We consider a rectangular camera pixel array without dead space between pixels, with n_x pixels in the x-direction and n_y pixels in the y-direction. In addition, let all pixels be rectangular, with size Δx in the x-direction and Δy in the y-direction and with the centre of pixel $q \in \{1,2,\cdots,n_x n_y\}$ located at (x_q, y_q).

In the absence of read-out noise, the photons collected on pixel q of the camera during iteration k can be modelled as realizations of a Poisson process [2]. The Poisson mean $\mu_{q,k}$ for each pixel reads:

$$\mu_{q,k} = \theta_I p_k(x,y,\phi^{\pm}_{x,k},\phi^{\pm}_{y,k}) E_x(x_q,\theta_x) E_y(y_q,\theta_y) + \theta_b, \tag{4.S7}$$

where the coordinates (θ_x,θ_y) (in m) denote the emitter position. θ_I (in photons) and θ_b (in photons/pixel) respectively denote the expected signal photon count over all iterations and the expected background photon count per pixel and pattern. These estimands are collected in the parameter vector $\boldsymbol{\theta} = [\theta_x,\theta_y,\theta_I,\theta_b]^T$. $E_u(u_q,\theta_u)$ (with $u = x$ or $u = y$) is given by:

$$E_u(u_q,\theta_u) = \frac{1}{2}\text{erf}\left(\frac{u_q - \theta_u + \frac{\Delta u}{2}}{\sigma_{\text{PSF}}\sqrt{2}}\right) - \frac{1}{2}\text{erf}\left(\frac{u_q - \theta_u - \frac{\Delta u}{2}}{\sigma_{\text{PSF}}\sqrt{2}}\right). \tag{4.S8}$$

Using this image formation model, the Fisher information for individual iterations can be computed. It is shown in [1, 2], that for a parameter vector $\boldsymbol{\theta}$, the entries of the Fisher information matrix $I_k(\boldsymbol{\theta})$ during each iteration k are given by (with $n_{\text{pixels}} = n_x n_y$):

$$[I_k(\boldsymbol{\theta})]_{i,j} = \sum_{q=1}^{n_{\text{pixels}}} \frac{1}{\mu_{q,k}} \frac{\partial \mu_{q,k}}{\partial \boldsymbol{\theta}_i} \frac{\partial \mu_{q,k}}{\partial \boldsymbol{\theta}_j}. \tag{4.S9}$$

4.S2. Van Trees inequality

In this section, we state the multivariate VTI and its assumptions, based on its formulation in [3, 4].

Let $\boldsymbol{x} = [x_1, x_2, ..., x_n]^T$ represent a data set, which can be seen a realization of independent and identically distributed random variables $[X_1, X_2, ..., X_n]^T$ with a distribution depending on an estimand vector $\boldsymbol{\theta} \in \mathbb{R}^m$. Suppose that the likelihood function $L(\boldsymbol{\theta}|\boldsymbol{x})$ is continuously differentiable with respect to $\boldsymbol{\theta}$ and that its support $\{\boldsymbol{x}|L(\boldsymbol{\theta}|\boldsymbol{x}) > 0\}$ does not depend on $\boldsymbol{\theta}$.

Let a prior probability density function $\lambda(\boldsymbol{\theta})$ on the estimands $\boldsymbol{\theta}$ be known. Suppose that $\lambda(\boldsymbol{\theta})$ is absolutely continuous and that λ converges to zero at the endpoints of its domain fast enough, such that $\boldsymbol{\theta}\lambda(\boldsymbol{\theta}) \to 0$ if $\boldsymbol{\theta}$ approaches the endpoints of the domain of λ.

Then, the mean squared error matrix, $\text{MSE}(\hat{\boldsymbol{\theta}}) = \mathbb{E}_{\lambda,L}[(\hat{\boldsymbol{\theta}} - \boldsymbol{\theta})(\hat{\boldsymbol{\theta}} - \boldsymbol{\theta})^T]$ of any estimator $\hat{\boldsymbol{\theta}}$ of $\boldsymbol{\theta}$ satisfies:

$$\left(\mathbb{E}_{\lambda,L}[(\hat{\boldsymbol{\theta}} - \boldsymbol{\theta})(\hat{\boldsymbol{\theta}} - \boldsymbol{\theta})^T] - (J_D + J_P)^{-1}\right) \succeq 0. \tag{4.S10}$$

That is, $\mathbb{E}_{\lambda,L}[(\hat{\boldsymbol{\theta}} - \boldsymbol{\theta})(\hat{\boldsymbol{\theta}} - \boldsymbol{\theta})^T] - (J_D + J_P)^{-1}$ is positive semi-definite, where the data information matrix J_D is given by

$$[J_D]_{i,j} = [\mathbb{E}_\lambda[I(\boldsymbol{\theta})]_{i,j}] = \mathbb{E}_\lambda\left[\mathbb{E}_L\left[\frac{\partial \ell(\boldsymbol{\theta}|\boldsymbol{x})}{\partial \boldsymbol{\theta}_i} \frac{\partial \ell(\boldsymbol{\theta}|\boldsymbol{x})}{\partial \boldsymbol{\theta}_j}\right]\right] = \mathbb{E}_\lambda\left[\int_{\mathbb{R}^n} \frac{\partial \ell(\boldsymbol{\theta}|\boldsymbol{x})}{\partial \boldsymbol{\theta}_i} \frac{\partial \ell(\boldsymbol{\theta}|\boldsymbol{x})}{\partial \boldsymbol{\theta}_j} L(\boldsymbol{\theta}|\boldsymbol{x}) \mathrm{d}\boldsymbol{x}\right], \tag{4.S11}$$

and where the prior information matrix J_P is given by

$$[J_P]_{i,j} = [I(\lambda)]_{i,j} = \mathbb{E}_\lambda\left[\frac{\partial \log(\lambda(\boldsymbol{\theta}))}{\partial \boldsymbol{\theta}_i} \frac{\partial \log(\lambda(\boldsymbol{\theta}))}{\partial \boldsymbol{\theta}_j}\right] = \int_{\mathbb{R}^m} \frac{\partial \log(\lambda(\boldsymbol{\theta}))}{\partial \boldsymbol{\theta}_i} \frac{\partial \log(\lambda(\boldsymbol{\theta}))}{\partial \boldsymbol{\theta}_j} \lambda(\boldsymbol{\theta}) \mathrm{d}\boldsymbol{\theta}. \tag{4.S12}$$

Furthermore, $(J_D + J_P)$ can be rewritten as J with $J_{i,j} = \mathbb{E}_{\lambda,L}\left[\frac{\partial \log(p(\boldsymbol{x},\boldsymbol{\theta}))}{\partial \boldsymbol{\theta}_i} \frac{\partial \log(p(\boldsymbol{x},\boldsymbol{\theta}))}{\partial \boldsymbol{\theta}_j}\right]$, where $p(\boldsymbol{x},\boldsymbol{\theta})$ denotes the joint probability density function of $\boldsymbol{x}$ and $\boldsymbol{\theta}$. The matrix J is called the Bayesian information matrix.

4.S3. Monte Carlo evaluation of Van Trees inequality

In many practical scenarios, the data information matrix of Eq. (4.S11) is difficult to compute analytically or it results in complicated expressions for the localization precision. Aside from certain special cases (see Section 4.S4), one generally resorts to numerical methods to evaluate the VTI [5, 6].

Due to the fact that we use a Gaussian prior, an appropriately chosen numerical integration method should be able to cover an infinite domain of integration, to ensure

convergence to the true data information matrix. Furthermore, as we consider a multivariate integral over $\mathbb{R}^4$, the curse of dimensionality may cause slow convergence. Therefore, numerical integration methods that efficiently distribute function evaluations are preferred.

As we can easily sample from a multivariate Gaussian distribution, simple Monte Carlo integration (SMC) is a suitable method to evaluate Eq. (4.S11). In short, SMC integration methods sample from a probability distribution of choice. These samples are used to evaluate the integrand, after which the value of the integral is estimated by averaging the obtained integrand values [7]. If the domain of the sampling probability distribution equals or contains the domain of integration, asymptotic convergence to the integral value is guaranteed [8].

Using the imeSMLM prior $\lambda_{k-1}(\boldsymbol{\theta})$, the VTI requires the following two expectations to be computed:

$$[J_{D,k}]_{i,j} = \mathbb{E}_{\lambda_{k-1}}\left[[I_k(\boldsymbol{\theta})]_{i,j}\right] = \int_{\mathbb{R}^m} [I_k(\boldsymbol{\theta})]_{i,j}\lambda_{k-1}(\boldsymbol{\theta})\mathrm{d}\boldsymbol{\theta}, \tag{4.S13}$$

$$\begin{aligned}[J_{P,k}]_{i,j} &= \mathbb{E}_{\lambda_{k-1}}\left[\frac{\partial \log(\lambda_{k-1}(\boldsymbol{\theta}))}{\partial \boldsymbol{\theta}_i}\frac{\partial \log(\lambda_{k-1}(\boldsymbol{\theta}))}{\partial \boldsymbol{\theta}_j}\right] \\ &= \int_{\mathbb{R}^m} \frac{\partial \log(\lambda_{k-1}(\boldsymbol{\theta}))}{\partial \boldsymbol{\theta}_i}\frac{\partial \log(\lambda_{k-1}(\boldsymbol{\theta}))}{\partial \boldsymbol{\theta}_j}\lambda_{k-1}(\boldsymbol{\theta})\mathrm{d}\boldsymbol{\theta}.\end{aligned} \tag{4.S14}$$

By randomly sampling $[\boldsymbol{\theta}_1, \boldsymbol{\theta}_2, \cdots, \boldsymbol{\theta}_{n_{\mathrm{MC}}}]^T$ from the independent and identically distributed random variables $[\boldsymbol{\Theta}_1, \boldsymbol{\Theta}_2, \cdots, \boldsymbol{\Theta}_{n_{\mathrm{MC}}}]^T$, each of which has the density function $\lambda_{k-1}(\boldsymbol{\theta})$, the SMC-estimates $\hat{J}_{D,k}$ and $\hat{J}_{P,k}$ of Eqs. (4.S15) and (4.S16) can be used to estimate $J_{D,k}$ and $J_{P,k}$, respectively.

$$[\hat{J}_{D,k}]_{i,j} = \frac{1}{n_{\mathrm{MC}}}\sum_{s=1}^{n_{\mathrm{MC}}} [I_k(\boldsymbol{\theta}_s)]_{i,j}, \tag{4.S15}$$

$$[\hat{J}_{P,k}]_{i,j} = \frac{1}{n_{\mathrm{MC}}}\sum_{s=1}^{n_{\mathrm{MC}}} \left(\left[\frac{\partial \log(\lambda(\boldsymbol{\theta}))}{\partial \boldsymbol{\theta}_i}\right]_{\boldsymbol{\theta}=\boldsymbol{\theta}_s}\left[\frac{\partial \log(\lambda(\boldsymbol{\theta}))}{\partial \boldsymbol{\theta}_j}\right]_{\boldsymbol{\theta}=\boldsymbol{\theta}_s}\right). \tag{4.S16}$$

4.S4. Analytical approximation of Van Trees inequality

In this section, theoretical limits on the localization precision are derived using the VTI. We limit ourselves to one-dimensional localization, where we ignore the effects of image discretization due to finite camera pixel size. Furthermore, we assume the expected signal photon count θ_I is a known constant (i.e. we do not estimate it) and we ignore background such that $\theta_b = 0$. Lastly, we assume that the point spread function is a Gaussian with standard deviation σ_{PSF}.

In the one-dimensional case when pattern positions $\phi^+_{x,k}$ and $\phi^-_{x,k}$ are used, the illumination pattern in iteration k is given by:

$$p_{x,k}(x) = c_k[2 + m\cos(\omega x - \phi^+_{x,k}) + m\cos(\omega x - \phi^-_{x,k})]. \tag{4.S17}$$

Under the presented assumptions, we find the expected photon count of Eq. (4.S18),

with its first partial derivative with respect to θ_x being given by Eq. (4.S19):

$$\mu_k(x) = \frac{\theta_I c_k (2 + m\cos(\omega\theta_x - \phi_{x,k}^+) + m\cos(\omega\theta_x - \phi_{x,k}^-))}{\sigma_{\mathrm{PSF}}(2\pi)^{1/2}} \exp\left(-\frac{(x-\theta_x)^2}{2\sigma_{\mathrm{PSF}}^2}\right), \tag{4.S18}$$

$$\begin{aligned}\frac{\partial \mu_k}{\partial \theta_x}(x) = \theta_I c_k \exp\left(-\frac{(x-\theta_x)^2}{2\sigma_{\mathrm{PSF}}^2}\right)\Bigg(-\frac{m\omega\left(\sin\left(\omega\theta_x - \phi_{x,k}^+\right) + \sin\left(\omega\theta_x - \phi_{x,k}^-\right)\right)}{\sigma_{\mathrm{PSF}}(2\pi)^{1/2}} \\ + \frac{\left((x-\theta_x)\left(2 + m\cos\left(\omega\theta_x - \phi_{x,k}^+\right) + m\cos\left(\omega\theta_x - \phi_{x,k}^-\right)\right)\right)}{\sigma_{\mathrm{PSF}}^3(2\pi)^{1/2}}\Bigg).\end{aligned} \tag{4.S19}$$

The Fisher information in iteration k is then given by:

$$I_k(\theta_x) = \int_{\mathbb{R}} \frac{1}{\mu_k(x)}\left(\frac{\partial \mu_k}{\partial \theta_x}(x)\right)^2 \mathrm{d}x \tag{4.S20}$$

$$\begin{aligned}&= \frac{\theta_I c_k\left(2 + m\cos\left(\omega\theta_x - \phi_{x,k}^+\right) + m\cos\left(\omega\theta_x - \phi_{x,k}^-\right)\right)}{\sigma_{\mathrm{PSF}}^2} \\ &+ \frac{\theta_I c_k \omega^2\left(m\sin\left(\omega\theta_x - \phi_{x,k}^+\right) + m\sin\left(\omega\theta_x - \phi_{x,k}^-\right)\right)^2}{2 + m\cos\left(\omega\theta_x - \phi_{x,k}^+\right) + m\cos\left(\omega\theta_x - \phi_{x,k}^-\right)}.\end{aligned} \tag{4.S21}$$

We choose the prior information available in iteration $k \geq 1$ to be normally distributed with mean $\hat{\theta}_{x,k-1}$ and variance $\sigma_{x,k-1} = \frac{1}{\sqrt{I_1(\theta_x)}}$ (for $k = 2$) or $\sigma_{x,k-1} = \frac{1}{\sqrt{J_{k-1}}}$ (for $k \geq 3$). The resulting prior information, its natural logarithm and its partial derivative with respect to θ_x are given by Eqs. (4.S22)-(4.S24):

$$\lambda_{k-1}(\theta_x) = \frac{1}{\sigma_{x,k-1}(2\pi)^{1/2}} \exp\left(-\frac{(\theta_x - \hat{\theta}_{x,k-1})^2}{2\sigma_{x,k-1}^2}\right), \tag{4.S22}$$

$$\log(\lambda_{k-1}(\theta_x)) = \log\left(\frac{1}{\sigma_{x,k-1}(2\pi)^{1/2}}\right) - \frac{(\theta_x - \hat{\theta}_{x,k-1})^2}{2\sigma_{x,k-1}^2}, \tag{4.S23}$$

$$\frac{\partial \log(\lambda_{k-1}(\theta_x))}{\partial \theta_x} = -\frac{2(\theta_x - \hat{\theta}_{x,k-1})}{2\sigma_{x,k-1}^2}. \tag{4.S24}$$

The Bayesian prior information in iteration k is given by:

$$J_{P,k} = \int_{\mathbb{R}}\left(\frac{\partial \log(\lambda_{k-1}(\theta_x))}{\partial \theta_x}\right)^2 \lambda_{k-1}(\theta_x)\mathrm{d}\theta_x \tag{4.S25}$$

$$= \frac{1}{\sigma_{x,k-1}(2\pi)^{1/2}} \int_{\mathbb{R}}\left(\frac{2(\theta_x - \hat{\theta}_{x,k-1})}{2\sigma_{k-1}^2}\right)^2 \exp\left(-\frac{(\theta_x - \hat{\theta}_{x,k-1})^2}{2\sigma_{x,-1}^2}\right)\mathrm{d}\theta_x \tag{4.S26}$$

$$= \frac{1}{\sigma_{x,k-1}^2}. \tag{4.S27}$$

The Bayesian data information in iteration k is given by:

$$J_{D,k} = \int_{\mathbb{R}} I_k(\theta_x)\lambda_{k-1}(\theta_x)\mathrm{d}\theta_x \tag{4.S28}$$

$$= \int_{\mathbb{R}} \frac{\theta_I c_k \left(2 + m\cos\left(\omega\theta_x - \phi^+_{x,k}\right) + m\cos\left(\omega\theta_x - \phi^-_{x,k}\right)\right)}{\sigma^2_{\mathrm{PSF}}}\lambda_{k-1}(\theta_x)\mathrm{d}\theta_x$$

$$+ \int_{\mathbb{R}} \frac{\theta_I c_k \omega^2 \left(m\sin\left(\omega\theta_x - \phi^+_{x,k}\right) + m\sin\left(\omega\theta_x - \phi^-_{x,k}\right)\right)^2}{2 + m\cos\left(\omega\theta_x - \phi^+_{x,k}\right) + m\cos\left(\omega\theta_x - \phi^-_{x,k}\right)}\lambda_{k-1}(\theta_x)\mathrm{d}\theta_x \tag{4.S29}$$

$$= \frac{\theta_I c_k}{\sigma^2_{\mathrm{PSF}}}\left(2 + \left(m\cos\left(\omega\hat{\theta}_{x,k-1} - \phi^+_{x,k}\right) + m\cos\left(\omega\hat{\theta}_{x,k-1} - \phi^-_{x,k}\right)\right)\exp\left(-\frac{\omega^2\sigma^2_{x,k-1}}{2}\right)\right)$$

$$+ \int_{\mathbb{R}} \frac{\theta_I c_k \omega^2 \left(m\sin\left(\omega\theta_x - \phi^+_{x,k}\right) + m\sin\left(\omega\theta_x - \phi^-_{x,k}\right)\right)^2}{2 + m\cos\left(\omega\theta_x - \phi^+_{x,k}\right) + m\cos\left(\omega\theta_x - \phi^-_{x,k}\right)}\lambda_{k-1}(\theta_x)\mathrm{d}\theta_x. \tag{4.S30}$$

We rewrite $\left(m\sin\left(\omega\theta_x - \phi^+_{x,k}\right) + m\sin\left(\omega\theta_x - \phi^-_{x,k}\right)\right)^2$:

$$\left(m\sin\left(\omega\theta_x - \phi^+_{x,k}\right) + m\sin\left(\omega\theta_x - \phi^-_{x,k}\right)\right)^2 \tag{4.S31}$$

$$= m^2\sin^2\left(\omega\theta_x - \phi^+_{x,k}\right) + m^2\sin^2\left(\omega\theta_x - \phi^-_{x,k}\right) + 2m^2\sin\left(\omega\theta_x - \phi^+_{x,k}\right)\sin\left(\omega\theta_x - \phi^-_{x,k}\right) \tag{4.S32}$$

$$= 2m^2 - m^2\cos^2\left(\omega\theta_x - \phi^+_{x,k}\right) - m^2\cos^2\left(\omega\theta_x - \phi^-_{x,k}\right) + 2m^2\sin\left(\omega\theta_x - \phi^+_{x,k}\right)\sin\left(\omega\theta_x - \phi^-_{x,k}\right) \tag{4.S33}$$

$$= \left(2 + m\cos\left(\omega\theta_x - \phi^+_{x,k}\right) + m\cos\left(\omega\theta_x - \phi^-_{x,k}\right)\right) \cdot \left(2 - m\cos\left(\omega\theta_x - \phi^+_{x,k}\right) - m\cos\left(\omega\theta_x - \phi^-_{x,k}\right)\right) - 4 + 2m^2 + 2m^2\cos\left(\omega\theta_x - \phi^+_{x,k}\right)\cos\left(\omega\theta_x - \phi^-_{x,k}\right) + 2m^2\sin\left(\omega\theta_x - \phi^+_{x,k}\right)\sin\left(\omega\theta_x - \phi^-_{x,k}\right) \tag{4.S34}$$

$$= \left(2 + m\cos\left(\omega\theta_x - \phi^+_{x,k}\right) + m\cos\left(\omega\theta_x - \phi^-_{x,k}\right)\right) \cdot \left(2 - m\cos\left(\omega\theta_x - \phi^+_{x,k}\right) - m\cos\left(\omega\theta_x - \phi^-_{x,k}\right)\right) - 4 + 2m^2\left(1 + \cos\left(\phi^-_{x,k} - \phi^+_{x,k}\right)\right). \tag{4.S35}$$

By substituting this into the expression for $J_{D,k}$, we get:

$$J_{D,k} = \frac{\theta_I c_k}{\sigma_{\mathrm{PSF}}^2}\left(2+\left(m\cos\left(\omega\hat{\theta}_{x,k-1}-\phi_{x,k}^{+}\right)+m\cos\left(\omega\hat{\theta}_{x,k-1}-\phi_{x,k}^{-}\right)\right)\exp\left(-\frac{\omega^2\sigma_{x,k-1}^2}{2}\right)\right)$$
$$+\int_{\mathbb{R}}\theta_I c_k\omega^2\left(2-m\cos\left(\omega\theta_x-\phi_{x,k}^{+}\right)-m\cos\left(\omega\theta_x-\phi_{x,k}^{-}\right)\right)\lambda_{k-1}(\theta_x)\mathrm{d}\theta_x$$
$$+\int_{\mathbb{R}}\frac{\theta_I c_k\omega^2\left(-4+2m^2\left(1+\cos\left(\phi_{x,k}^{-}-\phi_{x,k}^{+}\right)\right)\right)}{2+m\cos\left(\omega\theta_x-\phi_{x,k}^{+}\right)+m\cos\left(\omega\theta_x-\phi_{x,k}^{-}\right)}\lambda_{k-1}(\theta_x)\mathrm{d}\theta_x \tag{4.S36}$$

$$=\frac{\theta_I c_k}{\sigma_{\mathrm{PSF}}^2}\left(2+\left(m\cos\left(\omega\hat{\theta}_{x,k-1}-\phi_{x,k}^{+}\right)+m\cos\left(\omega\hat{\theta}_{x,k-1}-\phi_{x,k}^{-}\right)\right)\exp\left(-\frac{\omega^2\sigma_{x,k-1}^2}{2}\right)\right)$$
$$+\theta_I c_k\omega^2\left(2-\left(m\cos\left(\omega\hat{\theta}_{x,k-1}-\phi_{x,k}^{+}\right)+m\cos\left(\omega\hat{\theta}_{x,k-1}-\phi_{x,k}^{-}\right)\right)\exp\left(-\frac{\omega^2\sigma_{x,k-1}^2}{2}\right)\right)$$
$$+\int_{\mathbb{R}}\frac{\theta_I c_k\omega^2\left(-4+2m^2\left(1+\cos\left(\phi_{x,k}^{-}-\phi_{x,k}^{+}\right)\right)\right)}{2+m\cos\left(\omega\theta_x-\phi_{x,k}^{+}\right)+m\cos\left(\omega\theta_x-\phi_{x,k}^{-}\right)}\lambda_{k-1}(\theta_x)\mathrm{d}\theta_x. \tag{4.S37}$$

In the remaining integral, the integrand is non-positive. Furthermore, for good modulation $m\approx 1$ and for close pattern positions $\phi_{x,k}^{+}\approx\phi_{x,k}^{-}$, the contribution of the remaining integral to the Bayesian data information is negligible. We thus approximate $J_{D,k}$ from above by neglecting the remaining integral:

$$J_{D,k}\leq\frac{\theta_I c_k}{\sigma_{\mathrm{PSF}}^2}\left(2+\left(m\cos\left(\omega\hat{\theta}_{x,k-1}-\phi_{x,k}^{+}\right)+m\cos\left(\omega\hat{\theta}_{x,k-1}-\phi_{x,k}^{-}\right)\right)\exp\left(-\frac{\omega^2\sigma_{x,k-1}^2}{2}\right)\right)$$
$$+\theta_I c_k\omega^2\left(2-\left(m\cos\left(\omega\hat{\theta}_{x,k-1}-\phi_{x,k}^{+}\right)+m\cos\left(\omega\hat{\theta}_{x,k-1}-\phi_{x,k}^{-}\right)\right)\exp\left(-\frac{\omega^2\sigma_{x,k-1}^2}{2}\right)\right). \tag{4.S38}$$

Then the Bayesian information is given by:

$$J_k = J_{P,k}+J_{D,k}$$
$$\leq\frac{1+\frac{\theta_I c_k\sigma_{x,k-1}^2}{\sigma_{\mathrm{PSF}}^2}\left(2+\left(m\cos\left(\omega\hat{\theta}_{x,k-1}-\phi_{x,k}^{+}\right)+m\cos\left(\omega\hat{\theta}_{x,k-1}-\phi_{x,k}^{-}\right)\right)\exp\left(-\frac{\omega^2\sigma_{x,k-1}^2}{2}\right)\right)}{\sigma_{x,k-1}^2}$$
$$+\frac{\theta_I c_k\omega^2\sigma_{x,k-1}^2\left(2-\left(m\cos\left(\omega\hat{\theta}_{x,k-1}-\phi_{x,k}^{+}\right)+m\cos\left(\omega\hat{\theta}_{x,k-1}-\phi_{x,k}^{-}\right)\right)\exp\left(-\frac{\omega^2\sigma_{x,k-1}^2}{2}\right)\right)}{\sigma_{x,k-1}^2}. \tag{4.S39}$$

By the VTI, we find for the localization precision:

$$\begin{aligned}
&\sigma_{x,k} \geq (J_k)^{-\frac{1}{2}} \\
&\geq \sigma_{x,k-1}\left(1+\frac{\theta_I c_k \sigma^2_{x,k-1}}{\sigma^2_{\mathrm{PSF}}}\left(2+\left(m\cos\left(\omega\hat{\theta}_{x,k-1}-\phi^+_{x,k}\right)\right.\right.\right. \\
&\left.\left.\left.+m\cos\left(\omega\hat{\theta}_{x,k-1}-\phi^-_{x,k}\right)\right)\exp\left(-\frac{\omega^2\sigma^2_{x,k-1}}{2}\right)\right)+\theta_I c_k\omega^2\sigma^2_{x,k-1}\right. \\
&\left.\cdot\left(2-\left(m\cos\left(\omega\hat{\theta}_{x,k-1}-\phi^+_{x,k}\right)+m\cos\left(\omega\hat{\theta}_{x,k-1}-\phi^-_{x,k}\right)\right)\exp\left(-\frac{\omega^2\sigma^2_{x,k-1}}{2}\right)\right)\right)^{-\frac{1}{2}}.
\end{aligned} \tag{4.S40}$$

This expression can be rewritten as:

$$\sigma_{x,k} \geq (J_k)^{-\frac{1}{2}} \geq \frac{\sigma_{x,k-1}}{\sqrt{1+\sigma^2_{x,k-1}(F_{\mathrm{PSF}}+F_{\mathrm{illum}})}}, \tag{4.S41a}$$

$$F_{\mathrm{PSF}} = \frac{\theta_I c_k}{\sigma^2_{\mathrm{PSF}}}\left(2+\left(m\cos\left(\omega\hat{\theta}_{x,k-1}-\phi^+_{x,k}\right)+m\cos\left(\omega\hat{\theta}_{x,k-1}-\phi^-_{x,k}\right)\right)\exp\left(-\frac{\omega^2\sigma^2_{x,k-1}}{2}\right)\right), \tag{4.S41b}$$

$$F_{\mathrm{illum}} = \theta_I c_k\omega^2\left(2-\left(m\cos\left(\omega\hat{\theta}_{x,k-1}-\phi^+_{x,k}\right)+m\cos\left(\omega\hat{\theta}_{x,k-1}-\phi^-_{x,k}\right)\right)\exp\left(-\frac{\omega^2\sigma^2_{x,k-1}}{2}\right)\right). \tag{4.S41c}$$

If the pattern positions of Eq. (4.5) are substituted into Eq. (4.S41), we obtain:

$$\sigma_{x,k} \geq (J_k)^{-\frac{1}{2}} \geq \frac{\sigma_{x,k-1}}{\sqrt{1+\sigma^2_{x,k-1}(F_{\mathrm{PSF}}+F_{\mathrm{illum}})}}, \tag{4.S42a}$$

$$F_{\mathrm{PSF}} = \frac{\theta_I c_k}{\sigma^2_{\mathrm{PSF}}}\left(2-2m\cos\left(\omega\alpha\sigma_{x,k-1}\right)\exp\left(-\frac{\omega^2\sigma^2_{x,k-1}}{2}\right)\right), \tag{4.S42b}$$

$$F_{\mathrm{illum}} = \theta_I c_k\omega^2\left(2+2m\cos\left(\omega\alpha\sigma_{x,k-1}\right)\exp\left(-\frac{\omega^2\sigma^2_{x,k-1}}{2}\right)\right). \tag{4.S42c}$$

4.S5. Optimal distribution of signal photons

Using the analytical approximation of the VTI (see Section 4.S4), we can derive the optimal distribution of the signal photon budget under the assumptions that the pattern modulation is perfect and that $\omega\sigma_{x,k} \ll 1$ for all iterations k. As discussed in Section 4.S1, the coefficient c_k models the ratio of expected signal photons that are collected under imperfect illumination. We therefore parametrize $\theta_I c_k \propto \frac{\theta_{I,k}}{\alpha^2 J^{-1}_{k-1}}$, where $\theta_{I,k}$ describes the signal photon budget used in iteration k. The VTI given in Eq. (4.S42), written

for the final iteration M, now reduces to:

$$\sigma_{x,M}^2 \geq J_M^{-1} = \frac{J_{M-1}^{-1}}{1 + C J_{M-1}^{-1} \frac{\theta_{I,M}}{\alpha^2 J_{M-1}^{-1}}} \tag{4.S43a}$$

$$= J_{M-1}^{-1} \cdot \frac{1}{1 + \frac{\theta_{I,M}}{\beta^2}}, \tag{4.S43b}$$

where C is a numerical coefficient and where $\beta = \frac{\alpha}{\sqrt{C}}$.

In the first iteration, no prior information is available, so the localization precision follows from the CRLB:

$$\sigma_{x,1}^2 \geq I_{x,1}^{-1} = \frac{\sigma_{\text{PSF}}^2}{\theta_{I,1}}. \tag{4.S44}$$

By iteration of Eq. (4.S43), we obtain:

$$\sigma_{x,M}^2 \geq J_M^{-1} = J_{M-1}^{-1} \cdot \frac{1}{1 + \frac{\theta_{I,M}}{\beta^2}} \tag{4.S45a}$$

$$= I_{x,1}^{-1} \prod_{j=2}^{M} \frac{1}{1 + \frac{\theta_{I,j}}{\beta^2}} \tag{4.S45b}$$

$$= \frac{\sigma_{\text{PSF}}^2}{\theta_{I,1} \prod_{j=2}^{M} \left(1 + \frac{\theta_{I,j}}{\beta^2}\right)}. \tag{4.S45c}$$

To optimize the localization precision $\sigma_{x,k}$, we should maximize:

$$G = \theta_{I,1} \prod_{j=2}^{M} \left(1 + \frac{\theta_{I,j}}{\beta^2}\right), \tag{4.S46}$$

subject to the constraint:

$$\theta_I = \sum_{j=1}^{M} \theta_{I,j}. \tag{4.S47}$$

We use the method of Lagrange multipliers to solve this problem. The resulting system of equations is given by:

$$0 = \frac{\partial G}{\partial \theta_{I,1}} - \mu = \frac{G}{\theta_{I,1}} - \mu, \tag{4.S48a}$$

$$0 = \frac{\partial G}{\partial \theta_{I,j}} - \mu = \frac{G}{\beta^2 + \theta_{I,j}} - \mu, \forall\, j \in \{2, \ldots, M\}, \tag{4.S48b}$$

$$\theta_I = \sum_{j=1}^{M} \theta_{I,j}. \tag{4.S48c}$$

This system can be solved to:

$$\theta_{I,1} = \frac{\theta_I + (M-1)\beta^2}{M}, \tag{4.S49a}$$

$$\theta_{I,j} = \frac{\theta_I - \beta^2}{M}, \forall\, j \in \{2, ..., M\}. \tag{4.S49b}$$

Under the discussed assumptions, it is thus optimal to equally distribute the signal photon budget over iterations 2 to M. The resulting localization precision is given by:

$$G = \frac{(\theta_{I,1})^M}{(\beta^2)^{M-1}} = \beta^2 \left(1 + \frac{\theta_I - \beta^2}{\beta^2 M}\right)^M, \tag{4.S50a}$$

$$\sigma^2_{x,M} \geq \frac{\sigma^2_{\mathrm{PSF}}}{\beta^2 \left(1 + \frac{\theta_I - \beta^2}{\beta^2 M}\right)^M}. \tag{4.S50b}$$

4.S6. Supporting figures and tables

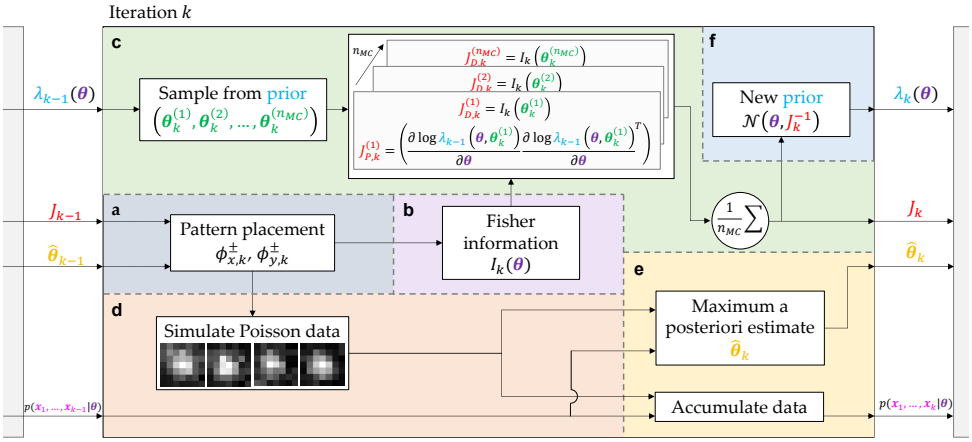

Figure 4.S1: Algorithm for simultaneous evaluation of the VTI and the MAP estimate on simulated Poisson data. (*a*) Based on the previous localization precision lower bound J_{k-1} and the previous MAP estimate $\hat{\boldsymbol{\theta}}_{k-1}$, the current illumination patterns are placed. (*b*) Using the pattern positions determined in (*a*), the Fisher information matrix $I_k(\boldsymbol{\theta})$ for the current iteration can be determined up to an unknown parameter $\boldsymbol{\theta}$. (*c*) SMC integration is used to approximate the VTI. n_{MC} samples are drawn from the prior distribution $\lambda_{k-1}(\boldsymbol{\theta})$, and the integrands of $J_{D,k}$ and $J_{P,k}$ are evaluated on each sample. The Bayesian information matrix J_k is approximately given by the average of $(J_{D,k} + J_{P,k})$ over all samples. (*d*) Poisson data is simulated using the pattern positions determined in (*a*). (*e*) The MAP estimate $\hat{\boldsymbol{\theta}}_k$ is computed, where $p(\boldsymbol{x}_1, \ldots, \boldsymbol{x}_{k-1}|\boldsymbol{\theta})$ is used as prior information and where $p(\boldsymbol{x}_k|\boldsymbol{\theta})$ describes the likelihood of the data from the current iteration. (*f*) The prior distribution on $\boldsymbol{\theta}$ for the next iteration is chosen as a multivariate Gaussian, with mean $\boldsymbol{\theta}$ and covariance matrix J_k^{-1}.

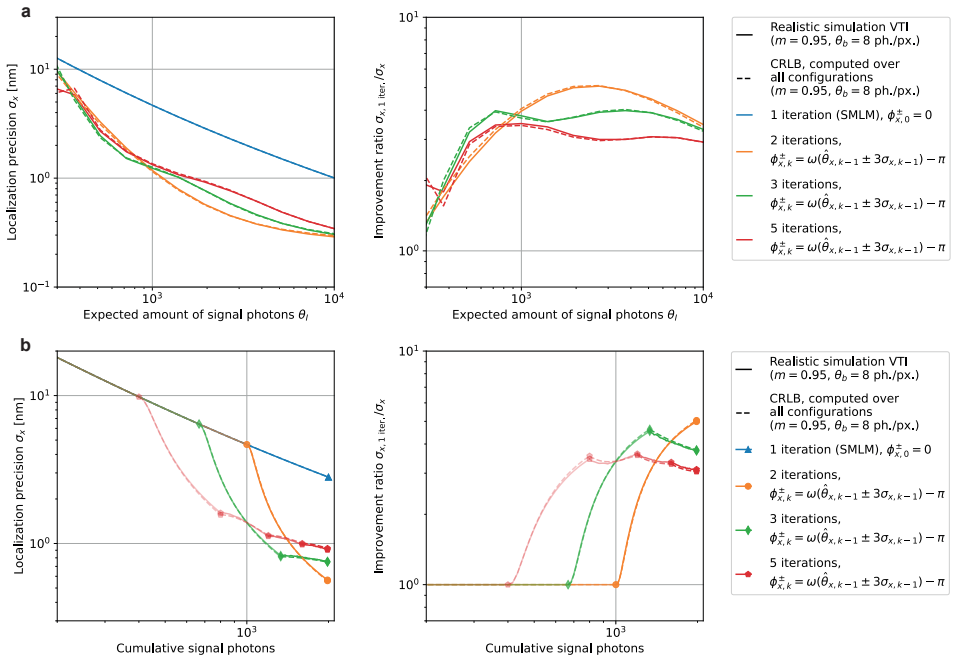

Figure 4.S2: Comparison of the VTI and the CRLB for different iteration counts. Simulated maximum localization precision in the x-direction as a function of (*a*) the expected signal photon count, and (*b*) the expected cumulative signal photon count, for different iteration counts and assuming a constant signal photon count per iteration. The localization precision limits are respectively simulated from the VTI and the CRLB over all iterations. In (*b*), the expected signal photon count θ_I was set to 2000 photons and markers indicate a transition between iterations.

	Data		Prior		Estimator and prior distribution	
Iteration 1: CRLB	$I_1(\boldsymbol{\theta})$	+	-	→	$\hat{\boldsymbol{\theta}}_1 \sim \mathcal{N}\left(\boldsymbol{\theta}, I_1^{-1}(\boldsymbol{\theta})\right)$	$\lambda_1(\boldsymbol{\theta})$ ←
Iteration 2: VTI	$J_{D,2} = \mathbb{E}_{\lambda_1}[I_2(\boldsymbol{\theta})]$	+	$J_{P,2} = I(\lambda_1)$	→	$\hat{\boldsymbol{\theta}}_2 \sim \mathcal{N}\left(\boldsymbol{\theta}, (J_{D,2} + J_{P,2})^{-1}\right)$	$\lambda_2(\boldsymbol{\theta})$ ←
Iteration 3: VTI	$J_{D,3} = \mathbb{E}_{\lambda_2}[I_3(\boldsymbol{\theta})]$	+	$J_{P,3} = I(\lambda_2)$	→	$\hat{\boldsymbol{\theta}}_3 \sim \mathcal{N}\left(\boldsymbol{\theta}, (J_{D,3} + J_{P,3})^{-1}\right)$	$\lambda_3(\boldsymbol{\theta})$ ←
Iteration 4: VTI	$J_{D,4} = \mathbb{E}_{\lambda_3}[I_4(\boldsymbol{\theta})]$	+	$J_{P,4} = I(\lambda_3)$	→	$\hat{\boldsymbol{\theta}}_4 \sim \mathcal{N}\left(\boldsymbol{\theta}, (J_{D,4} + J_{P,4})^{-1}\right)$	$\lambda_4(\boldsymbol{\theta})$ ←
⋮	⋮	+	⋮	→	⋮	

Figure 4.S3: Information flow to simulate the maximum localization precision of imeSMLM using the VTI. In the first iteration, the Fisher information matrix $I_1(\boldsymbol{\theta})$ is computed. The resulting MLE is asymptotically $\mathcal{N}(\boldsymbol{\theta}, I_1^{-1}(\boldsymbol{\theta}))$ distributed, and we choose this as a prior on the next iteration. In each subsequent iteration, the VTI is evaluated using the prior, resulting in the data information matrix $J_{D,k}$ and the prior information matrix $J_{P,k}$ in iteration k. As the next prior, we choose $\mathcal{N}(\boldsymbol{\theta}, (J_{D,k} + J_{P,k})^{-1})$. This iteration continues until the maximum amount of iterations M is reached.

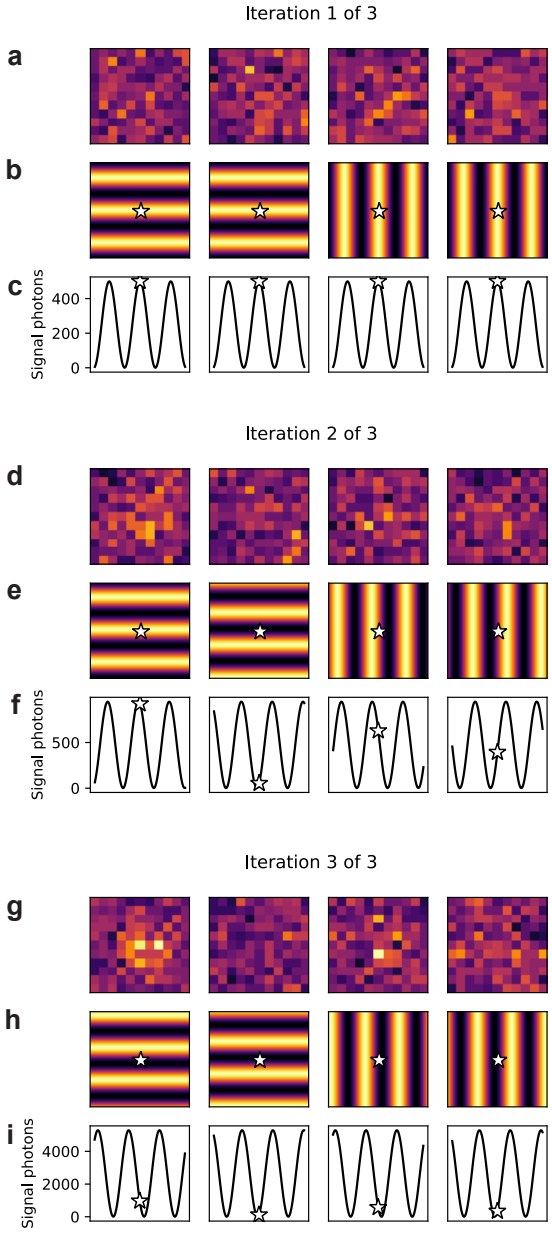

Figure 4.S4: Example of simulated data and illumination patterns during three iterations of an iterative localization experiment. In (*b*), (*c*), (*e*), (*f*), (*h*) and (*i*), the true emitter position is marked by a star. (*a*), (*d*), (*g*) Example of simulated regions of interest with 8 expected background photons per pixel, for iteration (*a*) 1, (*d*) 2 and (*g*) 3. (*b*), (*e*), (*h*) 2D projection of illumination patterns on the xy-plane, for iteration (*b*) 1, (*e*) 2 and (*h*) 3. . (*c*), (*f*), (*i*) Signal photon response as a function of the emitter x-position, for iteration (*c*) 1, (*f*) 2 and (*i*) 3. .

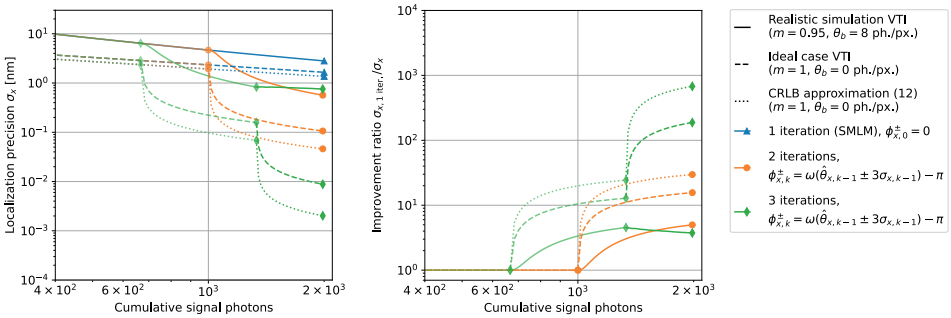

Figure 4.S5: Simulated localization precision in the x-direction as a function of the cumulative signal photon count, when 1, 2 or 3 iterations are used at an expected signal photon count of $\theta_I = 2000$ photons. Markers indicate a transition between iterations.

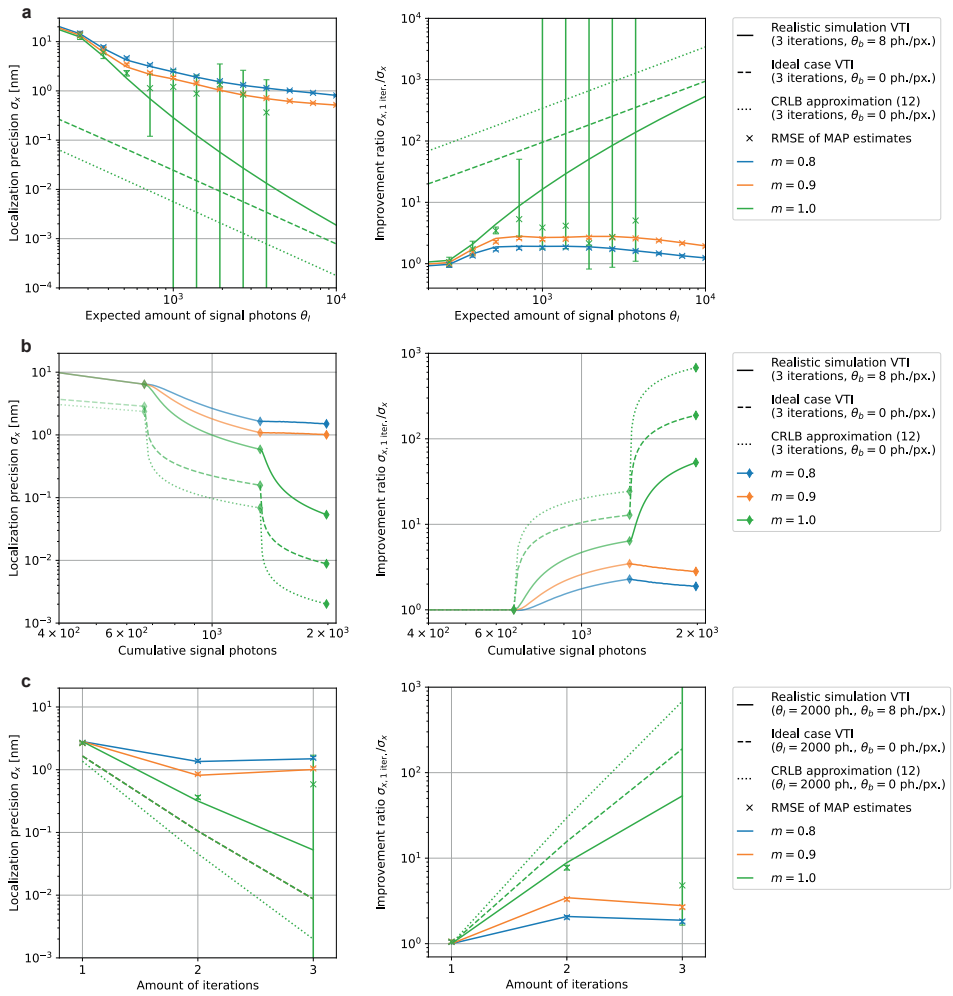

Figure 4.S6: Simulated localization precision in the x-direction as a function of (*a*) the expected signal photon count, (*b*) the expected cumulative signal photon count, and (*c*) the iteration count, for different modulation contrasts and assuming a constant signal photon count per iteration. The results are compared with the theoretical limit of Eq. (4.8) and the precision approximation of Eq. (4.9), assuming perfect modulation. In (*b*) and (*c*), the expected signal photon count θ_I was set to 2000 photons. In (*b*), diamond markers indicate a transition between iterations.

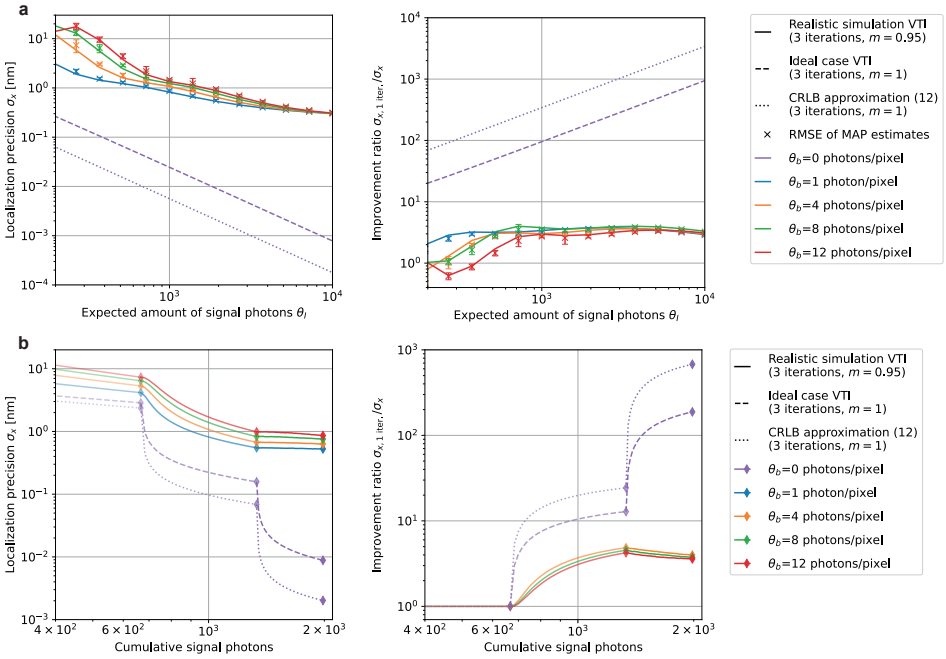

Figure 4.S7: Simulated localization precision in the x-direction as a function of (*a*) the expected signal photon count, and (*b*) the expected cumulative signal photon count, for different expected background counts and assuming a constant signal photon count per iteration. The results are compared with the theoretical limit of Eq. (4.8) and the precision approximation of Eq. (4.9), assuming perfect modulation. In (*b*), the expected signal photon count θ_I was set to 2000 photons and diamond markers indicate a transition between iterations.

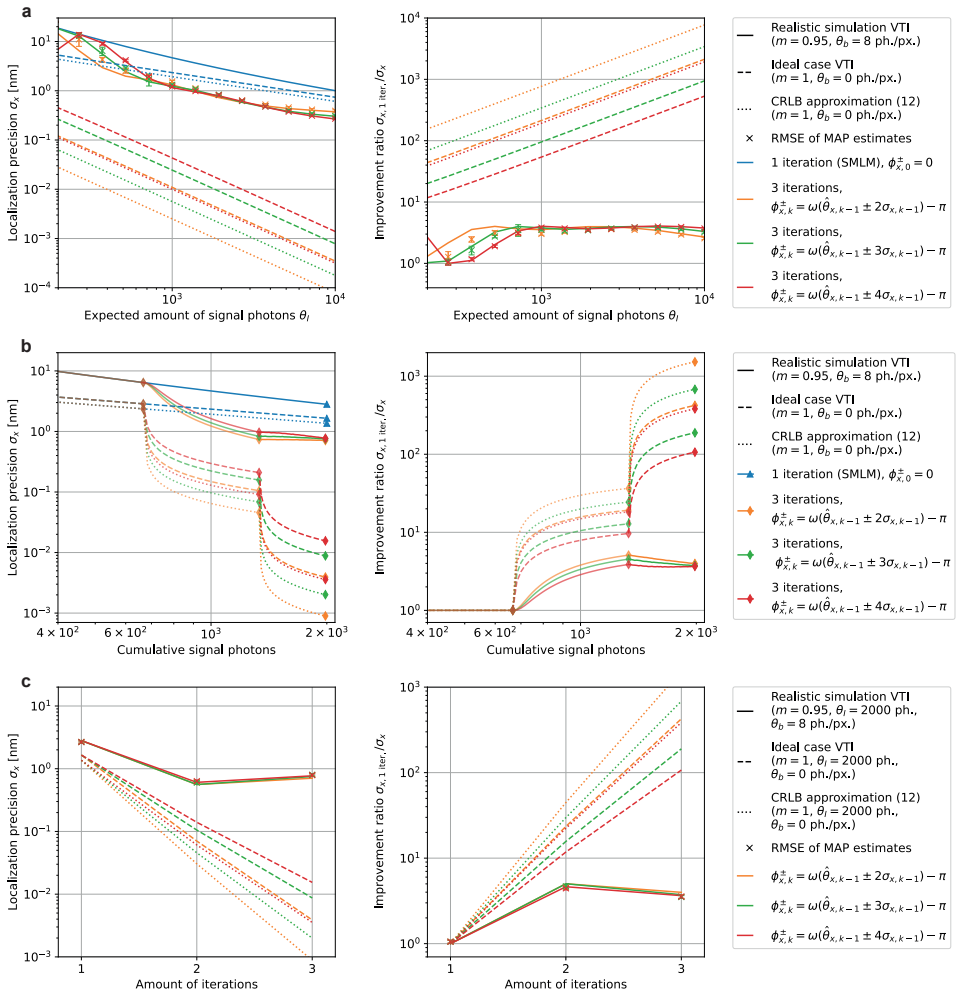

Figure 4.S8: Simulated localization precision in the x-direction as a function of (*a*) the expected signal photon count, (*b*) the expected cumulative signal photon count, and (*c*) the iteration count, for different pattern positioning strategies and assuming a constant signal photon count per iteration. The results are compared with the theoretical limit of Eq. (4.8) and the precision approximation of Eq. (4.9), assuming perfect modulation. In (*b*) and (*c*), the expected signal photon count θ_I was set to 2000 photons. In (*b*), diamond markers indicate a transition between iterations.

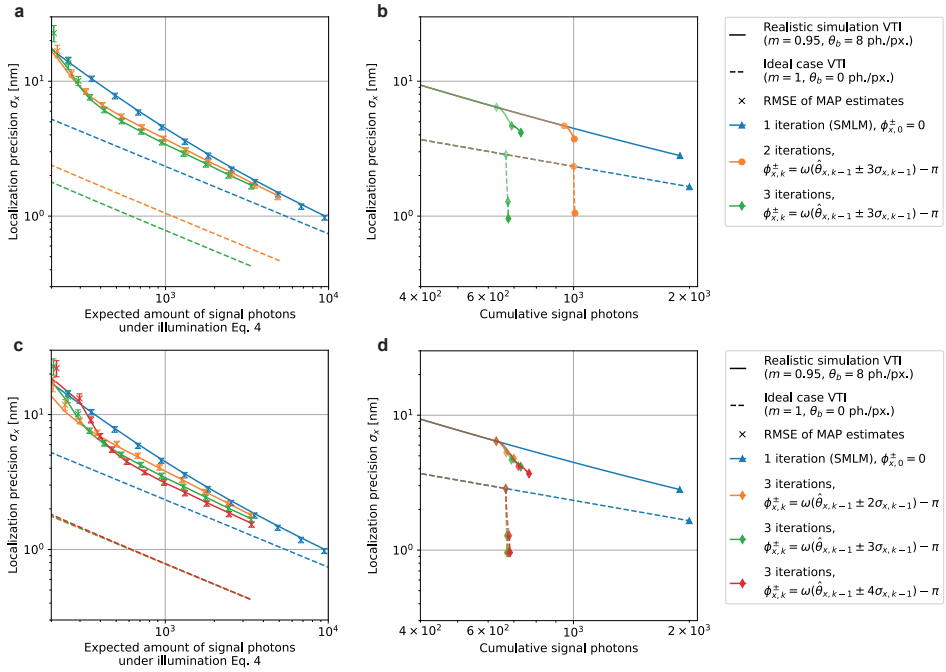

Figure 4.S9: Simulated localization precision in x direction, for different total iteration counts and pattern positioning strategies and assuming a constant imaging time and illumination intensity per iteration. The results are compared with the theoretical limit of Eq. (4.8), assuming perfect modulation. In (*b*) and (*d*), the expected signal photon budget θ_I was set to 2000 photons and markers indicate a transition between iterations. (*a*) Simulated localization precision in the x-direction as a function of the expected signal photon count under the illumination strategy of Eq. (4.5), when 1, 2 or 3 iterations are used. (*b*) Simulated localization precision in the x-direction as a function of the cumulative signal photon count, when 1, 2 or 3 iterations are used. (*c*) Simulated localization precision in the x-direction as a function of the expected signal photon count under the illumination strategy of Eq. (4.5), for different pattern positioning strategies. (*d*) Simulated localization precision in the x-direction as a function of the cumulative signal photon count, for different pattern positioning strategies.

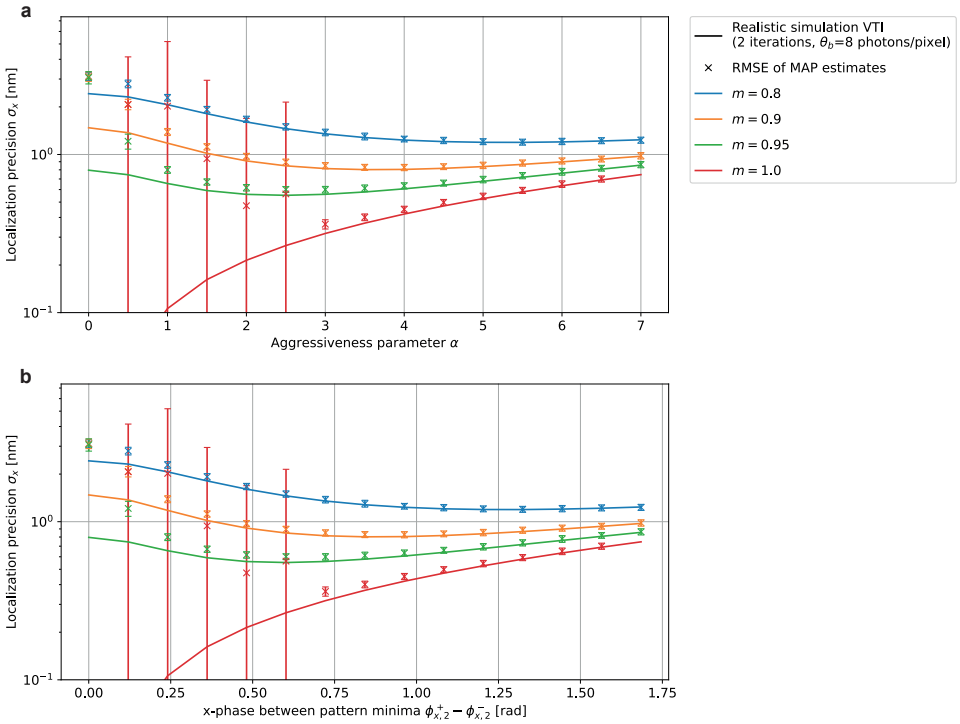

Figure 4.S10: Simulated localization precision in the x-direction as a function of (*a*) the aggressiveness parameter α, and (*b*) the distance between the pattern minima using the aggressiveness parameters α shown in (*a*), for different modulation contrasts and assuming a constant signal photon count per iteration. The expected signal photon count θ_I was set to 2000 photons.

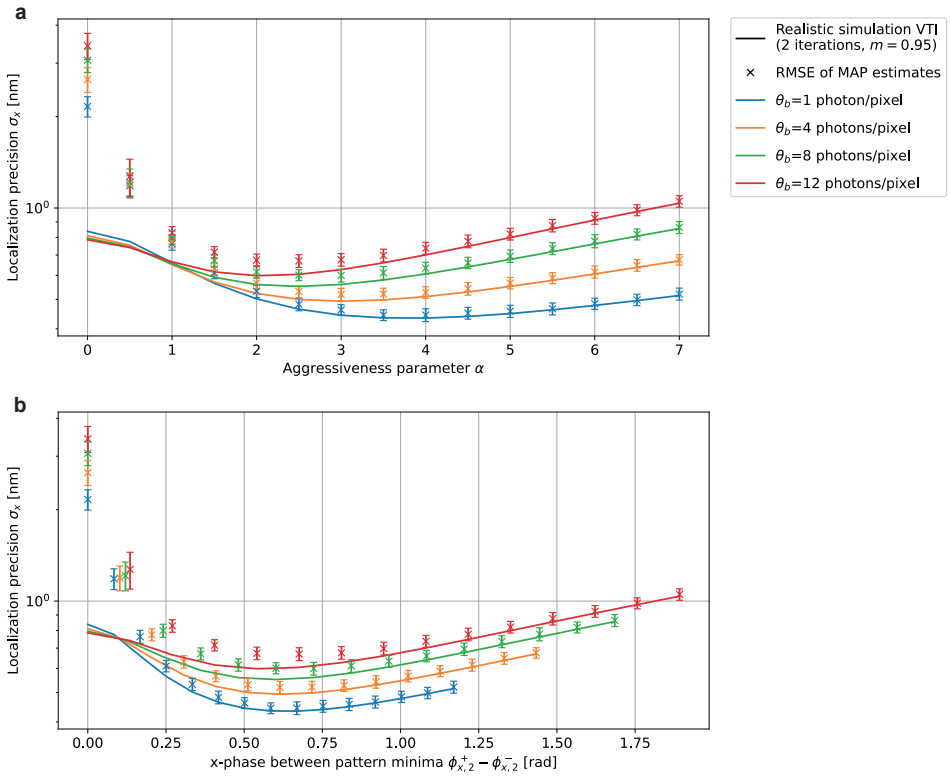

Figure 4.S11: Simulated localization precision in the x-direction as a function of (*a*) the aggressiveness parameter α, and (*b*) the distance between the pattern minima using the aggressiveness parameters α shown in (*a*), for different expected background counts and assuming a constant signal photon count per iteration. The expected signal photon count θ_I was set to 2000 photons.

Table 4.S1: Model parameters used in the localization precision simulations for sinusoidal illumination with a Gaussian point spread function.

Quantity	Symbol	Value
Wavelength of excitation light	λ_{ex}	687 nm
Wavelength of emission light	λ_{em}	680 nm
Emitter x-position (before randomizing subpixel position)	θ_x	0 nm
Emitter y-position (before randomizing subpixel position)	θ_y	0 nm
Expected background count per pattern	θ_b	8 photons/pixel
Pixel size (x-direction)	Δx	65 nm
Pixel size (y-direction)	Δy	65 nm
Amount of pixels in the x-direction	n_x	11 pixels
Amount of pixels in y-direction	n_y	11 pixels
Numerical aperture	NA	1.41
Standard deviation of PSF in x- and y-directions	σ_{PSF}	121 nm
Pattern frequency	ω	$25.8{\cdot}10^6$ rad/m
Modulation contrast	m	0.95

References

[1] J. Cnossen, T. Hinsdale, R. Ø. Thorsen, M. Siemons, F. Schueder, R. Jungmann, C. S. Smith, B. Rieger, and S. Stallinga. "Localization microscopy at doubled precision with patterned illumination". In: *Nature Methods* 17.1 (2019), pp. 59–63.

[2] C. S. Smith, N. Joseph, B. Rieger, and K. A. Lidke. "Fast, single-molecule localization that achieves theoretically minimum uncertainty". In: *Nature Methods* 7.5 (2010), pp. 373–375.

[3] H. L. Van Trees. *Detection, Estimation and Modulation Theory: Part 1*. Detection, Estimation, and Modulation Theory. Set (Volumes: I,II, III,IV). Nashville, TN: John Wiley & Sons, 2001.

[4] R. D. Gill and B. Y. Levit. "Applications of the van Trees Inequality: A Bayesian Cramér-Rao Bound". In: *Bernoulli* 1.1/2 (1995), p. 59.

[5] C. Fritsche, E. Özkan, L. Svensson, and F. Gustafsson. "A fresh look at Bayesian Cramér-Rao bounds for discrete-time nonlinear filtering". In: *17th International Conference on Information Fusion (FUSION)*. 2014, pp. 1–8.

[6] S. Bay, C. Herzet, J.-M. Brossier, J.-P. Barbot, and B. Geller. "Analytic and Asymptotic Analysis of Bayesian Cramér–Rao Bound for Dynamical Phase Offset Estimation". In: *IEEE Transactions on Signal Processing* 56.1 (2008), pp. 61–70.

[7] C. Robert and G. Casella. *Monte Carlo Statistical Methods*. 2nd ed. Springer Texts in Statistics. New York, NY: Springer, 2005.

[8] J. M. Hammersley and D. C. Handscomb. *Monte Carlo Methods*. Monographs on Statistics & Applied Probability. London, England: Chapman and Hall, 1964.

5

Conclusion and Outlook

Howl said, "I think we ought to live happily ever after," and she thought he meant it. Sophie knew that living happily ever after with Howl would be a good deal more eventful than any story made it sound, though she was determined to try.

Diana Wynne Jones, *Howl's Moving Castle*

5.1. Conclusion

Fluorescence microscopes are an important tool to visualize biology at the nanoscale, but they are limited by diffraction, which limits their resolution to approximately 200 nm. SMLM successfully circumvents the diffraction limit, by sequentially activating and subsequently localizing isolated emitters. SMLM reaches a resolution of approximately 20 nm, which makes it a major development in making the invisible visible. Through modern methods such as RESI or meSMLM, a localization precision in the order of magnitude of nanometres to Ångströms can now be attained.

The price we pay for this improvement is that images are no longer directly observable, but consist of estimated emitter positions. While super-resolution methods allow us to access the nanoscale, their findings are accompanied by the statistical uncertainty about whether the molecule positions that we retrieve correspond to the true underlying positions of emitters that are truly present in the sample. A fundamental objective of super-resolution microscopy is thus to give certainty about the localization uncertainty with which the position of a single molecule can be determined.

To make the uncertain certain, the CRLB is often used in SMLM literature. The CRLB represents the theoretical minimum uncertainty with which unbiased estimators can localize emitters. This makes it a reliable predictor to quantify the best possible localization precision in SMLM, and it can be used to design and optimize new microscopes. This suggests that the CRLB successfully brings certainty to the localization uncertainty of state-of-the-art meSMLM.

However, the CRLB leads to narrowly applicable, improperly represented or mathematically incorrect characterizations of the localization precision of meSMLM. Designing and optimizing meSMLM through the CRLB requires method-specific image formation models, which are not generally available. Furthermore, as the CRLB only bounds the localization variance, it misrepresents the localization uncertainty when the estimation error has a non-Gaussian distribution. The CRLB is not applicable at all when prior information is available, such as in iterative meSMLM, as it only applies to unbiased estimators. In this dissertation, we addressed these issues by developing new statistical models and methods for meSMLM, thereby making it possible to quantify the localization uncertainty of existing and future meSMLM methods with awareness of the full estimator distribution.

In Chapter 2, we derived a new and generalizable image formation model that integrates meSMLM in existing ISM setups that use a spinning disk in the illumination- and emission paths, leading to the theoretical design of a new meSMLM method called SpinFlux [1]. In the SpinFlux analysis, emitters are localized in the recordings from a sequence of individual pattern acquisitions, taking knowledge about the pattern into account. The precision improvement of SpinFlux is derived from retrieving the position of an emitter relative to individual illumination patterns, which adds to existing PSF information from SMLM.

Using the image formation model, we have derived and evaluated the theoretical minimum uncertainty of SpinFlux, by applying the CRLB to various illumination pattern configurations. Using Gaussian illumination patterns, SpinFlux reaches a twofold precision improvement in the x- and y-directions compared to SMLM, locally around the

emitter position. We also theorized the inclusion of a phase mask in the illumination and emission paths, with which illumination patterns with arbitrary diffraction-limited intensity profiles can be created. On the premise of that, we evaluated the localization precision of SpinFlux with donut-shaped illumination, and we found that this increases the maximum improvement over SMLM to a factor 3.5.

Based on these results, we additionally compared SpinFlux with an alternative theoretical approach, in which isolated emitters are localized in ISM reconstructions instead. We theoretically approximated that this approach results in an average global improvement of 1.48 over SMLM, or 2.10 with Fourier reweighting. In a recent publication, these approximations have been experimentally confirmed, showing a doubling of the localization precision [2]. We conclude that direct localization on ISM reconstructions is the most straightforward implementation and results in the largest global average improvement of the localization precision. On the other hand, SpinFlux shines when the excitation intensity is modulated to incorporate the maximum amount of information, as is the case when using donut-shaped patterns. The versatility of the image formation model makes SpinFlux analysis on arbitrary illumination patterns straightforward. This makes SpinFlux the method of choice for local refinements of the localization precision.

In Chapter 3, we analysed three-dimensional multiple emitter imaging, thereby discovering that high-density astigmatic imaging suffers from ambiguous solutions to the localization problem [3]. To show this, we created a Bayesian three-dimensional localization method called 3D RJMCMC. 3D RJMCMC is able to concurrently identify the amount of emitters in a ROI, as well as their positions. Yet rather than point estimates, 3D RJMCMC reconstructs the posterior density of emitter positions. For astigmatic and biplane imaging with an in-focus PSF standard deviation σ_{PSF}, 3D RJMCMC is capable of separating emitters up to a distance of respectively 1.0 σ_{PSF} and 0.75 σ_{PSF}, localizing emitters in three dimensions where traditional SMLM methods would fail.

The main use for the 3D RJMCMC algorithm is to analyse the estimator distribution for three-dimensional multiple emitter imaging. This is illustrated by our main finding that astigmatic multiple emitter imaging results in a multimodal posterior distribution when two emitters are separated by less than 1.0 σ_{PSF}. As astigmatic imaging is a well-known technique for three-dimensional imaging, it should be used with caution in multiple emitter localization.

With our analysis, we show the importance of including the appropriate uncertainty measures in localization algorithms. 3D RJMCMC reveals the full posterior distribution, which makes it possible to detect cases where the localization uncertainty for individual emitters is not accurately represented by Gaussian uncertainty ellipses. Traditional MLE point estimates would have resulted in overconfident position estimates, and the CRLB would have mischaracterised the localization uncertainty through solely the variance. Therefore, posterior density reconstruction is the tool of choice to identify potential PSF degeneracy problems in dense three-dimensional localization.

In Chapter 4, we analysed the localization precision of iterative meSMLM methods, which are able to locally improve the localization precision around an emitter position by using prior information derived from measurements in earlier iterations [4–6].

The CRLB, which requires estimators to be unbiased, cannot incorporate prior information and is thus not applicable to bound the precision of iterative meSMLM. However, the Bayesian VTI circumvents this mathematical limitation, and is therefore particularly suited to analyse iterative meSMLM.

We considered an iterative meSMLM method that uses standing-wave illumination patterns over the course of multiple iterations. We formulated an image formation model for this method, which includes the effects of imperfect pattern modulation and background fluorescence. Subsequently we used the VTI to analytically approximate lower bounds on the maximum localization precision. Using the analytical approximation, we have shown that for perfect modulation, it is optimal to distribute the signal photon budget equally over the number of iterations from iteration 2 onwards.

Additionally, we used Monte Carlo approximations of the VTI to determine the maximum precision of iterative meSMLM when subject to imperfect modulation of the illumination intensity pattern, as well as non-zero background fluorescence. We compared our findings to the scaling laws of MINFLUX (see Eqs. (1.12) and (1.13)), which respectively state that the precision is maximized when patterns are separated by the smallest possible distance, and that the precision increases exponentially as a function of the iteration count.

We showed that the smallest pattern separation distance does not lead to the maximum precision in a wide range of experimental conditions, which nuances Eq. (1.12) to only apply for perfect modulation and zero background. The optimal step size that maximizes the precision depends on the modulation contrast and signal-to-background ratio.

Secondly, we found that the exponential localization improvement as a function of the iteration count cannot be achieved in most experiments. This nuances Eq. (1.13) to only apply for perfect modulation and zero background, as the exponential scaling breaks down for slight imperfections in the modulation contrast. At 95% modulation and eight background photons per pixel, iterative meSMLM reaches at most a fivefold improvement over SMLM by using two iterations.

These findings indicate that established precision limits in MINFLUX and iterative MINFLUX appear to be more nuanced when viewed through mathematical methods specialized for the application. By deriving an image formation model containing both modulation- and background imperfections and by analysing iterative meSMLM with a Bayesian lower bound, we now know that the optimal selection of pattern positions, the number of iterations, and the time spent per iteration in iterative meSMLM depends on many factors, such as the signal photon budget, imperfections in the illumination system, and the expected background count. This makes the VTI the tool of choice when prior information is available for localization, and in particular for the optimal design and control of iterative meSMLM.

Together, the different findings in this dissertation convey the same message. In an everlasting pursuit to resolve the smallest possible structures, localization microscopy faces a fundamental question, namely with what uncertainty the position of a single molecule can be determined. In order to reflect the statistical uncertainty of the localization process, emitter position estimates need to be accompanied by a measure of their

estimation uncertainty. Defaulting to existing image formation models and the CRLB leads to narrowly applicable, overconfidently represented or mathematically unjustified characterizations of the localization uncertainty. Instead, image formation models and uncertainty quantification should be tailored to the application, letting the particularities of the application determine the choice of appropriate mathematical tools. As we have shown here, this treatment leads to new methods to improve the localization precision, and it advances our fundamental understanding of localization uncertainty in super-resolution microscopy, making it a necessary step to future-proof its trustworthiness for biological research and medicine development.

5.2. Recommendations

Based on the findings of this dissertation, we see various ways to further improve the work that transcend the scope of the recommendations that are already part of the individual chapters. Therefore we use this section to recommend future developments pertaining to the collection of works in this dissertation.

Perhaps self-evident, but nonetheless tremendously important, we first and foremost recommend the experimental realization of the models and methods developed in this dissertation. As it stands, the contributions in this dissertation remain theoretical. The advantage of this theoretical approach is that it gives the ability to thoroughly investigate and optimize models and methods, as computer simulations do not suffer from the material-, time- and ground truth-constraints of real experimental setups.

However, this disconnect from real life is also the drawback of a computer simulation. Real experiments are subject to one consistent set of physical laws, while computer simulations are subject to various sets of potentially contradictory assumptions and approximations made by researchers. Even though the choices made by researchers are usually explainable, they are not necessarily true.

For example in our work, the Gaussian emission PSF is used as a model as it simplifies analytical calculations, but we know it to be inaccurate in the case of aberrations [7, 8]. Alternative and more accurate models exist for these cases, such as the vectorial PSF [9] or data-driven models such as cubic splines [10, 11]. As a second example, we chose to model pinholes via a multiplicative window in Chapter 2 based on existing literature [12–14], thereby omitting a contradicting class of models where the pinhole is modelled as a convolution with the emission point-spread function [15, 16]. While the validity of our choice is supported by existing literature, only an experiment can show if it is also correct.

While scientists can come up with different models through rigorous derivations, thorough explanations and the best intentions, the physics of reality are unmerciful and will ultimately decide which results are true and which are false. For this reason, we strongly recommend and look forward to the experimental realization of SpinFlux, three-dimensional multiple emitter fitting with 3D RJMCMC and iterative meSMLM using the VTI.

Secondly, we recommend a global analysis of meSMLM, as opposed to a local analysis focused at isolated emitters. Most of the meSMLM research in this dissertation

presents results for isolated single-emitters, which is in line with existing theoretical meSMLM research [16–19]. On one hand, this choice for a local analysis is suitable to the research, as we look to quantify the maximum possible precision. In meSMLM, the precision improves locally around the targeted emitter position, so a local analysis is necessary to determine the maximum possible localization precision. Designing meSMLM for maximum precision through a local analysis therefore results in impressive precision improvements over SMLM, where nanometre- or Ångström-resolution becomes achievable.

On the other hand, this design approach equivalently means that the precision is suboptimal on positions different from the targeted emitter position. As the precision of meSMLM is inhomogeneous as a function of space, local optimization of the precision comes at the cost of global precision losses. As biological samples do not consist of isolated emitters, the impressive local precision improvements have limited relevance to practitioners. To address this problem, we recommend to analyse meSMLM from a global perspective, taking a field of view with thousands of emitters into account rather than a single ROI with a single emitter. Such an approach could focus on distributing the precision of meSMLM over the spatial frequencies present in the sample, rather than focusing on maximizing the precision on one position only. While this means that we need to let go of the fundamental, everlasting chase for increasingly better resolution in SMLM, a global optimization will result in meSMLM methods that have increased practical relevance.

The main goal of this dissertation was to improve the quantification and understanding of localization precision in SMLM and meSMLM by developing new statistical models and tools. While this goal was accomplished, our results give rise to new questions regarding the optimality of experimental design. Therefore we recommend to revisit the designs of the various microscopy techniques discussed in this work, aimed at minimizing the localization error using the statistical methods developed in this dissertation. We will propose suggestions for design improvements for each individual technique.

For SpinFlux we evaluated a large variety of illumination patterns and configurations, but we limited our analysis to a maximum of four illumination patterns. By stroboscopically illuminating the sample through a spinning disk, it is in principle possible to project hundreds of closely spaced illumination patterns onto emitters. This would bring it closer to approaches such as RASTMIN [20–23], which are able to extend the nanometre-level precision of MINFLUX to a larger field of view. We therefore recommend an analysis of SpinFlux when large amounts of illumination patterns are used, to be compared with RASTMIN.

In three-dimensional multiple emitter localization, we used 3D RJMCMC to identify cases where estimator distributions become multimodal, leading to ambiguous solutions to the localization problem. However, such cases can be mitigated by constraining the estimation. For the particular example of astigmatic imaging, we have seen that identified candidate emitter pairs are perpendicular to each other, belonging to different axial coordinates. By constraining the imaging depth to exclude one candidate pair, this multimodality can be fully avoided. If constraining the imaging depth is not a desirable option, an alternative would be to analyse to occurrence of multimodality when combin-

ing three-dimensional multiple emitter imaging with meSMLM. By using patterns with structure in the axial direction, as done in ZIMFLUX [24], ModLoc [25–27] and ROSE-Z [28], the ambiguity that occurs due to the PSF shape can be resolved by using the depth information generated by modulated excitation patterns. ZIMFLUX specifically already combines axial structure with astigmatic imaging, making it the most straightforward implementation to perform a multimodality analysis on.

For iterative meSMLM, we reached the important conclusions that the precision is not generally maximized by choosing the smallest possible pattern distance, nor by increasing the amount of iterations [6]. Instead, we discovered that the optimal pattern distance and iteration counts are both functions of the modulation contrast and signal-to-background ratio. This is a significant development for our fundamental understanding of precision in (iterative) meSMLM, as we now know which experimental designs do not optimize the precision. However, it is not a particularly actionable result in practice, as we did not answer which experimental designs do optimize the precision, given estimates of the modulation contrast and signal-to-background ratio of a microscope. We suggest to determine this through minimizing the VTI for iterative meSMLM by choosing the pattern separation distance, combined with an exhaustive search over iteration counts. As our simulations suggest that the localization precision is a convex function of the pattern separation distance (see Fig. 4.2*e*), such an optimization could be solved with global optimality guarantees.

These optimizations of meSMLM pave the way for optimal single-particle tracking with MINFLUX or other meSMLM-methods. Single-particle tracking aims to follow and localize a single emitter over time, thereby forming a track of how this molecule has moved [29]. Due to its ability to locally improve the precision in the neighbourhood of individual molecules, meSMLM is particularly suited for this task [30, 31] and has also been successfully used for this [17, 18]. Optimizing meSMLM for tracking maximally increases the information each signal photon carries about the position of the tracked molecule. This effectively means that the same localization precision can be retained with a reduced signal photon budget, thereby reducing the impact of photobleaching and improving the temporal resolution.

5.3. Future prospects

Based on general insights, literature and discussions throughout the doctoral studies, we envision recommendations that do not directly relate to the work discussed in this dissertation, but instead apply to the field of quantitative nanoscopy at large. We therefore use this section to speculate about possible future research directions pertaining to the research field. We distinguish two kinds of recommendations. Subsection 5.3.1 will contain research forecasts that are expected to be developed in the near future, where we take 2030 as a reference year. Some of the more grandiose expectations that we foresee to have a longer development time are discussed in Subsection 5.3.2.

5.3.1. Expected developments between 2026 and 2030

Starting with a fundamental research direction, we expect to see a concrete definition of spatial resolution within the coming five years, as well as target samples on which this spatial resolution can be evaluated. Since the invention of super-resolution microscopy, the definition of the spatial image resolution has become increasingly bloated. Already in two dimensions for a stationary target, the lateral resolution is impacted by aspects such as the spatial frequencies present in the sample, the labelling density, the diffraction limit of the system, the measurement noise, the detection precision and recall, the localization error and visual artifacts [32–36]. While various measures exist to quantify individual aspects contributing to the spatial resolution, the lack of an overarching method to quantify resolution makes it difficult to compare the performance of individual methods.

Initiatives such as the SMLM Challenge [37, 38] have been used to compare the performance of specifically localization algorithms, by introducing sets of benchmark measurements as well as a performance score that weighs various aspects contributing to image resolution. In spirit of the SMLM Challenge, we expect the introduction and adoption of both a concrete definition of the spatial resolution, as well as standardized benchmark samples to be used for the end-to-end quantification of the performance of microscopy methods.

A second development we expect in the near future is the merge of meSMLM with PSF engineering. While meSMLM uses illumination patterns to increase the information content per signal photon, PSF engineering encodes information in the shape of a PSF instead. For example, a PSF can be designed to encode axial information, such as in astigmatic imaging [39] or with the double-helix [40] or tetrapod PSFs [41, 42], or it can be designed to encode both the three-dimensional position as well as the emission wavelength [43].

While meSMLM and PSF engineering both aim to achieve the same goal of increasing the amount of information per signal photon, they have historically been treated mostly separately. This seems to resemble the parallel development of illumination-based and emission-based super-resolution methods, of which we have seen that a synergistic combination led to the development of meSMLM. As shown in this dissertation, a combination of meSMLM and PSF engineering can only serve to further increase the amount of information per signal photon, thereby making it theoretically possible to extract additional information in the localization step. This is emphasized by, for example, ZIMFLUX [24], where a combination of modulated excitation and astigmatic imaging results in a 1.5-fold improvement of the axial localization precision over using solely astigmatic imaging. We therefore expect an increase in methods that combine meSMLM with PSF engineering within the coming years.

In line with the previous suggestion, we expect a diversification within the field of meSMLM to focus on other tasks than localization. For localization, meSMLM has been great news, as MINFLUX and its follow-up methods breached the barrier to nanometre precision. As the emission intensity carries information about where emitters are located relative to the illumination pattern, photobleaching can be postponed by illumi-

nating with a low-intensity part of the pattern. This means that for localization specifically, it is beneficial to illuminate with low-intensity light.

Yet for other parts of the localization microscopy analysis, such as detection or drift correction, the reduced emission intensity may decrease the performance. Traditional algorithms for detection [44] or drift correction [45–47] often rely on the presence of signal. This becomes a problem when using meSMLM, as optimizing the localization precision results in low- or zero-intensity emissions. For this reason, maximizing the localization precision leads to a decreasing performance in other analysis tasks [48]. We expect that this can be avoided by tailoring detection and drift correction algorithms to take meSMLM-specific models for patterned illumination into account, as was done for localization tasks in this dissertation.

Lastly, we expect the field of quantitative nanoscopy to increasingly focus on improving other aspects than spatial resolution. Until RESI [49], MINFLUX [17, 18] and MINSTED [50, 51], the pursuit of improving the localization precision has been a fundamental objective for the field of SMLM. Now that the nanometre- and Ångström-scale have been reached, we have run into a new limit on the accuracy with which we can image molecules in fluorescence microscopy. As fluorescence microscopy images emitters that are attached to the molecule of interest, the limiting factor to the localization accuracy is now the size of the link between the target molecule and the fluorophore [18].

For this reason, we expect the focus of future information-increasing methods to be on other aspects of SMLM than lateral or axial localization precision. For example, we expect an increased interest in methods that improve the temporal resolution. One way to achieve this is to increase the labelling density at which molecules can still be individually localized. Deep learning has already made a significant improvement to the resolvability of densely-labelled samples in the recent years. With methods such as DeepSTORM [52, 53] and DECODE [54], approximately a tenfold higher labelling density can be used while retaining the same localization error as MLE-based SMLM analysis methods. A recent preprint shows that this can be further enhanced through meSMLM [55]. In the coming years, this research trend will continue, thereby increasing the acquisition speed of SMLM and improving the spatial and temporal resolution.

Another development aimed at improving the temporal resolution regards the detector. Historically, the electron multiplying charge-coupled device (EMCCD) and the scientific complementary metal-oxide-semiconductor (sCMOS) camera are commonly used array detectors for recording measurements. Recently, single photon avalanche diode (SPAD) arrays have been getting increased attention in SMLM [56–59]. SPAD arrays are sensitive to individual photons and can image with pico-second temporal resolutions. In 2021, we have already shown ourselves that measurements from a SPAD array can be modelled with a binomially distributed image formation model, which is nearly indistinguishable from the Poisson image formation model at imaging intensities typical for SMLM [58]. This makes the SPAD array an ideal detector for localization- or tracking applications where the temporal resolution matters and we therefore expect an increase in interest towards SPAD arrays in the coming years.

5.3.2. Expected developments after 2030

Looking at the next decade, we expect that deep learning has established itself as a dominant factor in SMLM analysis. While the performance of deep learning models for quantitative analysis is showing promising results, the black-box nature of deep learned models currently limits the interpretation of the prediction uncertainty, meaning that there is a risk of overconfident predictions if the test data contains features that were not included in training [60]. This sharply contrasts the fundamental objective of SMLM that is central to this dissertation, namely to determine the uncertainty with which the positions of single-emitters can be estimated. With the expected advance of deep learning, we therefore also expect an increase in scientific interest around the uncertainty with which deep learning models in SMLM perform their analysis.

To solve this uncertainty problem, machine learning literature is currently showing promising developments in the form of Bayesian deep learning [61, 62]. In Bayesian statistics, the prediction uncertainty can be explained as a combination of aleatoric and epistemic uncertainty. The aleatoric uncertainty describes the contribution to the prediction uncertainty that is caused by the inherent stochasticity of the underlying data used for the prediction. On the other hand, the epistemic uncertainty describes the contribution to the prediction uncertainty that is caused by uncertainty about the model itself. In other words, the epistemic uncertainty can be seen as the distribution of predictions by all possible models of identical structure that have the same performance on the training data. The objective of Bayesian deep learning is to quantify the epistemic uncertainty of the predictions made with a neural network, thereby creating a measure of how sensitive a prediction is to features that were not included in training.

Bayesian deep learning currently shows two main classes of quantification methods for the epistemic uncertainty. The first class of methods assumes a Gaussian distribution of the epistemic uncertainty and tries to quantify the variance of this distribution by enforcing prediction variety in existing neural networks. For example, the Monte Carlo dropout method randomly switches off network nodes during prediction to ensure prediction variety [63], whereas deep ensembling trains an ensemble of networks with identical architecture and randomized training settings to generate a collection of predictions [64]. These methods are popular due to them being applicable to existing neural networks, but they do not formally explain the epistemic uncertainty from a statistical point of view, nor are they able to represent the full distribution of the epistemic uncertainty. Nevertheless, these methods are currently finding their way into super-resolution microscopy, for example by using Monte Carlo Dropout to enhance neural network-based SIM reconstruction [65].

On the other hand, methods in the second class try to capture the full epistemic uncertainty distribution through approximate Bayesian inference methods, such as variational inference [66] or stochastic gradient Hamiltonian Monte Carlo [67, 68]. While these methods closely follow the statistical definition of epistemic uncertainty, the implementation of approximate Bayesian inference requires replacing classical backpropagation methods in deep learning with computationally more demanding inference methods. As an alternative to approximate inference, probabilistic circuits are able to efficiently perform exact Bayesian inference on a limited set of network operations [69, 70], but they currently do not support the architectural scale and diversity of mathematical

operations that neural networks can offer.

We expect that, after further developments in machine learning literature, Bayesian deep learning will become an integral part of neural network-based SMLM analysis. Having access to the prediction uncertainty associated with a network outcome will not only help in quantifying method performance, but can additionally be used to actively interact with the microscope hardware to improve the predictions. Namely, a predictor of the epistemic uncertainty can be used to identify regions of high uncertainty, thereby indicating a dissimilarity between the acquired measurements and the training data. Such a region can then be re-imaged experimentally, to reduce the uncertainty specifically in those parts of the sample where it matters.

In this line, a recent literature example used a scanning microscope to adaptively rescan patches of the sample, based on regions of that were estimated to have high uncertainty after neural network-based denoising [71]. This allows for a more efficient use of illumination light, thereby improving the imaging speed and reducing the sample damage. Combined with the increased availability of uncertainty predictors, we therefore also expect an increase in methods that actively use these predictions to locally reduce the uncertainty.

A second development we expect in the longer term is an increase in the accessibility of advanced super-resolution microscopes. In the race for ever-increasing resolution, microscopes are getting increasingly more advanced, using narrowly available, custom made and expensive components. This increase in setup complexity comes, quite literally, at a cost: openly available numbers by Abberior state that basic, commercially available confocal microscopes cost at least 100,000 US dollars, while the most advanced commercial systems for MINFLUX can cost well over 1 million US dollars [72]. Together, these factors hamper the reproducibility of results in microscopy, as well as the adoption of advanced microscopes by practitioners.

Various developments already increase the accessibility of high-resolution imaging. As we show ourselves with SpinFlux [1] or as shown in iSMLM [2], the localization precision in existing setups can be improved through alternative analysis with only minimal changes to the setup. Alternatively, we see research opportunities in cost-effective initiatives such as cellSTORM [73], which enables dSTORM imaging on a smartphone, or the miCube [74, 75], which enables SMLM through an open-source platform using commonly available parts and free software. As a parallel development, we also expect the production cost of advanced microscopes to drop throughout the coming centuries as a result of advances in manufacturing techniques, making commercial microscopes accessible to a wider variety of users.

Next, we expect the development of new modalities that do not just observe, but also interact with the sample. Rather than passively observing the sample, light can also be used to actively interact with the sample through optogenetics [76, 77]. Optogenetics makes it possible do directly influence biological processes through automated control, rather than having to control the imaging hardware [78, 79]. For example, a recent preprint shows the possibility of using light to control cell migration, thereby making it possible to force a cell to follow a predefined reference trajectory [80]. Optogenetic con-

trol comes with various advantages in medicine development, such as increasing the cost-effectiveness of drug discovery, or making it possible to better target the application area of gene therapy and vaccines [81]. For this reason, we expect an increase in scientific interest in optogenetic control during the coming century.

As a last prospect, we expect to see microscopy going back to its biological roots. In the time of Van Leeuwenhoek, the fates of microscopy and biology intertwined and this bond has been consistent throughout the development of newer and more advanced microscopes. For this reason, the experimental performance of super-resolution microscopy methods is typically still demonstrated on biological structures, such as microtubules or the nuclear pore complex [82]. Nevertheless, the biological application of super-resolution fluorescence microscopy remains limited to mostly well-characterized, static biological structures. We have yet to see super-resolution fluorescence microscopy enable breakthroughs in biology and medicine that are of a similar magnitude as the discoveries seen in (cryogenic) electron microscopy, which provided the first images of cell sections [83, 84], ribosomes [85] and the hepatitis B virus [86].

To a major degree, we attribute the lack of such breakthroughs to the highly specialized improvements gained through individual super-resolution modalities, leading to an absence of an end-to-end solution for biomedical application. Specifically, the increasing specialization of microscopy methods towards individual, narrowly focused goals creates a gap between what physicists, statisticians and computer scientists in microscopy do, and what live-cell biological imaging demands. In this dissertation, we have discussed the chase for improved lateral and axial localization precision at length, but this is only one of many factors that determine the applicability to live-cell biological imaging [30]. For example, biology is dynamic, which means super-resolution microscopes need to be able to track emitters at a high temporal resolution to capture movements. As another example, biology studies interactions between cell structures, proteins and molecules, meaning there is a demand for multicolor [87, 88] or co-localization [89, 90] approaches that can visualize and correlate these interactions. As a last example, biology consists of thick samples, which means there is value in the reduced photobleaching and background fluorescence offered by optical sectioning methods such as light-sheet microscopy [91–94], as well as adaptive optics to compensate for sample-induced aberrations [94–97].

To develop a microscope that is able to super-resolve live-cell biology, we think that a combination of multiple individual super-resolution modalities is needed. Yet this cannot be achieved by trying to fuse existing experimental setups, due to fundamental limitations of the individual methods. To motivate this, we consider an example where we aim to improve the spatio-temporal resolution through somehow experimentally combining SMLM and SIM, as we have seen this combination in meSMLM. From an experimental merge between SMLM and SIM, we would aim to harvest the spatial resolution of SMLM, and combine it with the temporal resolution of SIM. Namely, SMLM can attain a localization precision of approximately 20 nm, but the acquisition speed of SMLM is limited due to its reliance on sparsity in the emission signal. With exposure times between 10 to 100 ms, typical total acquisition times for SMLM can range from 2 to 30 minutes [98, 99]. On the other hand, modern SIM methods show faster acquisition rates of over 130

megapixels per second, but are limited to a spatial resolution of approximately 100 nm [100]. Yet a purely experimental merge of SMLM and SIM is not possible without picking and choosing elements of each modality as done in meSMLM, as SMLM fundamentally requires spatio-temporally separated emitters under uniform illumination, whereas SIM fundamentally requires all emitters to be visible under structured illumination patterns.

As such, we see more merit in fusing existing modalities computationally, through multi-image data fusion [101]. In computer vision, image fusion describes the task of computationally combining independently acquired images of the same underlying object, with the goal of extracting the relevant information from individual images and merging the information in one compound image. Image fusion is already commonly employed in applications areas that acquire measurements with multiple sensors. For example, it is common practice in automated driving to combine image- and depth data for object recognition [102, 103]. Recent approaches in fluorescence microscopy also show the advantages of image fusion, for instance through the fusion of ISM with super-resolution optical fluctuation imaging ISM (SOFISM, [104]). This implementation resulted in a spatial resolution comparable to that of SOFI and a signal-to-noise ratio comparable to that of ISM [105].

We therefore see computational image fusion as a promising way to combine the advantages of existing methods. Specifically, we foresee an implementation in which multiple individual modalities concurrently image a structure, after which the information from the individual sources is merged computationally after the acquisition. Yet this implementation of image fusion is not straightforward, as it relies on an advanced experimental design that allows for simultaneous imaging of the same structure with multiple imaging systems, in addition to the alignment of the individual acquisitions. We also expect that developments in fluorescent label design are needed to enable individual, independent measurements. In our previous example, a biological structure that is concurrently imaged with SMLM and SIM needs to be labelled twice with labels that have separate absorption and emission spectra, as SMLM relies on a blinking emitter while SIM does not.

In addition to the experimental development, appropriate image fusion algorithms need to be developed that can computationally combine the advantages of individual modalities. We expect that deep learning methods will be particularly useful for this task. No experimental ground truth is available for fusion, which either means that a simulation needs to be developed to obtain a simulated ground truth, or that the fusion needs to be performed blindly [106, 107]. To accomplish the latter, we see potential in unsupervised methods that learn the features present in data, which are then used to fuse images. For instance, this is possible via contrastive learning [105, 108, 109]. In contrastive learning, a model learns features present in the input data by generating augmentations and subsequently comparing two augmented images that correspond to the same object. By combining contrastive learning with fusion models, unsupervised image fusion becomes possible, as demonstrated in recent approaches that fuse infrared and visible image data [108, 110].

We expect that a complete end-to-end solution for super-resolving live-cell biology, similar to how Van Leeuwenhoek's microscope solved the magnification problem, is still far out. Nevertheless, we recommend and look forward to the development of such sys-

tems, thereby re-bridging the gap between microscopy, biological research and medicine development, and truly succeeding in making the invisible visible.

References

[1] D. Kalisvaart, S. Hung, and C. S. Smith. “Quantifying the minimum localization uncertainty of image scanning localization microscopy”. In: *Biophysical Reports* 4.1 (2024), p. 100143.

[2] N. Radmacher, O. Nevskyi, J. I. Gallea, J. C. Thiele, I. Gregor, S. O. Rizzoli, and J. Enderlein. “Doubling the resolution of fluorescence-lifetime single-molecule localization microscopy with image scanning microscopy”. In: *Nature Photonics* 18.10 (2024), pp. 1059–1066.

[3] R. van Dijk, D. Kalisvaart, J. Cnossen, and C. S. Smith. “Bayesian posterior density estimation reveals degeneracy in three-dimensional multiple emitter localization”. In: *Scientific Reports* 13.1 (2023).

[4] D. Kalisvaart, J. Cnossen, S. Hung, S. Stallinga, M. Verhaegen, and C. S. Smith. “Precision in iterative modulation enhanced single-molecule localization microscopy”. In: *Biophysical Journal* 121.12 (2022), pp. 2279–2289.

[5] A. R. Small. “Prior information improves resolution”. In: *Biophysical Journal* 121.12 (2022), pp. 2221–2222.

[6] C. Smith, D. Kalisvaart, and K. Prakash. “Unveiling the limits of precision in iterative MINFLUX”. In: *Journal of Microscopy* 296.2 (2024), pp. 129–132.

[7] B. Zhang, J. Zerubia, and J.-C. Olivo-Marin. “Gaussian approximations of fluorescence microscope point-spread function models”. In: *Applied Optics* 46.10 (2007), p. 1819.

[8] S. Stallinga and B. Rieger. “Accuracy of the Gaussian Point Spread Function model in 2D localization microscopy”. In: *Optics Express* 18.24 (2010), p. 24461.

[9] M. Siemons, C. N. Hulleman, R. Ø. Thorsen, C. S. Smith, and S. Stallinga. “High precision wavefront control in point spread function engineering for single emitter localization”. In: *Optics Express* 26.7 (2018), p. 8397.

[10] Y. Li, M. Mund, P. Hoess, J. Deschamps, U. Matti, B. Nijmeijer, V. J. Sabinina, J. Ellenberg, I. Schoen, and J. Ries. “Real-time 3D single-molecule localization using experimental point spread functions”. In: *Nature Methods* 15.5 (2018), pp. 367–369.

[11] Y. Li, W. Shi, S. Liu, I. Cavka, Y. Wu, U. Matti, D. Wu, S. Koehler, and J. Ries. “Global fitting for high-accuracy multi-channel single-molecule localization”. In: *Nature Communications* 13.1 (2022).

[12] O. Schulz, C. Pieper, M. Clever, J. Pfaff, A. Ruhlandt, R. H. Kehlenbach, F. S. Wouters, J. Großhans, G. Bunt, and J. Enderlein. “Resolution doubling in fluorescence microscopy with confocal spinning-disk image scanning microscopy”. In: *Proceedings of the National Academy of Sciences* 110.52 (2013), pp. 21000–21005.

[13] G. M. De Luca, R. M. Breedijk, R. A. Brandt, C. H. Zeelenberg, B. E. de Jong, W. Timmermans, L. N. Azar, R. A. Hoebe, S. Stallinga, and E. M. Manders. “Re-scan confocal microscopy: scanning twice for better resolution”. In: *Biomedical Optics Express* 4.11 (2013), p. 2644.

[14] J. Mertz. *Introduction to Optical Microscopy*. 2nd ed. Cambridge, England: Cambridge University Press, 2019.

[15] J. Pawley, ed. *Handbook of Biological Confocal Microscopy*. 3rd ed. New York, NY: Springer, 2006.

[16] E. Slenders and G. Vicidomini. “ISM-FLUX: MINFLUX with an array detector”. In: *Physical Review Research* 5.2 (2023).

[17] F. Balzarotti, Y. Eilers, K. C. Gwosch, A. H. Gynnå, V. Westphal, F. D. Stefani, J. Elf, and S. W. Hell. “Nanometer resolution imaging and tracking of fluorescent molecules with minimal photon fluxes”. In: *Science* 355.6325 (2017), pp. 606–612.

[18] K. C. Gwosch, J. K. Pape, F. Balzarotti, P. Hoess, J. Ellenberg, J. Ries, and S. W. Hell. “MINFLUX nanoscopy delivers 3D multicolor nanometer resolution in cells”. In: *Nature Methods* 17.2 (2020), pp. 217–224.

[19] E. Slenders, S. Patil, M. O. Held, A. Zunino, and G. Vicidomini. “Array detection enables large localization range for simple and robust MINFLUX”. In: *Light: Science & Applications* 14.1 (2025).

[20] L. A. Masullo, F. Steiner, J. Zähringer, L. F. Lopez, J. Bohlen, L. Richter, F. Cole, P. Tinnefeld, and F. D. Stefani. “Pulsed Interleaved MINFLUX”. In: *Nano Letters* 21.1 (2020), pp. 840–846.

[21] L. A. Masullo, L. F. Lopez, and F. D. Stefani. “A common framework for single-molecule localization using sequential structured illumination”. In: *Biophysical Reports* 2.1 (2022), p. 100036.

[22] L. A. Masullo, A. M. Szalai, L. F. Lopez, M. Pilo-Pais, G. P. Acuna, and F. D. Stefani. “An alternative to MINFLUX that enables nanometer resolution in a confocal microscope”. In: *Light: Science & Applications* 11.1 (2022).

[23] P. Zdańkowski, L. F. Lopez, G. P. Acuna, and F. D. Stefani. “Nanometer Resolution Imaging and Tracking of Single Fluorophores by Sequential Structured Illumination”. In: *ACS Photonics* 9.12 (2022), pp. 3777–3785.

[24] P. van Velde, B. Rieger, T. Hindsdale, J. Cnossen, D. Fan, S. Hung, D. Grunwald, and C. Smith. “ZIMFLUX: Single molecule localization microscopy with patterned illumination in 3D”. In: *Optics Express* 31.25 (2023), p. 42701.

[25] P. Jouchet, C. Cabriel, N. Bourg, M. Bardou, C. Poüs, E. Fort, and S. Lévêque-Fort. “In Depth 3D Single Molecule Localization Microscopy with Time Modulated Excitation”. In: *Biophysical Journal* 118.3 (2020), 149a.

[26] P. Jouchet, C. Cabriel, N. Bourg, M. Bardou, C. Poüs, E. Fort, and S. Lévêque-Fort. “Nanometric axial localization of single fluorescent molecules with modulated excitation”. In: *Nature Photonics* 15.4 (2021), pp. 297–304.

[27] P. Jouchet, C. Poüs, E. Fort, and S. Lévêque-Fort. “Time-modulated excitation for enhanced single-molecule localization microscopy”. In: *Philosophical Transactions of the Royal Society A: Mathematical, Physical and Engineering Sciences* 380.2220 (2022).

[28] L. Gu, Y. Li, S. Zhang, M. Zhou, Y. Xue, W. Li, T. Xu, and W. Ji. “Molecular-scale axial localization by repetitive optical selective exposure”. In: *Nature Methods* 18.4 (2021), pp. 369–373.

[29] M. K. Cheezum, W. F. Walker, and W. H. Guilford. “Quantitative Comparison of Algorithms for Tracking Single Fluorescent Particles”. In: *Biophysical Journal* 81.4 (2001), pp. 2378–2388.

[30] K. Prakash, D. Baddeley, C. Eggeling, R. Fiolka, R. Heintzmann, S. Manley, A. Radenovic, H. Shroff, C. Smith, and L. Schermelleh. “Resolution in super-resolution microscopy – facts, artifacts, technological advancements and biological applications”. In: *Journal of Cell Science* 138.10 (2025).

[31] T. Deguchi and J. Ries. “Simple and robust 3D MINFLUX excitation with a variable phase plate”. In: *Light: Science & Applications* 13.1 (2024).

[32] A. J. den Dekker and A. van den Bos. “Resolution: a survey”. In: *Journal of the Optical Society of America A* 14.3 (1997), p. 547.

[33] R. P. J. Nieuwenhuizen, K. A. Lidke, M. Bates, D. L. Puig, D. Grünwald, S. Stallinga, and B. Rieger. “Measuring image resolution in optical nanoscopy”. In: *Nature Methods* 10.6 (2013), pp. 557–562.

[34] B. Rieger, I. Droste, F. Gerritsma, T. ten Brink, and S. Stallinga. “Single image Fourier ring correlation”. In: *Optics Express* 32.12 (2024), p. 21767.

[35] J. Demmerle, E. Wegel, L. Schermelleh, and I. M. Dobbie. “Assessing resolution in super-resolution imaging”. In: *Methods* 88 (2015), pp. 3–10.

[36] Y. Li and F. Huang. “A statistical resolution measure of fluorescence microscopy with finite photons”. In: *Nature Communications* 15.1 (2024).

[37] D. Sage, H. Kirshner, T. Pengo, N. Stuurman, J. Min, S. Manley, and M. Unser. “Quantitative evaluation of software packages for single-molecule localization microscopy”. In: *Nature Methods* 12.8 (2015), pp. 717–724.

[38] D. Sage, T. Pham, H. Babcock, T. Lukes, T. Pengo, J. Chao, R. Velmurugan, A. Herbert, A. Agrawal, S. Colabrese, A. Wheeler, A. Archetti, B. Rieger, R. Ober, G. M. Hagen, J.-B. Sibarita, J. Ries, R. Henriques, M. Unser, and S. Holden. “Super-resolution fight club: assessment of 2D and 3D single-molecule localization microscopy software”. In: *Nature Methods* 16.5 (2019), pp. 387–395.

[39] S. Liu and K. A. Lidke. “A Multiemitter Localization Comparison of 3D Superresolution Imaging Modalities”. In: *ChemPhysChem* 15.4 (2013), pp. 696–704.

[40] M. Badieirostami, M. D. Lew, M. A. Thompson, and W. E. Moerner. “Three-dimensional localization precision of the double-helix point spread function versus astigmatism and biplane”. In: *Applied Physics Letters* 97.16 (2010).

[41] Y. Shechtman, S. J. Sahl, A. S. Backer, and W. E. Moerner. “Optimal Point Spread Function Design for 3D Imaging”. In: *Physical Review Letters* 113.13 (2014).

[42] Y. Shechtman, L. E. Weiss, A. S. Backer, S. J. Sahl, and W. E. Moerner. “Precise Three-Dimensional Scan-Free Multiple-Particle Tracking over Large Axial Ranges with Tetrapod Point Spread Functions”. In: *Nano Letters* 15.6 (2015), pp. 4194–4199.

[43] C. Smith, M. Huisman, M. Siemons, D. Grünwald, and S. Stallinga. “Simultaneous measurement of emission color and 3D position of single molecules”. In: *Optics Express* 24.5 (2016), p. 4996.

[44] C. S. Smith, S. Stallinga, K. A. Lidke, B. Rieger, and D. Grunwald. “Probability-based particle detection that enables threshold-free and robust in vivo single-molecule tracking”. In: *Molecular Biology of the Cell* 26.22 (2015). Ed. by J. Lippincott-Schwartz, pp. 4057–4062.

[45] Y. Wang, J. Schnitzbauer, Z. Hu, X. Li, Y. Cheng, Z.-L. Huang, and B. Huang. “Localization events-based sample drift correction for localization microscopy with redundant cross-correlation algorithm”. In: *Optics Express* 22.13 (2014), p. 15982.

[46] A. Elmokadem and J. Yu. “Optimal Drift Correction for Superresolution Localization Microscopy with Bayesian Inference”. In: *Biophysical Journal* 109.9 (2015), pp. 1772–1780.

[47] J. Cnossen, T. J. Cui, C. Joo, and C. Smith. “Drift correction in localization microscopy using entropy minimization”. In: *Optics Express* 29.18 (2021), p. 27961.

[48] K. Prakash. “At the molecular resolution with MINFLUX?” In: *Philosophical Transactions of the Royal Society A: Mathematical, Physical and Engineering Sciences* 380.2220 (2022).

[49] S. C. M. Reinhardt, L. A. Masullo, I. Baudrexel, P. R. Steen, R. Kowalewski, A. S. Eklund, S. Strauss, E. M. Unterauer, T. Schlichthaerle, M. T. Strauss, C. Klein, and R. Jungmann. “Ångström-resolution fluorescence microscopy”. In: *Nature* 617.7962 (2023), pp. 711–716.

[50] M. Weber, M. Leutenegger, S. Stoldt, S. Jakobs, T. S. Mihaila, A. N. Butkevich, and S. W. Hell. “MINSTED fluorescence localization and nanoscopy”. In: *Nature Photonics* 15.5 (2021), pp. 361–366.

[51] M. Weber, H. von der Emde, M. Leutenegger, P. Gunkel, S. Sambandan, T. A. Khan, J. Keller-Findeisen, V. C. Cordes, and S. W. Hell. “MINSTED nanoscopy enters the Ångström localization range”. In: *Nature Biotechnology* 41.4 (2022), pp. 569–576.

[52] E. Nehme, L. E. Weiss, T. Michaeli, and Y. Shechtman. “Deep-STORM: super-resolution single-molecule microscopy by deep learning”. In: *Optica* 5.4 (2018), p. 458.

[53] E. Nehme, D. Freedman, R. Gordon, B. Ferdman, L. E. Weiss, O. Alalouf, T. Naor, R. Orange, T. Michaeli, and Y. Shechtman. “DeepSTORM3D: dense 3D localization microscopy and PSF design by deep learning”. In: *Nature Methods* 17.7 (2020), pp. 734–740.

[54] A. Speiser, L.-R. Müller, P. Hoess, U. Matti, C. J. Obara, W. R. Legant, A. Kreshuk, J. H. Macke, J. Ries, and S. C. Turaga. “Deep learning enables fast and dense single-molecule localization with high accuracy”. In: *Nature Methods* 18.9 (2021), pp. 1082–1090.

[55] J. Cnossen, S. Hung, D. Fan, J. B. Passmore, L. C. Kapitein, N. Dekker, and C. S. Smith. “Patterned illumination enables denser deep-learning based single-molecule localization microscopy”. In: *bioRxiv* (2025).

[56] I. Gyongy, A. Davies, N. A. W. Dutton, R. R. Duncan, C. Rickman, R. K. Henderson, and P. A. Dalgarno. “Smart-aggregation imaging for single molecule localisation with SPAD cameras”. In: *Scientific Reports* 6.1 (2016).

[57] I. M. Antolovic, S. Burri, C. Bruschini, R. A. Hoebe, and E. Charbon. “SPAD imagers for super resolution localization microscopy enable analysis of fast fluorophore blinking”. In: *Scientific Reports* 7.1 (2017).

[58] Q. Houwink, D. Kalisvaart, S. Hung, J. Cnossen, D. Fan, P. Mos, A. Can Ülkü, C. Bruschini, E. Charbon, and C. S. Smith. “Theoretical minimum uncertainty of single-molecule localizations using a single-photon avalanche diode array”. In: *Optics Express* 29.24 (2021), p. 39920.

[59] S. Scholes, G. Mora-Martín, F. Zhu, I. Gyongy, P. Soan, and J. Leach. “Fundamental limits to depth imaging with single-photon detector array sensors”. In: *Scientific Reports* 13.1 (2023).

[60] D. P. Hoffman, I. Slavitt, and C. A. Fitzpatrick. “The promise and peril of deep learning in microscopy”. In: *Nature Methods* 18.2 (2021), pp. 131–132.

[61] R. M. Neal. *Bayesian Learning for Neural Networks*. Springer New York, 1996.

[62] A. G. Wilson and P. Izmailov. “Bayesian Deep Learning and a Probabilistic Perspective of Generalization”. In: *Proceedings of the 34th International Conference on Neural Information Processing Systems*. NIPS ’20. Vancouver, BC, Canada: Curran Associates Inc., 2020.

[63] Y. Gal and Z. Ghahramani. “Dropout as a Bayesian approximation: representing model uncertainty in deep learning”. In: *Proceedings of the 33rd International Conference on International Conference on Machine Learning - Volume 48*. ICML’16. New York, NY, USA: JMLR.org, 2016, pp. 1050–1059.

[64] B. Lakshminarayanan, A. Pritzel, and C. Blundell. “Simple and scalable predictive uncertainty estimation using deep ensembles”. In: *Proceedings of the 31st International Conference on Neural Information Processing Systems*. NIPS’17. Long Beach, California, USA: Curran Associates Inc., 2017, pp. 6405–6416.

[65] T. Liu, J. Liu, D. Li, and S. Tan. “Bayesian deep-learning structured illumination microscopy enables reliable super-resolution imaging with uncertainty quantification”. In: *Nature Communications* 16.1 (2025).

[66] D. M. Blei, A. Kucukelbir, and J. D. McAuliffe. “Variational Inference: A Review for Statisticians”. In: *Journal of the American Statistical Association* 112.518 (2017), pp. 859–877.

[67] T. Chen, E. B. Fox, and C. Guestrin. “Stochastic Gradient Hamiltonian Monte Carlo”. In: *Proceedings of the 31st International Conference on International Conference on Machine Learning - Volume 32*. ICML’14. Beijing, China: JMLR.org, 2014, II–1683–II–1691.

[68] Y. Saatchi and A. G. Wilson. “Bayesian GAN”. In: *Proceedings of the 31st International Conference on Neural Information Processing Systems*. NIPS’17. Long Beach, California, USA: Curran Associates Inc., 2017, pp. 3625–3634.

[69] R. Peharz, A. Vergari, K. Stelzner, A. Molina, X. Shao, M. Trapp, K. Kersting, and Z. Ghahramani. “Random Sum-Product Networks: A Simple and Effective Approach to Probabilistic Deep Learning”. In: *Proceedings of The 35th Uncertainty in Artificial Intelligence Conference*. Ed. by R. P. Adams and V. Gogate. Vol. 115. Proceedings of Machine Learning Research. PMLR, 2020, pp. 334–344.

[70] R. Peharz, S. Lang, A. Vergari, K. Stelzner, A. Molina, M. Trapp, G. Van Den Broeck, K. Kersting, and Z. Ghahramani. “Einsum Networks: Fast and Scalable Learning of Tractable Probabilistic Circuits”. In: *Proceedings of the 37th International Conference on Machine Learning*. Ed. by H. D. III and A. Singh. Vol. 119. Proceedings of Machine Learning Research. PMLR, 2020, pp. 7563–7574.

[71] C. T. Ye, J. Han, K. Liu, A. Angelopoulos, L. Griffith, K. Monakhova, and S. You. “Learned, uncertainty-driven adaptive acquisition for photon-efficient scanning microscopy”. In: *Optics Express* 33.6 (2025), p. 12269.

[72] Abberior. *The price of a STED microscope*. 2025. (Visited on 08/08/2025).

[73] B. Diederich, P. Then, A. Jügler, R. Förster, and R. Heintzmann. “cellSTORM—Cost-effective super-resolution on a cellphone using dSTORM”. In: *PLOS ONE* 14.1 (2019). Ed. by T. Waigh, e0209827.

[74] K. J. A. Martens, S. P. B. van Beljouw, S. van der Els, J. N. A. Vink, S. Baas, G. A. Vogelaar, S. J. J. Brouns, P. van Baarlen, M. Kleerebezem, and J. Hohlbein. “Visualisation of dCas9 target search in vivo using an open-microscopy framework”. In: *Nature Communications* 10.1 (2019).

[75] R. Strack. “The miCube open microscope”. In: *Nature Methods* 16.10 (2019), pp. 958–958.

[76] J. B. Passmore, W. Nijenhuis, and L. C. Kapitein. “From observing to controlling: Inducible control of organelle dynamics and interactions”. In: *Current Opinion in Cell Biology* 71 (2021), pp. 69–76.

[77] V. Emiliani, E. Entcheva, R. Hedrich, P. Hegemann, K. R. Konrad, C. Lüscher, M. Mahn, Z.-H. Pan, R. R. Sims, J. Vierock, and O. Yizhar. “Optogenetics for light control of biological systems”. In: *Nature Reviews Methods Primers* 2.1 (2022).

[78] T. R. Mumford, L. Roth, and L. J. Bugaj. “Reverse and forward engineering multicellular structures with optogenetics”. In: *Current Opinion in Biomedical Engineering* 16 (2020), pp. 61–71.

[79] P. E. Farahani, E. H. Reed, E. J. Underhill, K. Aoki, and J. E. Toettcher. “Signaling, Deconstructed: Using Optogenetics to Dissect and Direct Information Flow in Biological Systems”. In: *Annual Review of Biomedical Engineering* 23.1 (2021), pp. 61–87.

[80] J. B. Passmore, A. Rates, J. Schröder, M. T. P. van Laarhoven, V. J. W. Hellebrekers, H. G. van Hoef, A. J. M. Geurts, W. van Straaten, W. Nijenhuis, F. Berger, C. S. Smith, I. Smal, and L. C. Kapitein. “Outcome-Driven Microscopy: Closed-Loop Optogenetic Control of Cell Biology”. In: *bioRxiv* (2024).

[81] P. Tan, L. He, Y. Huang, and Y. Zhou. “Optophysiology: Illuminating cell physiology with optogenetics”. In: *Physiological Reviews* 102.3 (2022), pp. 1263–1325.

[82] K. Prakash, B. Diederich, R. Heintzmann, and L. Schermelleh. “Super-resolution microscopy: a brief history and new avenues”. In: *Philosophical Transactions of the Royal Society A: Mathematical, Physical and Engineering Sciences* 380.2220 (2022).

[83] A. Claude. “The Constitution of Protoplasm”. In: *Science* 97.2525 (1943), pp. 451–456.

[84] K. R. Porter, A. Claude, and E. F. Fullam. “A study of tissue culture cells by electron microscopy”. In: *Journal of Experimental Medicine* 81.3 (1945), pp. 233–246.

[85] G. E. Palade. “A small particulate component of the cytoplasm”. In: *The Journal of Cell Biology* 1.1 (1955), pp. 59–68.

[86] B. Böttcher, S. A. Wynne, and R. A. Crowther. “Determination of the fold of the core protein of hepatitis B virus by electron cryomicroscopy”. In: *Nature* 386.6620 (1997), pp. 88–91.

[87] M. Bates, B. Huang, G. T. Dempsey, and X. Zhuang. “Multicolor Super-Resolution Imaging with Photo-Switchable Fluorescent Probes”. In: *Science* 317.5845 (2007), pp. 1749–1753.

[88] S. Abrahamsson, J. Chen, B. Hajj, S. Stallinga, A. Y. Katsov, J. Wisniewski, G. Mizuguchi, P. Soule, F. Mueller, C. D. Darzacq, X. Darzacq, C. Wu, C. I. Bargmann, D. A. Agard, M. Dahan, and M. G. L. Gustafsson. “Fast multicolor 3D imaging using aberration-corrected multifocus microscopy”. In: *Nature Methods* 10.1 (2013), pp. 60–63.

[89] M. Heilemann, D. P. Herten, R. Heintzmann, C. Cremer, C. Müller, P. Tinnefeld, K. D. Weston, J. Wolfrum, and M. Sauer. “High-Resolution Colocalization of Single Dye Molecules by Fluorescence Lifetime Imaging Microscopy”. In: *Analytical Chemistry* 74.14 (2002), pp. 3511–3517.

[90] R. P. J. Nieuwenhuizen, L. Nahidiazar, E. M. M. Manders, K. Jalink, S. Stallinga, and B. Rieger. “Co-Orientation: Quantifying Simultaneous Co-Localization and Orientational Alignment of Filaments in Light Microscopy”. In: *PLOS ONE* 10.7 (2015). Ed. by K. Gaus, e0131756.

[91] Y. S. Hu, M. Zimmerley, Y. Li, R. Watters, and H. Cang. “Single-Molecule Super-Resolution Light-Sheet Microscopy”. In: *ChemPhysChem* 15.4 (2014), pp. 577–586.

[92] N. Saliba, G. Gagliano, and A.-K. Gustavsson. “Whole-cell multi-target single-molecule super-resolution imaging in 3D with microfluidics and a single-objective tilted light sheet”. In: *Nature Communications* 15.1 (2024).

[93] S. Hung, J. Cnossen, D. Fan, M. Siemons, D. Jurriens, K. Grußmayer, O. Soloviev, L. C. Kapitein, and C. S. Smith. “SOLEIL: single-objective lens inclined light sheet localization microscopy”. In: *Biomedical Optics Express* 13.6 (2022), p. 3275.

[94] S. Hung, A. Llobet Rosell, D. Jurriens, M. Siemons, O. Soloviev, L. C. Kapitein, K. Grußmayer, L. J. Neukomm, M. Verhaegen, and C. Smith. “Adaptive optics in single objective inclined light sheet microscopy enables three-dimensional localization microscopy in adult Drosophila brains”. In: *Frontiers in Neuroscience* 16 (2022).

[95] M. J. Mlodzianoski, P. J. Cheng-Hathaway, S. M. Bemiller, T. J. McCray, S. Liu, D. A. Miller, B. T. Lamb, G. E. Landreth, and F. Huang. “Active PSF shaping and adaptive optics enable volumetric localization microscopy through brain sections”. In: *Nature Methods* 15.8 (2018), pp. 583–586.

[96] S. Park, Y. Jo, M. Kang, J. H. Hong, S. Shim, and W. Choi. “Restoring Single-Molecule Localizations with Wavefront Sensing Adaptive Optics for Deep-Tissue Super-Resolution Imaging”. In: *Imaging and Applied Optics Congress 2022 (3D, AOA, COSI, ISA, pcAOP)*. AOA. Optica Publishing Group, 2022, OTh5B.4.

[97] M. E. Siemons, N. A. K. Hanemaaijer, M. H. P. Kole, and L. C. Kapitein. “Robust adaptive optics for localization microscopy deep in complex tissue”. In: *Nature Communications* 12.1 (2021).

[98] M. Lelek, M. T. Gyparaki, G. Beliu, F. Schueder, J. Griffié, S. Manley, R. Jungmann, M. Sauer, M. Lakadamyali, and C. Zimmer. “Single-molecule localization microscopy”. In: *Nature Reviews Methods Primers* 1.1 (2021).

[99] J. Basumatary, N. Baro, F. C. Zanacchi, and P. P. Mondal. “Temporally resolved SMLM (with large PAR shift) enabled visualization of dynamic HA cluster formation and migration in a live cell”. In: *Scientific Reports* 13.1 (2023).

[100] X. Xu, W. Wang, L. Qiao, Y. Fu, X. Ge, K. Zhao, K. Zhanghao, M. Guan, X. Chen, M. Li, D. Jin, and P. Xi. “Ultra-high spatio-temporal resolution imaging with parallel acquisition-readout structured illumination microscopy (PAR-SIM)”. In: *Light: Science & Applications* 13.1 (2024).

[101] H. Kaur, D. Koundal, and V. Kadyan. “Image Fusion Techniques: A Survey”. In: *Archives of Computational Methods in Engineering* 28.7 (2021), pp. 4425–4447.

[102] A. Voulodimos, N. Doulamis, A. Doulamis, and E. Protopapadakis. “Deep Learning for Computer Vision: A Brief Review”. In: *Computational Intelligence and Neuroscience* 2018 (2018), pp. 1–13.

[103] A. Mohamed, J. Ren, M. E. Gindy, H. Lang, and A. Ouda. “Literature survey for autonomous vehicles: sensor fusion, computer vision, system identification and fault tolerance”. In: *International Journal of Automation and Control* 12.4 (2018), p. 555.

[104] A. Sroda, A. Makowski, R. Tenne, U. Rossman, G. Lubin, D. Oron, and R. Lapkiewicz. “SOFISM: Super-resolution optical fluctuation image scanning microscopy”. In: *Optica* 7.10 (2020), p. 1308.

[105] L. M. Beck, A. Shocher, U. Rossman, A. Halfon, M. Irani, and D. Oron. “Improving correlation based super-resolution microscopy images through image fusion by self-supervised deep learning”. In: *Optics Express* 32.16 (2024), p. 28195.

[106] T. Michaeli and M. Irani. “Nonparametric Blind Super-resolution”. In: *2013 IEEE International Conference on Computer Vision*. IEEE, 2013, pp. 945–952.

[107] A. Shocher, N. Cohen, and M. Irani. “Zero-Shot Super-Resolution Using Deep Internal Learning”. In: *2018 IEEE/CVF Conference on Computer Vision and Pattern Recognition*. IEEE, 2018, pp. 3118–3126.

[108] J. Liu, R. Lin, G. Wu, R. Liu, Z. Luo, and X. Fan. “CoCoNet: Coupled Contrastive Learning Network with Multi-level Feature Ensemble for Multi-modality Image Fusion”. In: *International Journal of Computer Vision* 132.5 (2023), pp. 1748–1775.

[109] T. Chen, S. Kornblith, M. Norouzi, and G. Hinton. “A simple framework for contrastive learning of visual representations”. In: *Proceedings of the 37th International Conference on Machine Learning*. ICML’20. JMLR.org, 2020.

[110] X. Wang, Z. Guan, W. Qian, J. Cao, S. Liang, and J. Yan. “CS²Fusion: Contrastive learning for Self-Supervised infrared and visible image fusion by estimating feature compensation map”. In: *Information Fusion* 102 (2024), p. 102039.

Epilogue and Acknowledgements

Since the start of my doctorate, I have held the belief that scientific communication should be more like storytelling. Actors, writers and artists have mastered the technique of keeping your attention, activating and involving you by triggering emotions through art. As keeping attention and involving the reader in your story should be key objectives of scientific communication as well, scientists can learn something from art here. A good scientific storyteller can invoke desire for a solution in their readers, only to subsequently destroy said hope through an obstacle, with the science being the key event to overcome the obstacle and deliver on the desire. Many of my former students and coworkers will likely remember my mantra: get me in, take me along and make me want something... that I cannot get!

Yet a good story is more than a mantra. It needs a final act, in which the high-stakes, adrenaline-filled plot is doused by a quieting of activities and the closure of plot lines. You likely recognize this from fairytales, which usually end in "And they lived happily ever after". While this specific claim is a normalized mistake in fairytale writing, as it would be unnatural and most unlikely that people live in a state of everlasting happiness, I do endorse the importance of ending the story with a sizzling episode of closure. Therefore holding myself to my own beliefs, I will now close the story of my doctorate.

After five years of research, supervision, teaching and hard work, I have reached the end of my doctoral studies. As the main character of my own story, I faced various scientific and non-scientific obstacles, starting with the world finding its way out of a global pandemic in 2020, and ending with the writing of the dissertation that lies before you. Before the start of my doctorate, I was warned that it could be a tough and lonely journey. The rumours of the toughness are drastically understated, and I certainly needed perseverance, organization and dedication to push through. I do not relate to the loneliness aspect though. On the contrary, throughout my doctorate I have had the lovely pleasure of meeting a great variety of amazing people, both nationally and internationally, and I was able to rely on my existing network more than ever. For this reason, I want to close my story by thanking the people who mattered to make my doctoral studies happen.

First of all, I want to deeply thank my supervisor and promotor, dr. ir. Carlas S. Smith. Over the many years that we worked together, I have come to know Carlas as a thorough, ambitious scientist with a broad research interest and a deeply rooted passion for our field. On top of that, I see him as a compassionate group leader with a deep care for his lab and the well-being of his students. But more than anything else, Carlas taught me the importance of separating work from life. Some of my best memories take place in his office, whether that consists of deriving equations on the whiteboard, discussing challenges in teaching or just generally talking about the state of the world. I thank Carlas for the amazing journey and for all the freedom and trust he gave me throughout my doctoral studies, and I will carry his teachings with me for the rest of my career.

Secondly, my gratitude goes out to prof. dr. ir. Michel Verhaegen, who was my promotor during the first four years of my doctorate before his pension. In Michel, I see a rare combination of an adventurous attitude and scientific rigour. He is able to treat established, complicated scientific problems with an open mind and a will to explore, leading to innovative solutions that do not follow the beaten path. In addition, he is a one-of-a-kind teacher with a clear teaching philosophy, full of enthusiasm and personality. Working with Michel is highly motivating, and I made some of his life lessons and teaching philosophy my own.

I am also grateful to my coworkers of the Intelligent and Reliable Imaging Systems (IRIS) lab, in particular my promotor dr. Arjen Jakobi and dr. David Maresca, who made it possible to explore my scientific interests outside the field of fluorescence imaging. Especially during the early stages of the doctoral studies, we had frequent meetings and journal clubs where we discussed not just fluorescence imaging, but also ultrasound localization microscopy, cryogenic electron microscopy and developments in artificial intelligence for imaging applications. This made it possible to broaden my horizons beyond the scope of this thesis, which resulted in valuable feedback for my research. In addition, it sharpened my views on the societal relevance of the technology we develop. Through the IRIS lab, I had various fruitful collaborations in both teaching and research, with my personal high point being the interdisciplinary publication between ultrasound localization microscopy and single-molecule localization, achieved through co-supervision between our labs.

I also want to extend my thanks to dr. ing. Sergio Grammatico, who recognized potential in one of my assignments during my Master studies and decided to take a gamble on me. Under his supervision, I was able to first experience the depths of scientific research and make all my rookie mistakes, ultimately resulting in the first paper I ever wrote. The opportunity given by Sergio fostered my interest in science and was a major contributor to my decision to pursue my doctorate. This life-changing project was one of the first times I felt acknowledged for going the extra mile in my studies, which strengthened my teaching philosophy of always going for the extra mile in supervision and to recognize, foster and challenge excellence in my students.

A special thanks goes out to all the coworkers I met throughout the years, of which I will highlight some. In the first place, I thank my direct coworkers in the Quantitative Nanoscopy lab, with whom I had many fruitful scientific and non-scientific discussions, as well as collaborations in teaching and research. In addition, over the course of the past year I had the pleasure to work with a fantastic group of people in the AI PhD Activity Committee, as part of the TU Delft AI Initiative. Thanks to your open-minded attitude we were able to organize a great symposium, and our collaboration was a welcome distraction from writing the dissertation.

Everyone who knows me, knows that my research work is inextricably linked to my passion for education. I had the absolute joy of supervising three bachelor groups, ten master students, in addition to being a contact point for many students in the Quantitative Nanoscopy lab and a teacher to hundreds of students in the Stochastic Signal Analysis course. These experiences resulted in two teaching awards during my doctorate, but the biggest reward has always been the experience of teaching you. Over the

years, I have received many acknowledgments from you, so it is now my place to thank you for all the questions, difficult situations and beautiful moments that you decided to share with me. Through your individual teachings, I was able to become a better teacher and person myself.

Over the years, I had the pleasure of both receiving a Paper of the Year award, as well as making it to the cover of a journal. Because of this, I have come into contact with various illustrators, photographers, directors, interviewers, science communicators and journalists, and I have appreciated all the interactions I had. As a scientist, you tend to feel very responsible for and protective of your research, but I have learned that a professional will enhance your story in ways you never thought to be possible. I will never forget my first scientific interview, which truly taught me that no matter how hard you try to prepare an easy-to-follow story, a communication professional will do that same job twice as fast and ten times as good. A special thanks goes to Anna Sieben, who made the stunning cover of this dissertation. She was able to shape my abstract scientific dreams and my rebellious personal wishes into a drawn metaphoric reality, for which I am deeply thankful. Isolated stars in the sky, under the patterned illumination of the *aurora borealis*, take a background role to what is the soul and centre of our research line: life. The keen eye may even notice various Easter eggs on the cover...

The last acknowledgment always receives the most emphasis, and is therefore the most important. For this reason, I want to thank my amazing friends and family last. You have showed me your full, continuous and unconditional support throughout all of my studies. I have celebrated with you in my brightest moments and relied on you in my darkest. With you, I am able to explore the world, live my culinary dreams and experience the life of a lifetime. Thank you for always being there for me. I am glad to have each one of you in my life and I hope that I may revel in your love and friendship over the course of the rest of my life.

A special mention goes to my housemate and friend Daniel Scheer. From the first day of my Bachelor studies, Daniel has always been there for me. It was a pleasure to be locked in the house with you during the COVID-times, and it is still a pleasure to come back home every day. The fact that you were always there for me, even in those moments where I came home too tired to formulate a coherent sentence, and always listened to my whining and fixed me up with a good meal have been important success factors in my doctorate. For all you meant and continue to mean to me, I thank you deeply.

As a final mention, I want to thank my long-time friend Perttu Heikkilä. As a diversion during my doctorate, Perttu motivated me to pick up my old hobby of reading. Between Perttu and me, we therefore started a fantasy book club of sorts, in which we read and discussed the same books together. At the time of writing, we have read all of Terry Pratchett's Discworld, the Lord of the Rings trilogy, the Books of Earthsea, the Howl's Moving Castle trilogy and many other stand-alone novels. This resulted in inspiration for propositions, provoking quotes at the start of each chapter and my dutiful coffee mug, which states:

YOU DON'T HAVE TO BE MAD
TO WORK HERE BUT IT HELPS

Sharing quotes and discussing these books with you has been a fantastic diversion to some of the more mundane days of the doctorate. But on top of that all, you are an amazing friend with whom I can share everything. You showed me the beautiful nature of Finland in both summer and in winter, and our cabin trips have strengthened my appreciation of nature and taught me what it means to live in the moment, unplugged from water and electricity and therefore with full attention and appreciation for the people around me. Words cannot capture how much you mean me, but know that in my best moments and in my worst, you make me remember what it means to be alive. Thank you for always being there for me on this journey, and I appreciate and love you from the bottom of my heart.

And now, there is only one more person to thank: you, the reader. Thank you for reading my dissertation and for sticking with me through the story of my doctorate. While I was only able to give you a condensed overview of five amazing years of research and teaching, I hope you enjoyed reading it with the same passion as I had living through it.

Curriculum Vitæ

Dylan Kalisvaart

Feb. 21, 1997 Born in The Hague, the Netherlands.

Education

2008 - 2015 Gymnasium (*summa cum laude*)
Gymnasium Haganum, the Netherlands

2013 - 2015 Pre-University College
Leiden University, the Netherlands

2015 - 2018 BSc Mechanical Engineering (*cum laude and with honors*)
Delft University of Technology, the Netherlands
Thesis: Design of a modular 3D printable multicolor single-molecule localization microscope
Supervisor: dr. ir. C. S. Smith

2018 - 2020 MSc Systems & Control (*cum laude*)
Delft University of Technology, the Netherlands
Thesis: Precision in iterative modulation enhanced single-molecule localization microscopy
Supervisor: dr. ir. C. S. Smith

2020 - 2025 PhD
Delft University of Technology, the Netherlands
Thesis: Quantifying the localization uncertainty of modulation enhanced single-molecule localization microscopy: the invisible visible, the uncertain certain
Promotors: dr. A. Jakobi and dr. ir. C. S. Smith

Awards

2022	Biophysical Journal Paper of the Year Award 2022, for *Precision in iterative modulation enhanced single-molecule localization microscopy* (Biophysical Journal, 2022).
2024	Outstanding Teaching Assistant Award, for excellent contributions as a teaching assistant to the course *Stochastic Signal Analysis* (Delft Center for Systems and Control, 2024).
2024	Cover of Biophysical Reports, vol 4., no. 1, for *Quantifying the minimum localization uncertainty of image scanning localization microscopy* (Biophysical Reports, 2024).

List of Publications

Journal Publications - peer reviewed

8. G. Rijpkema, **D. Kalisvaart**, S. Korovin, D. Spengler, A. Pals, J. van der Weerd, and C. S. Smith. "Reducing Manual Labour in Forensic Microtrace Recognition with Deep Learning". In: *Forensic Science International* 379 (2026), p. 112714.

7. C. S. Smith, **D. Kalisvaart**, and K. Prakash. "Unveiling the limits of precision in iterative MINFLUX". In: *Journal of Microscopy* 296.2 (2024), pp. 129–132.

6. **D. Kalisvaart**, S. Hung, and C. S. Smith. "Quantifying the minimum localization uncertainty of image scanning localization microscopy". In: *Biophysical Reports* 4.1 (2024), p. 100143.

5. S. Hung, **D. Kalisvaart**, and C. S. Smith. "Image scanning microscopy: a vectorial physical optics analysis". In: *Optics Express* 32.2 (2024), p. 1524.

4. R. van Dijk[†], **D. Kalisvaart**[†], J. Cnossen, and C. S. Smith. "Bayesian posterior density estimation reveals degeneracy in three-dimensional multiple emitter localization". In: *Scientific Reports* 13.1 (2023).

3. M. Wiersma, B. Heiles, **D. Kalisvaart**, D. Maresca, and C. S. Smith. "Retrieving Pulsatility in Ultrasound Localization Microscopy". In: *IEEE Open Journal of Ultrasonics, Ferroelectrics, and Frequency Control* 2 (2022), pp. 283–298.

2. **D. Kalisvaart**, J. Cnossen, S. Hung, S. Stallinga, M. Verhaegen, and C. S. Smith. "Precision in iterative modulation enhanced single-molecule localization microscopy". In: *Biophysical Journal* 121.12 (2022), pp. 2279–2289.

1. Q. Houwink, **D. Kalisvaart**, S. Hung, J. Cnossen, D. Fan, P. Mos, A.C. Ülkü, C. Bruschini, E. Charbon, and C. S. Smith. "Theoretical minimum uncertainty of single-molecule localizations using a single-photon avalanche diode array". In: *Optics Express* 29.24 (2021), p. 39920.

Conference Publications - peer reviewed

1. **D. Kalisvaart**, J. Bonekamp, and S. Grammatico. "Bi-hormonal Linear Time-Varying Model Predictive Control for Blood Glucose Regulation in Type 1 Diabetes Patients". In: *2023 IEEE Conference on Control Technology and Applications (CCTA)*. IEEE, 2023, pp. 552–558.

Preprints

1. S. Korovin, **D. Kalisvaart**, S. Hung, J. Cnossen, C. de Visser, and C. S. Smith. "Using splines for point spread function calibration at non-uniform depths in localization microscopy". In: *bioRxiv* (2024).

[†] These authors contributed equally to this work.